Studies of the Response of Silicon Photomultipliers and Testbeam Data Analysis of a Highly Granular Analog Hadron Calorimeter Prototype

Dissertation

zur Erlangung des Grades

Doktor der Naturwissenschaften

am Fachbereich Physik, Mathematik und Informatik

der Johannes Gutenberg-Universität

in Mainz

Sascha Christian Krause

geboren in Wiesbaden

Mainz, den 03.09.2019

Zusammenfassung

Zukünftige Elektron-Positron Collider, wie der geplante International Linear Collider (ILC), sind auf Grund ihrer wohldefinierten Ausgangsbedingungen prädestiniert für Präzisionsmessungen, beispielsweise des Higgs-Bosons, und damit komplementär zu Proton-Proton Collidern wie dem Large Hadron Collider (LHC), welcher sich insbesondere durch bisher unerreichte Schwerpunktenergien von $\sqrt{s} = 13\,\text{TeV}$ auszeichnet und damit wesentlich zur Suche nach neuer Physik beiträgt. Präzisionsmessungen auf der anderen Seite ermöglichen die Validierung des Standardmodells, beziehungsweise die Suche nach möglichen Abweichungen.

Entscheidend für Präzisionsmessungen dieser Art ist eine hohe Energieauflösung der Teilchendetektoren, die mit Hilfe des Particle-Flow-Algorithmus erreicht werden soll, welcher eine hohe Granularität des Detektors voraussetzt. Das CALICE Analog Hadron Calorimeter (AHCAL) wird zu diesem Zweck entwickelt und basiert auf $30 \times 30 \times 3\,\text{mm}^3$ kleinen Szintillatorkacheln (Tile), welche von Silizium-Photomultipliern (SiPM) ausgelesen werden. SiPMs sind neuartige Photodetektoren, welche aus einem Array von bis zu einigen Tausend Pixeln bestehen, welche jeweils vergleichbar zu Avalanche-Photodioden im Geigermodus betrieben werden.

Diese Arbeit präsentiert die Untersuchung des Saturierungsverhaltens der Response von SiPMs, zum einen im eigenständigen Betrieb und zum anderem im kombinierten SiPM-Tile-System innerhalb eines AHCAL Prototypen unter Verwendung von Teststrahl Daten. Diese Daten umfassen μ^-, e^- und π^- Messungen, welche am Super Proton Synchrotron (SPS) am CERN im Juli 2015 aufgenommen worden sind. Die Analyse dieser Teststrahldaten mithilfe von Simulationen bildet dabei einen wesentlichen Teil dieser Arbeit.

Im Rahmen dieser Arbeit ist ein Teststand in Betrieb genommen worden, welcher die automatisierte Vermessung des SiPM Saturierungsverhaltens im eigenständigen Betrieb ermöglicht. Die Resultate der Messung werden mit unterschiedlichen Response Modellen verglichen und zeigen, wie zu erwarten, eine deutliche Abhängigkeit des Saturierungsverhaltens von der Anzahl der Pixel des SiPMs. Besonderen Einfluss auf die Response hat außerdem die Wahrscheinlichkeit für optisches Übersprechen. Für einige SiPMs wird zudem Übersaturierung beobachtet.

Die Analyse der Teststrahldaten des AHCAL Prototypen, welcher aus 14 aktiven Lagen besteht, bildet den zweiten großen Teil dieser Arbeit. Insbesondere die Nichtverfügbarkeit insgesamt vierer dieser Lagen, als auch die Verwendung unterschiedlicher Lagengenerationen mit abweichenden SiPM-Tile-Konfigurationen erschwert diese Analyse. Ein nicht vorgesehener niederenergetischer Untergrund in Elektron Daten erzwingt spezielle Ereignisselektionen und Anpassungen der Simulationen, um deren Vereinbarkeit zu gewährleisten. Eine Methode wird ausgearbeitet, mit welcher sich die Response des SiPM-Tile-Systems mit Hilfe der Teststrahldaten und Simulationen analysieren lässt. Es zeigt sich erneut eine deutliche Abhängigkeit von der Zahl der Pixel des SiPMs, sowie eine Abhängigkeit von der Wahrscheinlichkeit für optisches Übersprechen. In einem finalen Schritt werden die Linearität und Energieauflösung des Prototypen untersucht und Rückschlüsse für Optimierungsmöglichkeiten gezogen.

Abstract

Future electron-positron collider, as the planned International Linear Collider (ILC), are predestined for precision measurements, for instance of the Higgs boson, because of their well-defined initial conditions. They are therefore complementary to proton-proton colliders, as the Large Hadron Collider (LHC), which in particular stands out with the highest center of mass energy of up to $\sqrt{s} = 13\,\text{TeV}$ and significantly contributes to the search of new physics. On the other hand, precision measurements allow to validate the standard model, or rather to search for possible deviations.

A major requirement for such precision measurements is a high energy resolution of particle detectors, which is supposed to be achieved by means of the Particle Flow Approach, that requires a high granularity of the detector. The CALICE Analog Hadron Calorimeter (AHCAL) is developed for this purpose and is based on $30 \times 30 \times 3\,\text{mm}^3$ small scintillator tiles read out by Silicon Photomultipliers (SiPM). SiPMs are novel photo detectors, which consist of an array of up to thousands of pixels, each operated in Geiger-mode comparable to avalanche photodiodes. This thesis presents a study of the response saturation of SiPMs, on the one hand in a stand-alone operation and on the other hand in a combined SiPM-tile system within an AHCAL prototype, where testbeam data are utilized. These data comprise μ^-, e^- and π^- measurements which have been recorded at the Super Proton Synchrotron (SPS) at CERN in July 2015. The analysis of testbeam data by means of simulations are an essential part of this thesis. In the course of this thesis, a setup has been put into operation which enables an automated measurement of the response saturation of stand-alone SiPMs. The results of these measurements are compared to different response models and show, as expected, a significant dependence of the saturation behavior to the total number of pixels of a SiPM. Especially, the probability for optical crosstalk also shows a clear impact on the response. Moreover, over-saturation is observed for some SiPMs.

The second part of this thesis is about the analysis of testbeam data of the AHCAL prototype, which consists of 14 active layers. The non-availability of in total four of these layers, as well as the utilization of various layer generations with different SiPM-tile configurations, in particular complicate this analysis. An unforeseen low-energy background in electron data demands special event selections and adjustments to the simulation to ensure their compatibility. A method is developed which allows to analyze the response of the SiPM-tile system by utilizing testbeam data and simulation. Once again, a clear dependence to the total number of SiPM pixels is apparent, as well as to the optical crosstalk probability. In a final step, the linearity and energy resolution of the prototype are investigated and conclusions are drawn concerning optimization possibilities.

Contents

Introduction

In the past decades, more and more insides into the structure of matter and the interactions between particles have been gained. One cornerstone of this progress are particle collider experiments with over time increasing capability and complexity. By the acceleration and controlled collision of particles, energy is released from which new particles are generated and measured in particle detectors.

The leading particle accelerator with the highest center of mass energy of up to $\sqrt{s} = 13\,\text{TeV}$ for protons is the Large Hadron Collider (LHC) at CERN. Back in 2012, the Higgs boson was discovered at the LHC at two independent experiments, the ATLAS and the CMS experiments. [1, 2] This discovery completes the Standard Model of particle physics.

The International Linear Collider (ILC) is a planned linear lepton collider which is considered for complementary precision measurements, for instance of the Higgs boson, and discoveries. The collision of electrons and positrons at a planned center of mass energy of $\sqrt{s} = 250\,\text{GeV}$, upgradable up to $\sqrt{s} = 1000\,\text{GeV}$ in several stages, gives an advantage to precise measurements because of the well known initial situation, as both e^- and e^+ are fundamental particles in contrast to protons.

A large challenge for precision measurements at the ILC is a so far unprecedented jet energy resolution. A solution for this requirement is the Particle Flow Approach (PFA) which combines the information of all sub-detectors to optimize the energy resolution to about 3 to 4 %. [3]. For each particle in a jet, either the tracking system, the electromagnetic or the hadronic calorimeter is used for the momentum and energy reconstruction, depending on the best suited option. To distinguish between different particles in a jet, a high spatial granularity of the calorimeters is required.

The CALICE collaboration develops sampling calorimeter prototypes with high granularity. [4] The Analog Hadron Calorimeter (AHCAL) combines novel Silicon Photomultipliers (SiPMs) with plastic scintillator tiles to form channels of $30 \times 30 \times 3\,\text{mm}^3$, which are arranged in consecutive layers. SiPMs consist of an array of pixels, each operated in Geiger-mode and read out together. The AHCAL prototype with a variety of different layers has been tested with muon, electron an pion beams at CERN SPS in 2015.

This thesis covers two main aspects in the context of the AHCAL prototype. The first part is a self-contained study of the response saturation of stand-alone SiPMs. For this purpose, a setup is put into operation and measurement results of four SiPM types are analyzed and compared to three different response models. In the second part, various studies of testbeam data are performed. Challenging circumstances of both, the beam and the prototype configuration, require dedicated event selections and adjustments to simulation. The response of the SiPM-tile system is studied by utilizing testbeam data and simulation, investigating the impact of different layer configurations. Finally, the response linearity and energy resolution of the prototype is analyzed.

The first chapter gives an overview of the Standard Model and describes particle interactions with matter. Thereafter, the concept of calorimetry and of the PFA is explained.

The ILC is discussed in the second chapter, with details about the International Large Detec-

tor (ILD), where for instance details about the tracking system and the electromagnetic and hadronic calorimeters are given.

Chapter three goes into more detail about the AHCAL. Starting with the design, all essential parts of the calorimeter are explained, for example the HCAL Base Unit (HBU) to which the channels are attached and read out. Details about the SiPM-tile system are included, besides information about DAQ and readout electronics. The chapter ends with a short summary of the current status and future plans of the prototype.

From chapter four to six, the SiPM response analysis is discussed. Starting in the fourth chapter, the measurement concepts of SiPM characteristics are described. Afterwards, the response saturation behavior of SiPMs is focused and three different response models are presented.

Chapter five describes the SiPM response measurement setups built as part of this thesis, which extend existing SiPM setups at the PRISMA Detector Lab [5] at Mainz. Additional small setups are utilized to measure SiPM crosstalk and the linearity of readout devices.

The analysis of the SiPM response saturation is discussed in chapter six, starting with the calibration procedure and linearity measurements utilizing the small setups just mentioned. SiPM crosstalk is discussed in detail, as it has a large impact on the SiPM response. Finally, the response of four different SiPMs is analyzed, taking into account the three different SiPM response models.

Chapters seven to nine deal with analysis of testbeam data of the AHCAL technological prototype at CERN in 2015. In Chapter seven, the data handling is described, including the simulation, digitization, reconstruction and calibration procedure, which is required to prepare measured data and compare it to simulation.

In chapter eight, the analysis of testbeam data is started by estimating event selections for all three particle types on the basis of simulation. A low-energy electron contamination in electron data requires further investigations resulting in additional event selections and additional upstream absorber in the simulation. The simulation is further tuned concerning the absorber thickness and the tile-to-tile crosstalk in several layers.

Finally in chapter nine, the response of the SiPM-tile system is studied by a comparison of data to two different response models applied to simulation. The capabilities of these models are studied in detail layer by layer, with the goal to find an optimal model parametrization. Last but not least, the linearity of the response and the energy resolution of the AHCAL prototype are analyzed.

1

Theory Foundations and Detector Aspects

This chapter gives an introduction to the Standard Model (SM) of particle physics and the origin of mass via the Higgs mechanism. Afterwards, a description of the most common interactions between particles and matter with regards to the generation of particle showers is shown. That given, the concept of calorimetry is presented as a tool to estimate the energy of a primary particle. The end of this chapter gives a short overview of the Particle Flow Approach, which aims to improve the energy resolution of a detector.

1.1. Introduction to the Standard Model of Particle Physics

The Standard Model (SM) of particle physics is so far the most confirmed model which describes the properties and interactions of elementary particles. It has been formulated in the seventies of the last millennium after preceding progress in the theory of strong interactions [6] (Quantum Chromodynamic, QCD) and the unification of the electromagnetic and weak theory to a combined electroweak theory [7]. With the integration [8, 9] of the Higgs mechanism[10, 11], the standard model has been finalized in the form it has today.

The SM has been validated in several experiments over the last decades, which includes the observations of predicted particles. In 2012, the observation of the Higgs boson at the LHC at CERN has completed the SM. [1, 2]

The following discussion of the SM, the Higgs mechanism and the limits of the SM, is based on the references [12, 13, 14, 15] and formulas are taken from [14], if not stated otherwise.

The Standard Model divides all elementary particles into three groups: twelve fermions with spin $s = 1/2$ (this thesis uses the convention $\hbar = c = 1$, if not stated otherwise) which follow the Fermi-Dirac statistics [16], four gauge bosons with spin $s = 1$ and the Higgs boson with spin $s = 0$. Bosons with integer spin follow the Bose-Einstein statistics [17]. An illustration of the SM is shown in Figure 1.1 and an overview of SM particles and interactions is given in the following. Quantum numbers describe the properties of elementary particles, as for example the electric charge Q or the spin s.

1.1.1. Fermions

All matter is formed by *fermions*, which are subdivided into *quarks q* and *leptons l* of six different flavors each. These groups are further subdivided into three generations each, according to their masses. For each fermion, an antiparticle with the same mass but opposite additive quantum numbers, for instance inverse electric charge, exists.

The six leptons are divided into electrically charged leptons and neutral neutrinos of three gen-

erations each. The electron (e), muon (μ) and tau (τ) carry an electrical charge of $Q = -1$ in units of elementary charge q_e (omitted in the following). For each charged lepton, a respective neutral lightweight neutrino in the same generation exists (ν_e, ν_μ, ν_τ). It should be mentioned, that neutrinos first have been expected to be massless, but the observation of neutrino oscillations requires the neutrinos to have small masses [18].

The six quarks are separated in two groups of up-type quarks (u, c, t) with electrical charge of $Q = 2/3$ and down-type quarks (d, s, b) with electrical charge of $Q = -1/3$. They also carry color charge (red, green, blue) as well as the gluon does. Quarks are not observed as free particles but form color-neutral *hadrons* of a pair of quark and anti-quark, called meson ($q\bar{q}$), or of a triplet of three quarks or anti-quarks, called baryon (qqq) or anti-barion ($\bar{q}\bar{q}\bar{q}$), respectively. This feature of color-neutrality is called *color confinement*.

1.1.2. Gauge Bosons

The interactions between elementary particles are mediated by gauge bosons. In nature, four fundamental forces are known: the electromagnetic, the weak and the strong force as well as the gravitation. The latter is not included in the SM, but it's impact on the scale of elementary particles is expected to be negligible. The SM includes the first three forces, while the electromagnetic and the weak force are unified.

In the SM, forces are mediated by gauge bosons with spin 1.

The *electromagnetic force* is mediated by the massless photon (γ) and couples to electrically charged particles. Because it is massless, it's range is generally infinite.

The mediators of the *weak force* are the two electrically charged $W^\pm$ and the neutral Z^0 bosons. These bosons are heavy with masses of about 80.38 GeV and 91.19 GeV [19], respectively, which limits the range of the force to about 10^{-3} fm, [12] as described by the Yukawa-potential [20]. All elementary particles interact with the weak force which is responsible for interactions where flavor changes. Especially also neutrinos interact through the weak force, which furthermore has been the reason for the discovery of the weak force through the β^--decay.

The *strong force* which is responsible for holding all matter together, is mediated by eight massless gluons (g). A gluon mediates color charge and therefore only couples to quarks, not leptons. An important feature of a gluon is that it is self-interacting (as also the bosons of the weak interaction are) because it also carries color charge. This has the effect, that the potential between two particles with color charge increases with rising distance (*color confinement*, see above) such that from a certain distance on, the energy is high enough for quark-antiquark pair production. Though the gluon is massless, the range of the strong force is thus limited by this effect to the order of 1 fm. [12] On the other hand at small distances, quarks act as free particles referred to as *asymptotic freedom*. Quarks and gluons form color-neutral hadrons in a process called *hadronization*. In collider experiments, where for instance a quark-antiquark pair is generated in an electron-positron annihilation, these two particles commonly move apart from each other. With rising distance, gluons are radiated and new quark-antiquark pairs are generated due to color confinement as explained above, and form new color-neutral hadrons following the upper procedure. As such a cascade develops along a narrow cone, it is called a *jet*.

Standard Model of Elementary Particles
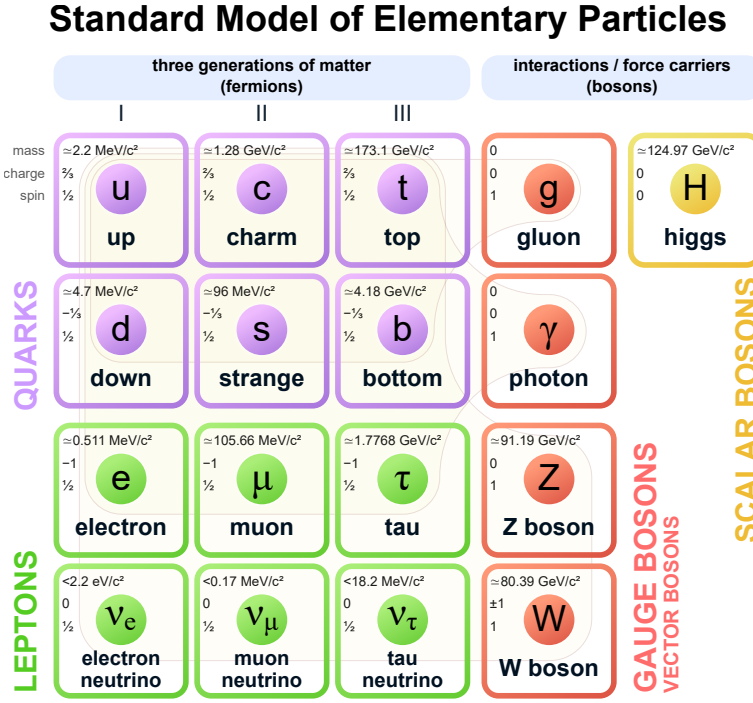
Figure 1.1.: Elementary particles of the Standard Model sorted in groups of 12 fermions, containing quarks (violet) and leptons (green), 4 gauge bosons (red) and the scalar Higgs boson (yellow). [21]

1.1.3. Gauge Symmetries

The quantum field theory (QFT) [22] is the mathematical framework of the Standard Model. Elementary particles are described by excitations of quantum (Dirac) fields ψ as a function of spacetime and the Lagrangian density $\mathscr{L}$ (short Lagrangian) determines the dynamics of quantum fields.

According to Noether's theorem [23], a conservation law exists for each symmetry of a physical system. Symmetries require the Lagrangian to be invariant under transformations, which, in case of the SM, can be formulated as the gauge group $SU(3)_C \times SU(2)_L \times U(1)_Y$, where $SU(2)_L \times U(1)_Y$ corresponds to the symmetry group of the electroweak interaction and $SU(3)_C$ to the strong interaction. These symmetry groups are *local* gauge symmetries, where the parameters of transformations depend on the spacetime coordinates. A local symmetry relates to a transformation of internal quantum numbers and thus to a transformation of one particle into another. The generators of these symmetry groups can be associated with the related gauge bosons.

To make it more concrete, the local gauge invariance of the $U(1)$ symmetry group of **quantum electrodynamics (QED)** is discussed in the following. The Lagrangian in Equation 1.1 describes a free fermion of mass m,

$$\mathscr{L} = i\bar{\psi}\gamma^\mu\partial_\mu\psi - m\bar{\psi}\psi \ , \tag{1.1}$$

with the gamma matrices γ^μ. Under a local phase transformation

$$\psi(x) \to e^{i\alpha(x)}\psi(x) \ , \tag{1.2}$$

where the phase α explicitly depends on spacetime x, the first term of the Lagrangian in Equation 1.1 is not invariant, instead, a term proportional to $\partial_\mu\alpha$ appears and thus breaks the invariance. In order to restore invariance by neutralizing the unwanted term, the covariant derivative $\mathcal{D}_\mu$ is constructed according to Equation 1.3,

$$\mathcal{D}_\mu = \partial_\mu - ieA_\mu \ , \tag{1.3}$$

with the charge e of the Dirac particle and a vector field A_μ which transforms as

$$A_\mu \to A_\mu + \frac{1}{e}\partial_\mu\alpha(x) \ , \tag{1.4}$$

In comparison to the Lagrangian in Equation 1.1, the adjusted Lagrangian then includes an additional term $e\bar{\psi}\gamma^\mu A_\mu\psi$ which is summarized as $-j^\mu A_\mu$ with the current density j^μ. This vector (gauge) field A_μ can be identified as the photon field which couples to the Dirac particle. By adding an invariant term to the Lagrangian which represents the kinetic energy of the photon field given by the *field strength tensor*

$$F_{\mu\nu} = \partial_\mu A_\nu - \partial_\nu A_\mu \ , \tag{1.5}$$

the Lagrangian of the QED is found as shown in Equation 1.6

$$\mathscr{L}_{QED} = \bar{\psi}(i\gamma^\mu\partial_\mu - m)\psi + e\bar{\psi}\gamma^\mu A_\mu\psi - \frac{1}{4}F_{\mu\nu}F^{\mu\nu} \ . \tag{1.6}$$

The first term corresponds to the kinetic energy and the mass of ψ, the second to the interaction of ψ with A_μ and, as just mentioned, the last to the kinetic energy of A_μ. It is important to note, that a term of the form $\frac{1}{2}m^2 A_\mu A^\mu$, which is related to a mass of the new vector field A_μ, cannot be added to the Lagrangian as this would break its gauge invariance, thus, the photon has to be massless.

In *quantum chromodynamics (QCD)*, similar is the case for the eight gluons which are related to the eight generators $\lambda_a/2$ with $a = 1, ..., 8$ of the non-Abelian $SU(3)_C$ symmetry group, which are also required to be massless to maintain local gauge invariance of the related Lagrangian of the QCD, which describes strong interactions of quarks.

In the **electroweak sector**, where the electromagnetic and the weak interactions are unified, the corresponding symmetry group is $SU(2)_L \times U(1)_Y$. In contrast to $U(1)$, which is an Abelian symmetry group, $SU(2)$ is non-Abelian. Together, the group has a total of four generators: $U(1)_Y$ represents the weak hyper charge (Y) group with the generator $Y/2$ and $SU(2)_L$ represents the weak isospin (T) group with the three component generators $\boldsymbol{T} = \boldsymbol{\sigma}/2$, where $\boldsymbol{\sigma}$ are the Pauli matrices. These generators are assigned to the gauge boson fields B_μ and $\boldsymbol{W}_\mu$, respectively.

The $SU(2)_L$ only couples to left-handed fermions, as indicated by the index L. Handedness is a

characteristic called helicity and corresponds to the projection of the spin to the momentum of a particle. This different treatment of left-handed and right-handed fermions is a special feature of the weak interaction which is not invariant under parity transformations.

Right-handed fermions transform as isospin singlets with $T = T_3 = 0$ with the third component of the weak isospin T_3, while left-handed fermions transform as doublets with $T = 1/2$ and $T_3 = +1/2$ for left-handed neutrinos (ν_L) and up-type quarks (u_L) or $T_3 = -1/2$ for left-handed electrons (e_L) and down-type quarks (d_L). For instance,

$$\psi_L = \begin{pmatrix} \nu \\ e \end{pmatrix}_L , \tag{1.7}$$

forms a left-handed electron and neutrino isospin doublet with the weak hyper charge $Y = -1$, while for example $\psi_R = e_R$ forms a right-handed electron isospin singlet with $Y = -2$.

The weak hyper charge Y is connected to the electric charge Q and to the third component of the weak isospin T_3 through the Gell-Mann-Nishijima formula [24] according to

$$Q = T_3 + \frac{1}{2}Y . \tag{1.8}$$

Each of the underlying symmetry groups have independent coupling strengths, g' for $U(1)_Y$ and g for $SU(2)_L$. Again requiring local gauge invariance, the electroweak Lagrangian for instance for an neutrino-electron pair is of the form

$$\mathscr{L}_{EW} = \bar{\psi}_L \gamma^\mu \left(i\partial_\mu - g\frac{\boldsymbol{\sigma}}{2}\boldsymbol{W}_\mu - g'\frac{Y}{2}B_\mu \right)\psi_L + \bar{\psi}_R \gamma^\mu \left(i\partial_\mu - g'\frac{Y}{2}B_\mu \right)\psi_R - \frac{1}{4}\boldsymbol{W}_{\mu\nu}\boldsymbol{W}^{\mu\nu} - \frac{1}{4}B_{\mu\nu}B^{\mu\nu}, \tag{1.9}$$

where the last two terms are field strength tensors and $B_{\mu\nu}B^{\mu\nu}$ corresponds to the kinetic energy of the B_μ field, whereas $\boldsymbol{W}_{\mu\nu}\boldsymbol{W}^{\mu\nu}$ contains the kinetic energy and an additional self-coupling term, which is a result of the non-Abelian characteristic of $SU(2)$, of the $\boldsymbol{W}_\mu$ fields. As shown in the second term, right-handed fermions do not interact through the weak interaction. Additional terms for other leptons and quarks can be added accordingly to Equation 1.9. Again here, to maintain local gauge invariance, the Lagrangian requires the gauge fields to be massless, where Section 1.1.4 will refer to in a moment.

The observed photon A_μ, the $W_\mu^\pm$ and the Z_μ bosons as introduced in Section 1.1.2 are obtained from equations 1.10 and 1.11,

$$W_\mu^\pm = \frac{1}{\sqrt{2}}\left(W_\mu^1 \mp iW_\mu^2 \right) , \tag{1.10}$$

$$\begin{pmatrix} A_\mu \\ Z_\mu \end{pmatrix} = \begin{pmatrix} \cos\theta_W & \sin\theta_W \\ -\sin\theta_W & \cos\theta_W \end{pmatrix} \begin{pmatrix} B_\mu \\ W_\mu^3 \end{pmatrix} , \tag{1.11}$$

where θ_W is the weak mixing angle, which also connects the electric charge e with the couplings g and g' according to

$$e = g\sin\theta_W = g'\cos\theta_W . \tag{1.12}$$

1.1.4. The Higgs Mechanism

The origin of mass in the SM has been a large challenge. In order to maintain local gauge invariance of the Lagrangian in electroweak interactions, the gauge fields have to be massless. Though this is consistent with the massless photon (and gluons in QCD), the experimental observation of heavy $W^{\pm}$ and Z bosons [25, 26] seemed to disagree to that requirement. The Higgs mechanism [10, 11] is a solution, which introduces scalar fields with a non-zero *vacuum expectation value* due to *spontaneous symmetry breaking*, which is discussed briefly in the following.

In the Higgs mechanism, four real scalar fields ϕ_i are introduced, which form a $SU(2) \times U(1)$ complex scalar isospin doublet, as for instance the choice

$$\phi = \begin{pmatrix} \phi^+ \\ \phi^0 \end{pmatrix} , \tag{1.13}$$

with $\phi^+ = 1/\sqrt{2}(\phi_1 + i\phi_2)$ and $\phi^0 = 1/\sqrt{2}(\phi_3 + i\phi_4)$. The Higgs field ϕ has a weak hyper charge of $Y = 1$ and keeps the Lagrangian in Equation 1.14 gauge invariant, which can be added to the electroweak Lagrangian (cf. Equation 1.9).

$$\mathscr{L} = \left(i\partial_\mu - g\frac{\boldsymbol{\sigma}}{2}\boldsymbol{W}_\mu - g'\frac{Y}{2}B_\mu \phi \right)^\dagger \left(i\partial^\mu - g\frac{\boldsymbol{\sigma}}{2}\boldsymbol{W}^\mu - g'\frac{Y}{2}B^\mu \phi \right) - V(\phi) \tag{1.14}$$

Here, the Higgs potential $V(\phi)$ is of the form

$$V(\phi) = \mu^2 \phi^\dagger \phi + \lambda(\phi^\dagger \phi)^2 , \tag{1.15}$$

with $\lambda > 0$. In case $\mu^2 > 0$, the Lagrangian would describe the interaction of massless gauge bosons with four scalar particles ϕ_i with mass μ. In contrast to this, if $\mu^2 < 0$, the potential $V(\phi)$ has a minimum at a non-zero values

$$\phi^\dagger \phi = -\frac{\mu^2}{2\lambda} . \tag{1.16}$$

As $\phi^\dagger \phi = \frac{1}{2}(\phi_1^2 + \phi_2^2 + \phi_3^2 + \phi_4^2)$, a particular minimum can be chosen, as for instance

$$\phi_0 = \frac{1}{\sqrt{2}} \begin{pmatrix} 0 \\ v \end{pmatrix} , \tag{1.17}$$

with $v^2 = -\frac{\mu^2}{2\lambda} = \phi_3^2$ and $\phi_1 = \phi_2 = \phi_4 = 0$. The selection of a minimum v, which is called *vacuum expectation value*, spontaneously breaks the symmetry.

Choosing a specific gauge, $\phi(x)$ can be chosen such that

$$\phi(x) = \frac{1}{\sqrt{2}} \begin{pmatrix} 0 \\ v + h(x) \end{pmatrix} , \tag{1.18}$$

where the Higgs field $h(x)$ is the only scalar field that remains.

By inserting $\phi(x)$ into the related Lagrangian, terms appear which can be identified as mass terms of one massive scalar and three massive gauge fields. Through the Higgs mechanism, the $W^\pm$ and Z bosons acquire mass through the terms written in Equation 1.19,

$$m_W = g\frac{v}{2} \ , \quad m_Z = \sqrt{g^2 + g'^2}\frac{v}{2} = \frac{m_W}{\cos\theta_W} \tag{1.19}$$

which also gives an explanation for the different masses of the W and Z bosons, while the photon remains massless, $m_\gamma = 0$. The mass of the Higgs boson can be expressed by $m_h = \sqrt{2}\mu = \sqrt{2\lambda}v$. Also, the couplings of the Higgs boson to gauge bosons (generalized to A) are found to be proportional to the square of their masses, as shown in Equation 1.20. [27]

$$g_{hAA} \propto \frac{m_A^2}{v} \tag{1.20}$$

Another important feature of the Higgs boson is that it also gives mass to fermions. This is achieved by adding Yukawa coupling terms to the Lagrangian as shown in Equation 1.21 [27], which describe couplings between the Higgs field and the fermion fields,

$$\mathscr{L} \supset -y_{ij}^u \bar{u}_{Ri}\widetilde{\phi}^\dagger Q_{Lj} - y_{ij}^d \bar{d}_{Ri}\phi^\dagger Q_{Lj} - y_{ij}^l \bar{l}_{Ri}\phi^\dagger L_{Lj} + h.c. \ , \tag{1.21}$$

where $Q_L = (u_L, d_L)^T$ and $L_L = (\nu_L, e_L)^T$ represent left-handed quark and lepton doublets, respectively, $\bar{u}_{Ri}$ and $\bar{d}_{Ri}$ are right-handed up-type and down-type quark fields, respectively, and $\bar{l}_{Ri}$ are right-handed lepton fields. The Yukawa coupling matrices y^u, y^d and y^l for up-type and down-type quarks as well as for charged leptons, respectively, are also part of the Lagrangian as well as $\widetilde{\phi} = i\sigma_2\phi^*$, which is the conjugate Higgs doublet.

From this Lagrangian, the Higgs couplings to fermions f can be connected to fermion mass terms m_f as shown in Equation 1.22. [27]

$$g_{h\bar{f}f} \propto \frac{m_f}{v} \tag{1.22}$$

More information about the experimental measurement of the Higgs parameters are presented later in Section 2.1.1.

1.1.5. Limits of the Standard Model

The Standard Model is a very successful theory as it shows a good agreement between predictions and physics observations. Still, it is presumed that this theory is not the final answer and there might be physics beyond the SM. For instance, gravity is not included at all and the SM does not give an explanation why there are three fermion generations. It is also not satisfying, that the SM currently has 18 (or more, if neutrino masses are taken into account) [28] degrees of freedom, for example the fermion masses, the gauge coupling constants, etc. These parameters have to be measured experimentally and inserted into the model. In the following, a short overview of open questions is given.

Grand Unification Theory

Similar to the unification of the electronic and weak theory, the Grand Unification Theory

(GUT) aims to combine the strong with the electroweak interaction. The idea is to interpret these interactions as different manifestations of one underlying interaction. This would require, that at a certain energy, the coupling constants (which actually depend on energy) of the strong, electromagnetic and weak interactions have the same strength. This might happen at the grand unification scale of around 10^{16} GeV, though without additional adjustments, for instance feasible by *supersymmetry* (SUSY), the constants do not coincide. [13] GUT theories predict an unstable proton, which has not been observed so far.

Matter/Antimatter Asymmetry

The Big Bang theory assumes the creation of equal amounts of matter and antimatter, so does the Standard Model. Instead today, the universe consists mainly of matter, thus an asymmetry preferring matter over antimatter is observed. Though CP violation [29], which occurs in the weak interactions of quarks, might give an explanation of this asymmetry, the impact of this effect is not high enough to account for the observed matter dominance.

Dark matter and dark energy

In the universe, only about 5 % [30] of the mass is made of baryonic matter as described in the Standard Model. This has been given evidence by several cosmological experiments, which study the Cosmological Microwave Background [31] and the velocity of galaxies [32]. The superior unknown invisible fraction of mass in the universe is called *dark matter* (about 20 %) and *dark energy* (about 75 %) [13] while the latter is connected to the acceleration of the expansion of the universe. Both are, unsurprisingly, not part of the SM and far from being understood. A candidate for dark matter are hypothetical weakly interacting massive particles (WIMPs) [33].

Neutrino Mass

In the Standard Model, neutrinos are supposed to have no mass. Still, the observation of neutrino oscillations entail that neutrinos are not massless.[18] Experimental measurements obtain an upper limit of the neutrino mass of $m_{\nu_e} < 2$ eV [19], but the process which generates this mass, is still unclear.

Hierarchy problem

The hierarchy problem is mainly associated to the Higgs boson mass if the SM should be valid until the Planck scale ($\approx 10^{19}$ GeV [19]). The observed mass of about 125 GeV requires an unnaturally considered fine-tuning of arbitrarily large quantum loop corrections from scalar bosons (the Higgs boson itself), vector bosons (gauge bosons) and fermions [34].

1.2. Particle Interactions with Matter

In this section, interactions between electromagnetic and hadronic particles with matter are discussed with regards to the generation of showers. The first subsections concentrate on electromagnetic showers generated by $e^{\pm}$ and γ and their energy losses in matter. Thereafter, the interaction of charged heavy particles with matter is discussed as well as the development of hadronic showers. The references [19, 35] are the basis of the following discussion and fomulars are taken from there, if not stated otherwise.
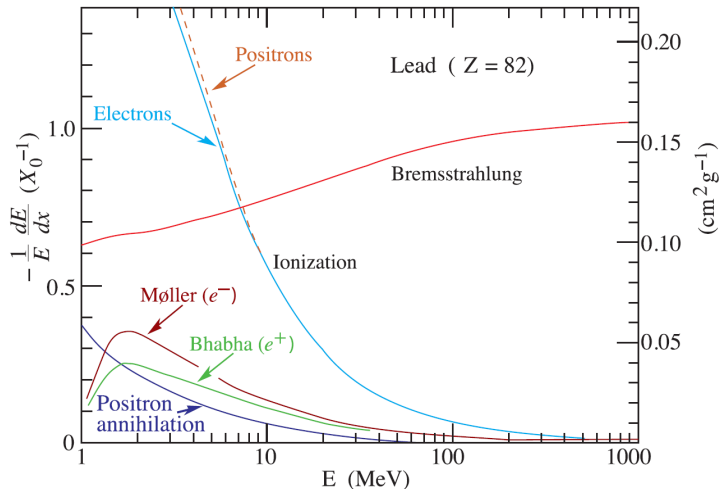
Figure 1.2.: Different processes contributing to the fractional energy loss of electrons and positrons in lead, shown as a function of energy.[19]

1.2.1. Energy Loss of Electrons in Matter

If charged particles, for instance electrons, traverse matter, different kinds of interactions result in a loss of their energy. The kind of interaction and the amount of lost energy mainly depend on the type, mass and kinetic energy of the particle and on the atomic number of the absorber. In the following, a short overview of the main interactions is given.

The dominant effect of energy loss in matter for electrons with energies below approximately the order of 10 MeV is through *ionization* of the target atom (more details in Section 1.2.4). Besides this, other smaller effects reduce the energy of the incoming electron, like positron annihilation, electron-electron scattering (Bhabha scattering) and electron-positron scattering (Møller scattering).

For higher energies, the *Bremsstrahlung* process dominates the energy loss of electrons in matter. Figure 1.2 shows the different contributions to the energy loss of electrons and positrons in dependance of the energy.

Bremsstrahlung

The Bremsstrahlung process is discussed now as it is of high relevance for the generation of electromagnetic showers. Due to the interaction of charged particles with the coulomb field of a nucleus, a fraction of its energy is radiated in form of a photon with an energy cross section which is proportional to $d\sigma/dE_\gamma \propto 1/E_\gamma$. [35] The energy loss of the initial electron per path length dx scales linear with the energy E as given in Equation 1.23.

$$\frac{dE}{dx} = -\frac{E}{X_0} \tag{1.23}$$
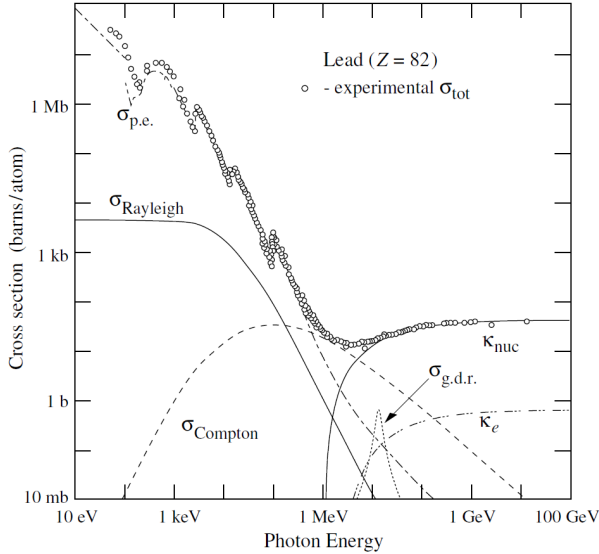
Figure 1.3.: Different processes contributing to the total cross sections for photons in lead, shown as a function of the photon energy.[19]

Here, X_0 is the *radiation length* in units of cm. After a path length $x = X_0$, the remaining energy of the electron corresponds to $1/e$ of the initial energy. X_0 can approximately be estimated for all elements except for Helium with less than 2.5 % deviation by Equation 1.24,

$$\rho X_0 \approx \frac{A \cdot 716.4 \, \text{g cm}^2}{Z(Z+1) \cdot \ln(\frac{287}{\sqrt{Z}})} \ , \tag{1.24}$$

where ρ is the density in g/cm^3 and Z the atomic number of the target.

A material characteristic is the critical energy E_k given in Equation 1.25 for solid matter, where the energy losses of electrons due to ionization and Bremsstrahlung are equal.

$$E_k \approx \frac{610 \, \text{MeV}}{Z + 1.24} \tag{1.25}$$

As an example for electrons in iron, the critical energy is approximately $E_k = 21.7 \, \text{MeV}$. [35]

1.2.2. Energy Loss of Photons in Matter

The interaction of photons with matter are summarized next. Photons mainly interact with matter via three processes: the photoelectric effect, the Compton scattering and pair production.

If an incoming photon is absorbed by an atom, which then releases the absorbed energy by emitting an electron, this process is called *photoelectric effect*. The energy of the photon has to be at least as large as the binding energy of the electron, which then carries the remaining energy. For a fixed photon energy, the probability for the absorption is higher for strong bound then for less bound electrons. Absorption edges appear in the total cross section as shown in Figure 1.3 for lead absorber, as with increasing photon energy, the binding energy of electrons in lower shells is reached. The photoelectric effect is dominant for photon energies below $\lesssim 1 \, \text{MeV}$

and decreases with rising energy.

The main process at high photon energies is *pair production*. If a photon is within a coulomb field of a heavy nucleus and has an energy which corresponds to at least twice the rest mass of an electron ($E_\gamma \approx 2 \times 511\,\text{keV}$), it can decay into an electron-positron pair.

Additionally, *Compton scattering* refers to a process, where a photon elastically scatters with an electron. If the photon scatters with an atom, this process is called Rayleigh scattering. In both cases, the photon is not absorbed. These effects have the highest impact on the cross section in the energy region around 1 MeV.

Figure 1.3 also shows additional smaller contributions to the cross section of photons in matter. Rayleigh scattering refers to elastic scattering of a photon with an atom. The curve marked with κ_e refers to pair production in an electron field and the small peak marked with $\sigma_{g.d.r.}$ refers to the Giant Dipole Resonance of photonuclear interactions, in which the target nucleus is broken up.

1.2.3. Electromagnetic Cascade

Electromagnetic cascades (or so called showers) are generated when high energetic electrons, positrons or photons traverse a thick absorber. This mainly happens by successive Bremsstrahlung of electrons and positrons and pair production of photons, which generates new electrons, positrons and photons, called secondaries, with less energy. Rossis 'Approximation B' [36] describes the main features of longitudinal electromagnetic shower profiles. In this approximation, only Bremsstrahlung and pair production are considered and energy loss via ionization is energy independent and equals the critical energy E_k per radiation length X_0. Also, the approximation does not account for multiple scattering.

At high energies E, secondaries of both processes, Bremsstrahlung and pair production, are mainly produced in forward direction according to Equation 1.26,

$$\theta = \frac{1}{\gamma} = \frac{m_e}{E} \ , \tag{1.26}$$

where θ is the scattering angle, γ the Lorentz factor and m_e the electron rest mass. For both processes, a characteristic length is the radiation length X_0 (cf. Equation 1.24), which is proportional to Z^{-2}. X_0 is connected to the mean free path λ_γ of high energetic photons via Equation 1.27, which corresponds to the mean distance traveled until a high energy photon interacts via pair production.

$$\lambda_\gamma \approx \frac{9}{7} X_0 \tag{1.27}$$

The total deposited energy E_0 of an electromagnetic shower is proportional to the number N of new generated electrons and positrons according to Equation 1.28.

$$N \approx \frac{E_0}{E_k} \tag{1.28}$$

Here, the assumption enters, that the interaction of electrons, positrons and photons ends, as soon as the remaining energy reaches the critical energy. The remaining energy is deposited without further radiation processes. Like this, the energy of a primary electron can be observed
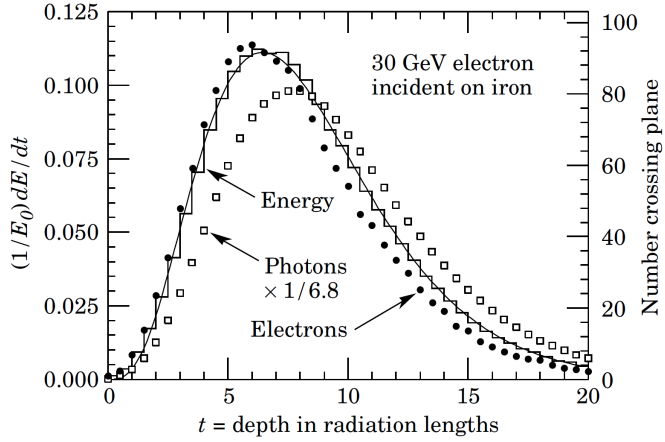
Figure 1.4.: Simulation of a longitudinal profile of a 30 GeV electron shower in iron. The curve is a gamma-function fit to the distribution, while the squares indicate the (scaled, see Figure) number of photons and the circles the number of electrons, both only counted for energies $E \geq 1.5$MeV. [19]

by 'counting' the number of generated secondaries, which is for instance accounted for in sampling calorimeters (more details in Section 1.3).

Figure 1.4 shows a simulated longitudinal shower profile of a primary electron of 30 GeV in iron. With increasing shower depth, photons carry a larger fraction of the energy compared to electrons. The total distribution can be described by a gamma function [37] as given in Equation 1.29,

$$\frac{dE}{dt} = E_0 b \frac{(bt)^{a-1}e^{-bt}}{\Gamma(a)} \ ,\tag{1.29}$$

where $t = s/X_0$ is the depth (s) of the shower per radiation lengths and a and b are parameters, which depend on Z and E_0. The maximum of Equation 1.29 is called shower maximum t_{max} and is given by $t_{max} = (a-1)/b$. It can be obtained by the empirical formula in Equation 1.30.

$$t_{max} = \ln \frac{E_0}{E_k} + \begin{cases} -0.5 & \text{electrons,} \\ +0.5 & \text{photons.} \end{cases}\tag{1.30}$$

The maximum scales with the logarithm of the energy of the shower which is an important note for the construction of calorimeters. About 98 % of the shower energy is deposited within approximately $t_{98\,\%} \approx t_{max} + 13.6$.

The lateral development of high energetic electromagnetic showers is mainly determined by multiple scattering of low-energetic charged particles and photons which interact via Compton scattering. Following Equation 1.26, the Bremsstrahlung and pair production processes for high energy particles have less impact on the shower width. The lateral development is expressed by the Molière radius R_M as given in Equation 1.31,

$$R_M = \frac{E_s}{E_k}X_0 \ ,\tag{1.31}$$
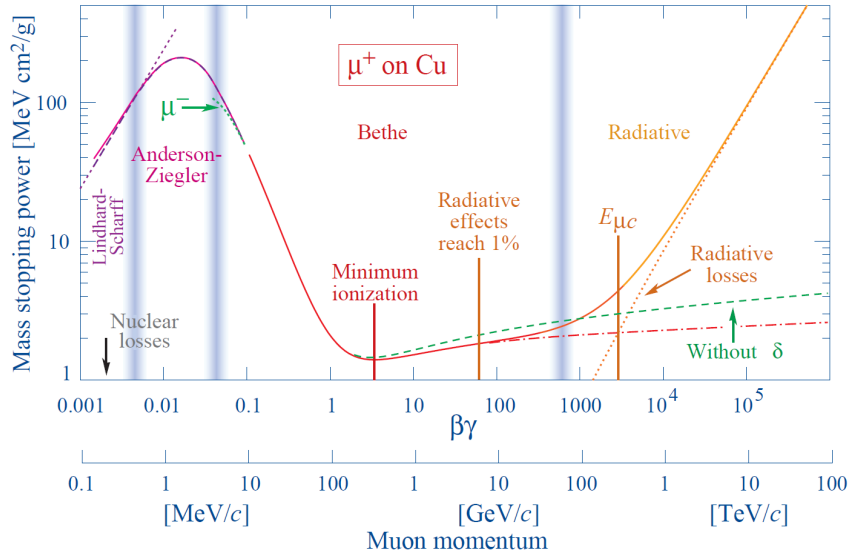
Figure 1.5.: Mean energy loss $\langle \frac{dE}{dx} \rangle$ of positive muons in copper as a function of the muon momentum and of $\beta\gamma$. Vertical lines indicate transitions from one theoretical description to another.[19]

where $E_s \approx 21.2$ MeV. 90 % of the energy is deposited within a cylinder of radius R_M around the shower axis. Thus, in order to estimate the location of a shower, the granularity of a detector has at most to be of the order of R_M.

1.2.4. Interactions of Charged Heavy Particles with Matter

As mentioned above, *ionization* is dominant for small electron energies. For heavier particles such as hadrons, ionization is more relevant also for high energies, as Bremsstrahlung scales with the inverse squared mass of the particle according to $1/m^2$. [35] The incoming particle interacts electromagnetically with an orbital electron of the target atom and the mean energy loss per path length $\langle \frac{dE}{dx} \rangle$ of the particle can be expressed by the Bethe-Bloch formula in Equation 1.32.

$$\left\langle -\frac{dE}{dx} \right\rangle = K z^2 \frac{Z}{A} \frac{1}{\beta^2} \left[\frac{1}{2} \ln \frac{2 m_e c^2 \beta^2 \gamma^2 W_{max}}{I^2} - \beta^2 - \frac{\delta(\beta\gamma)}{2} \right] \tag{1.32}$$

Here, Z is again the atomic number and A the mass number of the nucleus, z is the charge and β the velocity of the incoming particle and γ the Lorentz factor as above. K is a constant $K = 4\pi N_A r_e^2 m_e c^2$ with the Avogadro constant N_A, the electron radius r_e and rest mass m_e. As an exception, c is written here. W_{max} is the maximum possible energy transfer to an orbital electron in a central impact, I is the mean energy which is required to ionize the medium and δ a density correction factor depending on $\beta\gamma$. The accuracy of the Bethe Bloch equation is a few percent in the region $0.1 \lesssim \beta\gamma \lesssim 1000$. [19]

Figure 1.5 shows the mean energy loss of muons in copper as a function of the particle momentum and of $\beta\gamma$. For $\beta\gamma \gtrsim 1000$, radiative losses begin to dominate the energy loss (cf. Bremsstahlung). For low momentum, $\beta\gamma \lesssim 0.1$, the energy loss can be described by the empirical Anderson Ziegler approximation and for even smaller momentum by the theoretical Lindhard-Scharff model. In this region, elastic nucleus scattering dominates the energy loss.

15
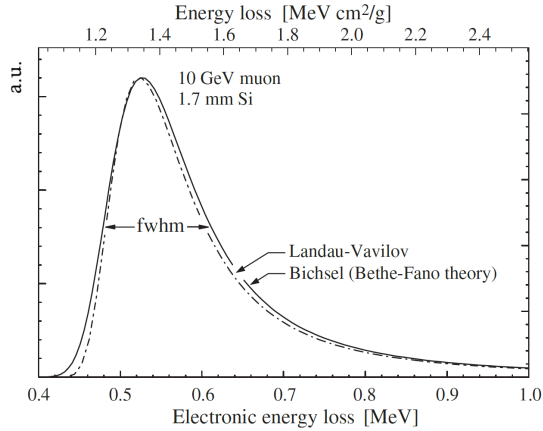
Figure 1.6.: Two parametrizations of energy depositions of a 10 GeV muon traversing a silicon layer of 1.7 mm. Adapted figure taken from [38], original from [39].

The most important range for the application here is the Bethe Bloch sector, where the energy loss first decreases as it is dominated by $\frac{1}{\beta^2}$, followed by a broad minimum which lies in the region around $\beta\gamma \approx 3$ to 4. Particles in this kinematic range are called *minimum ionizing particles* (MIPs) and it shall be noticed, that for higher momentum the mean energy loss is only slightly increasing with the dominant term $\ln(\gamma)$, as T_{max} becomes proportional to γ for high γ.

As shown in Figure 1.6, the energy loss probability distribution of a charged particle in a thin layer (of the order of a few mm) of scintillator or silicon can be described by a highly-skewed Landau distribution. [39] The most probable energy loss (MPV) corresponds to only about 62 % of the mean of the distribution because of the large tail to higher energies, while about 90 % of all events have energy losses below the mean. [39] The high energy entries can reach up to W_{max} which might even be at several GeV. Because the MPV of the energy loss distribution is less affected by the momentum of the traversing particle compared to the mean of the energy loss, the MPV is often chosen as an energy deposition scale in calorimeter applications.

1.2.5. Hadronic Cascade

If a high energetic hadron interacts with matter, the interaction products can themselves also interact further with matter as holds for and happens in electromagnetic cascades. Like this, they can initiate particle showers, which allows (under some restrictions as discussed below) to measure the deposited energy in calorimeters. In contrast to leptons, hadrons also interact strongly through diverse inelastic reactions with target nuclei which complicates the theoretical description of hadronic showers.

Figure 1.7 illustrates the first interactions of a hadronic cascade which is triggered by an incoming pion. A high energetic charged hadron may ionize atoms along the path through an absorber medium, until at some depth, a strong nuclear reaction with a nucleon in the absorber medium can occur. Both, the incoming hadron as well as the target nucleon might change their identity and emit a variable number of various nuclear fragments. Because these products might introduce both, electromagnetic and hadronic cascades, a hadronic shower generally contains
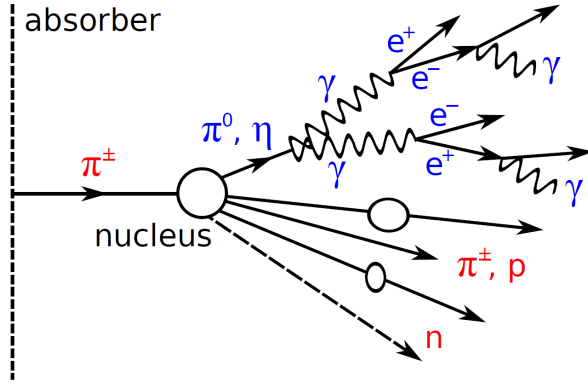
Figure 1.7.: Schematic drawing of the first interactions of a hadronic cascade which is introduced by an incoming pion in an absorber medium. A development of an electromagnetic (to the top) and of a hadronic component (to the bottom) is shown. [40]

both, electromagnetic and hadronic components. More details follow below.

The mean free path of a hadronic particle, until it interacts strongly with a nucleon, is given by the *nuclear interaction length* λ_n. The relation to the radiation length X_0 can be approximately expressed by Equation 1.33,

$$\frac{\lambda_n}{X_0} \approx 0.37 \cdot Z \ , \tag{1.33}$$

and scales with the atomic number Z. For instance for iron, the ratio is $\frac{\lambda_n}{X_0} \approx 9.5$ and thus hadronic showers tend to penetrate absorber further than exclusively electromagnetic showers do, what is important for the design of hadronic calorimeters. Due to the character of the strong interaction, there are large statistical fluctuations of both, the longitudinal and the lateral shower profile. λ_n accounts for the nuclear interaction length of protons, while the pion interaction length λ_π is about a factor 3/2 larger. [41]

The average shower maximum can be expressed by the empirical approximation in Equation 1.34 for hadronic showers in a range between a few GeV up to a few 100 GeV.

$$t_{max} \approx 0.2 \ \ln{(E/\text{GeV})} + 0.7 \tag{1.34}$$

Here, t_{max} is given in units of λ_n and is - again - proportional to the logarithm of E. On the longitudinal axis, about 95 % of the energy is deposited within $t_{95\%} \approx t_{max} + 2.5\lambda_n(E/\text{GeV})^{0.13}$. Compared to electromagnetic showers, these average values have higher fluctuations.

The electromagnetic component of hadronic showers leads to a dense core in the lateral energy deposition profile of hadronic showers, while especially neutrons cause relatively long outliers. Roughly 95 % of the lateral deposited energy is included in a cylinder of radius $R_{95\%} \approx \lambda_n$.

In the following, the hadronic and the electromagnetic components of hadronic showers are discussed a little further.

Hadronic Component

New high energy particles are generated by inelastic interactions of an incoming high energetic hadron with a target nucleus. These new hadrons are mainly generated in forward direction and

can themselves generate new particles in inelastic scatterings with other nuclei if their energy is large enough to escape the initial nucleus. Like this, a *high energetic cascade* is generated. These new hadrons are predominantly generated in an interaction with a single nucleon of the nucleus. The nucleus than becomes excited due to interactions of the new generated hadrons with other nucleons. What follows, is a process called *spallation*, in which the nucleus dispenses excess energy by emitting nucleons and nuclear fragments with energies of a few 100 MeV each, which can lead to an *intra-nuclear cascade*, in which the new particles themselves scatter inside the nucleus and generate new particles, until they escape from the nucleon, or their energy drops below a certain threshold. This spallation process is the first stage and happens within a time scale of about 10^{-22} s. [35] Charged products of the spallation process interact mainly via ionization with the medium, while neutrons cause new nuclear reactions. If the absorber material is lead or uranium, these neutrons can moreover trigger nuclear fission.

After the spallation process has stopped, the nucleus is in a highly excited state. In a second stage, it then *evaporates* nucleons and nuclear fragments with energies of a few MeV on a time scale of about 10^{-18} s. [35] The relation between evaporated protons and neutrons is roughly balanced in iron. Neutrons cool down by elastic scattering until they might be captured by a nucleus. This and the energy deposition from gamma radiation of nuclear decays can happen very delayed ($> \mu s$). Thus the integration time of a signal in a calorimeter is crucial for the detection of these energy depositions. Otherwise, they are not visible and called *invisible energy*. Also, the nuclear binding energies are lost in the following process and thus also invisible. On the other hand, charged fragments are strongly ionizing but only have a small range, thus they might also not be detected as they might not make it into the active medium of a detector (for example in sampling calorimeters, as discussed later in Section 1.3). In iron, the total fraction of invisible energy is of the order of $\approx 20\,\%$ [41]. Besides the processes mentioned above, also target recoil energy and the energy carried out by neutrinos, which are generated due to weak interactions in the decay of charged hadrons, add to the invisible energy.

Electromagnetic Component

In the strong interaction of a hadron with a target nucleus, also neutral hadrons, as for example neutral pions π^0 and η-mesons, can be produced. While most of the hadrons generated in a high energetic cascade are pions, about $1/3$ of them are neutral pions with a short life time of about $\tau \approx 10^{-16}$ s [19]. These decay most dominantly with about $99\,\%$ in two photons: $\pi^0 \to \gamma\gamma$. The η-meson on the other hand decays to two photons with $39\,\%$ width and with about $33\,\%$ to three π^0. [19]

The photons can then initialize electromagnetic cascades as discussed above and do generally not contribute any further to the hadronic component, which allows to consider them separately. The mean electromagnetic fraction f_{em} of the deposited energy in a hadronic shower, mainly due to π^0 decays, scales with the energy E of the initial hadron and can be expressed by Equation 1.35,

$$f_{em} \approx 1 - \left(\frac{E}{E_0}\right)^{k-1} \;,\tag{1.35}$$

where $k \approx 0.82$ is a parameter, which is related to particle multiplicities in nuclear interactions and is adjusted to data. The mean energy, which is required for the generation of π^0, is given

by the Z-dependent scale energy E_0, which is about $0.7\,\mathrm{GeV}$ for iron. [42] A hadronic shower introduced by a pion in copper for instance has a mean electromagnetic fraction of $f_{em} \approx 0.38$ for $E = 10\,\mathrm{GeV}$, which increases to $f_{em} \approx 0.59$ for $E = 100\,\mathrm{GeV}$. [41]

1.3. Concept of Calorimetry

Calorimeters are utilized to obtain the energy of particles by total absorption of the particle and measurement of the deposited energy. If not otherwise stated, the discussion in this section is based on [35]. Typical requirements for calorimeters are optimal energy and spatial resolutions as well as a complete hermetical coverage of the spatial angle. The realization of these requirements often comes in hand with additional requirements and constraints due to the feasibility and costs, which involves compromises.

To reconstruct the total energy of an incoming particle, it is important to cover most parts of a shower to reduce leakage, which would otherwise result in a wrongly too low reconstructed energy. As discussed in the previous section and shown in equations 1.30 and 1.34, the longitudinal maximums of electromagnetic and hadronic shower energy depositions scale only with the logarithm of the energy. This allows to construct calorimeters with reasonable depth even for showers with very high energy.

In calorimeters, both *active* and *passive* medium can be utilized. Active refers to a medium, in which a signal generated by shower particles can be obtained, for instance due to the detection of ionization charge, scintillation or Cherenkov light. In modern calorimeters, the signals are read out electronically. Passive medium on the other hand refers to a medium, in which a shower develops without being measured. Active medium is often separated in several smaller active parts, called channels, in order to grant a better spacial resolution.

Usually, two different geometries are considered: a projective and a non-projective geometry. In the first case, also called pointing geometry, the alignment of active and (if utilized) passive medium points to the interaction point. In the second case, the geometry is independent of the interaction point. A pointing geometry has the advantage of an optimum spacial resolution, which is uniform all over the detector. On the downside, this requires the production of various module shapes. Also, photons might travel through support structures which are also pointing but include no active medium, thus their energy might not be obtained at all. Therefore, often a not completely pointing geometry is chosen.

Typically, there are two main concepts of calorimeters: *homogenous*, with only active medium, and *sampling* calorimeters with both, active and passive medium.

In **homogenous calorimeters**, only one sensitive material is utilized which fulfills both functions of shower generation and detection. Appropriate scintillator materials are for example NaI(TI), BGO and $PbWO_4$, which feature relatively high densities and short radiation lengths. For instance, $PbWO_4$ has a density of $8.28\,\mathrm{g/cm^3}$, a radiation length of $X_0 = 0.89\,\mathrm{cm}$ and a Molière radius of $2.2\,\mathrm{cm}$ and is also considered radiation hard. [43] Especially the short radiation length and the small Molière radius allow for a very compact design of electromagnetic calorimeters (ECAL). $PbWO_4$ scintillator is for instance utilized in the ECAL of the CMS (Compact Muon Solenoid) detector, which reaches a very good energy resolution of

$\sigma_E/E \approx 2.8\,\%/\sqrt{E/\text{GeV}} \oplus 0.128\,\text{GeV/E} \oplus 0.3\,\%$. [44] More detailed information about the energy resolution σ_E/E of calorimeters and the meaning of the three terms are given below in Section 1.3.1. By now note, that the first term, which accounts for stochastic fluctuations, is relatively low in homogenous calorimeters. Typical electromagnetic energy resolutions of homogenous calorimeters are in the range $\sigma_E/E \approx (3-5)\,\%/\sqrt{E/\text{GeV}}$.

Sampling calorimeters on the other hand, combine both, active and passive medium, often in an alternating arrangement called *sandwich calorimeter*. In the passive medium, the shower develops and is measured in the active medium only. Like this, the shower is *sampled* while it develops through the calorimeter. Due to this separation, more options exist for the selection of active and passive material. For passive medium, a high density material (called absorber) with a high atomic number Z is favorable in contrast to active medium, where small Z are reasonable.

Typical passive materials are lead, tungsten or uranium, while also steel is considered as it provides a solid structure. As active materials, for instance scintillator detectors or ionization chambers are considered.

In comparison to homogenous calorimeters, sampling calorimeters have the advantage of commonly less cost and lower required amount of material and space, because of the utilization of dense absorber. Like this, sampling calorimeters are in particular suited for hadronic calorimeters (HCAL), which have to contain longer depth of hadronic showers (cf. discussion in Section 1.2.5). On the downside, because of sampling fluctuations, the energy resolution is worse compared to homogenous calorimeters as discussed below.

For electromagnetic showers, the fraction of the visible energy E_{vis} and the deposited energy E_{dep} is called *sampling fraction* f_s, as shown in Equation 1.36 and is typically of the order of a few percent. [35]

$$f_s = \frac{E_{vis}}{E_{dep}} \tag{1.36}$$

In order to have a spatial resolution of the particle shower, the active material of sampling calorimeters is typically segmented. A longitudinal segmentation is automatically provided by the alternating passive and active material, called layers, while the lateral segmentation is achieved by separating the active layer into small channels.

A current example for a hadronic sampling calorimeter is the ATLAS Tile Calorimeter [45], (TileCal) which consists of alternating 14 mm thick iron and 3 mm thick scintillator layers, and covers 7.4 nuclear interaction length λ. The scintillators are read-out by wave-length shifting fibers, which direct the light to two photomultiplier tubes (PMTs) each. The electromagnetic sampling fraction is 2.7 % and it is under-compensating with $e/h = 1.36$, as will be discussed in a moment. It achieves a stand-alone hadron energy resolution of $\sigma_E/E \approx 52\,\%/\sqrt{E/\text{GeV}} \oplus 5.7\,\%$ (see next Section 1.3.1), which is - as expected due to sampling fluctuations and features of hadronic showers, as for instance invisible energy - clearly worse than the electromagnetic energy resolution of the upper example of the CMS ECAL. As an example for a sampling ECAL, the ATLAS ECAL reaches a resolution of $\sigma_E/E = 10\,\%/\sqrt{E/\text{GeV}} \oplus 0.7\,\%$ for electromagnetic showers which is poorer compared to a typical homogenous calorimeter. [46] The ECAL is a Pb/LAr detector with lead absorber and accordion-shaped kapton electrodes and covers ap-

proximately 22 to 24 radiation lengths, depending on the angle.

1.3.1. Energy Resolution and Linearity

The above mentioned **energy resolution** σ_E/E is an important quality criterion of a sampling calorimeter and is typically parametrized as Equation 1.37

$$\frac{\sigma_E}{E} = \frac{A}{\sqrt{E/\text{GeV}}} \oplus \frac{B}{E/\text{GeV}} \oplus C \; , \tag{1.37}$$

where σ_E and E are given in units of GeV and the parameters A, B and C are unit-less.
The first term $A/\sqrt{E/\text{GeV}}$, which is called *stochastic term*, accounts for stochastic fluctuations, mainly of the shower development and of the sampling fraction. The fluctuation of the number of shower particles N, which are proportional to the initial energy E, can be expressed by the standard deviation of N, which is described by the Poisson statistic yielding $\sqrt{N}$. Therefore, the energy resolution is proportional to $\sigma_E/E \propto \sqrt{N}/N = 1/\sqrt{N} \propto 1/\sqrt{E}$.
In case of a sampling calorimeter, the number of visible shower particles N_{vis}, which is proportional to E_{vis}, has to be considered, which depends on f_s (cf. Equation 1.36). This adds another contribution to the energy resolution by $1/\sqrt{f_s E/\text{GeV}}$.
For hadron showers, additionally, the fluctuation of the fraction of invisible energy also contributes to the stochastic term, as well as the fluctuation of the fraction of the electromagnetic component f_{em}.
The term $B/(E/\text{GeV})$ accounts for energy independent fluctuations of electronic noise. This term, called *noise term*, is dominant for small energies and defines the threshold of the smallest measurable energy.
The final term C accounts for fluctuations of energy leakage and calibration uncertainties, as well as for electronic and mechanic inhomogeneities of the calorimeter. These are all fluctuations, which scale with the energy. It adds a constant to the energy resolution, therefore it is called *constant term*, and is dominant at high energies.

Besides the energy resolution, the response **linearity** of a calorimeter is an important characteristic. The linearity of a calorimeter might be reduced by several aspects, for instance due to the electronic read-out, which might saturate at high exposures and due to energy leakage, which increases with $\ln(E)$ (cf. Equation 1.30 and 1.34). To improve the linearity of a calorimeter, the response of read-out channels can be analyzed and thereafter de-saturated. Also, particle beams with well known energy can be used to calibrate the linearity of a detector.

1.3.2. Compensation

The total signal S in a hadron calorimeter, which is generated by a hadron shower, can be described as a sum over all components f_i of the deposited energy of different sources (electromagnetic, hadronic), multiplied with the related detection efficiency ϵ_i: $S = \sum f_i \epsilon_i$. The hadronic component can be split into several parts, taking into account energy depositions induced by, for instance, ionization, neutrons, gamma rays and the invisible energy.

The efficiencies for these processes are not equal, especially the total efficiency ϵ_h to hadronic energy depositions is typically smaller compared to the efficiency ϵ_{em} to electromagnetic energy depositions. In particular, as about 20 % (cf. Section 1.2.5) of the hadronic energy is invisible, the energy response of a calorimeter to hadron showers is typically lower compared to the response to electromagnetic showers.

In such a case, which is typical for a calorimeter, the ratio between both efficiencies is $e/h = \epsilon_{em}/\epsilon_h > 1$. Such a calorimeter is called *under-compensating*. The opposite case is called *over-compensating*, when $e/h < 1$. A calorimeter with $e/h = 1$ is called compensating.

With increasing energy, the electromagnetic fraction f_{em} of a hadronic shower increases (compare to Equation 1.35), thus the ratio e/h decreases.

To improve the resolution and the linearity of a hadron calorimeter, a ratio $e/h \rightarrow 1$ should be aimed at. To achieve that goal, either ϵ_{em} has to be reduced or ϵ_h has to be increased. A possible way to reduce ϵ_{em} is to select absorber material with a high atomic number Z as for example uranium of lead instead of lighter iron or copper, as in the first two cases, a larger fraction of the energy of the electromagnetic component is deposited already inside the absorber and does not pass on to the active layer. [35]

On the other hand, a higher ϵ_h can be achieved by improving the efficiency of the detection of energy depositions, especially of neutrons from the nuclei spallation process. These neutrons can transfer their energy in elastic scatterings, especially with light nuclei in active medium, to ionizing particles, which then can be detected. The relative energy loss of neutrons in an elastic scattering with a nucleus is roughly proportional to $1/A$, with the mass number A. [35] Therefore, a light active medium is well suited, as for example organic scintillators or gases with a high hydrogen concentration.

As both techniques, to improve ϵ_h and reduce ϵ_{em}, depend on the thickness of the active and passive medium, respectively, the ratio between active and passive medium can be optimized to reach $e/h \approx 1$. An example for such a compensating calorimeter is the ZEUS calorimeter, which utilizes thickness optimized uranium and plastic scintillator layers and achieves a stochastic term of the energy resolution of $35\,\%/\sqrt{E/\text{GeV}}$ [47].

Besides the adjustment of the efficiencies ϵ_{em} and ϵ_h, other techniques as software compensation can be applied. This method takes advantage of the fact, that local high energy densities are most commonly related to electromagnetic components, while hadronic components usually expand further. Also, the different time developments of electromagnetic and hadronic showers can be taken into account, as electromagnetic showers and electromagnetic components of hadronic showers propagate at the speed of light, while hadronic components in hadronic showers propagate slower as mentioned in Section 1.2.5. By applying different weights to these energy depositions, the ratio e/h can be optimized. This requires a high granularity of the calorimeter, in order to distinguish between both fractions.

1.4. Particle Flow Approach

In this section, a new approach to achieve unprecedented jet-energy resolutions is summarized. If not otherwise stated, these references [35, 48] are the basis of the following discussion.

The Particle Flow Approach (PFA) has been developed in the context of the International
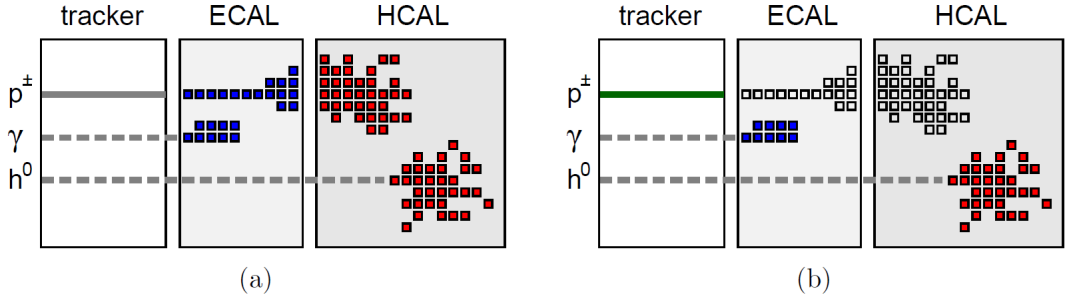
Figure 1.8.: (a) In the classical way, the ECAL and HCAL measure the deposited energy of all particles in a jet. $p^{\pm}$ accounts for all charged particles, γ for photons and h^0 for neutral hadrons. (b) In the PFA, the momentum of all charged particles is measured in the tracking system, the energy deposition of showers induced by photons is measured in the ECAL and of neutral hadrons in the HCAL.[40]

Linear Collider (ILC, see Chapter 2) in order to improve the jet energy resolution, especially for di-jets from decays of vector bosons. The ILC physics goals require a jet energy resolution of about $\sigma_E/E \approx 3\,\%$ to $4\,\%$ [3] for energies above $E_{jet} \approx M_Z/2$ in order to cleanly separate hadronic decays of W and Z bosons, as this resolution would be of the order of their decay widths $\Gamma_W/m_W \approx \Gamma_Z/m_Z \approx 2.7\,\%$. [19, 48]

The classical approach to measure the energy of hadronic jets is to sum up the deposited energies in the electromagnetic and in the hadron calorimeter. In case of software compensation, different weights can be applied to measured energies as discussed above. Like this, the stochastic term of the energy resolution is typically of the order of $\gtrsim 60\,\%/\sqrt{E/\mathrm{GeV}}$ and the constant term of the order of a few percent. This resolution is significantly worse than what is required for the ILC. To reach the requirements of the ILC, the stochastic term has to be $\lesssim 30\,\%/\sqrt{E/\mathrm{GeV}}$.

The PFA aims to utilize the best suited sub-detector for the energy reconstruction of each particle in a jet. About $62\,\%$ of the energy of a hadronic jet is carried by charged particles, $27\,\%$ by photons, $10\,\%$ by long-lived neutral hadrons and a small fraction of about $1\,\%$ to $2\,\%$ by neutrinos for jet energies below $250\,\mathrm{GeV}$. For higher energies, the electromagnetic fraction increases according to previous Equation 1.35. Typically, hadron calorimeter energy resolutions are of the order of $\approx 60\%/\sqrt{E/\mathrm{GeV}}$ as mentioned above, while the energy resolution of sampling ECALs is typical around $15\,\%/\sqrt{E/\mathrm{GeV}}$ and the momentum resolution of tracking detectors is of the order of $\Delta p/p^2 \approx 10^{-4}/\mathrm{GeV}$. [48]

Instead for instance measuring all hadrons in the HCAL with a poor resolution, the jet energy resolution can significantly be improved by measuring all charged particles in the tracking detector only. The PFA thus aims to measure all charged particles in the tracking detector, while photons are measured in the ECAL and only neutral hadrons in the HCAL. Like this, only about $10\,\%$ of the jet energy, which is carried by neutral hadrons, is measured in the HCAL with the poorest resolution.

This can only be done, if different particles in a jet can be separated in order to distinguish between energy depositions of different particle types. This requires an excellent tracking system because roughly 62% of the jet will be measured there, as well as a high lateral and longitudinal segmentation (or *granularity*) of the calorimeter. Figure 1.8 shows a schematic of the principle of the PFA in comparison to the classical approach.

Simulations show, that with the PFA, energy resolutions of $\sigma_E/E \approx 2.9 - 3.7\%$ in the jet energy range from $E_{jet} = 45\,\text{GeV}$ to $250\,\text{GeV}$ can be reached. [48]

A limiting factor for the energy resolution with the PFA is a feature called *confusion*. Confusion takes into account wrong allocations of energy depositions of different particles. For example, if energy depositions of charged and a neutral hadron are too close to each other or overlap, the allocation of the deposited energy in the calorimeter is complicated. This might lead to any mixture of two mistakes: double counting of energies, if the energy depositions are assigned to the neutral hadron only, or on the opposite, not counting energy depositions at all, which would result in the loss of the energy of the neutral hadron. Other confusion can occur for example in a wrong allocation of photon induced showers and charged hadron showers, which might also start already in the ECAL. Confusion increases with rising energy, as the potential for the overlap of showers increases and thus limits the resolution at high energies.

Figure 1.9a shows the contributions to the PFA jet energy resolution and the total resolution. As discussed, the contribution from confusion increases with energy and so does the contribution from leakage, while the first is more dominant.

Figure 1.9b shows a simulated functional form of the PFA jet energy resolution, estimated for a detector of the ILC, in comparison to the expected resolution obtained in the classical approach, where the energy is obtained from the total calorimetric energy depositions. The energy resolution obtained with the PFA is significantly better and agrees well with the goal of the ILC for a wide range of jet energies. Also, a comparison to the parametrized resolution with a stochastic term of $60\,\%/\sqrt{E/\text{GeV}}$ is shown, as well as the contribution from confusion. The PFA has been investigated in experimental tests with a prototype of a detector for the ILC. The results for beam data and simulation are in a good agreement and thus support the validity of simulation studies discussed above. [50]
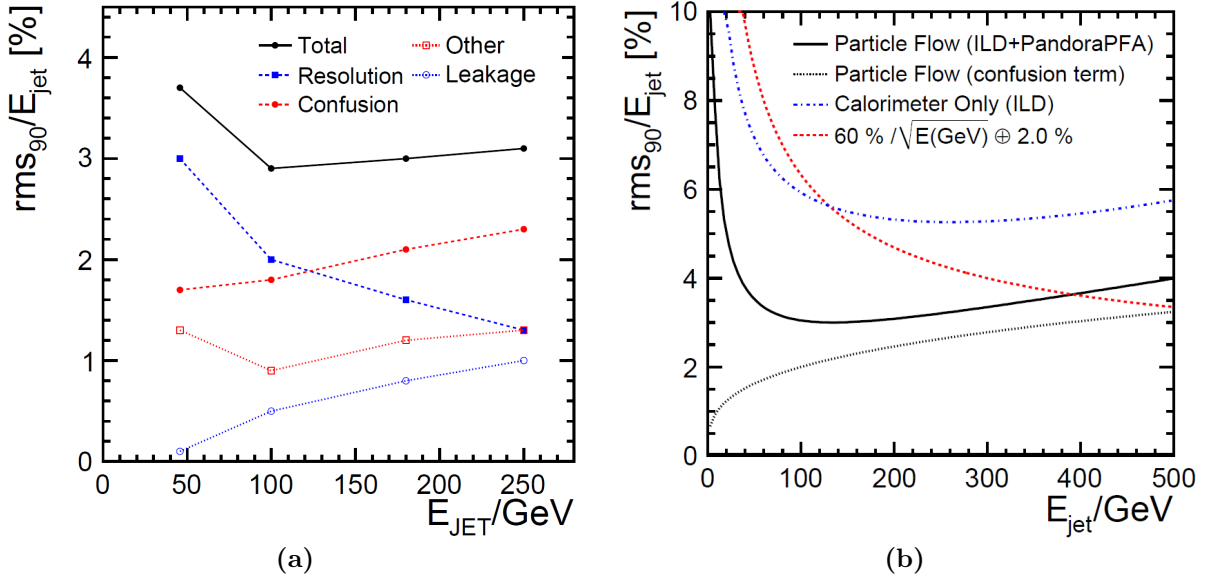
Figure 1.9.: (a) The different contributions to the jet energy resolution using the PFA, shown as a function of the jet energy. rms_{90} refers to the root mean square (RMS) estimated in a reconstructed energy region around the mean of the distribution that contains 90 % of all events. The total resolution entries are estimated from the quadrature sum of all components.[49] (b) Simulated functional form of the jet energy resolution utilizing PFA with the ILD detector (black curve). The black dotted curve represents the contribution of confusion. A parametrization of the jet energy resolution, received by using the total calorimetric energy deposition, is shown as the blue dot-dashed curve. Additionally, a typical jet energy resolution parametrization using a traditional approach, $60\,\%/\sqrt{E} \oplus 2\,\%$, is shown in red.[49]

2

The International Linear Collider (ILC)

The International Linear Collider (ILC) is a planned electron-positron collider. As circular accelerators have to deal with energy losses arising from synchrotron radiation, the ILC utilizes a linear acceleration to overcome this issue. It is designed for high resolution measurements complementary to existing hadron colliders as the LHC. After discussing the motivation for the ILC in Section 2.1, the design is discussed in Section 2.2. Two detectors are foreseen to be installed at the interaction region for alternating measurements, the International Large Detector (ILD) and the Silicon Detector (SiD), both under development, as presented in Section 2.3. The *ILC Technical Design Report* [3, 4, 27, 51, 52] is the basis of the discussion in this chapter, if not stated otherwise.

2.1. Motivation for the ILC

In this section, the motivation for the ILC is discussed. A detailed description is given in the ILC Technical Design Report as mentioned above, as well as in a review article [53] and in this document [54]. These are the basis of the following discussion.

In the recent years, both electron-positron and hadron colliders have paved the way for a better knowledge of particle physics. The Large Hadron Collider (LHC) at CERN features so far unreached center of mass energies of $\sqrt{s} = 13$ TeV for proton-proton collisions. In 2012, the discovery of the Higgs boson [1, 2] with a mass of 125 GeV completes the Standard Model (SM). Still, precise measurements of the characteristics of the Higgs boson are required to validate the SM. Any deviation from SM predictions might be a sign for physics beyond the SM. The fact that protons are composite particles complicates the reconstruction of events at the LHC, as collisions happen on the parton level and produce a large fraction of background QCD events. Lepton colliders have to deal with the limitation in circular accelerators induced by synchrotron radiation. As the energy loss is proportional to $E^4/(Rm^4)$, with the accelerator ring radius R and the energy E and mass m of the particle, light particles as electrons are more affected compared to protons for example. Thus, a linear acceleration is needed to reach high lepton energies close to 1 TeV.

In the following, an overview of the advantages of lepton colliders in contrast to hadron colliders is given.

A major point is the cleanliness of events, as the environment in lepton collisions is benign compared to hadron collisions. Electrons and positrons are point-like particles which interact electroweak, thus there is no complicating underlying QDC background but only a small background from photon-photon collisions. Thus, the initial state is well defined.
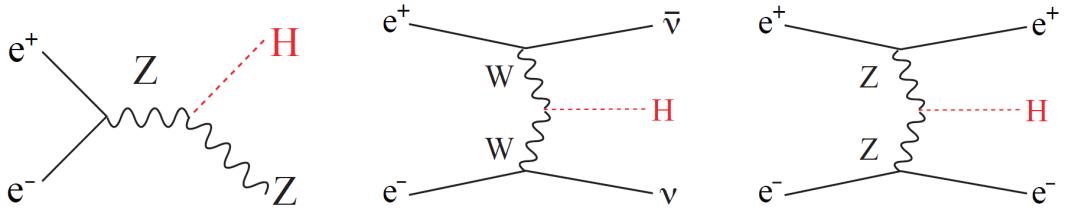
Figure 2.1.: The major processes of Higgs production at the ILC, shown as Feynman diagrams. The processes are called (from left to right): Higgsstrahlung, W-fusion and Z-fusion. [27]

This also has implications on the design of the detectors. In hadron colliders, radiation hard material has to be used and the calorimeters have to be large in order to cover a wide range of energies which often entails the placement of solenoids inside the calorimeters. On the other hand for the ILC, less radiation hard material is required, which allows to use very thin tracking detectors, which can be placed close to the interaction point. Like this, the tracking capabilities are expected to improve the momentum resolution by one order of magnitude compared to the LHC. [27] Also, the dimensions can be smaller, which allows to place the calorimeter closer to the interaction point and inside the solenoid, which improves the jet energy resolution.

Due to the large background in hadron colliders, a complex trigger system is required to select and process only interesting events. The ILC has the advantage, that not only the most characteristic events can be used for analysis, but also all final states of a decaying particle. Thus it does not require complex triggers but is capable to record all bunch crossings and perform event selections offline. The cross sections of e^+e^- annihilations, for example to lepton-antilepton and quark-antiquark pairs, to W^+W^- or to single Z, are at a pb level, while the hadronic decay modes of W and Z are easy to recognize because of the low hadronic background.

Concerning the Higgs boson, the production rate at the ILC is approximately $1\,\%$ of all e^+e^- annihilations. The next subsection describes the measurement of Higgs parameters at the ILC.

2.1.1. Measurement of Higgs Parameters

The measurement of Higgs boson characteristics at a percent level is required for the validation of the Standard Model. Besides the mass, which is now known with $0.2\,\%$ accuracy [19], these characteristics are for example the full decay width and the coupling to SM particles. The ILC allows a model independent measurement of these Higgs parameters, which will prove if the Higgs boson is a fundamental scalar particle or can be described by a supersymmetric or composite model.

The three major modes of Higgs production at the ILC are shown as Feynman diagrams in Figure 2.1: the *Higgsstrahlung* process, $e^+e^- \to Zh$, the *W-fusion* process, $e^+e^- \to \nu_e\bar{\nu}_e h$ and the *Z-fusion* process, $e^+e^- \to e^+e^-h$.

As shown in Figure 2.2, the Higgs production cross sections at the ILC has a maximum at $\sqrt{s} \approx 250\,\text{GeV}$ which is dominated by the Higgsstrahlung process. With increasing center of mass energy, the cross section of the fusion processes increases and exceeds the Higgsstrahlung cross section above approximately $\sqrt{s} \gtrsim 450\,\text{GeV}$. The polarization of the beam at the ILC is important for the W-fusion process, which requires left-handed electrons and right-handed
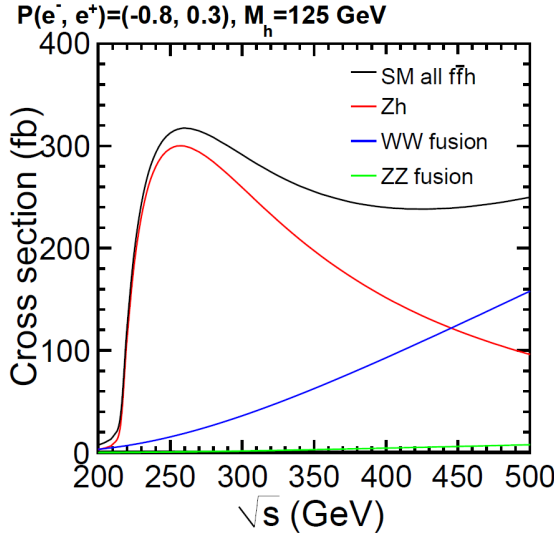
Figure 2.2.: Higgs production cross sections as a function of the center of mass energy for the three processes shown in Figure 2.1. A Higgs mass of 125 GeV and a polarization of the beam of $P(e^-, e^+) = (-0.8, 0.3)$ is assumed. [27]

positrons.

The ILC will be able to individually identify all major decay modes of the Higgs boson, which are dominated by the process $h \to b\bar{b}$ with a branching ratio of about 58.4 % [19], as well as in descending order the Higgs decays to W^+W^-, gg, $\tau\bar{\tau}$, $c\bar{c}$ and ZZ. Decays of the Higgs boson to $\gamma\gamma$, $\mu^+\mu^-$ and $Z\gamma$ have smaller rates. [19]

2.1.1.1. Higgs Recoil

A significant advantage of lepton colliders is that the initial state of the e^+e^- collisions is well known, which allows to measure the *recoil* of the Z boson against the Higgs boson in the Higgsstrahlung process. This offers a model independent method to identify the Higgs boson, as the Higgs decay itself is not taking into account at all and no assumptions have to be applied. Like this, the mass, the full decay width and the couplings of the Higgs boson can be estimated with high accuracy. Also, possibly exotic or invisible decay modes of the Higgs decay below 1 % can be observed like this.

Especially the decay mode of the Z boson to e^+e^- or $\mu^+\mu^-$ allows a precise estimation of the mass of the Higgs, as the recoil mass M_{rec} is given by Equation 2.1.

$$M_{rec}^2 = (p_{CM} - (p_{l+} + p_{l-}))^2 \tag{2.1}$$

Here, $p_{l\pm}$ are the measured four-momenta of the leptons from the Z decay and p_{CM} is the sum of the four-momenta of the colliding particles. To select such events, the invariant mass of the l^+l^--system has to agree to the Z mass.

Figure 2.3 shows a simulated recoil mass distribution for the decay of the Z boson to $\mu^+\mu^-$ for a Higgs mass of 125 GeV and an integrated luminosity of 250 fb^{-1} at a center of mass energy of 250 GeV. The distribution features a sharp maximum which allows to measure the Higgs
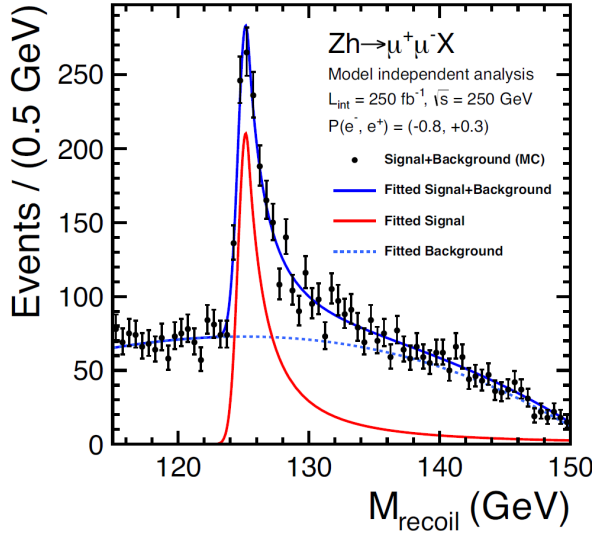
Figure 2.3.: Recoil mass distribution after the Higgsstrahlung process for the decay process $Z \to \mu^+\mu^-$, assuming a Higgs mass of $m_h = 125$ GeV and 250 fb^{-1} integrated luminosity at $\sqrt{s} = 250$ GeV with polarized beams. [54]

mass with a precision of 32 MeV if both, e^+e^- and $\mu^+\mu^-$ decay modes are combined. A model independent uncertainty of 2.5 % can be achieved on the corresponding Higgs production cross section $\sigma(e^+e^- \to Zh)$, which can be further improved by also taking into account the decay of the Z boson to quarks.

2.1.1.2. Higgs Coupling

The measurement of Higgs coupling strengths is attractive, as small deviations of the expected couplings are predicted in models for physics beyond the SM. [55] The coupling of the Higgs boson to a SM particle A is expressed by g_{hAA} and expected to be proportional to the mass m_A.

What is actually measured in a collider experiment is the event rate for a specific final state, which is proportional to the product of the cross section, for instance of the Higgs production, and the branching ratio (BR). The branching ratio can be expressed by the total Higgs decay width, Γ_h, and the partial decay width, $\Gamma(h \to A\bar{A}) \propto g_{hAA}^2$, as shown in Equation 2.2.

$$BR(h \to A\bar{A}) = \frac{\Gamma(h \to A\bar{A})}{\Gamma_h} \qquad (2.2)$$

As explained above, the cross section of the Higgsstrahlung process $\sigma(e^+e^- \to Zh)$ can be measured at the ILC, which is proportional to the quadrature of the hZZ coupling, $g_{hZZ}^2 \propto \sigma(e^+e^- \to Zh)$. By dividing the measured rate of the W-fusion process ($e^+e^- \to \nu_e\bar{\nu}_e h$) with the following decay $h \to b\bar{b}$ by $BR(h \to b\bar{b})$ obtained from Higgsstrahlung, the hWW coupling can be measured. The branching ratio $BR(h \to b\bar{b})$ is estimated from the ratio between the events with $h \to b\bar{b}$ and the full Higgsstrahlung cross section. As the partial width $\Gamma(h \to WW)$ is proportional to the squared hWW coupling, $\Gamma(h \to WW) \propto g^2(hWW)$, the total width Γ_h can
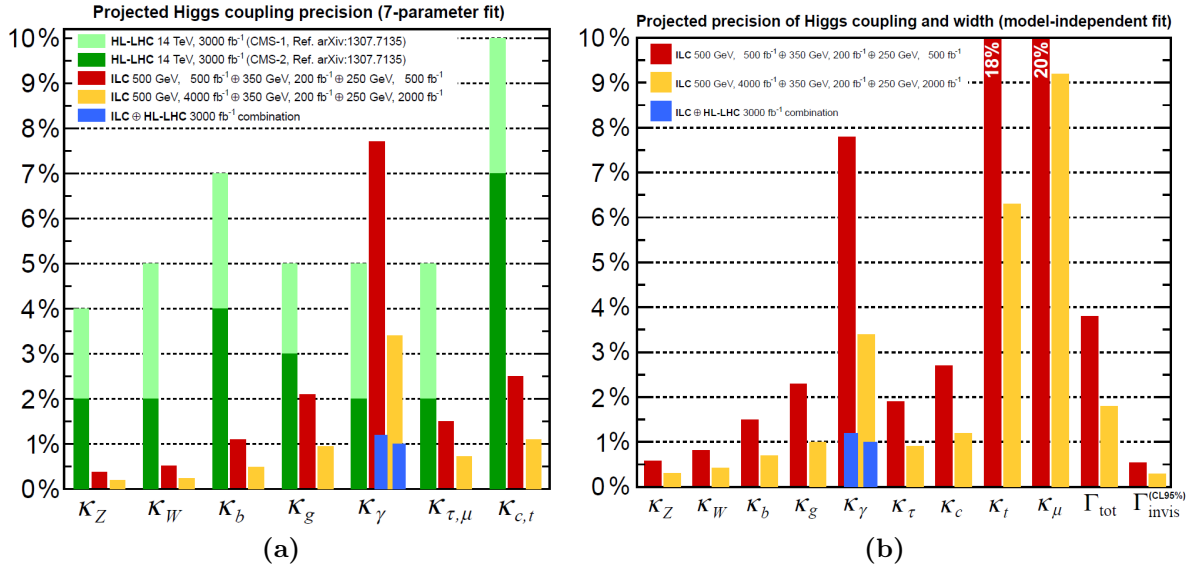
Figure 2.4.: Expected relative precisions of Higgs couplings, expressed by κ_A which is the ratio between the $hA\bar{A}$ coupling and the expectation of the SM. (a) Here, a model-dependent fit is used with expected data of the High-Luminosity LHC (HL-LHC) with an optimistic (CMS-2) and pessimistic (CMS-1) assumptions on uncertainties, as well as of the initial and full data set of the ILC. Also, a combined precision of the ILC and HL-LHC is shown. (b) Expected ILC data is used here to estimate the relative precisions extracted from a model-independent fit. [54]

be estimated in a model-independent way with Equation 2.2.

Figure 2.4a shows the achievable relative precisions of Higgs couplings of the ILC using the initial and full data set, in comparison to the LHC after the High-Luminosity upgrade using a model-dependent global fit to all measured cross sections times branching ratios. In the most cases, the ILC reaches about one order of magnitude better precisions. For the most couplings, the goal of 1 % accuracy can be reached with the ILC. The poorer accuracy of the ILC for the $\gamma\gamma$ coupling is due to the low branching ratio of 0.2 % in the SM. Figure 2.4b shows the relative precisions reachable with only model-independent analysis at the ILC.

2.1.1.3. Higgs Coupling using hadronic Z decays

As discussed above, the Higgs boson coupling can be estimated using leptonic decay modes of the Z boson in the Higgsstrahlung process. Another possibility is presented in reference [56] and briefly summarized here. This method also utilizes a recoil mass technique but takes into account hadronic decays $Z \rightarrow q\bar{q}$. As the branching ratio of this decay is around one magnitude [19] larger compared to leptonic decays, a better statistic can be accomplished using this method. At the ILC, a precision of the cross section $\sigma(e^+e^- \rightarrow Zh)$ of $\pm 1.8\,\%$ is estimated for an integrated luminosity of 500 fb^{-1} at a center of mass energy of $\sqrt{s} = 350$ GeV. This method requires an excellent jet energy resolution as discussed in the following.

The leptonic decays of the Z boson can be cleanly identified in the ILC, as discussed above. In contrast, the hadronic decays $Z \rightarrow q\bar{q}$ are more complicated to reconstruct, as the selection efficiency depends on the Higgs decay mode, which might also be hadronic as $h \rightarrow b\bar{b}$. A clear suppression of Standard Model background reaction to hadronic jets is required as well

(a)   **(b)**
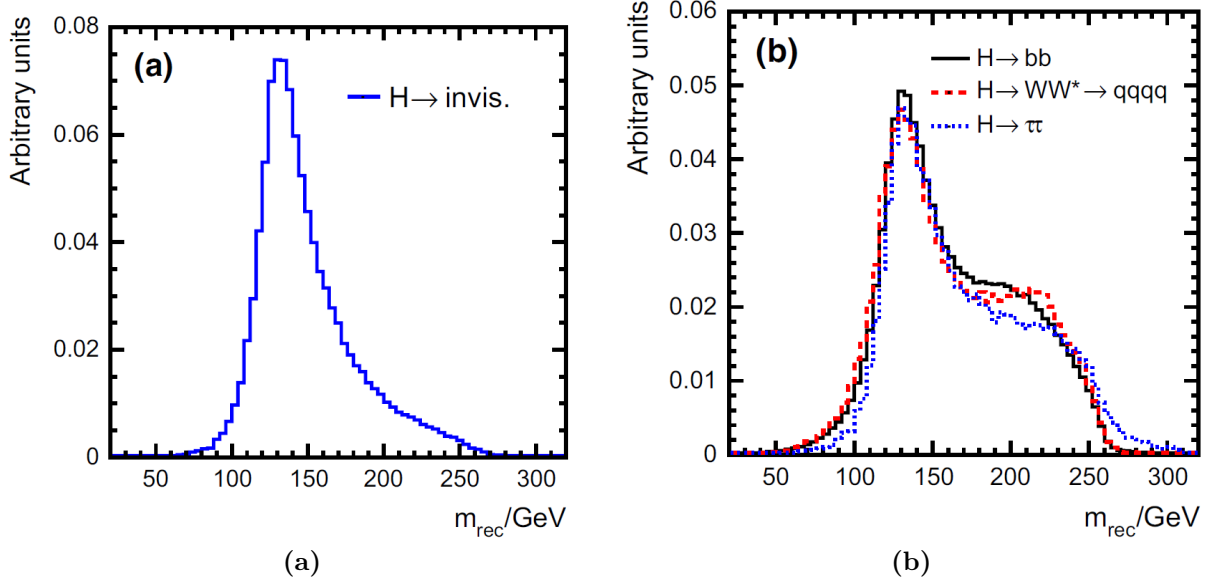
Figure 2.5.: Expected reconstructed distributions of the recoil mass from invisible (a) and visible (b) Higgs decays, estimated with hadronic $Z \to q\bar{q}$ decays. [56]

as the allocation of the hadronic jets to the related decay processes. This requires a jet energy resolution of the order of the decay width of the Z boson, thus about 3 % [19, 48]. This is difficult to accomplish, as the event selection shall be based on the Z decay without biasing any Higgs decay modes. The method first separates all events of Higgs decays in two categories, possibly "invisible" and visible final states. In the visible channel, the di-jet systems are compared to the invariant mass of the Z boson which allows an assignment to the Z decay. In the invisible channel, the di-jet is directly assigned to the Z decay. If the background is too large, the event is rejected.

Figure 2.5 shows the from simulations reconstructed recoil mass distributions for invisible and visible Higgs decays. In both distributions, a clear peak at the Higgs mass is visible. In the visible decay channel, the distributions for different decay modes look similar.

The above mentioned cross section $\sigma(e^+e^- \to Zh)$ is calculated using a likelihood approach with functions taking into account signal and background events. The variables used in the likelihood selection are based on the hadronic Z decay. The two-dimensional distribution of the recoil mass m_{rec} and the mass of the di-jet system $m_{q\bar{q}}$, is one of these variables. Figure 2.6 shows such distributions for signal and background. For signal, a peak at $m_{q\bar{q}} \approx m_Z$ and $m_{rec} \approx m_h$ is visible. The achievable width of the peak mainly depends to the energy jet resolution of the detector, as the natural widths are clearly narrower (see [19]).

2.1.1.4. Higgs Self-Coupling

Another important feature of the ILC is the possible measurement of the trilinear Higgs boson self-coupling [54]. This self-coupling determines the shape of the potential of the Higgs field, which allows further insights on the nature of phase transitions from the symmetric state in the weak theory in the early universe to the broken symmetry state, where the value of the Higgs
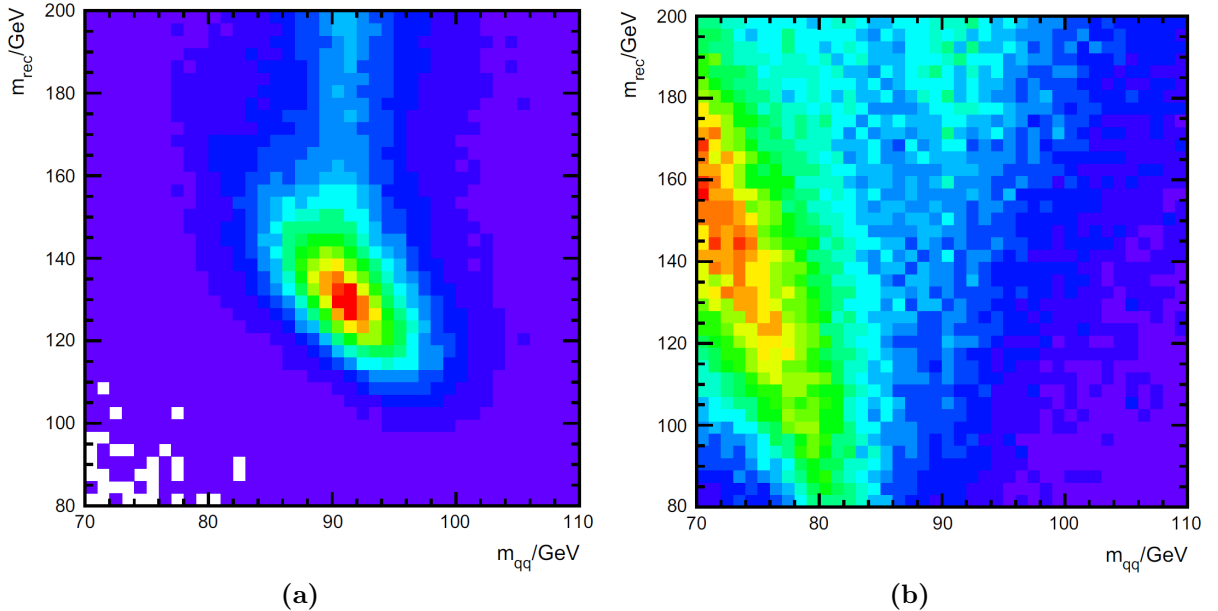
Figure 2.6.: Two-dimensional distributions of the reconstructed recoil mass, m_{rec}, versus the invariant mass, $m_{q\bar{q}}$, of the Z boson decaying to $Z \to q\bar{q}$ for events (a) and background (b). [56]

field is nonzero. The Higgs self-coupling allows to seek possible Higgs CP violating interactions, which would allow feedback to the baryon-antibaryon asymmetry.

This Higgs boson self-coupling can be measured at the ILC from a center of mass energy of $\sqrt{s} = 500\,\mathrm{GeV}$ on through the process $e^+e^- \to Zhh$, while all decay modes are observable. A precision of the Higgs self-coupling of 26 % [57] is predicted taking into account only the decay modes $hh \to b\bar{b}b\bar{b}$ and $hh \to b\bar{b}W^+W^-$ and an integrated luminosity of $4\,\mathrm{ab}^{-1}$. Studies that combine measurements at $\sqrt{s} = 500\,\mathrm{GeV}$ and $\sqrt{s} = 1\,\mathrm{TeV}$, where also the process $e^+e^- \to \nu\bar{\nu}hh$ is taken into account, expect an improved precision of 18 % [58] of the Higgs self-coupling.

2.1.2. Other Physics Goals

Besides the Higgs boson, many other physics goals are addressed by the ILC. A short summary shall be given here, before going into detail about the ILC design in the next section. For a detailed analysis of the physics processes, meant to be studied with the ILC, please refer to Reference [27].

The ILC is capable to perform ultra-precision measurements of the Z and W bosons by the following production processes: $e^+e^- \to Z$, with a center of mass energy of 91 GeV in the Z resonance, and $e^+e^- \to W^+W^-$ with a center of mass energy of 160 GeV, corresponding to the threshold of this process. At higher energies $> 340\,\mathrm{GeV}$, the sensitivity to possible discrepancies to the SM couplings at high energies increases for the reaction $e^+e^- \to W^+W^-$.

Another big topic is the precise measurement of the top quark mass and couplings within a few GeV around 350 GeV, where the threshold for the top quark pair production, $e^+e^- \to t\bar{t}$ is passed. The top quark has no stable bound states, but a short lifetime of about 10^{-25} s with the dominant decay mode $t \to bW^+$. [19] At the ILC, a precision of the top mass of 100 MeV will be possible, while the accuracy is around 400 MeV [19] at the moment. An energy scan of
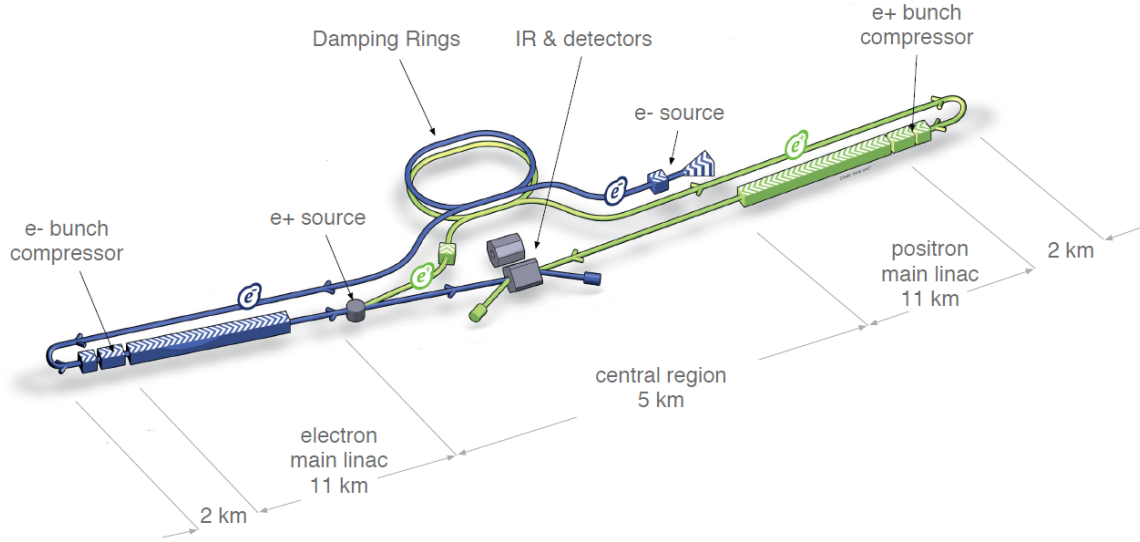
Figure 2.7.: Schematic layout of the ILC with major subsystems. Not to scale. [3]

the top production cross section in the threshold region around 350 GeV can be performed with the ILC, as the energy can be tuned, which allows certain conformity tests with theory. [59]

The search for new particles, for example supersymmetry particles or extended Higgs states, will begin at center of mass energies of 500 GeV, as well as the upper described precision measurements will be increased.

In the region around 1 TeV, measurements concerning Higgs boson self coupling, coupling to the top quarks and composite models of the Higgs boson will be addressed as well as the search for new exotic particles.

2.2. The ILC Design

The planned International Linear Collider is designed to accelerate and collide e^+ and e^- at high luminosity with 200 to 500 GeV center of mass energy which can be extended up to 1 TeV. Currently, discussions are ongoing as the ILC is planned to be built in Japan with 250 GeV center of mass energy, because the discovery of the Higgs boson with a mass of 125 GeV allows the ILC to be operated at lower energy, hence lower cost. [60] A luminosity of $0.75 \times 10^{34} \mathrm{cm}^{-2}\mathrm{s}^{-1}$ can be reached in the first stage at 250 GeV and would be improved to $1.8 \times 10^{34} \mathrm{cm}^{-2}\mathrm{s}^{-1}$ at 500 GeV.

To reach the aimed high energies, the ILC design is based on linear accelerators built with 1.3 GHz superconducting radio-frequency (SCRF) cavities with an average accelerating gradient of 31.5 MV/m. They were developed at DESY and are an integral part for the acceleration of electrons in the European X-Ray Free-Electron Laser (XFEL) [61], where mass production has already been proven.

A schematic layout of the ILC, with about 31 km length, is shown in Figure 2.7. 90 % polarized electrons are generated in a GaAs photocathode DC gun by laser illumination. The electrons are bunched and pre-accelerated to 76 MeV using normal-conducting devices. Thereafter, the beam is accelerated to 5 GeV in a superconducting linear accelerator (linac) and injected into
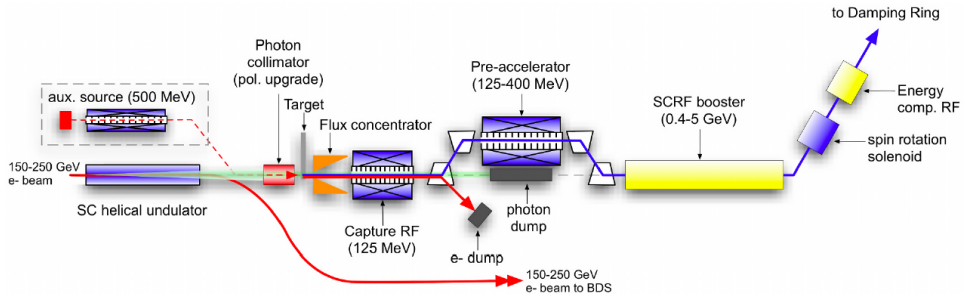
Figure 2.8.: Schematic layout of the positron source. [52]

the damping ring, which is a tunnel with a circumference of 3.2 km. Before injection, the spin vector is rotated into the vertical and the vertical emittance of the beam is reduced by five orders of magnitude to 20 nm by means of superconducting magnets and wigglers [62], which comprise a series of magnets utilized to adjust the beam acceleration by deflecting the beam and damping synchrotron radiation.

Subsequently, the electron beam enters the Ring to Main Linac (RTML), which transports the beam approximately 15 km to the main linac, including a 180° turn around after which the beam is accelerated further from 5 GeV to 15 GeV.

The main linac accelerates the beam from 15 GeV to the intended beam energy up to 250 GeV, utilizing 7400 of the upper mentioned SCRF cavities, which are cooled down to 2 K within around 850 cryomodules.

For the generation of positrons, the primary electron beam is directed to the positron source system, as schematically shown in Figure 2.8. Depending on the electron energy, photons with energies between 10 MeV and 30 MeV are generated inside a 147 m superconducting helical undulator. The electron beam is guided apart from the photon beam, while the latter are collimated onto a thin Ti-alloy target with 0.4 radiation length, due to which electron-positron pairs are produced. After acceleration to 125 MeV, the remaining photons and electrons are dumped and the positrons are accelerated further to 400 MeV. A SCRF booster, which is similar to the one used for electrons, accelerates the positrons up to 5 GeV, rotating their spin into the vertical and finally injecting them into a second damping ring, which is housed in the same tunnel as the electron damping ring.

A polarization of 80 % for electrons and 30 % for positrons can be reached. A second RTML transports the positron beam from the damping ring to the second linac, similar to the setup for electrons. A Beam Delivery System (BDS) directs the high energy electron and positron beam to the interaction region (IR), where they collide. Two different detectors can alternately be placed into operation at the IR.

The collision rate of the ILC is 5 Hz. The structure of the beam consists of bunch trains with 1312 bunches. A bunch includes 2×10^{10} particles and is separated by 554 ns. Therefore, collisions happen only within less than 1 ms, followed by 199 ms silence. This idle time allows power pulsing of the electronics to save power and cost as well as reducing temperature and thus the need for cooling. Power pulsing has successfully been tested in 2016 for a new generation
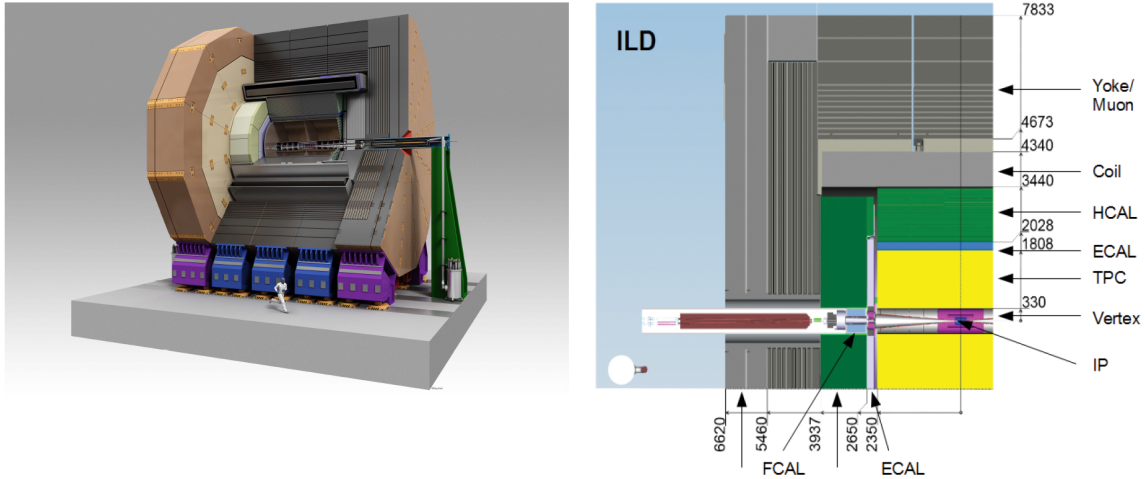
Figure 2.9.: Concept of the ILD detector. The right scheme shows a quadrant view of the different sub-detectors with dimensions in mm. [3]

of the AHCAL technological prototype (more details in Chapter 3), a calorimeter prototype for one proposed detector for the ILC. [63].

2.3. Detectors for the ILC

As discussed above, the interaction region of the ILC is occupied by two detectors. Refer to Reference [4] for more detailed information. The utilization of two detectors has the advantage of independent experiments which allows cross-checks of results. The two proposed detectors are the International Large Detector (ILD) and the Silicon Detector (SiD), which are discussed in the following subsections.

To meat the requirements of the physics program (cf. Section 2.1), significant improvements of detector performances are vital. A main objective is a relative jet energy resolution of $\Delta E/E = 3\,\%$ to $4\,\%$ in order to separate W and Z di-jet final states, which is expected to be achieved with the utilization of the Particle Flow Approach (cf. Section 1.4). The PFA requires a high efficient tracking system and a high granularity of electromagnetic and hadronic calorimeters. For charged tracks, a momentum resolution of $\Delta p/p^2 = 5 \times 10^{-5}\,\mathrm{GeV}^{-1}$ is required in order to measure the recoiling Higgs mass from the Z boson in the Higgs-strahlung process. Another requirement is a high impact parameter resolution for flavor and quark-charge tagging, which can be achieved by latest generation vertex detectors.

2.3.1. The International Large Detector (ILD)

Although the ILD is designed to match the requirements of the PFA, it is a multi-purpose detector. Figure 2.9, shows a schematic of the complete ILD with a designed length of around 13 m and a radius of around 7.8 m on the left and a quadrant view of the sub-detectors on the right. A magnetic field of 3.5 T parallel to the beam axis is provided by a superconducting solenoid coil with 3.4 m radius, inside which the tracking and calorimeter systems are placed. The sub-systems are discussed in the following.

Tracking System

The main task of the tracking system is to measure the momentum of charged particles.

In the center is a high-precision multi-layer pixel vertex detector (VTX) with a barrel geometry very close to the interaction point (IP). The reconstruction of short-lived processes and of the exact interaction point are main objectives and a minimum material thickness is a key feature of the VTX, required for optimum calorimeter and PFA performance. Different detector geometries are proposed, for example a geometry consisting of three sub-layers, while the innermost layer closest to the IP only has half the length of the other two in order to reduce the impact of background hits. The first layer is located at a radius of around 16 mm. Depending on the layer, the VTX features a position resolution between $\sigma < 3\,\mu\text{m}$ and $\sigma < 6\,\mu\text{m}$ with a material budget lower than $0.15\,\%\,X_0/\text{layer}$.

Three different pixel technologies are developed for the ILC, which all meet the requirements for the ILD: the CMOS Pixel Sensors (CPS) [64, 65], the Depleted Field Effect Transistor (DEPFET) sensors [66, 67] and the Fine Pixel CCD (FPCCD) sensors [68]. Between the vertex detector and the Time Projection Chamber (TPC), two layers of silicon strip detectors (Silicon Inner Tracker, SIT) fill the gap. For low angle tracking, five silicon-strip discs (Forward Tracker, FTD) are placed in the forward region. The SIT and the FTD feature position resolutions of less than $\sigma = 7\,\mu\text{m}$ and $\sigma < 6\,\mu\text{m}$, respectively, with a material budget of $0.65\,\%\,X_0$.

The large-volume TPC allows a three dimensional reconstruction of trajectories of charged particles and also particle identification via the specific energy loss dE/dx with around 5 % resolution utilizing up to 224 points per track. It starts at a radius of 330 mm and lasts until 1808 mm and consists of a gas amplification system. The gas within the TPC is ionized by charged particles traversing the medium. Free electrons are generated and drift to the endplates of the TPC due to an electric field, where they are measured. The 3D trajectory is reconstructed by using the arrival time information of the drift electrons at the endplates. The endplates are located at $z = 2350\,\text{mm}$, with the z-axis along the beam direction, and support stability to the TPC. For the detection of the amplified signals at the endplates, two systems are proposed; the Micro-Mesh-Gaseous Structure (Micromegas) [69] and the Gas Electron Multipliers (GEM) [70] system.

Because of continuous tracking, the moderate point resolution of $\sigma < 100\,\mu\text{m}$ can be compensated. It features a double hit resolution of $< 2\,\text{mm}$ in the z-direction. An advantage is the very low material budget of $5\,\%\,X_0$ within the radius and $< 25\,\%\,X_0$ including the readout endplates. A momentum resolution of approximately $\Delta p/p^2 \approx 10^{-4}\,\text{GeV}^{-1}$ can be achieved in the TPC within the magentical field of 3.5 T.

Two additional Si-strip detectors, which provide high-precision spatial resolution, fill the space between the TPC and the calorimeter system described next. For high momenta, the combined tracking system, including the VTX, TPC etc., can achieve a momentum resolution of $\Delta p/p^2 = 2 \times 10^{-5}\,\text{GeV}^{-1}$.

Calorimeter System

The calorimeter system of the ILD consists of an electromagnetic and a hadronic sampling calorimeter inside the solenoid magnet. It features a highly granular design in order to fulfill the requirements of the Particle Flow Approach to reach the pursued jet energy resolution of $\Delta E/E = 3\,\%$ to $4\,\%$ as mentioned above.

The inner calorimeter is the electromagnetic calorimeter (ECAL) with the initial role to identify and measure the energy of photons by separating different showers generated by them. Also, as hadronic showers might start in the ECAL, too, a high granularity enhances the hadron hadron separation. The ECAL design consists of 30 layers with channels of $5 \times 5\,\text{mm}^2$, read out by silicon diodes (called SiECAL). An alternative design consists of scintillator strips of $5 \times 45\,\text{mm}^2$ with alternating layers turned by $90°$, to resolve the a similar resolution (called ScECAL). Tungsten[1] has been selected as absorber material between the active layers, which results in $24\,X_0$ within $20\,\text{cm}$ of the compact ECAL.

The measurement of neutral hadrons is the main task of the hadron calorimeter (HCAL), as well as the separation of neutral hadrons (approximately $10\,\%$ within a jet) from the large number of charged hadrons in a shower, as the latter shall be reconstructed in the tracking detectors. The HCAL consists of 48 layers of alternating steel[2] absorber plates and active medium and covers about 6 nuclear interaction lengths.

Two designs are proposed, one that uses scintillator tiles of $3 \times 3\,\text{cm}^2$, read out by an analogue system (discussed in detail in Chapter 3) and the other uses gas-based channels of $1 \times 1\,\text{cm}^2$, processed by a semi-digital readout.

A system of high-precision calorimetric detectors are foreseen at low angles for beam luminosity and -quality measurements, which require radiation hardness.

Finally, the iron yoke, which returns the magnetic flux of the solenoid, is equipped with resistive plate chambers (RPC) or scintillator strips. Like this, it can be utilized as a tail-catcher calorimerter as well as a muon detector and -filter.

No traditional hardware trigger is foreseen for the readout of the detector, as discussed previously in Section 2.1.

2.3.2. The Silicon Detector (SiD)

The SiD is a general purpose high precision detector designed for the ILC and only a short overview is given here in regards to the main differences to the ILD. A schematic model of the SiD is shown in Figure 2.10.

The SiD design as well as its performance is in many ways similar to the design of the ILD, but features a larger magnetic field of $5\,\text{T}$ that allows overall smaller dimensions. Instead of a TPC, the tracking system is utilized completely with silicon detectors. The ECAL is equipped with silicon active layers divided in hexagonal pixels. Though the HCAL has first been considered to utilize gas as active medium with RPC readout, recent developments resulted in an adjustment of the design to instead utilize scintillator-tiles.

---

[1]Tungsten: radiation length $X_0 \approx 0.35\,\text{cm}$, interaction length $\approx 9.9\,\text{cm}$, Molière radius $\approx 0.93\,\text{cm}$. [71]
[2]Iron: radiation length $X_0 \approx 1.8\,\text{cm}$, interaction length $\approx 17\,\text{cm}$, Molière radius $\approx 1.7\,\text{cm}$. [72]
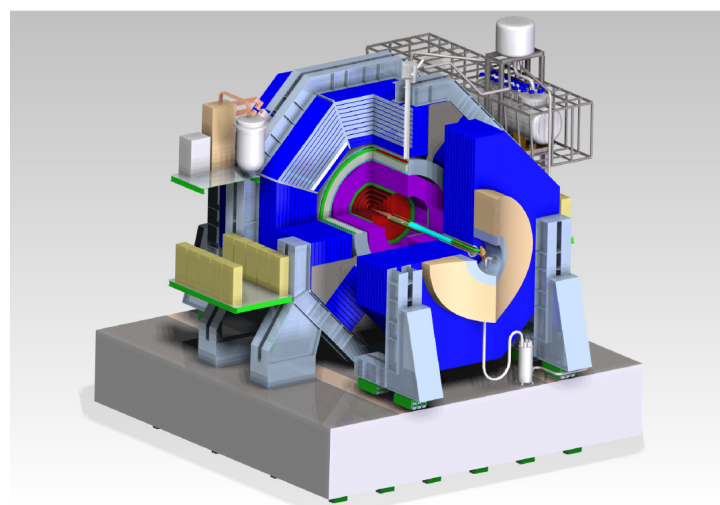
Figure 2.10.: Model of the Silicon Detector. [3]

3

The CALICE Analog Hadron Calorimeter

The Analog Hadron Calorimeter (AHCAL) is intended to be utilized in the ILD and is under development by the CALICE (Calorimeter for a Linear Collider Experiment) collaboration. Many years of research and development has flown into different prototypes of the AHCAL, which have been constructed and tested in various testbeam campaigns. In July 2015, the technological AHCAL prototype has been shipped to CERN in order to perform measurements with different particle showers, with the purpose to prove the scalability to a full detector and to draw conclusions for optimizations of the utilized technology.

Before the measurements are discussed later from Chapter 8 on, this chapter first gives an overview of the AHCAL design. This includes details about the readout technology and the base units on which the readout channels are placed. Each channel consists of a Silicon Photomultiplier (SiPM) coupled to a scintillator tile, while different channel designs are utilized. The chapter closes with a short outlook of the upcoming new generation of a technological prototype, utilizing evolved designs and components.

The following discussion is based on the *ILC Technical Design Report - Volume 4* [4], if not stated otherwise.

3.1. AHCAL Design

The AHCAL is designed as a highly granular sampling calorimeter with alternating active layers and steel absorber plates, which also secure the stability of the structure of the calorimeter. The high granularity of the calorimeter is required to maximize the efficiency of the Particle Flow Approach (PFA) to reach the pursued goal of 3-4 % jet energy resolution. With this approach, the energy of neutral hadrons is measured in the HCAL, which requires a separation from charged hadrons and other particles in a shower. Because on average 10 % [4] of the jet energy is carried by neutral hadrons, the contribution of the relatively poor resolution of hadronic calorimeter can be reduced concerning the total jet energy resolution.

The realization of high granularity is challenging, as it requires millions of channels which have to be biased, controlled and read out. To accomplish this high complexity and reduce the number of connections going in and out of the detector, the active layers directly include the front-end electronics, which handle the named tasks and only forward prepared data out of the detector. Besides the electronic challenges, other issues have been addressed, as the mechanical structure, which is optimized to very low amount of insensitive areas, as well as power consumption and temperature handling. This can be achieved by power-pulsing of the readout electronics, due to which no active cooling is required within the calorimeter volume. Also important concerning
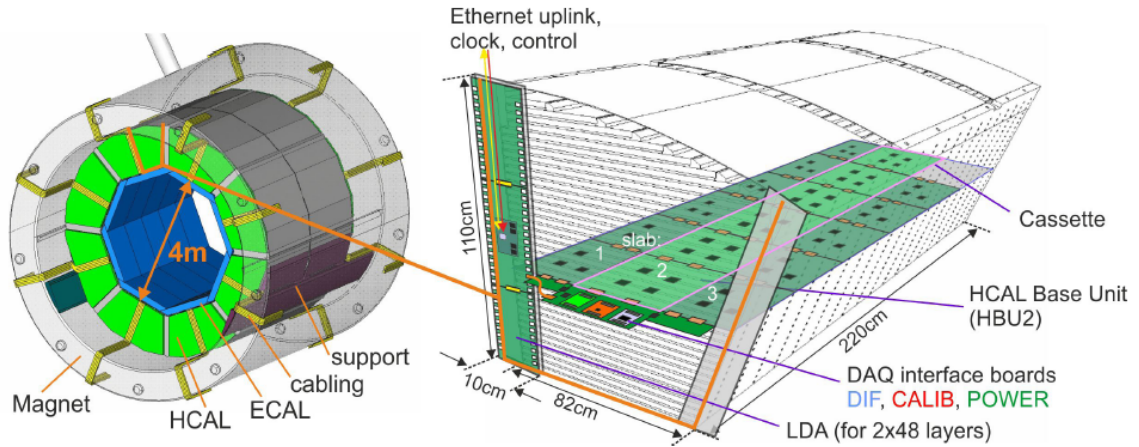
Figure 3.1.: Schematic of the ILD with a detailed draft of one calorimeter segment. [73]

power and temperature is the utilization of Silicon Photomultipliers (SiPM), which require only low bias voltage. The steel absorber structure is self-supporting and requires no additional support for stability.

Figure 3.1 shows a schematic of the ILD with a zoomed look of one calorimeter segment. The baseline design of the HCAL consists of two rings of 16 segments with a weight of 20 tons each. A segment consists of 48 absorber plates, each 16 mm thick. Between two absorber plates there is room for the active layers. The active layers consist of 3 mm thick scintillator tiles and SiPMs and readout devices. The active layers are fastened by surrounding steel plates of 0.5 mm thickness. Per layer, up to 18 separate readout devices, called HCAL Base Units (HBU) (see Section 3.2), are instrumented. The HBUs are designed such that they are easily interchangeable. In total, only 16 data connections for all 32 segments are foreseen to leave the calorimeter, as two neighboring sections share one concentrator board, called Link Data Aggregator (LDA), where the data of all connected layers are collected and forwarded.

Within the last decades, two main versions of AHCAL prototypes have been constructed and investigated within the CALICE collaboration. While the *physics prototypes* [74] have demonstrated the feasibility and performance of highly granular hadronic calorimeters with scintillator tiles and SiPM readout in several testbeam campaigns back in 2007 to 2009, the *technological prototypes*, aim to optimize the technology by using enhanced and integrated readout electronics and testing various different layer configurations. This thesis mainly deals about the small technological prototype which has been tested in 2015 and consists of 14 layers. The latest constructed technological prototypes from 2016 on aim to prove the scalability of the prototype to a full calorimeter for the ILD. This requires several automation steps of which an overview is given in Section 3.3. To make a distinction between the different generations of technological prototypes, in this thesis the latest generation prototypes from 2016 on are referred to as *engineering prototypes* [75], as similar done in [76].

3.1.1. SiPM Introduction

As mentioned before, the AHCAL utilizes channels made of scintillator tiles read out by Silicon Photomultipliers (SiPM).

The next Chapter 4 discusses SiPMs in detail, as the responses of these photo detectors are a main object of this thesis. For now, a short introduction is given.

A SiPM is a solid state semiconductor photo detector which is capable to detect single photons. It consists of an array of pixels, each operated in Geiger-mode, creating an electric field inside the pixels. In case a photon is absorbed in a pixel, an electron-hole pair can be generated which then drifts apart due to the electric field and triggers secondary ionization, yielding an avalanche of charge carriers. This process is called *firing* and the probability to trigger an avalanche is called photon detection efficiency (PDE). The amplification reached by this process is defined as the *gain* of a SiPM.

Typically, SiPMs have hundreds up to tens of thousands of pixels on a small area of a few mm^2. All pixels are connected in parallel such that the signal of the SiPM is the sum of all pixel charges. By estimating the gain, the measured signal can be converted back to the number of pixels fired. Due to the finite number of pixels, the response of a SiPM saturates at high light exposures. Various kinds of noise falsely increase the signal of a SiPM, as for example *dark noise* gives a constant contribution, while *optical crosstalk* between pixels depends for instance on the number of pixels fired and is thus associated with correlated noise. Dark noise is taken care of in the readout electronics of the AHCAL by applying a certain threshold. As an outlook, within this thesis, a method to handle noise effects of optical crosstalk is applied by means of a SiPM response model, as discussed in Section 9.2.

Through the years, different SiPM types have been utilized in various AHCAL prototypes. Mayor improvements have been achieved to SiPM performances in the last decades, parallel to a reduction of cost as they have entered the commercial market. Nowadays, pixel numbers of the order of 10^4 per SiPM are available which reduces the impact of saturation of the response. One major improvement has been made concerning the PDE of SiPMs, which now feature a high efficiency in the range between approximately 350 nm to 1000 nm with a maximum efficiency in the region of blue light around 450 nm [77], removing the need for wavelength shifting fibers in scintillator tiles. Also, the dark noise has been reduced due to optimized production procedures and the optical crosstalk between pixels has nearly been prevented ($< 1\,\%$) by optical trenches between pixels. [78]

3.2. HCAL Base Unit

A major part of the AHCAL is the HCAL Base Unit (HBU), a 36×36 cm^2 Printed Circuit Board (PCB). It carries a total of 144 channels in a 12×12 scheme. The channels consist of $30 \times 30 \times 3$ mm^3 scintillator tiles, read out by SiPMs. On the top side of the HBU, four Application Specific Integrated Circuits (ASIC) are soldered to read out the 144 SiPMs, as discussed below in Section 3.2.1.

Figure 3.2 shows the top and bottom side of a HBU. The HBU features self-calibration of the channels by LEDs, which are placed on the PCB under the scintillator tiles. Short light pulses of a few ns width and small amplitudes allow to calibrate the SiPMs.

Various generations of HBUs have been developed to meet the demands of different SiPM types. In the beginning, SiPMs with connector pins have been used, which have required dedicated
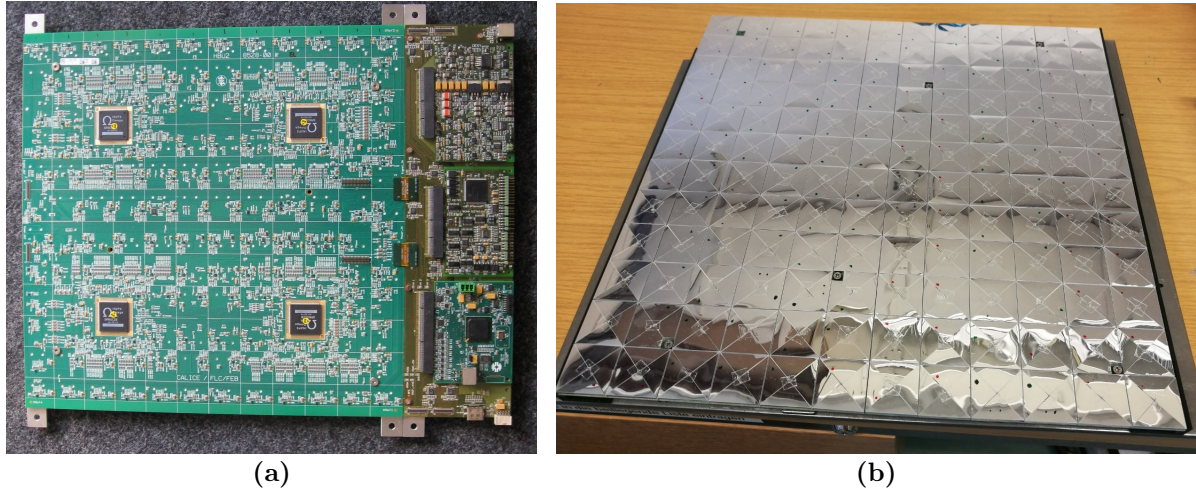
Figure 3.2.: Top (a) [79] and bottom (b) [80] view of a HBU module. The four ASICs are visible on the top side as well as the 144 wrapped scintillator tiles with SiPM readout on the bottom side. The picture (a) also shows connected modules for power supply, readout and calibration of the channels.

connection holes inside the PCB and complicated alignment procedures in combination with the tiles. Nowadays, due to the advancements of SiPMs, SMD[1] SiPMs are available, which can directly be soldered onto the HBU, making the construction much easier and allowing for an automated placement.

A picture of a scintillator tile and a SiPM with connector pins, which is placed at one edge of the tile, is shown in Figure 3.3a. The tile also includes a wavelength shifting (WLS) fiber which shifts the wavelength of collected light to a region of high SiPM efficiency and guides it onto the SiPM. The edges of the tile are chemically etched to reduce tile-to-tile crosstalk. In Figure 3.3b, the latest design is shown, which utilizes SMD SiPMs soldered in the center of a scintillator tile. The tile features an optical dimple that reflects photons onto the SiPM. Various optimizations studies of the tile-dimple design have been performed at Mainz [81]. The latest generation tiles are wrapped in reflective foil in order to improve the light yield of the channel and to inhibit tile-to-tile crosstalk.

3.2.1. SPIROC ASIC

For the readout and digitization of SiPM signals, an Application Specific Integrated Circuit (ASIC) has been developed by the OMEGA [82] group. This chip is called SPIROC [83], for SiPM Integrated Read-Out Chip. It is designed to match the requirements of the AHCAL and is capable to control 36 SiPMs.

The tasks of the SPIROC involve channel-wise biasing in order to tune the gain of all connected SiPMs, charge and time measurements of SiPM signals and their digitization. It also includes an adjustable charge threshold in order to feature the auto trigger mode, which reduces the data volume. Finally, the SPIROC has a capability for power pulsing in order to reduce the power consumption to $25\,\mu\text{W}$ per channel, which is sufficient to not require active cooling. [84].

---

[1]SMD: Surface-Mounted Device
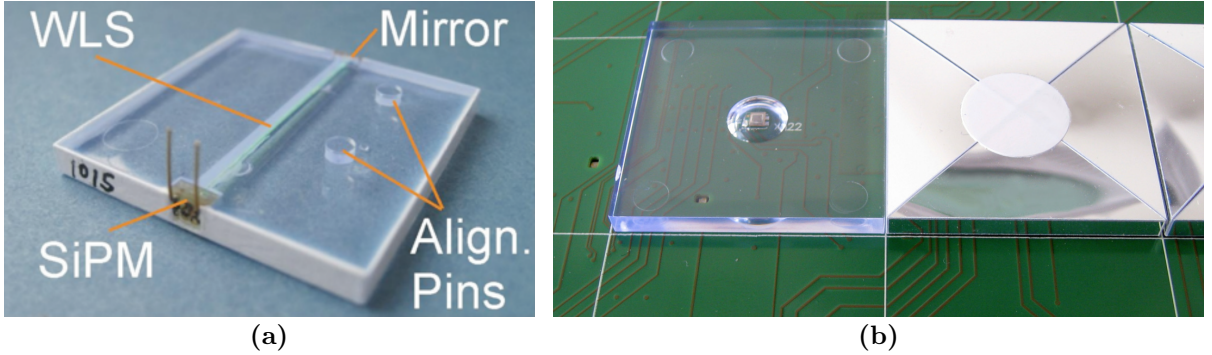
Figure 3.3.: Pictures of the SiPM and tile system. (a) Design with WLS fiber. The SiPM has connection pins which are later connected to the HBU. The edges are chemically etched to reduce tile-to-tile crosstalk. [4] (b) Enhanced design without WLS fiber and individual wrapped reflective foil. The left tile is not yet wrapped to show the dimple inside the tile and the SMD SiPM centered underneath it. [75]

The following discussion is based on references [84, 85].

Figure 3.4 shows a diagram of the signal processing by means of a single channel. The SiPM is connected to the two *IN* squares. The 8-bit Digital Analog Converter (DAC) allows channel wise fine tuning of the SiPM bias voltage in the range between 0 and 5 V above the similarly to all SiPMs on this HBU applied bias voltage.

The signal of a SiPM is split and amplified with two different preamplifiers, one with low and the second with high amplification, which is refereed to low-gain (LG) and high-gain (HG) mode, respectively. The ratio between the HG and LG amplification has been fixed to a ratio of about 10 : 1. This dual mode increases the dynamic range of the readout and allows for instance to measure a small number of pixels fired, which is required for the SiPM gain estimation in HG mode, while being capable of reconstructing thousands of pixels fired in LG mode.

The SPIROC can be processed in two modes: the external trigger (ET) mode and the auto trigger (AT) mode. In ET mode, an external signal triggers the sampling of the SiPM signals. This mode is chosen for the LED calibration. The AT mode is the default ILC physics mode. In AT mode, the signal after the high-gain preamplifier is compared to a threshold. Therefore, a fast shaper is used as shown in the diagram to rapidly compare the signal amplitude to the threshold. If this signal passes the threshold, the slower shaped HG and LG signals are stored in analog memory buffers (called *memory cells*). Up to 16 amplitudes can be stored sequentially in the memory cells.

Once a buffer is completely filled, a readout command triggers the digitization of the buffered amplitudes after a gain selection, using the 12-bit Wilkinson ADC. The gain selection secures that only the amplitude with the best resolution is processed, that means if the HG amplitude is not saturated, this value will be digitized. A gain-notifier bin is stored with the amplitude and marks the selected gain mode.

In parallel, a time measurement is performed within the SPIROC, using a time to amplitude converter. The basic principle can be described by a linear voltage ramp that increases with time and is stored once a signal over threshold is detected. The amplitude is then stored in an analog memory buffer with a depths of 16 and digitized analogically to the signal amplitudes
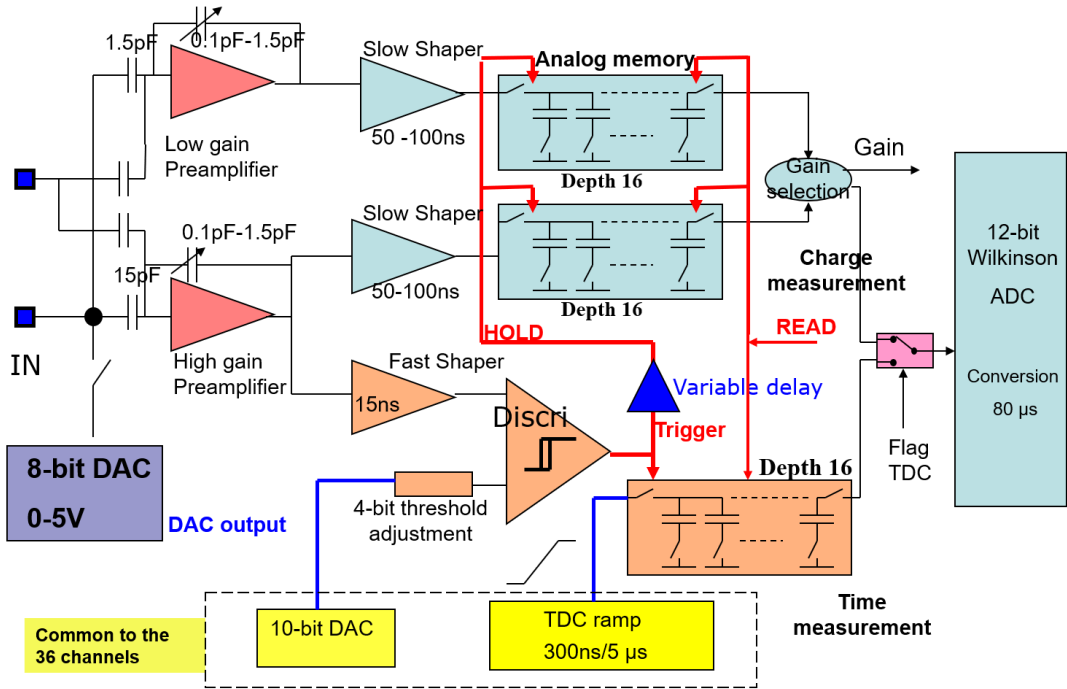
Figure 3.4.: Diagram of the signal processing for a single channel on the SPIROC chip. [86]

once the readout command triggers the digitization.

A short remark: for the intercalibration between HG and LG mode, the two HG and LG buffers are digitized and processed further instead of the time buffer.

The design of the SPIROC allows to make use of power pulsing, which can be done because of the ILC beam frequency of 5 Hz, with the collisions happening within 1 ms and 199 ms idle time. Not needed parts of the SPIROC can be switched off in case they are not needed for the moment.

The digitized amplitudes are then further processed by the detector interface board which forwards the signal to the Link Data Aggregator (LDA), which itself aggregates the data of all connected interface boards and forwards it out of the detector.

For the supply of bias voltage to the SiPMs, the ASICs and other electronic modules, the Power Board is utilized. The Calib Board manages the LED system and triggers pulses with variable voltage in order to allow measurements with different light intensities, as variations in the LED positions and different SiPM types require different light amplitudes for the gain measurement. These three boards are also part of Figure 3.2a.

3.3. Current Status and Outlook

As mentioned before, different prototypes have been developed by the CALICE collaboration in the past years. The **technological prototype** has been investigated in various testbeam campaigns at DESY and CERN in 2014 to 2015, testing the performance with steel and tungsten

Figure 3.5.: Picture of the AHCAL technological prototype in 2015. Left: The front of the detector is to the right. Only 14 slots are equipped with active layers. [88] Right: Picture taken in the measurement area H2 at CERN SPS. [89]

absorber stacks.

This thesis concentrates on the data taken in July 2015 at CERN SPS H2 [87]. Details about the configuration of the prototype and of the beamline are discussed later in Section 8.1. In short, the prototype utilizes a steel absorber stack with 48 absorber plates, each 17 mm thick. The stack is not completely equipped, instead only 14 active layers are inserted: two ECAL Base Units (EBUs, which fulfill similar tasks as HBUs), eight single HBUs and four big layers made of 2×2 HBUs. The HBUs consist of different SiPM-tile configurations. While older modules utilize SiPMs with pins and only 800 pixels in combination with tiles with WLS fiber, new generation modules consist of SMD SiPMs with 1600 pixels and individually wrapped tiles. The large variety allows for comparisons and optimization studies.

The first 10 modules are paced in the first 10 slots of the absorber stack and the four big layers are inserted such that empty slots remain between them in order to have some active layers in the middle and in the back of the stack. Like this, the last layer is placed in slot 31 which roughly corresponds to 30 X_0 and 3.1 nuclear interaction lengths, not taking into account the material of active layers. In total, the prototype includes 3744 channels. A picture of the prototype is shown in Figure 3.5.

An overview of the latest generation AHCAL technological prototype (in this thesis called **engineering prototype** as mentioned before) is given in the following and is based on [75, 90, 91], unless otherwise stated. The prototype has been constructed in 2017 and testbeam measurements have been successfully performed in a total of 10 weeks in 2018 and additional measurements are planned for 2019. It consists of 38 layers with more than 99 % active channels, instead of approximately only about 85 % in the previous prototype. The prototype includes 608 ASICs which control around 22000 channels.

The main objective of this prototype is to prove the scalability to a full ILD calorimeter. Therefore, *mass production* capacity has been addressed in the construction of the new prototype. To achieve this, the following changes have been applied in contrast to previous prototypes:

(a)   **(b)**
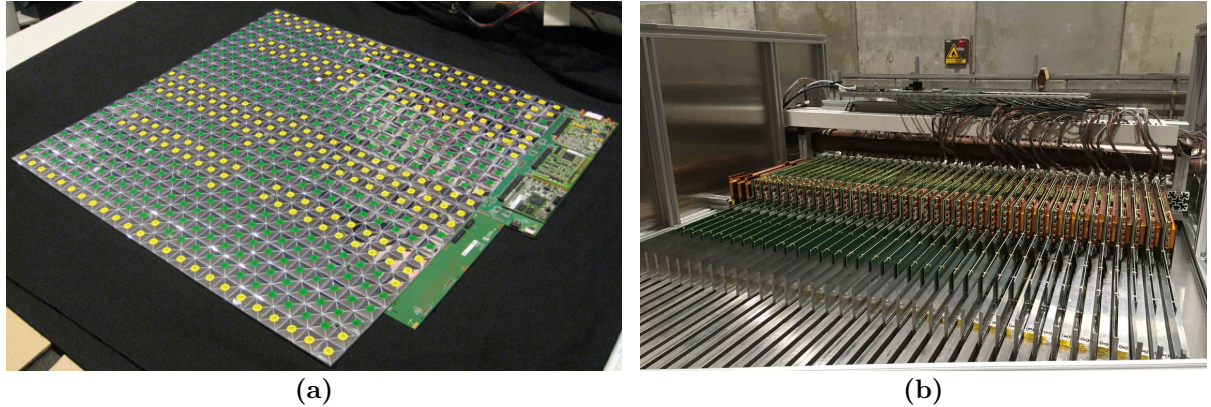
Figure 3.6.: (a) Picture of a big layer consisting of 2×2 HBUs equipped with SMD-SiPMs and automatically wrapped tiles. On the right edge, interfaces for power, DAQ and LED are connected. (b) Picture of the AHCAL engineering prototype steel absorber stack equipped with 38 big layers. [75]

Only one type of SMD SiPM with 2668 pixels is directly soldered on all HBUs. This has the advantage that no complicated alignment with SiPM connector pins is required, as well as that the same bias voltage can be applied to all SiPMs, which makes channel-wise adjustments redundant.

Also, the production procedure of the scintillator tiles has been adapted. Instead of cutting the optical dimple into each tile, which is time-consuming, the polystyrene tiles are injection molded with a mold that already includes the dimple.

Afterwards, the tiles are automatically wrapped with 3M ESR reflector foil in an automated procedure, which first uses a laser cutter to insert slits without completely cutting through the thin foil. This allows to easily bend the foil around the tile using a wrapping machine developed by the University of Hamburg. [92].

Finally, the placement of the tiles on the HBU is performed by a screen printer and a pick-and-place machine at the University of Mainz. [90] The screen printer is used to place a defined quantity of glue on intended places on the bottom side of a HBU. Once the glue is on the board, the HBU is placed inside a pick-and-place machine, which automatically places the tiles. With this method, about four HBUs have been assembled per day, which is a large improvement in speed and repeatability compared to before, where each tile had to be placed manually.

Figure 3.6a shows a big layer consisting of 2×2 HBUs, fully assembled in the just discussed way. Different color markings are used for the pick-and-place machine to recognize different tile alignments, needed for LED-holes for example, as there are different position configurations. Figure 3.6b shows the AHCAL absorber stack with 38 equipped active layers, each consisting of 2×2 HBUs.

During the various testbeam campaigns, the operation of the prototype has been proven to be reliable as well as capable for power pulsing. Also, a combined testbeam of the AHCAL prototype with the CMS HGCAL [93] has been performed in October 2018 testing the synchronization capacity of both prototypes. The HGCAL is a high granularity calorimeter designed for particle-flow calorimetry after the planned LHC high luminosity upgrade. Analysis of the results of these testbeam campaigns are ongoing.

In the future, *megatiles* [94] are considered as a faster alternative to the upper described process of the tile production and wrapping. Besides studies of possible improvements to the existing prototype, a combined testbeam of the AHCAL and the ECAL is aspired to perform realistic performance studies in the future.

Nevertheless, the next steps will be determined by the progress concerning linear collider projects, not only of the ILC.

4

SiPM Characterization Basics

This and the following two chapters describe one of the main parts of this thesis: the Silicon Photomultiplier (SiPM) response measurement.

This chapter gives an introduction by explaining SiPM properties and their implementation into a test stand. Especially the measurement concepts of important SiPM characteristics are discussed in Section 4.2. This, for example, includes explanations on how to measure the gain and optical crosstalk effects of a SiPM. SiPM saturation and the principle of the SiPM response measurement are described in Section 4.3. This includes the definition of the number of seeds, an important parameter representing the incoming light intensity and explains the method used to calculate it. Finally, Section 4.3.3 lists different SiPM response models, which will later on be tested in the results.

The methods explained in this chapter will later on be used in Chapter 6, where the SiPM response measurement is discussed in detail.

4.1. SiPM Properties

Silicon Photomultipliers, also called Multi-Pixel Photon Counters (MPPC) [95], are robust and efficient solid-state semiconductor photo sensors. They consist of an array of hundreds to thousands of pixels on a sensitive area of about one to a few square millimeters. Therefore, a typical pixel pitch is of the order of ten to hundred micrometers. Each pixel is comparable to an avalanche photodiode (APD) in combination with a quenching resistor, as indicated in Figure 4.1, right.

SiPMs boast an excellent time and photon counting resolution. Compared to photomultiplier tubes (PMTs), SiPMs have major advantages. Besides their small size, they require low bias voltages (< 100 V) and are insensitive to magnetic fields [97]. Since a few years, they are also available as surface-mounted device (SMD) components, which makes them capable of mass assembly. This makes them perfectly suited for applications in particle physics detectors within magnetic environments.

Yet, the limited dynamic range of SiPMs to high light exposures might be one disadvantage. Figure 4.1 shows two pictures of two different SiPMs on a test-PCB, as they are used in the following measurements.

In the following, a detailed description of SiPM properties is given.

Figure 4.2 schematically shows a sketch of a SiPM topology and of the electric field E induced by the reverse bias voltage. The low doped p^- layer on top of the higher doped p^+ layer generates a rather low electric field called drift region. Between the $n^+ - p^+$ layer, called depletion region, the electric field is rather high in the order of 10^5 V/cm [98].
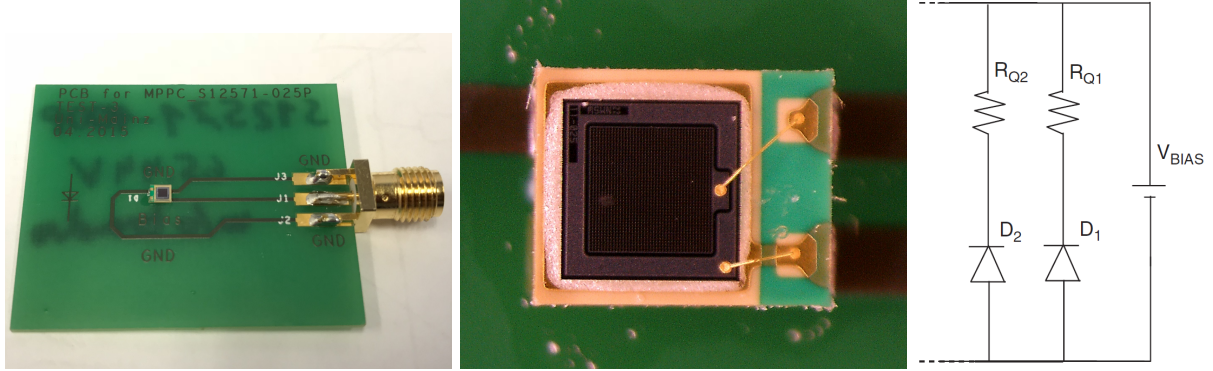
Figure 4.1.: Pictures of SiPMs on small test-PCBs. Left: Complete picture including connector. Different to what is written on the PCB, MPPC S12571-100P with 100 pixels is soldered on it. Middle: This microscope shot allows a view of the array of pixels. This SiPM consists of 1600 pixels with a pitch of 25 µm. Middle picture kindly provided by Y. Liu, JGU Mainz. Right: Sketch of parallel circuit of APDs (pixels) and quenching resistors R_Q. [96]
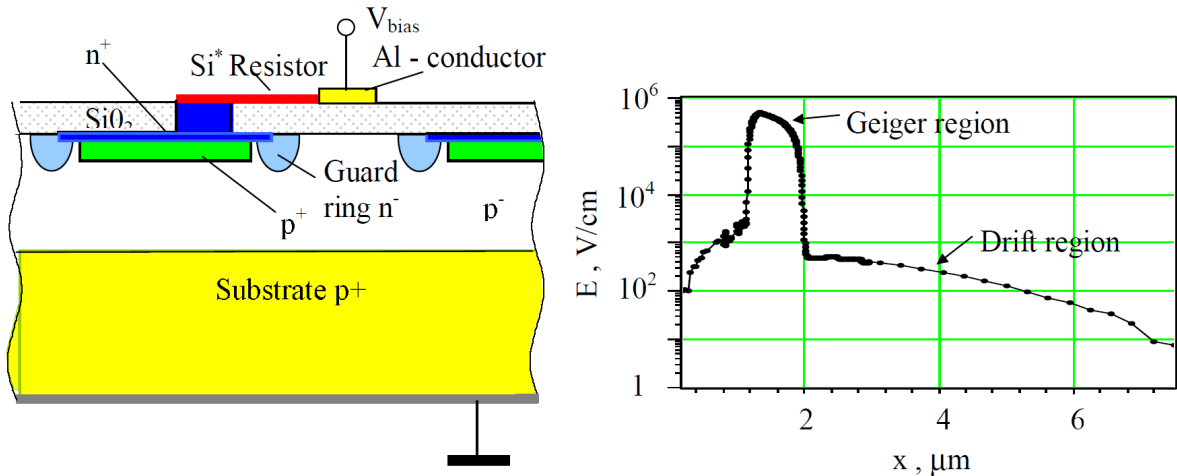
Figure 4.2.: Left: Topology of a Silicon Photomultiplier. Right: Exemplarily electric field in a SiPM pixel as a function of depth x. Compared to the left scheme, x increases from top to bottom. [98]

The SiPM is operated in Geiger mode, that means the reverse bias voltage U_{bias} applied to the pixels is larger than the breakdown voltage U_{break}. The breakdown voltage is defined by the value of the reverse bias voltage, from which on the arising electric field is strong enough so that free and accelerated charge carriers can itself generate secondary free charge carriers due to impact ionization.

If a photon is absorbed in the pixel, it can generate a free electron-hole pair. The probability is high that they do not recombine directly, but drift apart due to the high electric field which accelerates them further and leads to secondary ionization in the depletion region. This process results in an avalanche, called Geiger discharge. Often, the complete process is referred to as *firing*. The current is regulated by quenching resistors connected to each pixel, R_q, in order to limit the discharge by reducing the effective voltage below breakdown voltage. The time it takes to recover the pixel defines its dead time, which affects the dynamic range of a SiPM. From the
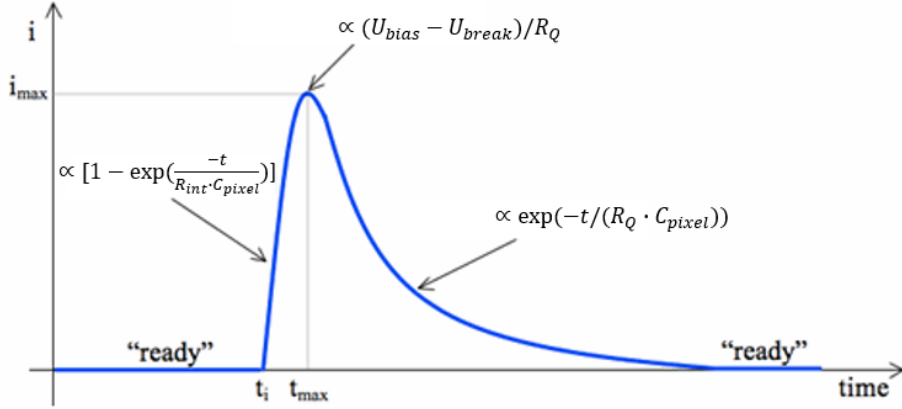
Figure 4.3.: SiPM signal shape of a firing pixel. [100]

moment the pixel is quenched, the pixel capacitance C_{pixel} begins recharging while the current of the pixel decreases exponentially with the recovery time constant τ, which is typically in the range between tens to hundreds nanoseconds:

$$\tau = R_q \cdot C_{pixel} \tag{4.1}$$

The pixel capacitance has its origin in the pn-junction of the pixel and depends on the doping profile and on the pixel size. After the pixel is recovered, it is able to fire again.

The *shape* of a SiPM signal is exemplarily shown in Figure 4.3 and consists of a very fast (order ns) leading and smoothly falling edge. The leading edge is proportional to $1 - \exp(-t/(R_{int} \cdot C_{pixel}))$, with the time t and the internal resistance of the entire pixel, R_{int} ($R_{int} \ll R_Q$). Because of the quenching process and after the maximum $I_{max} \approx (U_{bias} - U_{break})/R_Q$ is reached, the falling edge of the signal decreases as Equation 4.2 [99]:

$$I(t) \propto I_{max} \cdot \exp(\frac{-t}{R_Q \cdot C_{pixel}}) \tag{4.2}$$

The total charge of a fired pixel, q_{pixel}, is given by the integration of the current signal over time. It depends on C_{pixel} and on the bias voltage over breakdown voltage, assigned to the over-voltage, U_{over} as shown in Equation 4.3.

$$U_{over} = U_{bias} - U_{break} \tag{4.3}$$

Detailed analysis show that [99, 100]:

$$q_{pixel} = C_{pixel} \cdot (U_{bias} - U_{break}) = C_{pixel} \cdot U_{over} \tag{4.4}$$

Since a SiPM consists of many pixels, the dynamic range is increased compared to a one-pixel device, but still limited due to a finite number of pixels, which will be discussed in Section 4.3 and finally measured in Chapter 6. All pixels are connected to the same output and therefore,

SiPM	N_{total}	Pixel Pitch [µm]	Sensitive Area $\left[\mathrm{mm}^2\right]$	Typical Gain	Trenches
MPPC S13360 -1325PE	2668	25	1.3×1.3	$7.0 \cdot 10^5$	yes
MPPC S12571 -25P	1600	25	1×1	$5.2 \cdot 10^5$	no
MPPC S12571 -50P	400	50	1×1	$1.3 \cdot 10^6$	no
MPPC S12571 -100P	100	100	1×1	$2.8 \cdot 10^6$	no

Table 4.1.: Basic characteristics of the utilized SiPMs, values provided by HAMAMATSU. [95, 101]

the signal Q of the SiPM is the sum over all fired pixel charges q_{pixel}, or, as given in Equation 4.5,

$$Q = q_{pixel} \cdot N_{fired} \ , \tag{4.5}$$

with the number of pixels fired, N_{fired}, and under the assumption that all pixels yield identical q_{pixel}.

The *gain* G is proportional to the applied over-voltage as given in Equation 4.6 and corresponds to the number of generated charge carriers in an avalanche,

$$G = \frac{q_{pixel}}{q_e} = \frac{C_{pixel} \cdot U_{over}}{q_e} \ , \tag{4.6}$$

with the elementary charge q_e. The gain of a SiPM is typically in the order of 10^5 to 10^7. A method to measure the gain of a SiPM is discussed in Section 4.2.1.

Table 4.1 summarizes typical gain values of the SiPMs under test, as provided by the manufacturer. It also includes the total number of pixels, N_{total}, the pixel pitch as well as the dimensions of the sensitive area and an indicator, whether the SiPMs are equipped with optical trenches, as will be discussed later in this section. As written in the table, the utilized SiPMs cover a range from $N_{total} = 100$ to 2668 pixels, with pixel pitches between 25 µm and 100 µm on a sensitive area of $1 \times 1 \ \mathrm{mm}^2$ to $1.3 \times 1.3 \ \mathrm{mm}^2$.

Under the conditions of simultaneously incoming photons, the dynamic range of a SiPM in first order depends on the finite total number of pixels, N_{total}, of the device. A detailed description is given in Section 4.3.

The *photon detection efficiency* (PDE) of a SiPM corresponds to the probability of an incoming photon to produce an output signal. The PDE, ϵ_{PDE}, depends on the quantum efficiency, ϵ_{QE}, the geometrical fill factor, ϵ_{fill}, and the probability to trigger a Geiger discharge, $\epsilon_{trigger}$ [97]:

$$\epsilon_{PDE} = \epsilon_{QE} \cdot \epsilon_{fill} \cdot \epsilon_{trigger} \tag{4.7}$$

The quantum efficiency is the probability of an incident photon to produce an electron-hole pair. This probability particularly depends on the wavelength of the incident photon and on the structure of the SiPM pixel, while the later can be optimized to absorb photons of a certain wavelength inside the depletion layer by means of the Beers-Lambert law [99]. The SiPM utilized here are most sensitive to blue light around 450 nm [95, 101].

The probability of an electron-hole pair to trigger a Geiger discharge depends particularly on the applied over-voltage which defines both, the strength of the electric field, important to inhibit direct recombination, and the width of the avalanche region in the pixel.
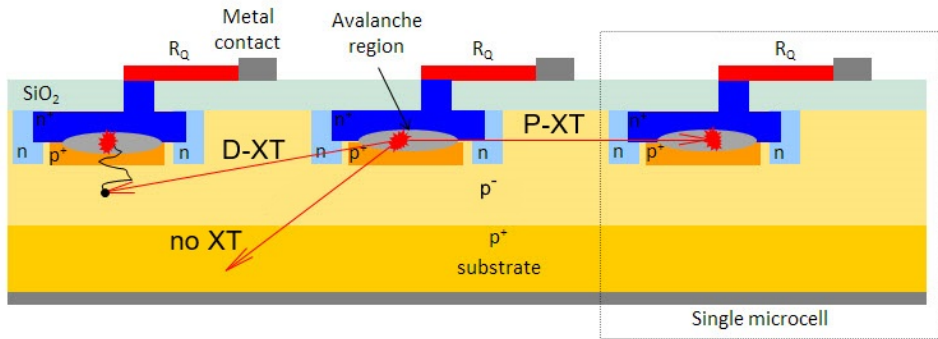
Figure 4.4.: Sketch of prompt (P-XT) and delayed (D-XT) optical crosstalk in a SiPM. [99].

The fill factor is defined as the ratio between the active surface and the total surface of a SiPM. Dependent on the design, it takes values between 20 % and 80 % [35, p. 432].

Since a single electron-hole pair is sufficient to trigger an avalanche and might also be generated by thermal excitations and quantum tunneling, SiPM pixels can fire, although no incident photon is absorbed (or present). The number of these dark noise events per unit time is defined as the *dark count rate* (DCR) and is typically in the order of 10^5 to 10^6 Hz.
Especially the thermal excitation of charge carriers increases with rising temperature and depends on the purity of the semiconductor.
If during an avalanche a charge carrier is trapped in an impurity of the silicon crystal long enough to exceed the recovery time of the pixel, it might trigger a secondary avalanche when it is released, called *after-pulse*. Therefore, it depends, inter alia, on the recovery time τ of the pixels.

Another correlated noise is *optical crosstalk*. Whenever photons are emitted due to a recombination of electrons and holes during avalanche, these photons have a potential to be absorbed in a neighboring pixel and to trigger an additional avalanche. One has to distinguish between prompt- and delayed optical crosstalk as sketched in Figure 4.4. In case of prompt optical crosstalk (P-XT), the secondary photon is absorbed in the avalanche region of the pixel. In contrast to after-pulses, prompt crosstalk happens virtually simultaneous to the primary pixel fired and increases the observed number of pixels fired, N_{fired}.
In case of delayed crosstalk (D-XT), the secondary photon is absorbed close to the avalanche region of a pixel. Due to the lower electric field in this region, the charge carrier diffuses to the avalanche region. The time it takes to enter the avalanche region and to trigger a secondary Geiger discharge depends on the travel distance and on the electric field [99, 102]. Since prompt optical crosstalk usually has a higher probability than the delayed version [103], the indication *prompt* is often dropped.
The probability for optical crosstalk increases with the number of free charge carriers and therefore with the over-voltage generating the electric field.
Latest generation SiPMs utilize so called *optical trenches* in between pixels, in order to reduce prompt optical crosstalk. Crosstalk photons are reflected at these trenches and therefore the pixels are isolated optically from each other. Nevertheless, D-XT is not reduced by this approach. A method to measure optical crosstalk is described in Section 4.2.2.
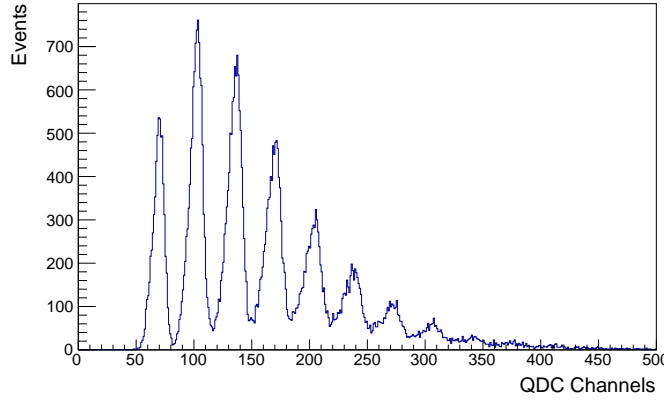
Figure 4.5.: Typical single photon spectrum (SPS) of preamplified MPPC S12571 -25P at $U_{bias} = 67\,V$, recorded with a QDC. Each peak corresponds to a number of pixels fired, while the first (from left) peak corresponds to the pedestal and the second to one pixel fired (1 p.e.) etc.

Many SiPM properties are temperature dependent. Besides the already discussed dark noise dependency, especially the break down voltage U_{break} increases with rising temperature, because the mobility of the charge carriers inside the valence band, $\mu \propto \frac{1}{T}$, decreases [104, p. 18]. Typical temperature dependencies of utilized SiPMs are of the order of $\Delta U_{break}/\Delta T \approx 60\,\text{mV/K}$ [95, 101]. With rising temperature, the chance for an accelerated charge carrier to scatter at the crystal lattice increases due to increased lattice vibrations, resulting in an energy loss of the charge carrier potentially below the required ionization energy.

Since the gain as well as the crosstalk probability primary depend on the over-voltage and therefore on the breakdown voltage, both characteristics decrease with rising temperature at stable bias voltages.

Detailed SiPM temperature dependency measurements for older generation SiPMs have been done in a previous study [78].

4.2. Measurement Concepts

This section deals with the measurement concepts of the gain and the optical crosstalk probability of a SiPM, both being important parameters in the course of this thesis.

4.2.1. SiPM Gain

The gain is one of the most important parameters of a SiPM, especially since a high gain allows the detection of single photons. This section describes the concept of the SiPM gain measurement. The SiPM is illuminated with a pulsed laser and low light intensity. A QDC (charge to digital converter, detailed information can be found in Section 5.2.7) is utilized to simultaneously integrate the SiPM signal within an integration window of a width between $50\,\text{ns}$ to $100\,\text{ns}$, depending on the SiPM type and signal shape.

Figure 4.5 exemplarily shows a histogram where each entry corresponds to one QDC integrated SiPM signal. The SiPM signal is amplified beforehand using a preamplifier with gain $G_{PreAmp} \approx$

8 to simplify the explanation of this method. In principal, the measurement of the SiPM gain does not need a preamplification, provided the intrinsic SiPM gain and the resolution of the QDC are both high enough.

Each peak in the spectrum corresponds to a certain number of pixels fired, N_{fired}. From left to right, the first peak belongs to events, where no pixel has fired, called pedestal. This is a feature of the QDC, as it still outputs a non-zero QDC value if no input signal is present during the integration window (see Section 5.2.7). The second peak is associated to events with one pixel fired (1 p.e., photon equivalent), the third peak corresponds to events with two pixels fired, etc. This kind of histogram is called *single photon spectrum* (SPS).

As discussed in the previous section, the gain is defined in Equation 4.6 as the ratio of the charge of one pixel fired due to an impacting photon, q_{pixel}, and the elementary charge q_e. Under the assumption of essentially identical pixels and because of Equation 4.5, the distance ΔQ_{qdc} of two adjacent peaks in the QDC spectrum is a measure of the gain, as given in Equation 4.8:

$$G = \frac{q_{pixel}}{q_e} = \frac{\Delta Q_{qdc} \cdot \kappa_{qdc}}{q_e \cdot G_{PreAmp}} \qquad (4.8)$$

The factor κ_{qdc} (in this case $\approx 25\,\text{fC/QDC}$ channel, see Section 5.2.7) converts the QDC channel to unit charge. If no preamplifier is appropriated, $G_{PreAmp} = 1$. Later in this thesis, the gain is often expressed as $\mathfrak{S} = \Delta Q_{qdc}$, as the other factors are constants and a gain in units of QDC channels is sufficient for the analysis.

The actual gain measurement of the four utilized SiPM is presented in Section 6.1.4.

4.2.2. SiPM Optical Crosstalk

Optical Crosstalk is a mayor effect, which influences the response and photon counting probability of a SiPM, especially because it is correlated noise. Nevertheless, if the impact of optical crosstalk on the signal of a SiPM is well known, it can be accordingly corrected. Note, that optical crosstalk is not constant but decreasing for high light exposures, since a crosstalk photon can only trigger an avalanche in a non-fired (or recovered) pixel. The number of non-fired pixels is reduced with a higher number of incoming photons - and accordingly higher number of pixels fired.

Still, optical crosstalk can be assumed to be constant as long as a low fraction of pixels (approximately $< 5\% \cdot N_{total}$) is fired. The concept of the measurement of (prompt) optical crosstalk, as it is utilized in this theses, is discussed in the following.

First of all and to facilitate the issue, the impact of optical crosstalk is discussed with the help of an oscilloscope. The SiPM is placed inside a dark box and connected to a preamplifier, which is connected to the scope. After applying a bias voltage to the SiPM, but not adding any light source, the SiPM still generates some output signals because of dark noise, as discussed earlier in Section 4.1. Figure 4.6 shows two scope shots for two different SiPMs at these conditions, while the scope triggers on the falling edge of the SiPM signal. Going from top to bottom (because of the negative polarity of the signal), the first and smallest peak corresponds to a triggered event with one pixel fired (1 p.e.), the second smallest peak to an event with two pixels fired simultaneously (2 p.e.), etc. Due to the high gain of the SiPM, single photons can be distinguished.
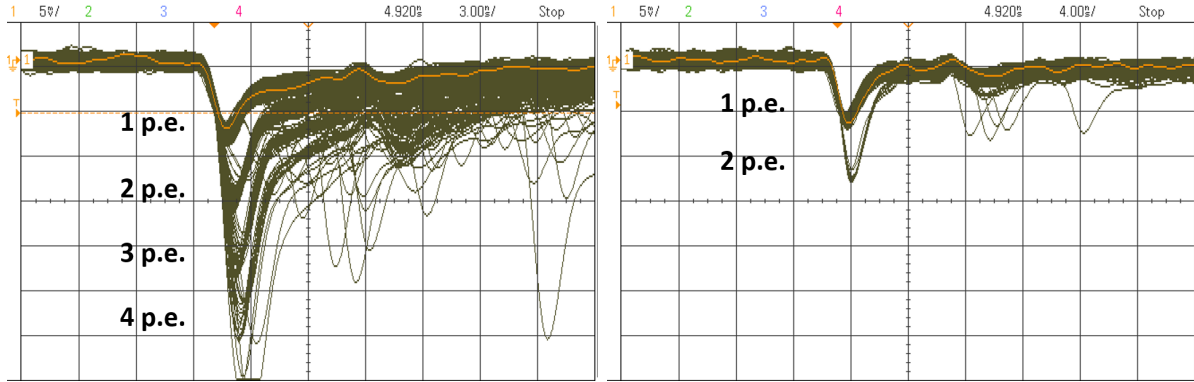
Figure 4.6.: Scope shots showing noise events without light exposure. Left: MPPC S12571-25P (1600 pixels) at 67.0 V (Axis: 3 ns/digit in X, 5 mV/digit in Y). Right: New generation MPPC S13360-1325PE (2668 pixels) at 56.1 V with optical trenches and consequently lower crosstalk probability (Axis: 4 ns/digit in X, 5 mV/digit in Y). The number of photon equivalents (p.e.) are written left to the corresponding signal heights.

Since at this example no light source is utilized, all visible signals have their origin in dark noise. The 1 p.e. peak is allocated to pure dark noise events, while the 2 p.e. peak most probably corresponds to events with one dark noise event triggering one additional pixel via optical crosstalk, which sums up to two simultaneously pixels fired. The chance for two single dark noise events to occur at the very same time and result in the same 2 p.e. signal is very low and neglected. To get an idea, lets assume a dark count rate of $r_{DCR} = 10^5$ Hz, than the probability for a second dark noise event to occur within a time window of for example 0 to 2 ns after the initial dark noise event, where we assume they are still in time, is given by $P = 2\,\text{ns} \cdot r_{DCR} = 0.02\,\%$.

Therefore, all larger signals are associated with multiple optical crosstalk events, for example a 3 p.e. signal might be introduced by a dark noise event causing two crosstalk photons to trigger two additional pixels, or, one dark noise event leading to one crosstalk photon triggering one additional pixel, which then itself invokes a second crosstalk photon to trigger a third pixel. The more simultaneous pixels fired are observed, the more possible paths exist.

By comparing the two different SiPMs in Figure 4.6, MPPC S12571-25P (left) is obviously stronger affected by optical crosstalk compared to the MPPC S13360-1325PE (right). This will be discussed in detail in Section 6.3 and has its origin in the optical trenches added between the pixels of the latter SiPM, dramatically reducing optical crosstalk, as mentioned in Section 4.1. Also visible are a few pulses after the initial triggered pulse, corresponding to correlated after-pulses or uncorrelated dark noise events. Still, the fraction of these pulses is very low.

To actually measure the optical crosstalk probability, a readout chain of a discriminator and a scaler is used instead of the scope. The details of this setup are described in Section 5.1.2. In short, the discriminator sets a variable threshold and each time the SiPM pulse exceeds that threshold, the scaler adds 1 to an internal storage n_{events}. After a fixed time t_{count}, the scaler is read out and the storage is reset to zero. This offers an easy and robust way to measure rates $r = n_{events}/t_{count}$ as a function of the discriminator threshold.

Figure 4.7 exemplarily shows a dark count rate (DCR) spectrum. Typical for this spectrum is the staircase behavior, which represents the pulse heights (absolute value) of the photo-peaks.
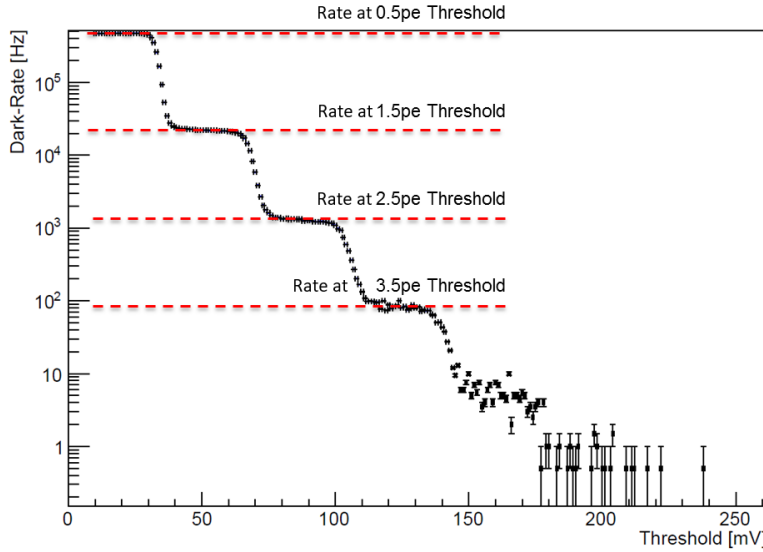
Figure 4.7.: Typical dark count rate (DCR) spectrum showing the rate of dark events measured with a scaler as a function of a threshold set by a discriminator. This plot has already been published in [78] for an older generation MPPC S10362-11-025C at 71.8 V. It is reused here for demonstration purposes, because a larger preamplification (factor 50) of the SiPM signal has been used in that measurement, simplifying the distinction between the observed plateaus.

The upper plateau belongs to thresholds lower than the pulse height of the 1 p.e. peak, that's why it's named 0.5 p.e. threshold level. The second plateau belongs to thresholds between SiPM pulse heights of 1 p.e. and 2 p.e., titled 1.5 p.e. threshold, etc.

Like this, the average rate at 0.5 p.e. threshold is a measure of all dark noise events per unit time, including the initial dark noise event and if so any correlated optical crosstalk events. The average rate at 1.5 p.e. threshold is a measure of all events per unit time with more than one pixel fired, therefore including only optical crosstalk events (assuming no double dark noise events as discussed before). Note, that this includes any multiplicity of optical crosstalk events. Under these conditions, the probability for a minimum of one correlated optical crosstalk event can be estimated by the ratio of the two rates at 0.5 p.e. and 1.5 p.e. threshold as shown in Equation 4.9:

$$P(\geq 1\text{XT event}) \approx \frac{r_{1.5\,\text{p.e.}}}{r_{0.5\,\text{p.e.}}} \tag{4.9}$$

The measurement of optical crosstalk is discussed in Section 6.3.

In some scenarios, not only the probability of optical crosstalk, $P(\geq 1\text{XT event})$, but also the average number of pixels fired due to correlated noise, expressed by the *average factor of correlated noise*, μ_C, is a major parameter. Because of the possible multiplicity of optical crosstalk events, this parameter cannot be directly converted from $P(\geq 1\text{XT event})$. In this thesis, the Borel model of correlated noise is utilized. Detailed information about this model and on the application with SiPMs can be found in Reference [105]. By default, it summarizes all kinds of correlated noise in one combined correlated noise factor: optical crosstalk and after-pulses. Nevertheless, after-pulses are assumed to play a negligible role and therefore dropped here. The reason is, that first of all, the probability for after-pulses is low compared to the

probability of optical crosstalk (at least for three of the four SiPM under test [101], while the latest generation also features a tiny optical crosstalk probability [95]). The second reason has its origin in the way, the SiPM signal will be read out in the following measurements: As already mentioned in Section 4.2.1, a QDC is used to integrate the SiPM signal during an integration window. This time window is rather short (during 50 ns to 100 ns, adjusted to the signal width) and therefore cuts off after-pulses which are too delayed.

As described in Reference [105], the equation of the Borel model to be solved is given by:

$$\xi(e^{-\xi} - 1) = \frac{N_2}{N_1} + \log(\frac{N_1}{N_0})$$

(4.10)

with the expected value μ_C:

$$\mu_C = \frac{1}{1 - \xi}$$

(4.11)

while $\xi[0, 1]$ corresponds to the average number of correlated signals produced at each step of the chain [105, p. 5], N_0 equals the total number of events exceeding the 0.5 p.e. threshold, N_1 equals all events with exactly one pixel fired - especially not triggering an optical crosstalk event; and N_2 equals all events with exactly one optical crosstalk event - two pixels fired in total. The average factor of correlated noise, μ_C, includes the first triggering event and any average number of correlated hits, hence it can only take values larger or equal to 1.

The values N_i can be easily reconstructed from a dark count rate spectrum as shown in Figure 4.7, for example. The rates r are converted to N_0, N_1 and N_2 by applying Equation 4.12,

$$N_0 = r_{0.5} \cdot t_{count} \ , \quad N_1 = (r_{0.5} - r_{1.5}) \cdot t_{count} \ , \quad N_2 = (r_{1.5} - r_{2.5}) \cdot t_{count} \ ,$$

(4.12)

with the time t_{count} during which signals are counted with the scaler. The implementation of μ_C in the analysis of the following SiPM response measurement is explained in Section 4.3.2 and the actual measurement is discussed in Section 6.3.2.

4.3. Saturation Behavior and Measurement Principle

This section discusses the response saturation of SiPMs and gives insights concerning the modeling and measurement of the SiPM response.

4.3.1. SiPM Saturation

Since SiPM pixels are operated in Geiger mode, it is irrelevant, whether one or many photons hit the same pixel at the same time and would each trigger an avalanche; the charge generated by the pixels avalanche always has the same value. The current is regulated by the quenching resistors on a SiPM, which is reflected in a constant and finite gain. The signal of the SiPM is the sum over all pixels fired, compare to Equation 4.5. As long as all incoming photons hit different pixels, the response of the SiPM is linear.

The probability for a number of incoming photons N_γ to hit the same pixel and therefore not to be distinguishable anymore, increases with the number of incoming photons and decreases with the total number of pixels on the device, N_{total}. Here the assumption is made, that incoming
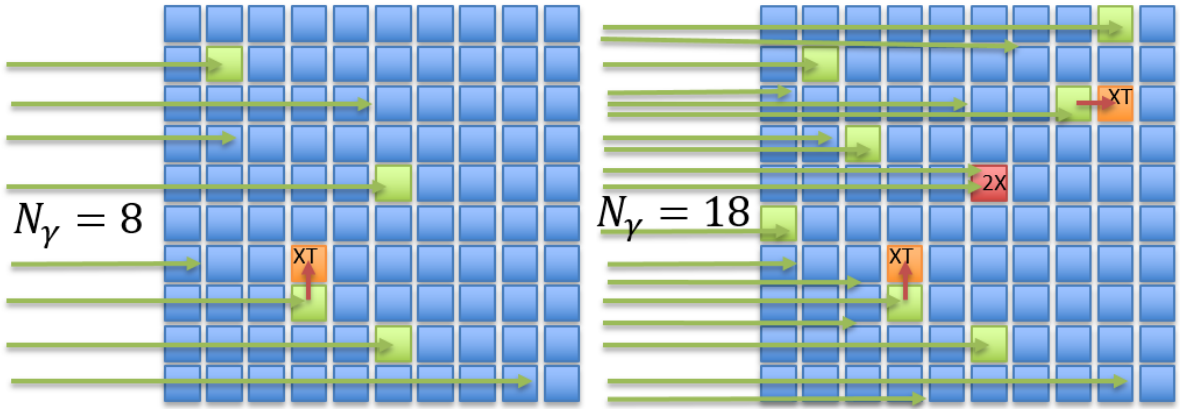
Figure 4.8.: Illustration of SiPM behavior. Green arrows correspond to incoming photons and squares represent SiPM pixels, while blue squares correspond to pixels which are not fired, green squares to pixels fired, orange squares to pixels fired by optical crosstalk and red squares to pixels fired, where two photons triggered an avalanche (double hit). Left: Calibration region: No saturation, with optical crosstalk. Right: Saturation region: with saturation and optical crosstalk.

photons are randomly distributed onto all existing pixels. Such an issue can be described by means of Equation 4.13 [106, 107, 108],

$$N_{fired} = N_{total} \cdot \left(1 - \exp \left(-\frac{\epsilon_{PDE} \cdot N_{\gamma}}{N_{total}} \right) \right) \ , \tag{4.13}$$

where ϵ_{PDE} describes the photon detection efficiency of the SiPM. As shown, the response, N_{fired} saturates according to an exponential dependance proportional to $1 - \exp(-N_{\gamma})$. Thus, for small N_{γ}, the relation between N_{γ} and N_{fired} is close to linear, while with increasing N_{γ}, N_{fired} increases less and converges to N_{total}. A similar model is described in Section 4.3.3.1 where also a plot is shown as an illustration. This SiPM response model does not take into account any effects of correlated noise.

4.3.2. Definition of Number of Seeds

Comparable to [108], the number of seeds N_{seed} is defined as the number of incident photons N_{γ} times the photon detection e ϵ_{PDE} of a SiPM and therefore represents the number of photons, which hit the sensitive area of a SiPM, generate an electron-hole pair and trigger an avalanche (discribed by ϵ_{PDE}) in case of linear behavior (no multi-hits on pixels):

$$N_{seed} = N_{\gamma} \cdot \epsilon_{PDE} \tag{4.14}$$

With this definition, an easier interpretation of the results is possible without the exact knowledge of the PDE of each SiPM.

In contrast to [108], this analysis includes effects from optical crosstalk (correlated noise) as discussed in Section 4.2.2. In the following, the average factor of correlated noise, μ_C, is included.

First of all, consider the example shown in Figure 4.8, which illustrates the SiPM behavior in two different photon exposure regions. In this example, the assumption of $\epsilon_{PDE} = 50\ \%$

and $\mu_C = 1.25$ flows in. In the so called 'calibration region' (Fig. 4.8, left), where N_γ is small compared to N_{total}, it can be assumed that:

- each photon hits a different pixel and therefore saturation effects are negligible and

- the impact of correlated noise is constant.

Both items are not given outside of the calibration region. In the calibration region, the relation between N_{seed} and the number of pixels fired, N_{fired}, is given by:

$$N_{seed} = N_{fired}/\mu_C \qquad (4.15)$$

The measurement of the number of pixels fired, N_{fired}, will be described in Section 6.4.2. In this example, $N_\gamma = 8$ incident photons hit the sensitive area of the SiPM and trigger $N_{seed} = 4$ avalanches (compare to Eq. 4.14). One crosstalk event triggers an additional avalanche in a neighboring pixel, which then leads to (Eq. 4.15) $N_{fired} = 4 \cdot 1.25 = 5$ pixels fired. To represent that N_{fired} is linear in this region, it is also defined as N_{fired}^{linear}.

Outside the calibration region, where saturation affects the response of the SiPM and the impact of correlated noise is not constant anymore because of the the decreasing number of non-fired pixels, a combined description of both effects is needed to describe the behavior of the SiPM. This region is called 'saturation region' and an example is shown in Fig. 4.8, right. Here, $N_\gamma = 18$ photons lead to finally $N_{fired} = 10$ pixels fired, while two of them are correlated noise events and one of the pixels is hit twice by photons (saturation), which would both trigger an avalanche. Therefore, the number of seeds is $N_{seed} = 9$ (7 single pixels hit & 1 double hit). Obviously, the relation between N_{fired} and N_{seed} needs an enhanced function to describe both effects.

The dependencies of N_γ, N_{seed}, N_{fired} are schematically shown in Figure 4.9 as a function of the current of a reference diode I_{ref} for both regions. I_{ref} is proportional to the initial number of photons, N_γ. N_{seed} can be obtained from N_γ via Equation 4.14 by a applying ϵ_{PDE}. In the calibration region (left), the number of pixels fired, $N_{fired} \equiv N_{fired}^{linear}$ is given by Equation 4.15 by taking into account μ_C. I_{ref} can be calibrated to N_{seed} and later extrapolated for larger light intensities. This will be discussed in Section 6.4.3.

Outside the calibration region - and thus inside the saturation region, N_{fired} saturates and the relation to N_{seed} is given by a function f so that $N_{fired} = f(N_{seed})$. This function f has to handle both, saturation and correlated noise.

4.3.3. Modeling SiPM Response

As already discussed, SiPM response is essentially affected by saturation because of a finite total number of pixels on the device. Still, correlated noise and the recovery of pixels and therefore higher order effects influence the response function. Until now, the recovery of pixels has only been considered in the context of after-pulses.

While in the previous discussion, only infinitely short photon pulses have been considered, but in an experimental environment, the incoming photons might be distributed over a certain time window. If a pixel fires and recovers during the integration window of the readout, this pixel
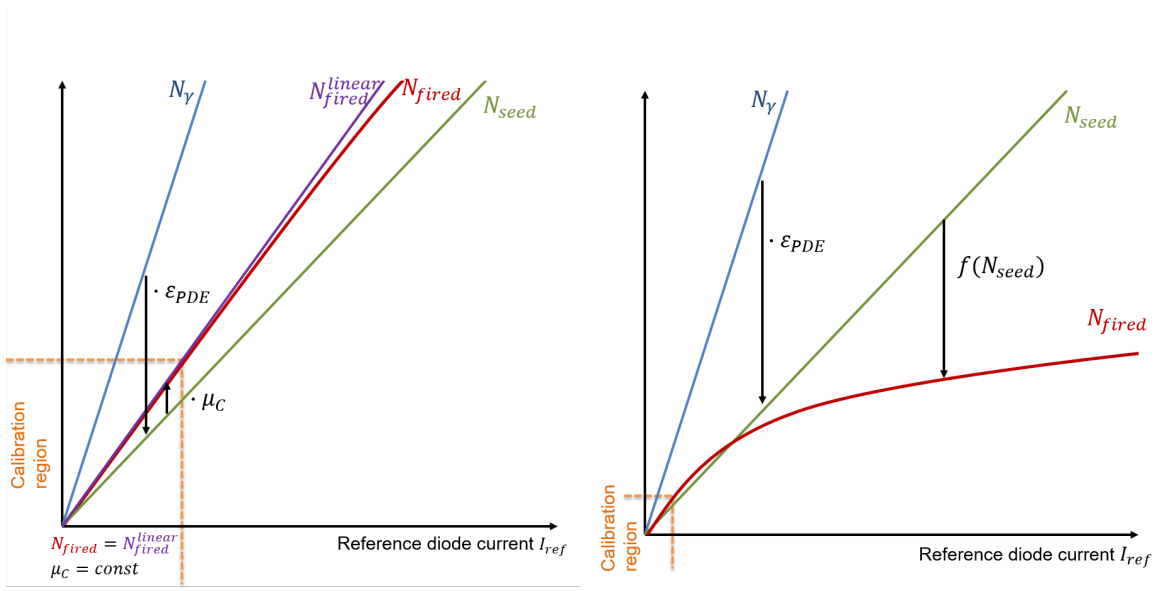
Figure 4.9.: Calibration Method. Schematic dependencies of N_γ, N_{seed}, N_{fired} and I_{ref}. The number of seeds is always defined as $N_{seed} = N_\gamma \cdot \epsilon_{PDE}$. Left: Calibration region, where $N_{fired} \equiv N_{fired}^{linear} = N_{seed} \cdot \mu_C$. In this region, the reference diode current I_{ref} can be calibrated to N_{seed}. Right: Saturation region, where the relation between N_{fired} and N_{seed} can be described by an advanced function $N_{fired} = f(N_{seed})$ which handles saturation and correlated noise. Inspired by [108].

might be hit by a delayed photon of the same pulse or from delayed crosstalk and thus fire twice. This might lead to so called *over-saturation*, where the number of pixels fired exceeds the total number of pixels: $N_{fired} > N_{total}$.

In this section, different response models are introduced, which will later on in Section 6.5 be applied to the measurement results in order to test and verify them.

4.3.3.1. Exponential Model

The easiest response model is only taking into account the saturation of a SiPM. It utilizes the assumption of a simple exponential behavior between the number of pixels fired N_{fired} and the number of total pixels N_{total}, similar as introduced in Section 4.3.1:

$$N_{exp} = N_{total} \cdot \left(1 - \exp \left(-\frac{N_{seed}}{N_{total}} \right) \right) \tag{4.16}$$

This model does not take into account any correlated noise or recovery effects. Figure 4.10 shows two visualizations of the model for two different N_{total}. As discussed in Section 4.3.1, $N_{exp} = N_{fired}$ increases nearly linearly for small N_{seed}, but then saturates and converges to N_{total} for higher N_{seed}.

To still deal with the partial recovery of pixels and consequently a higher measured number of pixels fired, the parameter N_{total} can be interpreted and replaced by an *effective* total number of pixels N_{total}^{eff}, which can be larger than the physical number of pixels.
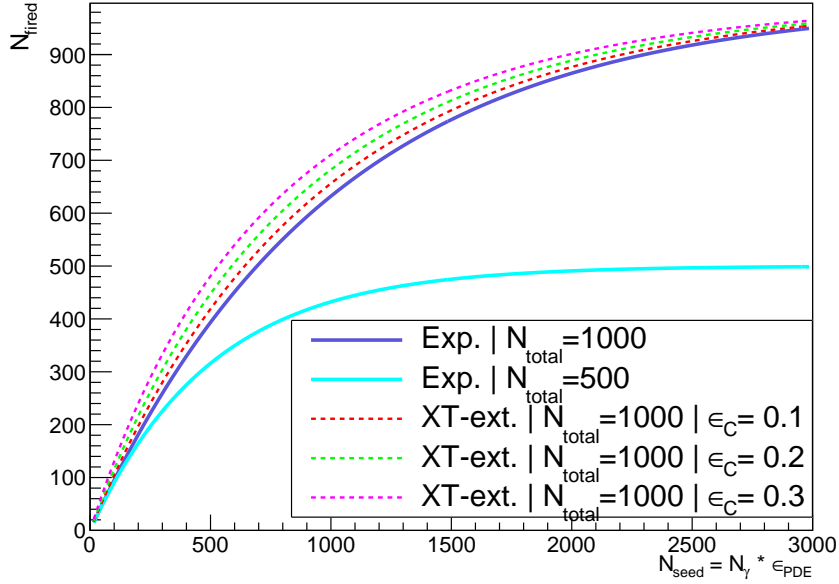
Figure 4.10.: Plots of the simple exponential model for $N_{total} = 500$ and $N_{total} = 1000$ and plots of the crosstalk-extended model for $N_{total} = 1000$ with three different crosstalk values.

4.3.3.2. Crosstalk-Extended Exponential Model

A model taking into account optical crosstalk, is given in Equation 4.17 (adapted from [106]). It extends the simple exponential model with a quotient including a factor representing crosstalk,

$$N_{XT-ext} = N_{total} \cdot \frac{1 - X}{1 - (\epsilon_C \cdot X)} \ , \tag{4.17}$$

with $X = \exp\left(-N_{seed}/N_{total}\right)$ and ϵ_C representing contributions from optical crosstalk. The relation between ϵ_C and μ_C is given by: $\mu_C \approx 1 + \epsilon_C$.

For an easier understanding of the influence of crosstalk in this model, Figure 4.10 shows visualizations for different crosstalk contributions. The simple exponential model (Equation 4.16), which is also plotted, can be used as a comparison. For $\epsilon_C = 0$, this model is equivalent to the simple response model: $N_{XT-ext}(\mu_C = 0) = N_{exp}$. Optical crosstalk in this model leads to a higher number of pixels fired N_{fired}, especially for a low to medium number of incoming photons. The influence of optical crosstalk decreases with a rising number of incoming photons, because of the decreasing amount of non-fired (and therefore free) pixels. Therefore, the difference between N_{XT-ext} and N_{exp} reduces at high N_{seed} and both converge to N_{total}. Also here, in order to take into account the recovery of pixels and thus over-saturation, the *effective* total number of pixels N_{total}^{eff} can be utilized instead of the physical N_{total}.

4.3.3.3. Advanced Model

An advanced SiPM response model has been developed by Dr. K. Kotera et al. on behalf of the CALICE collaboration as discussed in detail in [107]. The aim is to not only take into account

correlated noise as crosstalk, but also the recovery of fired pixels. If a pixel recovers during the charge integration window of the readout, it might happen, that a delayed photon triggers an additional avalanche in the very same pixel.

It has to be mentioned, that the delayed photons, as they are described in the cited paper, are introduced by a scintillator coupled to the SiPM. This is not the case in the direct SiPM response measurement presented in the following, where a SiPM is directly illuminated with a picosecond laser pulse. Still, as presented in the results later, SiPM pixel recovery plays a role also in this direct measurement, because the number of pixels fired exceeds the total number of pixels of some of the tested SiPMs at a certain point. This over-saturation is observed and might be introduced by fast after-pulses and delayed optical crosstalk.

This model includes six free parameters: the total number of pixels, N_{total}, a scale factor ϵ[1] for incoming photons, two parameters representing the recovery of pixels and the charge contribution of the number of photons on a pixel, α and β, respectively, which allow a description of over-saturation, and finally two parameters describing correlated noise: optical crosstalk, ϵ_C, and after-pulses, ϵ_A.

Starting from the simple exponential function as given in Equation 4.16 and renamed in Equation 4.18, the advanced SiPM response model function is constructed in four steps. This section only gives an overview of the response model, for a more detailed description of the individual steps and parameters, please refer to [107].

$$f_{exp} = N_{total} \cdot \left(1 - \exp\left(-\frac{N_{seed}}{N_{total}}\right)\right) \tag{4.18}$$

In the second step in Equation 4.19, simple recovery of pixels is taken into account with the recovery parameter α:

$$f_{recovery} = f_{exp} + \alpha \cdot (N_{seed} - f_{exp}) \tag{4.19}$$

Thereafter in Equation 4.20, the approximate charge contribution of a number of photons on a pixel is taken into account by the parameter β. Here it is considered, that an avalanche discharge in for instance a not fully recovered pixel generates a smaller signal compared to a completely recovered pixel.

$$f_{charge} = f_{recovery} \cdot (\beta + 1)/(\beta + \frac{N_{seed}}{f_{exp}}) \tag{4.20}$$

Equation 4.21 finally gives the advanced response function and includes the parameters for optical crosstalk and after-pulses, ϵ_C and ϵ_A, respectively.

$$N_{adv} = f_{charge} \cdot (1 + \epsilon_C \cdot \exp(-\frac{N_{seed}}{N_{total}})) \cdot (1 + \epsilon_A) \tag{4.21}$$

Figure 4.11 shows two plots including examples of the advanced SiPM response model for different parameters, while the simple exponential model is also shown as comparison.

The number of pixels fired again follows the already familiar exponential behavior with a first close to linear slope, which then saturates. Optical crosstalk has a comparable effect as already

---

[1]The scale factor ϵ is fixed to 1 in this study, because N_{seed} is assumed to be known.

seen in the previous model. In difference to the decreasing influence of optical crosstalk with a rising number of pixels fired, after-pulses affect the response function in a constant way by up scaling N_{fired}, because they only affect the very same pixel where the after-pulse is generated and therefore depend mainly on the SiPM signal integration time window and the recovery parameters of the pixels.

The recovery and charge parameters α and β allow to increase or decrease the measured number of pixels fired as visible in the bottom of Figure 4.11. Higher α and β result in higher $N_f ired$ and thus reduce the impact of saturation by taking into account recovery and charge contributions. There are several parameter combinations, for which the advanced model agrees exactly to the simple exponential model $N_{adv} = N_{exp}$. For example if $\epsilon_C = 0$ and $\epsilon_A = 0$, the here shown combination of $\alpha = 1$ and $\beta = 0$; or for instance $\alpha = 0.5$ and $\beta = 1$, lead to the simple model function. At the moment it is uncertain, whether or not the two parameters α and β might be correlated ([109], p. 27).
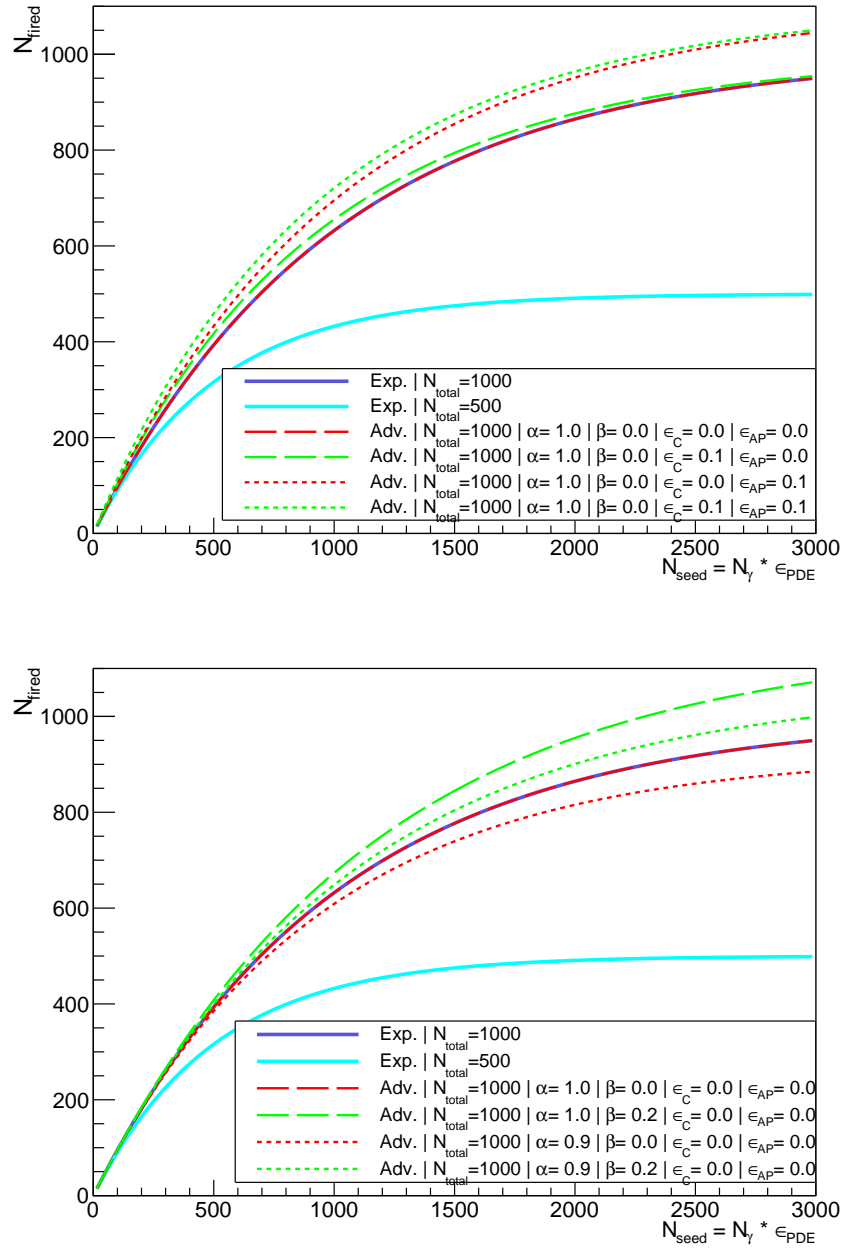
**Figure 4.11.:** Plots of the simple exponential model for $N_{total} = 500$ and $N_{total} = 1000$ and plots of the advanced model for $N_{total} = 1000$, $\epsilon = 1$ and different exemplary α, β, ϵ_C and ϵ_A.

5

SiPM Measurement Setups

This chapter is the second chapter concerning the SiPM response measurement. After the measurement concepts have been explained in the previous chapter, this chapter focuses on the setups used to measure all properties of interest. Section 5.1 includes a setup to measure the sought-after SiPM response and a setup to measure the optical crosstalk probability. Additionally, a setup to measure the linearity of readout devices, such as the direct circuit box and the preamplifier, as well as a setup to scan the uniformity of an optical device, the engineered diffuser, are presented. After this presentation, the major utilized components are discussed in Section 5.2.

The setups presented here extend existing SiPM characterization setups at the PRISMA Detector Lab at Mainz, which have been developed in a previous study [77, 78].

5.1. Setups

This section describes the setups utilized to measure the SiPM response as a function of the incoming light intensity. Also, the impact of optical crosstalk, the linearity of the readout devices and the uniformity of the engineered diffuser have to be studied in order to validate the response measurement. A detailed description of the components is presented thereafter in Section 5.2.

All of the presented setups are automated with software written in C [110] and C++ [111] in order to speed up the data taking and to secure the reproducibility of results. Like this, the setup can easily be used to measure the response of additional SiPMs.

5.1.1. SiPM Response Setup

The setup presented here allows to measure the SiPM response in dependence of the incoming light intensity. Therefore, a picosecond laser diode is utilized, which provides a tunable number of photons that are directed onto a SiPM and onto a reference diode. By comparing the number of pixels fired of the SiPM to the current of the reference diode, the SiPM response can be measured. In addition and as part of this setup, it is also used to measure SiPM characteristics as the gain and the breakdown voltage and to perform calibration measurements. Figure 5.1 shows the scheme of the setup.

  All optic components, the SiPM and the reference diode, are placed inside a dark box. The picosecond laser output is directly coupled to an optical fiber connected to a inline beam splitter with two outputs.
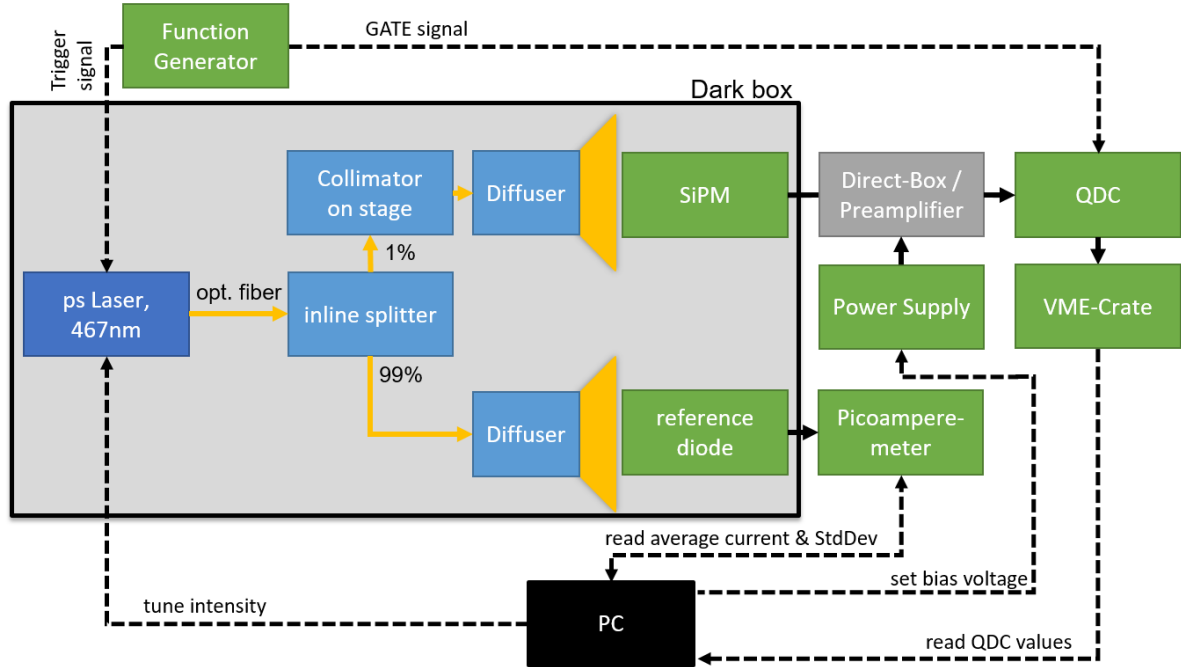
Figure 5.1.: Scheme of the SiPM response saturation measurement setup. (This figure has been created in the course of this thesis and also appears adjusted in [112], where some of the results of this SiPM response measurement have been published in the meantime.)

About one percent of the light intensity is directed through a output fiber, which is connected to a collimator on a movable XYZ-stage. An engineered diffuser then diffuses the just collimated laser beam and in addition converts its Gaussian profile into a top-hat profile with near-uniform energy density. The SiPM itself is soldered on a small PCB and is fixed to a mechanical mount. The distance between to diffuser and the SiPM is adjusted in a way, that at least the complete SiPM surface is illuminated. The previously mentioned stage can be controlled by a PC (connection not drawn) and is used to center the beam spot behind the diffuser onto the SiPM.

The remaining approximately 99 percent of the light intensity are directed onto another diffuser and onto the reference diode, which is connected to a picoamperemeter in order to measure the photo-current.

The SiPM is connected to either a so called *direct circuit box* or to a *preamplifier* via a short SMA cable. By default, the direct circuit box is used, which does not amplify the signal, and the preamplifier is only needed in case the SiPM gain is too low to distinguish between different numbers of pixels fired without any further signal amplification (see e.g. Section 6.1.4 or Section 6.2.2). The power supply to bias the SiPM is connected accordingly to one of the devices and the voltage is forwarded to the SiPM.

Independent of which device is used, the remaining signal is then processed with a QDC inside a VME crate. The gate signal for the QDC integration of the SiPM signal is provided by a function generator which simultaneously triggers the picosecond laser pulse. The frequency is set to 20 kHz in order to allow fast measurements and to still be slow enough to ensure a full recovery of the SiPM, before the next pulse occurs.
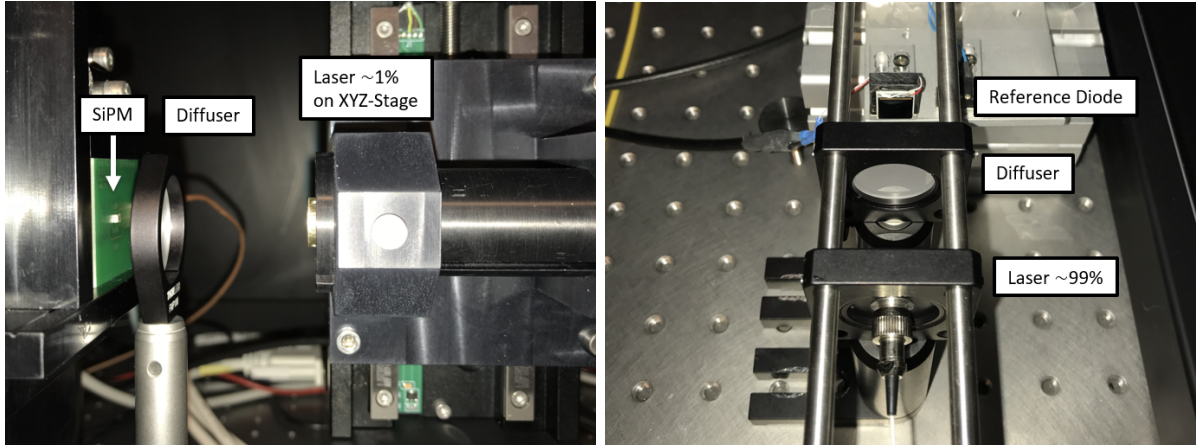
Figure 5.2.: Left: Picture showing a part of the setup inside a dark box. The laser collimator is fixed on a computer controlled movable stage. About 1% of the total laser intensity is directed onto the surface of the engineered diffuser from where the light is uniformly diffused onto the SiPM surface. Right: Picture showing the part of the setup, in which another diffuser is used and the reference diode is illuminated with about 99% of the total laser intensity.

The PC fulfills different tasks besides the already mentioned control of the movable stage. First, it reads out the QDC via the VME interface and the picoamperemeter via an USB connection. Second, it operates the power supply via serial (RS232) connection, which biases the SiPM through the direct circuit box or preamplifier. Third, it defines the tune value and therefore the intensity of the picosecond laser. Like this, the complete SiPM response measurement is automated and controlled by a single program which has been written in C for that purpose. The user can define many environment variables, as for example the range and the scan steps of the laser tune, the bias voltages applied to the SiPM and the measurement statistics. The latter defines the number of readout circles of the QDC readout and the number of stored currents of the picoamperemeter per measured tune value. In particular these both influence the total duration of the measurement.

Figure 5.2 shows two pictures of the setup inside the dark box. The left picture from right to left shows the laser collimator on the movable stage, the engineered diffuser in the path of the beam and the SiPM, which is soldered on a small PCB and fixed to a mount. The right picture shows the parallel measurement of the reference diode. In this case, the laser beam is not collimated but simply diffused with the ground glass diffuser onto the larger surface of the reference diode. A stable cage system, consisting of mounts and two metallic rails, helps to align the beam to the center of the reference diode.

5.1.2. SiPM Optical Crosstalk Setup

Even if the SiPM is not illuminated, dark events can occur due to thermal excitation and quantum tunneling in the depletion region of the pixel. In addition, correlated noise, especially optical crosstalk, can increase the number of pixels fired (see Section 4.1). The measurement of dark noise and optical crosstalk are important features of this analysis.

This Section describes the setup for the measurement of dark noise and optical crosstalk of a SiPM, which is similar to the setup utilized in [77]. The method has been introduced in
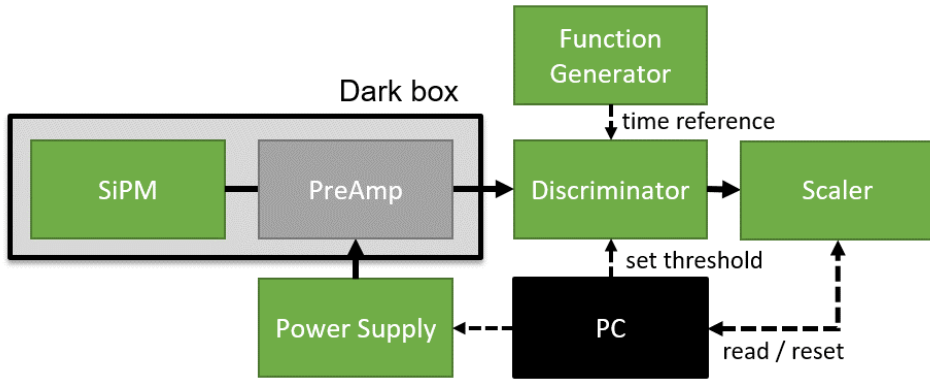
Figure 5.3.: Scheme of the setup used to measure the dark count rate and optical crosstalk of a SiPM. The preamplified SiPM signals and a well known pulse from the function generator are connected to two channels of a VME discriminator, which features a tunable threshold. Pulses that pass the threshold are counted by means of the VME scaler. The two VME modules are controlled by a PC.

Section 4.2.2. As shown in Figure 5.3, the dark count rate (DCR) is measured by a combination of a discriminator and a scaler module. Inside a dark box, the SiPM itself is connected to the preamplifier in order to facilitate an easier distinction between the different pulse heights corresponding to different numbers of pixels fired, as also introduced in Section 4.2.2. Similar to the previous setup, the SiPM bias voltage is supplied by a power supply connected to the preamplifier, which forwards it to the SiPM.

The discriminator is programmed via VME bus in a way that it generates a positive output signal each time, the input SiPM signal exceeds a prior threshold. In this way generated output signals are counted by the scaler. After the scaler is read out, the measurement is reset by the PC.

The function generator is used to provide a time reference of the measurement. A well known pulse at a frequency of 10 kHz is fed into a second port of the discriminator and accordingly counted by the scaler on a second channel. Like this, the real time that has passed during a measurement can be easily estimated and the rate of the SiPM dark noise can accordingly be obtained, since the dark count rate is defined as the number of events per unit time.

The measurement is automatized with software written in C in a way that the threshold of the discriminator is automatically adjusted in a range between $-2\,\text{mV}$ and $-250\,\text{mV}$ in 1 mV steps. For each threshold step, the scaler is reset and read out after a variable period of time, usually defined as 10 seconds. Whenever the number of counted SiPM signals over threshold drops below 10 counts after one scaler readout, the measurement is stopped. Also, the software loops over a predefined range of SiPM bias voltages.

With this setup, the dark count rate can be measured as a function of the discriminator threshold, which facilitates the determination of optical crosstalk as discussed in Section 4.2.2. The actual measurement is presented in Section 6.3.
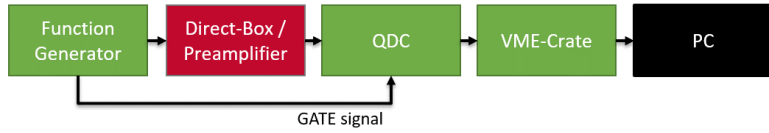
Figure 5.4.: Scheme of the setup for the calibration measurement of the direct circuit box and the preamplifier.

5.1.3. Preamplifier & Direct Circuit Box Linearity Setup

Especially when very low and up to high light exposures on a SiPM are measured during the response measurements, the linearity of the preamplifier and the direct circuit box have to be estimated to validate the measurement and to define systematic uncertainties.

Figure 5.4 shows the scheme of the setup used to measure the linearity of the two devices. The function generator injects a user controlled pulse into the direct circuit box or preamplifier, which is then read out with the simultaneously gated QDC. Like this, it is a combined measurement of the direct circuit box/preamplifier and QDC, which is permissible since these devices are always used in this combined chain. The QDC value is read out with a PC via a VME interface.

Because this measurement is only done once for the two devices, this measurement is only semi-automated. The user defines an input pulse height of the function generator in the range between 1 mV and 800 mV with a smallest possible pulse duration of 16 ns. The readout of the QDC is then automated for a number of predefined cycles. For each input pulse height, the measurement has to be repeated.

The measurements of the linearity of the direct circut box and the preamplifier are presented in Sections 6.2.1 and 6.2.2. The direct circuit box is expected to behave linear over a wide range, while the preamplifier is supposed to only be used up to output signal heights of 1 V after amplification. A non-linearity, for example a saturation of the preamplifier is therefore expected at some point.

5.1.4. Diffuser Scan Setup

The engineered diffuser is an optical device which fulfills two tasks: it diffuses the laser beam and transforms the energy profile from a Gaussian to a top-hat profile with near-uniform energy density. Like that it should be ensured that each pixel on the SiPM has the same probability to be hit by incoming photons.

This section describes the measurement setup to estimate the uniformity of the engineered diffuser in order to define systematic uncertainties arising from non-uniformities.

Figure 5.5 shows the scheme of the setup. In many points it is similar to the SiPM response measurement setup discussed in Section 5.1.1. Not needed parts are dropped. Since this setup focuses on the scan of the engineered diffuser, the optical setup is shown in more detail.

The laser beam leaves the collimator on the PC-controlled stage with a Gaussian energy profile and hits the engineered diffuser. The beam diameter has a size of about 2 mm when it hits the diffuser surface. Behind the diffuser, the beam diverges and, as said before, the energy density should be close to uniformity. After a short distance, the beam hits the SiPM which is fixed to a mount. By moving the collimator in the parallel plain of the SiPM and the engineered
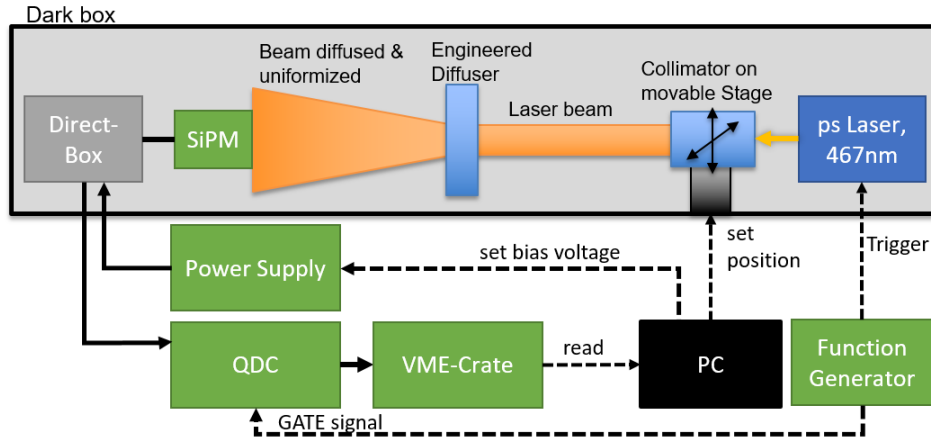
Figure 5.5.: Scheme of the optical setup used to scan the uniformity of the engineered diffuser.

diffuser surfaces, the energy profile behind the diffuser can be measured as a function of the spatial coordinates X and Y.

Software has been written in order to automatically move the collimator on stage from starting positions X_{min} and Y_{min} to end positions X_{max} and Y_{max} in steps of $200\,\mu\text{m}$. For each position, the SiPM is read out with the QDC automatically. For the steering of the stage, a software [113] developed within the PRISMA detector lab has been customized and combined with the readout software. The laser is tuned to a fixed medium intensity.

The triggering of the laser and the gating of the QDC as well as the readout of the latter are done in the same way as described in Section 5.1.1.

The measurement results are discussed in Section 6.2.3.

5.2. Components

Many components are utilized in the setups used to measure the SiPM response. This section lists the major components and describes their features. It starts with optical devices followed by readout electronics.

5.2.1. PiLas Picosecond Laser

As a light source, the picosecond diode laser (PiLas [114], also called ps laser) by A.L.S. GmbH is utilized, which features a pulse duration of around 60 ps (FWHM) and a wavelength of $\lambda = 467\,\text{nm}$, which is close to the peak sensitivity of the measured SiPMs of 450 nm [95, 101]. The average radiant power at a maximum repetition rate of 1 MHz is $50\,\mu\text{W}$, while the peak radiant power reaches a maximum of 400 mW.

The laser diode is controlled and biased by an external control unit which includes RS232 and USB interfaces to facilitate remote control by a PC. The main tasks of the control unit are the triggering and the tuning of the laser diode. An internal trigger can be used, but since the laser pulses have to be simultaneous to the signal readout of the QDC, an external trigger is induced. The amplitude of a laser pulse can be adjusted by changing the pumping current applied to the

laser diode. This can be controlled by so called *tune value* which can take values from 0 to 1000. While a value of 0 corresponds to the full amplitude, higher tune values result in a decreased amplitude of a laser pulse and also in a little increased pulse duration. The latter remains well below 1 ns in any case.

An optical fiber is directly coupled to a collimator of the laser diode head.

5.2.2. Beam Splitter

In order to measure the intensity of the laser by a reference diode parallel to the SiPM, a beam splitter is utilized. The 2x2 Fiber Optic Coupler from Thorlabs [115] features two input and two output fibers, while only one input (ps Laser) and two output fibers are connected. The coupler is optimized for a wavelength of 488 ± 15 nm and therefore does not perfectly match the wavelength of the laser diode. That's why the splitting ratio, which is defined by $99 : 1$, might differ a bit and the insertion losses might increase. Since the splitting ratio and the insertion losses are assumed to be constant factors and no absolute values are needed, it is still sufficient for the applications in this setup.

5.2.3. Diffuser

Two different diffusers are used in the setups while different criteria are met. They are optical devices which are placed in front of the SiPM and the reference diode.

The engineered diffuser (ED1-S20-MD) by Thorlabs [116] is used in combination with a SiPM, where a uniform illumination is important. It diffuses an incoming collimated laser beam by around 20° and is engineered to transform input illumination with a Gaussian intensity profile (as the laser diode provides) into an output square pattern of homogeneous intensity.

The other diffuser (DG10-220) [117] is a simple ground glass diffuser with less complexity, which makes it much cheaper. This diffuser is used to widen the laser beam before it hits the reference diode (see Section 5.2.9). In contrast to the SiPM, uniform illumination is not crucial for the reference diode.

5.2.4. Movable Stage

The movable stage fulfills two tasks: it allows to scan the engineered diffuser in order to verify its uniformity and centers the laser collimator to the SiPM in the response measurement.

The stage consists of three single stages (M-403.2DG) [118] combined into a three axis system. All axes have a travel range of 50 mm and a minimum incremental motion of 0.2 μm and are driven by DC gear motors. The resolution is given as 0.018 μm.

The stage is controlled by a four axis motion controller (C-884) [119] with an USB interface to enable remote control via a PC.

5.2.5. Preamplifier & Direct Circuit Box

For the amplification of SiPM signals, a fast wideband amplifier (A1423B) [120] is used. It features a bandwidth of about 1.5 GHz and a modifiable gain in the range between +18 dB to +54 dB. The output signal is inverted and restricted to about ± 1 V, which limits its usability for
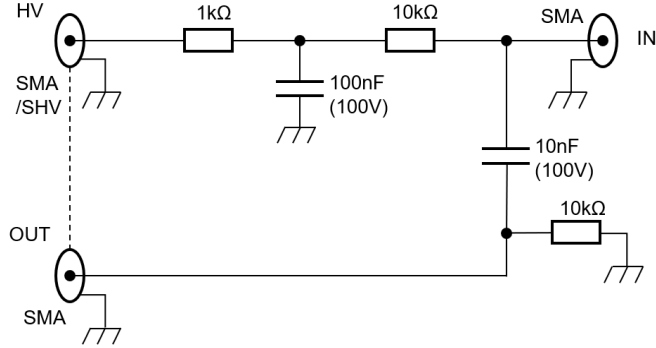
Figure 5.6.: Diagram of the direct circuit box. Adapted from [121].

high SiPM signals. Throughout the whole SiPM response measurement, the lowest amplification is used whenever the preamplifier is utilized in order to maximize the accessible range. The preamplifier includes a port for the bias voltage, which is forwarded to the SiPM. The linearity of the preamplifier is tested and discussed in Section 6.2.2.

Whenever no amplification of the SiPM signal is needed and in order to bypass the issue of a maximum output of the preamplifier, a for this purpose built *direct circuit box* [1] is used to bias the SiPM and to forward the signal. This circuit is placed inside a small metallic box in order to help shielding it from interference frequency. To allow an easy and fast exchange between the preamplifier and the direct circuit box, the connectors are similar to each other. For example, both devices include SMA connectors for the SiPM bias voltage, for the SiPM signal input and for the output. A scheme of the circuit is shown in Figure 5.6. The linearity of the two devices is measured in Section 6.2.1 over a wide range of input signals.

5.2.6. Data Readout: VME Crate

To process SiPM signals, different readout modules are chosen for the the different setups as discussed before. The following two described readout chains are both compatible with the VME-bus, (Versa Module Eurocard-Bus). That allows a similar implementation into the automation software and a fast data transmission. The connection between the VME crate and the PC is established by a PCI-Express board (Struck SIS1100e [122]) on the PC side and by a VME interface (Struck SIS3104 [122]) on the VME side, both connected with an optical cable. Two different readout chains are utilized in the setups. The first one consists of a single QDC module, the second of a combination of a discriminator and a scaler module. Both are described in the following.

5.2.7. VME QDC

The Charge-to-Digital-Converter (QDC) integrates currents in a certain time window, which is defined as the *integration window* or *gate*, t_{int}, and which is provided by an external function generator. The integration window is chosen to be synchronous to incoming light pulses and to include about one SiPM pulse, which is beforehand checked by means of a scope. An intrinsic

---

[1]The circuit was developed and built with the friendly assistance of M. Reinecke (DESY Hamburg), A. Brogna and Q. Weitzel (PRISMA Detectorlab Mainz) and R. Degele (JGU Mainz).

delay of 15 ns of the integration signal inside the QDC has to be taken into account. Like this, the charge q, contained in the signal during the integration window, is measured.

In this thesis, the CAEN V965A [123], a 8 channel dual range multievent QDC is utilized. The input signal is first converted to a voltage level and then converted to a digital number using two different 12-bit ADCs with two different preceding gain stages. The ratio between the different ADC gain stages is about 1:8.

Like this, it features a dual range to cover small pulses with high resolution and also allows to obtain large input signals in a high-range mode with less resolution.

In low-range (LR), it covers an input charge between 0 pC and 100 pC (conversion factor $\kappa_{qdc} \approx$ 25fC/QDC count) and in high-range (HR) between 0 pC and 900 pC ($\kappa_{qdc} \approx$ 200fC/QDC count). Both values are read out by the data acquisition software. In the overlap region between 0 pC and 100 pC, a HR to LR conversion factor can be estimated to take advantage of both ranges. This conversion is discussed in Section 6.1.3.

In case of no input signal, the QDC still outputs a non-zero QDC value called *pedestal*. A detailed description can be found in [123]. Basically, the origin of this effect is mainly due to the integration of an additional VME-programmable current, which is overlaid with the input. Therefore, the pedestal depends linearly on the integration time.

Consider an illuminated SiPM read out by a QDC: By adding several QDC-charge values into a histogram, a charge spectrum, as already exemplarily shown in Figure 4.5, can be measured. From this spectrum, for example the QDC pedestal, q_{ped}, the SiPM gain, G, and the number of pixels fired, N_{fired}, can be estimated as discussed below in Chapter 6.

5.2.8. VME Discriminator & VME Scaler

The second readout chain consists of a VME discriminator module (CAEN V895, 16 Channel Leading Edge Discriminator) [124] and a VME scaler (Struck SIS3808, Deadtimed VME Multiscaler) [125] module, which are used for the measurement of dark noise and optical crosstalk. The SiPM is connected to the discriminator. Signals that pass a certain VME-programmable threshold lead to a positive output signal of the discriminator. The number of positive output signals are counted by the scaler module. Like this, and with a reference to the time which has passed during the measurement, a dark count rate spectrum can be measured, as already discussed in Section 4.2.2.

5.2.9. Reference Diode & Picoamperemeter

A calibrated silicon photodiode (FDS1010-CAL by Thorlabs) [126] is utilized to reference the light intensity of the laser pulses, that's why its called *reference diode*. This device has an active surface of 10×10 mm^2 which makes the alignment of the reference laser beam much easier compared to the smaller SiPMs. With its small deviation of maximum 1 % from linearity [127], it is well suited for a reference measurement.

The reference diode is directly connected to a picoamperemeter (Model 6485 by Keithley) [128] which measures the photo current. Typically and depending on the laser intensity, the measured photo currents in the following SiPM response measurements are of the order of tens of

pico- to nano-ampere. With an accuracy of 0.4 % + 0.4 pA, it delivers accurate results. For each measurement, 100 readings are performed in order to reduce statistic fluctuations and the arithmetic mean and the standard deviation are obtained and passed to the PC via a serial RS232 interface.

5.2.10. Power Supply

The power supply (EA-PSI 6150) [129] is used to provide the bias voltage for the SiPM. With an output voltage of 0 V to 150 V, it can bias all tested SiPMs. It also comprises a serial interface that allows a remote configuration via a PC, which makes it capable for an automated measurement.

5.2.11. Function Generator

The function generator (33500B by former Agilent, now Keysight Technologies) [130] has one programmable output and one synchronous (sync) output.

It fulfills different tasks: Whenever the laser is utilized, the function generator triggers the laser controller through its sync output in order to initiate a laser pulse. Simultaneously, the programmable output is used to form a gate signal for the QDC. The width of the gate signal defines the integration window of the QDC and it is crucial, that the integration window is aligned to the laser pulse in order to integrate the corresponding SiPM pulse. This can be done by checking both, the SiPM signal and the gate signal with a scope.

The function generator also supplies well defined pulses for linearity measurements of readout devices as discussed in Section 5.1.3. In another application, the function generator is used to define a time reference for the VME scaler module, as described in Section 5.1.2.

6

SiPM Response Analysis

This chapter describes the response measurement of state-of-the-art SiPMs by utilizing the setups presented in Chapter 5. To receive meaningful results, several steps are necessary. First of all, a calibration of all used equipment is required. Section 6.1 explains the calibration procedure in detail. This includes measurements of the QDC pedestal, the QDC high- to low-range conversion, the calibration of the readout circuits like the direct circuit box and the preamplifier and detailed measurements of SiPM properties as the gain and optical crosstalk.

The following Section 6.2 focuses on the linearity and uniformity of the used devices and optics. A detailed measurement of SiPM optical crosstalk is presented in Section 6.3. Optical crosstalk adds a major part to correlated noise and crucially affects the response of a SiPM. With a good knowledge of the crosstalk effect, the SiPM response can be accordingly corrected.

With all the preparations done, the actual measurement and analysis of the SiPM response is discussed in Section 6.4. It describes in detail, how the SiPM signal is converted to the value of interest, the number of pixels fired, N_{fired}, and how the reference measurement of the laser intensity is converted to the number of seeds, N_{seed} (proportional to the number of incoming photons), applying the method already introduced in Section 4.3.2.

Last but not least, the results for all four SiPMs are discussed in Section 6.5 and are compared to different SiPM response models.

The software for this analysis has been developed in ROOT[1]. Unless otherwise stated, all measurements are done at room temperature at $(22 \pm 0.3)°$C.

The SiPM response measurements are performed with respect to the application at the CAL-ICE testbeam campaigns in 2015 and 2016 (see Chapter 8). Previous Table 4.1 includes basic information about the measured SiPMs. Two (S13360 -1325PE, S12571 -25P) of the four measured SiPMs were used during these test beam campaigns. Therefore, the bias voltages applied to these two SiPMs in the following response measurements are defined by the bias voltages applied during testbeam. For the other two SiPMs (S12571 -50P, S12571 -100P), the bias voltage suggested by the manufacturer is applied. In any case, these bias voltages are allocated as the *bias voltages of interest*, $U_{bias}^{interest}$.

6.1. Calibration

To study the response of a SiPM, an accurate calibration of the used electronic components and of the basic SiPM properties, as its gain, is essential. This section describes this calibration.

---

[1]ROOT is a software toolkit for scientific applications as data analysis. It is mainly based on C++ and developed at CERN. [131]
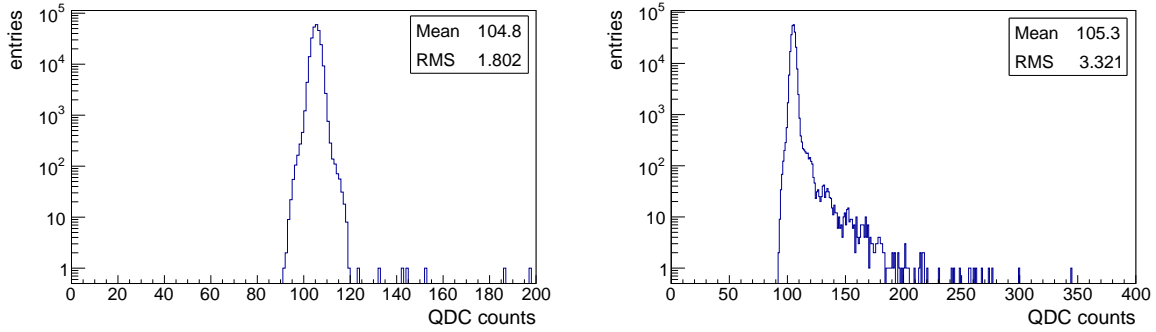
Figure 6.1.: Raw QDC spectrum without (left) and with (right) applied bias voltage to the SiPM without laser beam. Shown for MPPC S12571-100P, no pedestal or dark noise subtracted here.

6.1.1. Mean of the QDC Spectrum

In the following analysis, SiPM signals are recorded with a QDC, which integrates the signal over a certain time window. Each readout results in a corresponding QDC charge q_{QDC}^{raw} (raw indicates the direct observable without any pedestal correction, refer to Section 6.1.2). To increase the statistics of a measurement point, many read out cycles are repeated at the same conditions, resulting in a single photon spectrum (SPS) as previously shown in Figure 4.5. To estimate the mean charge, the arithmetic mean is calculated using Equation 6.1.

$$\overline{q_{QDC}^{raw}} = \frac{1}{n} \sum_{i=1}^{n} q_{QDC,i}^{raw} \tag{6.1}$$

for n measurements.

6.1.2. QDC Pedestal & SiPM Dark Noise

As mentioned in Chapter 5.2.7, the SiPM signal is processed via a QDC. For a time window t_{int}, the QDC integrates the input signal. Given the case, that non of the pixels on the SiPM fires during this integration time, the QDC still outputs a non-zero QDC value, which is called *pedestal*, as described in Section 5.2.7. As a reminder, the pedestal depends linearly on the integration time window.

Since the QDC value of the pedestal corresponds to an input of zero charge, it is a good idea to subtract the pedestal value from all following QDC measurements.

To measure the pedestal, the same setup as shown in Figure 5.1 is used, whereas the laser and the reference diode are not active during this measurement. Also, to exclude any real events of the measured SiPM, no bias voltage is applied to the SiPM. Figure 6.1, left, exemplary shows a QDC spectrum for MPPC S12571-100P under these circumstances. The sharp peak corresponds to the pedestal. Usually, the mean value of this plot would be used to define the mean position of the pedestal.

In this thesis, and in order to negate effects from SiPM dark noise events (cf. Section 4.1), the bias voltage is set to the actual voltage that will be applied during the following measurements.

Since the integration window is very short (50 ns to 100 ns, adjusted to the SiPM pulse width), dark noise events only happen rarely during this integration window.[2]

Figure 6.1, right, shows an example plot for such a measurement. By applying bias voltage to the SiPM, the mean value of the spectrum slightly increases because of dark noise events happening rarely inside the integration window of the QDC. Since later on measurements will be performed in both ranges of the QDC (high- and low-range), pedestal and dark noise measurements are done for both ranges. The mean value of each spectrum is defined as the pedestal and dark noise value $\overline{q_{ped\&DCR}}$.

In the following analysis, QDC mean values, as introduced in Equation 6.1, are pedestal and dark noise subtracted:

$$\overline{q_{QDC}} = \overline{q_{QDC}^{raw}} - \overline{q_{ped\&DCR}} \tag{6.2}$$

Here it has to be mentioned, that the assumption is made, that dark noise effects are constant over the full measurement range. In reality, the effect decreases with increasing number of pixels fired on the SiPM, since a dark noise event can only trigger a new avalanche in a non-fired pixel or - including secondary order effects - in a partially recovered pixel, while this is the dominating effect for a large numbers of pixels fired and therefore a reason to still keep this correction. Since the total effect is very low in any case as discussed before, this adds only a negligible systematic uncertainty.

6.1.3. QDC High-range to Low-range Intercalibration

The SiPM signal is read out with a dual-range 12-bit QDC. The dual-range helps to cover a wide range of input signals, which is especially useful for a SiPM response measurement, where a range from a few to thousands of pixels fired should be covered.

To convert signals from high-range (HR) to low-range (LR), an intercalibration is necessary. This intercalibration can be performed in the overlap region where input signals are in the range between 0 pC and 100 pC.

The setup of this measurement is equivalent to the setup used for the saturation measurement shown in Figure 5.1. The laser is tuned in a way, that only a few pixels fire on the SiPM.

To estimate the QDC intercalibration, many measurements for different laser tune values are performed and for each event, the HR- and LR-QDC values are fed into a scatter plot as shown in Figure 6.2, left, for MPPC S12571-25P. The linear intercalibration function is given by:

$$q_{QDC}^{LR}(q_{QDC}^{HR}) = p0 + p1 \cdot q_{QDC}^{HR} \tag{6.3}$$

, with q_{QDC}^{LR} and q_{QDC}^{HR} being the QDC values in LR- or HR-mode, respectively, $p0$ the constant and $p1$ the slope of the function. To fit this function to the data, the scatter plot is beforehand converted to a profile. An exemplary result is shown in Figure 6.2, right.

In the following analysis, all HR-QDC values are converted to the scale of LR-QDC values using Equation 6.3.

---

[2]Given a dark count rate of $r_{DCR} = 10^5$ Hz and an integration window of $t_{int} = 50$ ns, than the probability for a dark event to happen during the integration window is given by $P = t_{int} \cdot r_{DCR} = 50$ ns $\cdot 10^5$ Hz $= 5\%_0$. This does not take into account, that the dark event will only be integrated partially if it does not appear at the beginning of the integration window. The probability for a completely integrated dark event is even smaller.
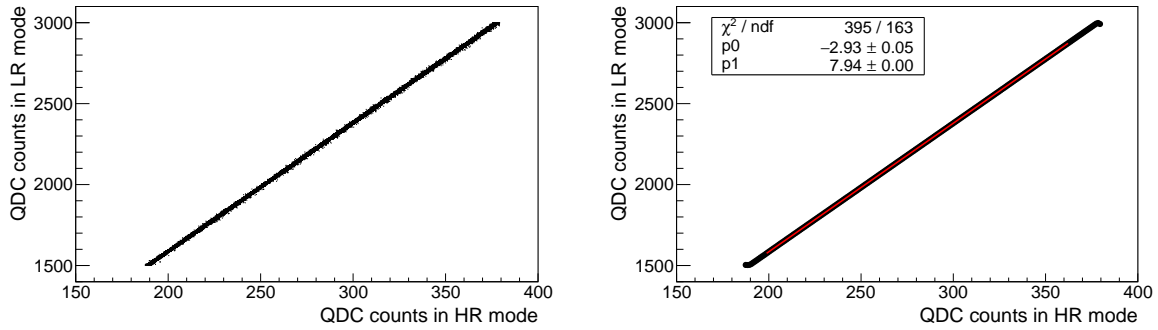
Figure 6.2.: Typical low-range QDC values vs. high-range QDC values. Left: Scatter plot. Right: Profile and linear fit used for conversion from HR to LR. The fit parameters are obtained as $p0 = -2.93 \pm 0.05$ and $p1 = 7.94 \pm 0.00$. Shown for S13360-1325PE at $U_{bias} = 56.1$ V.

6.1.4. SiPM Gain Analysis

The gain is one of the most important characteristics of a SiPM and strongly dependent on the supplied bias voltage. The concept of the gain measurement has been described in Section 4.2.1. The knowledge of the gain is necessary to convert the SiPM charge signal, q_{QDC}, into units of pixels fired, N_{fired} (see Section 6.4.2). To measure the gain $\mathfrak{S}$, which is given in units of QDC counts, the pulsed laser is used to illuminate the SiPM with a low amount of photons synchronously to the readout of the QDC. This measurement is done before the actual response measurement, but within the same conditions concerning temperature, integration time etc. The relation between the common gain G and $\mathfrak{S}$, expressed in units of QDC counts, is given by Equation 6.4

$$G = \mathfrak{S} \frac{\kappa_{qdc}}{q_e \cdot G_{PreAmp}} \ , \tag{6.4}$$

with the elementary charge q_e, the gain of an optional preamplifier G_{PreAmp} ($G_{PreAmp} = 1$ if no preamplifier is used) and the previously defined conversion factor of the QDC, $\kappa_{qdc} \approx 25$fC/QDC count (in LR mode).

Figure 6.3, left, shows a typical single photon spectrum (SPS) of a SiPM under laser illumination for one bias voltage. Each peak corresponds to the number of pixels fired, starting from the first peak that belongs to events with no pixel fired, called pedestal (see Section 6.1.2), to the second peak associated to events with one pixel fired (1 photon equivalent, p.e.), etc. The distance between two consecutive peaks defines the gain of the SiPM. Therefore, Gaussian fits are applied to the peaks and the distance between their mean values are used to determine the gain. Red triangles indicate peaks which have been found by a peak finder algorithm supplied by ROOT.

To automatically process the data, software has been written to find the position of a local maximum q_i^{max} of up to five peaks in each spectrum and fit each of them with an Gaussian function. Parts of this software has been reused from the previous study in [77]. The fits are applied around the peaks in a range of $\pm 1/3$ of the mean distance between found peaks.
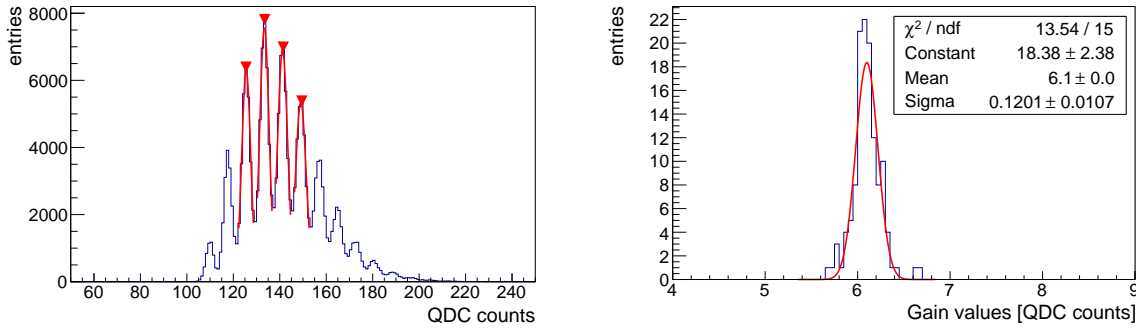
Figure 6.3.: The left plot shows a typical single photon spectrum (SPS) of MPPC S13360-1325PE at U_{bias} = 63.3 V. This spectrum has been recorded with a QDC, while the SiPM has been illuminated with a pulsed laser. Gaussian fits are applied to the peaks and their mean values are used to determine the gain. The right plot shows a histogram of 124 average gain values $\overline{\mathfrak{S}(U_{bias})}$ in units of QDC counts of MPPC S12571 -50P at $U_{bias}^{interest}$ = 66.5 V. A Gaussian fit is applied to estimate the final gain value.

Up to $i_{total} \leq 4$ gain values $\mathfrak{S}_i$ [QDC counts] are measured by subtracting the mean values $q^{GaussMean}$ of two subsequent Gaussian fits,

$$\mathfrak{S}_i(U_{bias}) = q_{i+1}^{GaussMean} - q_i^{GaussMean} \ , \tag{6.5}$$

with the number i of the peak (from left to right). Like this, an average gain value $\overline{\mathfrak{S}(U_{bias})}$ for this bias voltage can simply be computed as:

$$\overline{\mathfrak{S}(U_{bias})} = \left(\sum_{i=1}^{i_{total}} \mathfrak{S}_i(U_{bias}) \right) / i_{total} \tag{6.6}$$

Depending on the behavior of each SiPM, three different methods are used to measure each final gain at the corresponding bias voltages of interest, $U_{bias}^{interest}$:

- Direct measurement at $U_{bias}^{interest}$ (S12571 -100P, S12571 -50P),

- In case the resolution of the QDC is too low for a direct measurement (S13360 -1325PE), the gain is extrapolated from measurements with higher bias voltages as discussed below.

- In case the resolution of the QDC is too low and noise impedes the measurement at higher bias voltages (S12571 -25P), a preamplifier is utilized for the measurement, as discussed in Section 6.1.5.

To increase the statistics in the first case for S12571 -100P and S12571 -50P, many single measurements are performed for the bias voltage of interest. For each measurement, the corresponding average gain value $\overline{\mathfrak{S}(U_{bias})}$ is added to a histogram as exemplarily shown in Figure 6.3, right. A Gaussian fit is applied to estimate the mean position and statistical uncertainty of the final gain value.

In any case, the gain is measured for a bunch of different bias voltages. Each of the average gain values are plotted as a function of the applied bias voltages, as exemplarily shown in
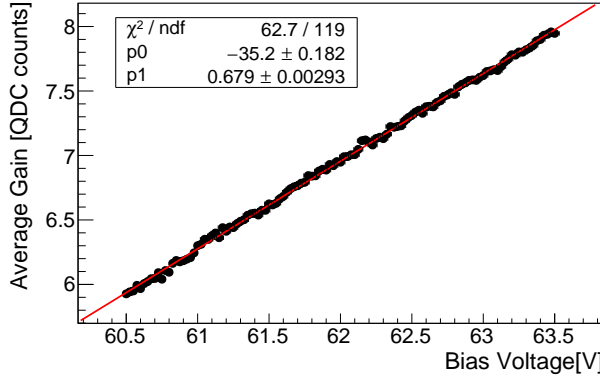
Figure 6.4.: Resulting average gain values $\overline{\mathfrak{S}(U_{bias})}$ as a function of bias voltage for MPPC S13360-1325PE. A linear fit is applied to estimate the breakdown voltage U_{break} and to allow the extrapolation of gain values for smaller bias voltages.

Figure 6.4. Error bars are computed from the uncertainties of the Gaussian fits to the mean position and using error propagation for the cases of averaged values.

To estimate the breakdown voltage U_{break} and to extrapolate the gain for a lower bias voltage in case of MPPC S13360 -1325PE, a linear fit is applied to the data:

$$\mathfrak{S}^{fit}(U_{bias}) = p0_{gain} + p1_{gain} \cdot U_{bias} \tag{6.7}$$

Again, statistical uncertainties are computed using error propagation.

The breakdown voltage U_{break} of the SiPM can be estimated from these parameters. By comparing Equation 6.7 and 4.6 and by taking into account Equation 6.4, the dependency between the parameters can be resolved as follows:

$$
\begin{aligned}
G &= -\frac{C_{pixel}}{q_e} U_{break} + \frac{C_{pixel}}{q_e} \cdot U_{bias} = (p0_{gain} + p1_{gain} \cdot U_{bias}) \frac{\kappa_{qdc}}{q_e} \\
&\Leftrightarrow \frac{C_{pixel}}{\kappa_{qdc}} = p1_{gain} \quad , \quad U_{break} = -p0_{gain}/p1_{gain}
\end{aligned}
\tag{6.8}
$$

with the pixel capacity C_{pixel} and under the assumption of no utilized preamplifier.

6.1.5. Preamplifier and Direct Circuit Box Intercalibration

For three of the four SiPMs, their gain can be measured as discussed in Section 6.1.4. For MPPC S12571-25P (1600 pixels), the gain measurement is not possible like this because of two criteria:

1. For low bias voltages, the gain of the SiPM and the resolution of the QDC is too low to separate single peaks in the QDC spectrum.

2. For higher bias voltages, the noise increases and creates a blurry spectrum. This noise is created by electrical noise on one hand, and by SiPM noise on the other hand, mainly due to increasing dark count rate and after-pulses. The electrical noise could to some
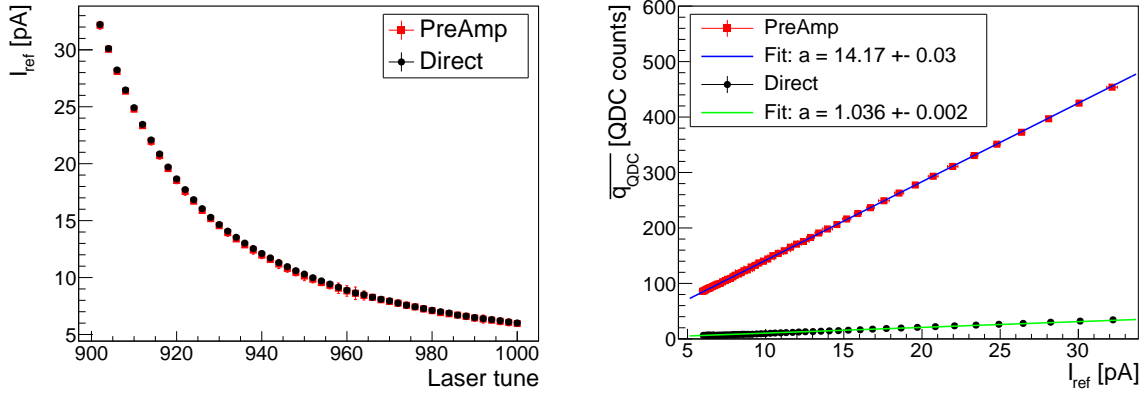
Figure 6.5.: Left: Reference diode current vs. laser tune values. Right: SiPM $\overline{q_{QDC}}$ values vs. reference diode currents. Linear fits are applied to each of the data sets, requiring the fits to cut at (0|0). Slopes a and the resultant conversion factor are printed. In both plots, the measurements are done using the preamplifier (PreAmp, black) or the direct circuit box (Direct, blue) to read out the SiPM.

degree be reduced by the utilization of shorter shielded cables, which is unfortunately not possible due to the distances between the SiPM inside the dark box and the readout device outside.

Therefore, a preamplifier is used to avoid the first issue. It replaces the direct circuit box as indicated in Figure 5.1. Unfortunately, the preamplifier starts to saturate for output voltages above 1 V, as remarked in its manual [120] and discussed below in Section 6.2.2. To be sure, that measurements are done in the linear part only, a maximum laser tune value is clarified beforehand, to be well below the point of saturation, by checking the output signal of the preamplifier with a scope.

As shown in Figure 6.5, left, the laser intensity is measured with the reference diode for the both cases, where the direct circuit box or the preamplifier are used. The intensity of the laser diode increases non-linearly from high to small tune values (from right to left). This non-linear increase is actually the reason why the reference diode is required. Small fluctuations of the laser intensity of both measurements at the same tune values are visible, which is not uncommon, but expected by the manufacturer [114]. That is why the reference measurement is always performed in parallel to the SiPM readout. Therefore, in Figure 6.5, right, the mean values $\overline{q_{QDC}}$ of the QDC spectrum of the SiPM (see Section 6.1.1) are plotted vs. the corresponding reference diode current I_{ref} for both, the direct and the preamplified measurement. Linear fits are applied to each data set (f_{Direct} to the direct, f_{PreAmp} to the preamplified measurement), requiring the fits to cross at (0|0). From the respective slopes a_{Direct} and a_{PreAmp} of the fits, the conversion factor α can be estimated:

$$\alpha = \frac{f_{Direct}}{f_{PreAmp}} = \frac{a_{Direct}}{a_{PreAmp}} = (7.31 \pm 0.02) \cdot 10^{-2} \tag{6.9}$$

85

for MPPC S12571-25P. Uncertainties are evaluated using error propagation.

With this conversion factor, the gain value of the preamplified measurement $\mathfrak{S}_{PreAmp}$ can be converted to the gain value of the direct measurement $\mathfrak{S}$:

$$\mathfrak{S} = \alpha \cdot \mathfrak{S}_{PreAmp} \tag{6.10}$$

With this method, the gain $\mathfrak{S}_{PreAmp}$ of MPPC S12571-25P is measured with the preamplifier, using the analysis described in Section 6.1.4 and afterwords converted to the gain $\mathfrak{S}$ using Equation 6.10.

6.1.6. SiPM Gain Results

Table 6.1 summarizes the final gain values for the four different SiPMs at the bias voltages of interest, $U_{bias}^{interest}$, and the corresponding breakdown- and over-voltages (see Equation 4.3).

As listed, the SiPM with the largest pixel pitches and therefore largest pixels (MPPC S12571 -100P with 100 µm pixel pitch, cf. Table 4.1) features the highest gain, while the two SiPMs with the smallest pixel pitches (first two rows) have the smallest gain. This is expected, as the gain is proportional to the capacity of a pixel (see Equation 4.6), which scales with the pixel area. [77] Still, a direct comparison is only possible at similar over-voltages, as the gain is also proportional to the applied over-voltage. But as the over-voltage of MPPC S12571 -100P is even smaller compared to the others, the dependance of the gain to the pixel pitch (or pixel size) is even clearer. The relative gain $\mathfrak{S}/U_{over}$ of MPPC S12571 -25P is about 9 % larger compared to S13360 -1325PE, though the pixel pitches agree. This might be related to the optical trenches, which are placed between pixels on S13360 -1325PE and possibly reduce the active area of pixels by maintaining a constant pixel pitch of 25 µm.

SiPM	$U_{bias}^{interest}$ [V]	gain $\mathfrak{S}$ [QDC counts]	U_{break} [V]	U_{over} [V]
MPPC S13360 -1325PE	56.10	2.95 ± 0.02	51.76 ± 0.04	4.34 ± 0.04
MPPC S12571 -25P	67.00	2.46 ± 0.01	63.69 ± 0.00	3.31 ± 0.05
MPPC S12571 -50P	66.50	6.10 ± 0.01	64.04 ± 0.03	2.46 ± 0.04
MPPC S12571 -100P	65.50	15.15 ± 0.02	63.84 ± 0.01	1.66 ± 0.06

Table 6.1.: Gain, breakdown- and corresponding over-voltages of SiPMs for the bias voltages of interest, $U_{bias}^{interest}$.

6.2. Linearity & Uniformity Measurements

For a significant response analysis, it is key to know the linearity of the used equipment. This section describes the linearity measurements performed for the direct circuit box and the preamplifier and also a uniformity scan of the engineered diffuser.
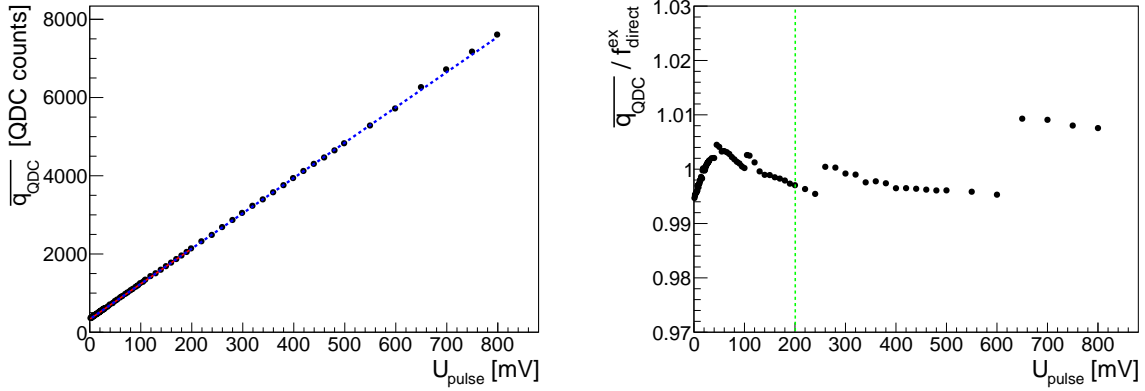
Figure 6.6.: Linearity measurement of the direct circuit box. Left: QDC response of the direct circuit box $\overline{q_{QDC}}$ vs. input pulse height U_{pulse} of the function generator. The red line indicates the linear fit function which is fitted in the range between $0\,\mathrm{mV}$ and $200\,\mathrm{mV}$, where linearity is expected. The blue dotted line f_{direct}^{ex} is the extrapolation of this function. Right: Ratio between the response of the direct circuit box $\overline{q_{QDC}}$ and the extrapolated function f_{direct}^{ex}. The green dashed line indicates the pulse height from where on the extrapolation begins.

6.2.1. Direct Circuit Box Linearity

The direct circuit box is the default circuit used to transmit the SiPM pulse to the QDC readout. The setup used to measure the linearity of this circuit can be found in Section 5.1.3. In short, a function generator injects a well known pulse into the direct circuit box, which then is read out with a QDC. Like this, it is a combined linearity measurement of the circuit and the QDC. Since the two devices are always used in combination, it is sufficient to measure both of them in one run.

The result of the linearity measurement of the direct circuit box is shown in Figure 6.6, left. The QDC mean value $\overline{q_{QDC}}$ is plotted as a function of the input pulse height U_{pulse} of the function generator. Following the assumption, that the relation between input and output is linear, especially for low input voltages, a linear function (red line) is fitted in the range between $0\,\mathrm{mV}$ and $200\,\mathrm{mV}$ input pulse height. The extrapolation f_{direct}^{ex} of this linear function for higher input voltages is shown in blue.

To prove the linearity, the ratio between the QDC mean value $\overline{q_{QDC}}$ and the extrapolated function f_{direct}^{ex} is calculated and plotted in Figure 6.6, right. The visible jumps have their origin in range-changes of the function generator. Even though, a linear behavior well within 1% deviation is found over the complete measurement range.

6.2.2. Preamplifier Linearity

The preamplifier is used to estimate the gain of MPPC S12571-25P (refer to Section 6.1.5) on one hand and to measure the crosstalk of the four different SiPMs on the other hand. Therefore it is important to know the (non-)linearity of the device. The setup used to measure the linearity of the preamplifier is introduced in Section 5.1.3 and is equivalent to the setup for the direct circuit box linearity measurement, while the two devices are exchanged. As described before in Section 5.1.3, the preamplifier is read out by the QDC and therefore it is a combined linearity
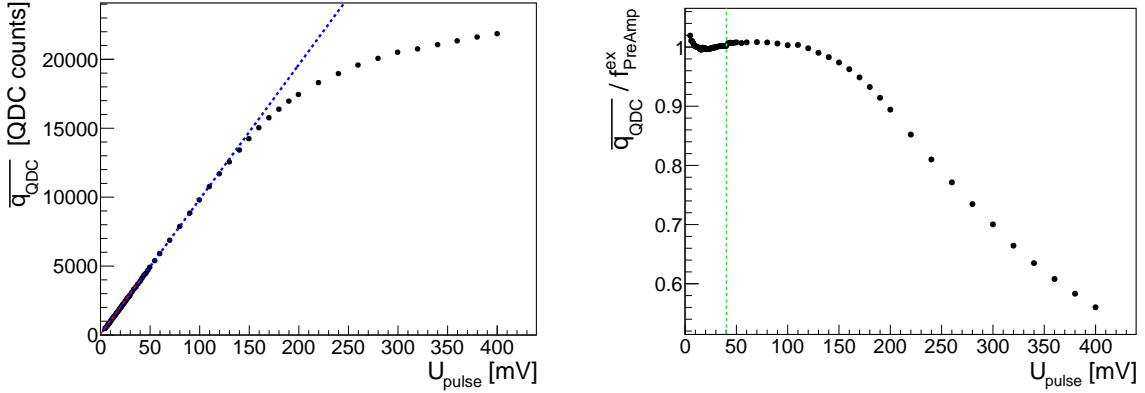
Figure 6.7.: Linearity measurement of the preamplifier. Left: QDC response of the preamplifier $\overline{q_{QDC}}$ vs. input pulse height U_{pulse} of the function generator. The red line indicates the linear fit function, which is fitted in the range between $0\,\mathrm{mV}$ to $40\,\mathrm{mV}$, where linearity is expected. The blue dotted line f^{ex}_{PreAmp} is the extrapolation of this function. Right: Deviation between the response of the preamplifier and the extrapolated function. The green dashed line indicates the pulse height from where on the extrapolation begins. A clear saturation of the preamplifier is visible, starting around $U_{pulse} \gtrsim 130\,\mathrm{mV}$.

measurement of both devices, but still sufficient since the preamplifier is always used in this chain.

Figure 6.7, left, shows the result of the linearity measurement of the preamplifier. A clear non-linearity is observed for input pulse heights larger $U_{pulse} \gtrsim 130\,\mathrm{mV}$, which corresponds to a resulting output voltage of around $1\,\mathrm{V}$, assuming an amplification factor of around 8 (which is set manually on the preamplifier and corresponds to the lowest possible amplification). Since the preamplifier shall be used only within an output voltage of $\pm 1\,\mathrm{V}$ [120], saturation and thus a non-linearity is expected. To prove the linearity for lower values, a linear function (red line) is fitted in the range between $0\,\mathrm{mV}$ to $40\,\mathrm{mV}$ and the resulting function f^{ex}_{PreAmp} is extrapolated for higher values (blue dotted line), comparable to the preceding section. Finally, the ratio between the data points $\overline{q_{QDC}}$ and the extrapolated function f^{ex}_{PreAmp} is plotted in Figure 6.7, right. A linear behavior within $1\,\%$ to $2\,\%$ deviation is found for input pulse heights smaller $130\,\mathrm{mV}$.

6.2.3. Diffuser Scan

It is important, that the incoming photons are distributed homogeneously onto the active surface of the SiPM. Therefore, an engineered diffuser is used, which transforms the Gaussian energy profile of the laser beam into a near-uniform top-hat profile. Like that, every single pixel has the same probability to be hit by incoming photons. Otherwise, hot- and dark-spots would reduce the significance of the SiPM response measurement.

The optical setup used to scan the engineered diffuser is explained in Section 5.1.4. The laser collimator on the computer controlled stage is automatically moved in an X-and Y-chain and for each position, the $\overline{q_{QDC}}$ value is estimated with the SiPM S12571-25P. Figure 6.8 shows the result of the 2D-scan, while the $\overline{q_{QDC}}$ values are relatively scaled to the maximum to be 1. The
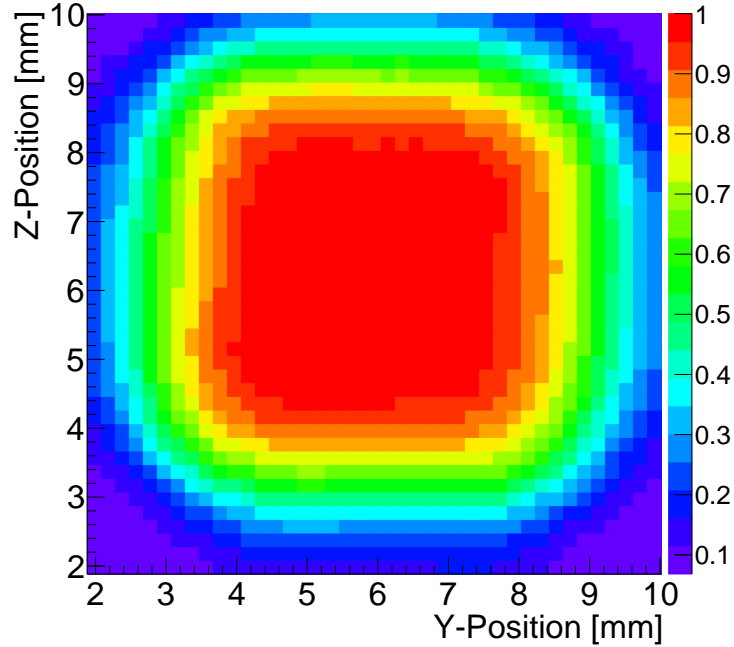
Figure 6.8.: SiPM response 2D-scan behind the engineered diffuser. The color scheme represents the scaled $\overline{q_{QDC}}$ values and therefore represents the measured light intensity. The values are scaled in a way that the maximum value is 1. Shown for MPPC S12571-25P.

red area indicates a very uniform illumination of the SiPM. During the following SiPM response measurements, the SiPM will be positioned in the center of the red area. The green halo corresponds to the cases, where only parts of the SiPM are hit. The maximum deviation from uniformity is found to be less than 1.5% in the inner area within about $4.7\,\text{mm} \leq Y \leq 6.6\,\text{mm}$ and $5.1\,\text{mm} \leq Z \leq 7.4\,\text{mm}$.

6.3. SiPM Optical Crosstalk Analysis

This section describes the measurement of optical crosstalk effects of SiPMs. The measurements are performed under the same conditions concerning temperature and SiPM bias voltage as during the SiPM response measurements. These two criteria are known to have a large impact on the optical crosstalk probability of SiPMs, as, for example, demonstrated in [78]. This measurement is done without any light source. First in Subsection 6.3.1, the measurement and analysis of the dark count rate and of the crosstalk probability is discussed, both comparable to [77], where older SiPMs were tested. In contrast, the analysis here goes further by obtaining the average factor of correlated noise in Subsection 6.3.2.

6.3.1. Dark Count Rate and Optical Crosstalk Probability

To estimate the optical crosstalk probability of a SiPM, the dark count rate (DCR), r_{DCR}, is measured as a function of the SiPM minimum pulse height by applying a certain threshold, as
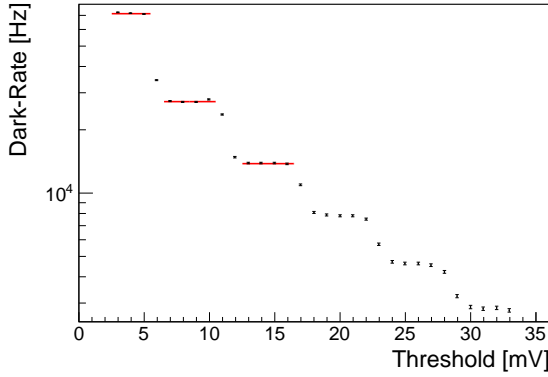
Figure 6.9.: Dark count rate as a function of the discriminator threshold, exemplarily shown for
MPPC S12571-100P with 100 pixels at $U_{over} = 1.66\,\text{V}$. Constant functions are fitted to the first
three plateaus in order to estimate the corresponding rates.

explained in Section 4.2.2. Therefore, the preamplified signal of a SiPM is fed into a discrimina-
tor, which generates a positive output once the input signal exceeds a threshold. These positive
output signals are then counted with a scaler. The setup for this measurement is discussed in
detail in Section 5.1.2. The rate is defined as the number of SiPM pulses exceeding a certain
threshold per unit time.

The scaler has a dead time, during which two different pulses can not be distinguished. There-
fore and similar to [77], the DCR is corrected for dead time losses of the scaler by applying
Equation 6.11:

$$r_{DCR} = \frac{r_{DCR}^{raw}}{1 - r_{DCR}^{raw} \cdot \tau_{dead}} \tag{6.11}$$

with the dead time $\tau_{dead} = 5\,\text{ns}$ and the measured rate r_{DCR}^{raw}.

A typical resulting dead time corrected DCR spectrum as a function of the discriminator
threshold is shown in Figure 6.9 for MPPC S12571-100P. For the other SiPM types, the shape
looks similar, though the rates as well as the widths of the plateaus vary. Typical for this kind
of measurement is the stair-like behavior of the DCR, which depend on the pulse heights of the
photo-peaks. The wider the plateaus are, the better is the single photon resolution.

The total DCR r_{DCR}^{total} is defined as the rate at 0.5 p.e. threshold and corresponds to the upper
stair plateau and represents all SiPM noise events. The next two plateaus can be used to
estimate the impact of optical crosstalk of the SiPM. Therefore, the first three plateaus are each
fitted with a constant function to estimate the rates $r_{DCR}^{total} = r_{0.5\,\text{p.e.}}$, $r_{1.5\,\text{p.e.}}$ and $r_{2.5\,\text{p.e.}}$. As
only a small number of events are within one plateau, the fit ranges have been chosen manually.
In case the plateaus would have included more entries, which would have required a higher
preamplification of the SiPM signals, the procedure could have also been automated as discussed
in [77], where another preamplifier with a higher amplification is utilized. Unfortunately, no
higher amplification has been utilized here.

This measurement is repeated for different bias voltages. In order to compare all four SiPMs,
Figure 6.10, left, shows the measured total DCR r_{DCR}^{total} as a function of the over-voltage U_{over}
for all four SiPMs.

The total DCR increases with rising bias voltage. This can be explained by the fact, that
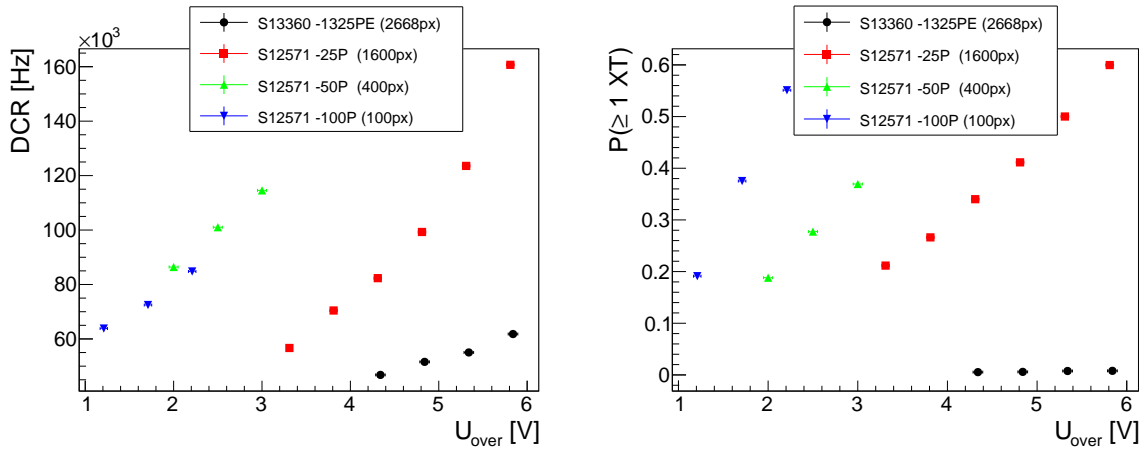
Figure 6.10.: Combined plots showing the total DCR r_{DCR}^{total} (left) and the probability for a minimum of one crosstalk event $P(\geq 1\,\mathrm{XT})$ (right) as a function of the over-voltage U_{over} for all SiPM types.

the electrical field between the n- and p- dotted areas within the semiconductor increases with higher bias voltage. As a result, the efficiency increases that allows a free charge carrier, which might be generated by thermal excitations, to trigger an avalanche.

Comparing the behavior as a function of the over-voltage, the two SiPMs with 25 µm pixel pitch have a lower total DCR compared to the two SiPMs with larger pixel pitches, while the latest generation SiPM (S13360 -1325PE) has the lowest total DCR. A direct dependency between the total DCR and the pixel pitch cannot be confirmed, since the estimated total DCR of the -100P is lower compared to the -50P SiPM in the observed range. This might have its origin in different purities of the semiconductors. Refer to Table 6.1 to compare the over-voltages to the bias voltages of interest, which are used in the SiPM response measurement. The number of pulses exceeding the 0.5 p.e. threshold per second can be found in Table 6.2, listed under N_0.

The optical crosstalk probability can be estimated from these DCR spectra. Usually [78], the optical crosstalk probability is defined as the ratio between the rate of events exceeding the threshold at 1.5 p.e. compared to the rate of events exceeding the 0.5 p.e. threshold, as shown in the previous Equation 4.9.

Here the assumption is made, that all events exceeding the 1.5p.e. threshold are crosstalk events, since the chance to overlay two dark events within a few ns pulse duration is assumed to be negligible.

It is important to note, that this optical crosstalk (XT) probability describes the probability for *more than or equal to one* crosstalk event after an initial triggering event, thus it is called $P(\geq 1\,\mathrm{XT})$ here. Resulting probabilities can be found in Table 6.2. The latest generation SiPM S13360 -1325PE features the smallest crosstalk probability with about 1 %, though the applied over-voltage is the highest. MPPC S12571 -100P has the highest crosstalk probability with about 38 %. The same generation SiPMs with smaller pixel pitches feature smaller crosstalk probabilities but still remain above 21 % at the given over-voltages. Therefore, there is a large gap between the two generations S13360 and S12571, which is clearly related to the optical trenches added between pixels in the S13360 generation.

Uncertainties are estimated from the uncertainties of the constant fits and applied error propa-

gation. It has to be noted, that the probability $P(\geq 1\,\mathrm{XT})$ is only defined to be equal or larger than 0, no matter if uncertainties suggest a lower value in case of MPPC S13360 -1325PE, where the probability is close to zero and the uncertainty is relatively high because of low crosstalk probability and low measurement statistics compared to the other three SiPMs.

Figure 6.10, right, shows the measured $P(\geq 1\,\mathrm{XT})$ as a function of the over-voltage U_{over}. The latest generation MPPC S13360 -1325PE has the lowest crosstalk probability (over all lower 1%), which can, as already discussed, be traced back to the fact, that this SiPM is equipped with trenches to reduce optical crosstalk between pixels. The optical crosstalk probabilities of the other three SiPM S12571 types, without trenches, are significantly higher. Therefore, it is important to take crosstalk effects into account for a response measurement at these circumstances. For all SiPMs, $P(\geq 1\,\mathrm{XT})$ increases with rising U_{over}. This can be explained by the fact, that the gain G increases with rising bias voltage (as discussed in Section 6.1.4) and therefore more charge carriers contribute to an avalanche. If there are more electrons and holes, the chance for a recombination and a subsequent optical crosstalk event increases. For S12571 types, the increase is much faster with rising over-voltage compared to MPPC S13360 -1325PE. It is remarkable that the dimensions of the pixels of the SiPMs have an influence on the optical crosstalk probability: the smaller the pixels, the smaller the crosstalk probability and vice versa for comparable over-voltages. This behavior is expected due to the dependance between the pixel size and the gain, again refer to [78].

6.3.2. Average Factor of Correlated Noise

For the following SiPM response analysis, not the knowledge about the probability for more or equal to one crosstalk event $P(\geq 1\,\mathrm{XT})$ is necessary (as discussed previously), but the expected average number of correlated pixels fired is required. Therefore, the average factor of correlated noise μ_C has been introduced in Section 4.2.2 and its application for the SiPM response analysis has been explained in Section 4.3.2.

To estimate this factor, the Borel model of correlated noise is utilized. For a detailed description, please refer to [105]. In this analysis the assumption is made, that only optical crosstalk adds to the correlated noise of a SiPM. Especially after-pulses are ignored and assumed to play a negligible role because of the short integration windows within $t_{int} = 50\,\mathrm{ns}$ to $100\,\mathrm{ns}$, depending on each SiPM pulse width, used to integrate the charge of the SiPM pulses with the QDC.

As a reminder and as already described in Section 4.2.2, the equation of the Borel model includes three parameters N_0, N_1 and N_2 (see Equation 4.10) while N_0 is the total number of events exceeding the 0.5 p.e. threshold, N_1 includes all events with exactly one pixel fired and N_2 represents all events with exactly one optical crosstalk event. By solving Equation 4.10 for ξ, which corresponds to the average number of correlated signals produced at each step of the chain [105, p. 5], the expected value μ_C can be estimated with Equation 4.11.

To obtain N_1 and N_2, the number of events per second exceeding the 1.5 p.e. and 2.5 p.e. threshold are estimated using constant fit functions as described before and shown in Figure 6.9. These rates are converted to N_0, N_1 and N_2 by applying Equation 4.12.

By solving Equation 4.10 and 4.11, ξ and μ_C are computed. The resulting values can be found in Table 6.2. As expected, the values for the S13360 type are significantly smaller compared to the S12571 types. While $\mu_C = 1.01$ for the first mentioned SiPM with optical trenches, μ_C
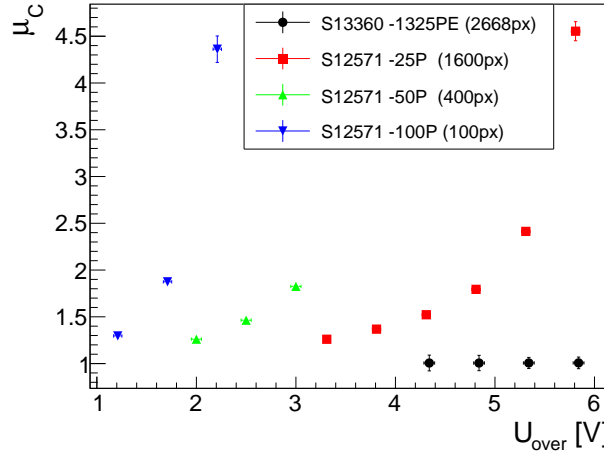
Figure 6.11.: Combined plot showing μ_C as a function of the over-voltage U_{over} for all SiPM types.

increases within the S12571 generation from small to large pixel pitches and results in a very high $\mu_C = 1.89$ for S12571 -100P. As a clarification, this means, that the measured signal (the number of pixels fired) of this SiPM is 1.89 times larger due to optical crosstalk than it would be without crosstalk, assuming no saturation.

Uncertainties are estimated in to following procedure: First, error propagation is used to estimate the uncertainty of the right side of Equation 4.10. Then, Eq. 4.10 is solved for ξ, $\xi + \Delta\xi$ and $\xi - \Delta\xi$. The maximum absolute difference between ξ and $\xi \pm \Delta\xi$ is defined as the uncertainty of ξ. The uncertainty of μ_C is then determined using error propagation. It has to be noted, that in any case, μ_C is only defined to be larger or equal to 1 and cannot become smaller due to uncertainties. This is, as already pointed out at the discussion of $P(\geq 1\,\mathrm{XT})$, important for MPPC S13360 -1325PE, where μ_C is close to 1 and the uncertainty relatively high. This has its origin in the very low number of crosstalk events and therefore small statistics compared to the other three SiPMs. Nevertheless in case of this SiPM, it is worth to point out that the measured μ_C is around 1.01 for any measured over-voltage. Since the SiPM response measurement will be performed at the lowest over-voltage in this specific case, a upper cut of μ_C is obtained from the result at $U_{over} = U_{over}^{interest} + 1\,\mathrm{V} = 5.34\,\mathrm{V}$ with $\mu_C(U_{over} = 5.34\,\mathrm{V}) = 1.01 \pm 0.06$, where the uncertainty is a bit lower.

Figure 6.11 shows μ_C as a function of the over-voltage U_{over} for all four SiPMs. Similar to the already discussed crosstalk probability, the correlated noise factor μ_C grows with the SiPM pixel size for the S12571 types and with increasing over-voltage, μ_C increases exponentially. As already discussed, the average factor of correlated noise μ_C is significantly smaller for the latest generation SiPM (S13360 -1325PE) compared to the older series S12571, especially smaller compared to the -25P type, with the same pixel pitch (25 μm) but without trenches.

Systematic uncertainties, for example arising from the variation of fit ranges for the constant fit functions in Figure 6.9 are small compared to the statistical uncertainties and therefore neglected. Still, a higher preamplification of the SiPM pulses would have been useful to increase the number of entries in the plateaus, especially for SiPMs with relatively small intrinsic gain.

SiPM MPPC	N_{total}	$P(\geq 1\,XT)$	N_0	N_1	N_2	ξ	μ_C
S13360 -1325PE	2668	0.54%	46789	46535	251	0.006	1.01
@ $U_{over} = 4.34$ V		$\pm 0.65\%$	(100%)	(99.46%)	(0.54%)	± 0.077	± 0.06
S12571 -25P	1600	21.22%	56123	44211	8819	0.208	1.26
@ $U_{over} = 3.31$ V		$\pm 0.39\%$	(100%)	(78.78%)	(15.71%)	± 0.015	± 0.02
S12571 -50P	400	27.98%	99877	71935	17380	0.318	1.47
@ $U_{over} = 2.46$ V		$\pm 0.29\%$	(100%)	(72.02%)	(17.40%)	± 0.009	± 0.02
S12571 -100P	100	38.18%	71307	44082	13420	0.470	1.89
@ $U_{over} = 1.66$ V		$\pm 0.28\%$	(100%)	(61.82%)	(18.82%)	± 0.008	± 0.03

Table 6.2.: Results of the crosstalk measurement of the four SiPMs. Listed are the total number of pixels N_{total}, the probability for at least one crosstalk event, $P(\geq 1\,XT)$, the total number of events, N_0, the number events without opt. crosstalk, N_1 and the number of events with exactly one crosstalk event, N_2. The numbers in brackets represent the fraction of the related number of events N_i compared to the total number of events N_0. With [105], the average number of correlated counts that are generated at each step of the chain, ξ, and finally, the average factor of correlated hits, μ_C, are calculated using the Borel model of correlated noise.

6.4. SiPM Response Measurement

The SiPM response measurement in the following is discussed by means of the latest generation SiPM with 2668 pixels and low optical crosstalk probability. The setup has been discussed in detail in Section 5.1.1. In short, a laser diode illuminates a SiPM and a reference diode in parallel with variable light intensity, while the response of the SiPM is read out with a QDC and the response of the reference diode is read out with a picoamperemeter.

6.4.1. Laser Intensity

To measure the SiPM response as a function of the incoming light intensity, the laser diode is tuned in a way that a range between about 10^0 to 10^3 SiPM pixels fired is covered. For each laser tune value, the current of the reference diode I_{ref} (see Section 5.2.9) and the SiPM QDC-spectrum (Section 5.2.7) is recorded.

Figure 6.12 shows the typical current measured by the reference diode with respect to the laser tune value. This current directly corresponds to the intensity of the laser diode and can be used as a reference. Approximately 99% of the light intensity is led onto the reference diode and 1% onto the SiPM. Starting from a high tune value, the laser intensity increases with lowering tune. First, this increase is slow, which makes it easy to calibrate the SiPM number of pixels fired, N_{fired}, later on in this analysis, then starts to increase stronger at around a tune value of 870. The intensity reaches its maximum shortly before a tune value of 0. The highest tune value shown in Figure 6.12 is chosen such that the SiPM response of the parallel measurement presented next, is well above electronic noise.

6.4.2. SiPM QDC Conversion to Number of Pixels

In contrast to the preceding section, where 99% of the laser intensity is directed onto the reference diode, this section describes the analysis of the remaining 1% of the laser intensity directed onto the SiPM. As a reminder, the light is distributed uniformly over the active area of the
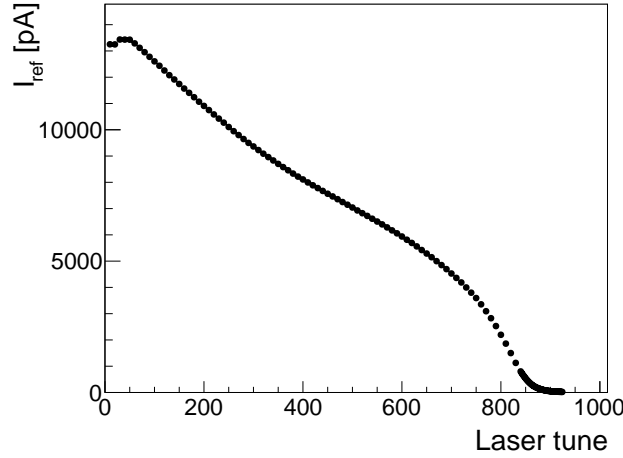
Figure 6.12.: Current of the reference diode I_{ref} vs. tune value of the laser diode. Statistical uncertainties are smaller than points.
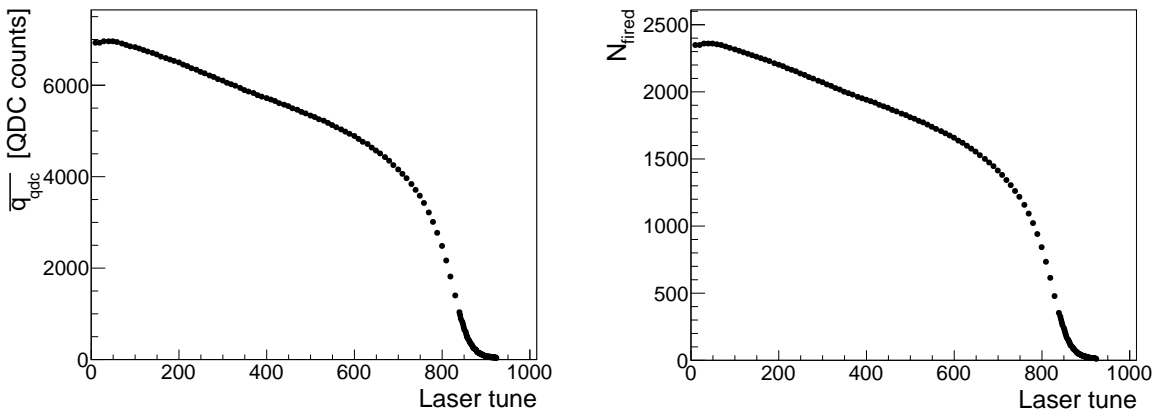
Figure 6.13.: Left: SiPM QDC mean values $\overline{q_{QDC}}$ vs. laser tune value. Right: SiPM number of pixels fired N_{fired} vs. laser tune value. Both shown for MPPC S13360-1325PE. Statistical uncertainties are smaller than points.

SiPM using the engineered diffuser (see Section 6.2.3).

Figure 6.13, left, shows the corresponding SiPM QDC mean values $\overline{q_{QDC}}$ (as defined in Section 6.1.1) as a function of the tune value of the laser. Going from right to left, the $\overline{q_{QDC}}$ shows a similar behavior at high laser tune values as already observed at the reference diode current I_{ref} in Figure 6.12. For smaller tune values, thus higher intensities, $\overline{q_{QDC}}$ increases slower compared to I_{ref}, which is already a hint for saturation. The $\overline{q_{QDC}}$ values exceed the 12 bit (4096) resolution of the QDC, which is possible due to its dual range and the conversion from high- to low-range as described in Section 6.1.3.

To convert the $\overline{q_{QDC}}$ values to the number of pixels fired N_{fired}, it has to be divided by the gain $\mathfrak{S}$ (in units of QDC counts, see Section 6.1.4) of the SiPM:

$$N_{fired} = \frac{\overline{q_{QDC}}}{\mathfrak{S}} \tag{6.12}$$
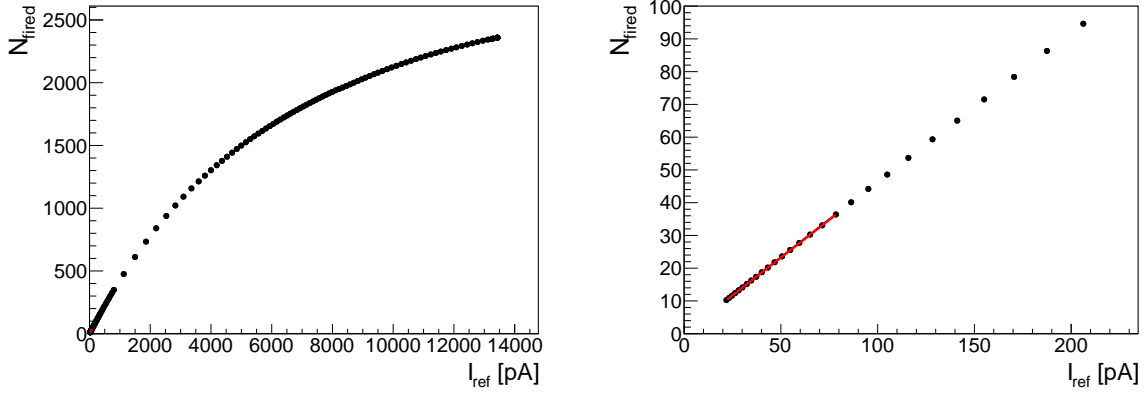
Figure 6.14.: Number of pixels fired N_{fired} vs. reference diode current I_{ref}. Left: Full range. Right: Zoom into the calibration region, where a linear fit is applied. Shown for MPPC S13360-1325PE. Statistical uncertainties are smaller than points.

The result is plotted in Figure 6.13, right, as a function of the laser tune value. Following Equation 6.12, the shape of N_{fired} equals the shape of $\overline{q_{QDC}}$. As the gain $\mathfrak{G} > 1$, (see Table 6.1), the absolute values result accordingly in smaller values N_{fired}.

6.4.3. Reference Charge Conversion to Number of Seeds

Next in Figure 6.14, left, the number of pixels fired N_{fired} is plotted as a function of the reference diode current I_{ref} by equating their laser tune values of each corresponding measurement point. Since I_{ref} is a measure of the laser intensity, this plot allows a first comparison between the light input and the SiPM output which shows a clear saturation and will finally be discussed in detail in Section 6.5.

For a low number of pixels fired on the SiPM, a linear behavior is expected between the number of seeds $N_{seed} = N_\gamma \cdot \epsilon_{PDE}$ (cf. Section 4.3.2) and N_{fired}. This low light region, where no saturation effects and a constant optical crosstalk probability is assumed, is called calibration region. Therefore, a linear fit $N_{fired}^{linear}(I_{ref}) = p0 + I_{ref} \cdot p1$ is applied to the data in Figure 6.14 in a range up to $N_{fired} = 40$ on the Y-axis. This range differs from SiPM to SiPM, depending on its total number of pixels N_{total}. It is chosen to be well within the expected calibration region. A detailed view of the fit is shown in Figure 6.14, right. In this case of MPPC S13360-1325PE, the fit results in $N_{fired}^{linear}(I_{ref}) = (0.20 \pm 0.12) + I_{ref} \cdot (0.462 \pm 0.003)$.

The resulting fit parameters $p0$ and $p1$ are used to convert the reference diode current I_{Ref} into the number of Seeds N_{seed} using Equation 4.15 and the corresponding correlated noise factor μ_C. It has to be noted, that this correction performed for the correlated noise factor is important, since these factors are not negligible (except for the SiPM S13360 series with optical trenches), especially because of the high over-voltages applied to the SiPMs. This is a special feature of this analysis compared to other SiPM response measurements performed in the past, for example in [108].

6.5. SiPM Response Results

This section discusses the results of the SiPM response measurement for the four different SiPMs. Some of the results have been presented at the *International Conference on the Advancement of Silicon Photomultipliers* (ICASiPM) [132] and at the *14th Pisa Meeting on Advanced Detectors* [133], both in 2018; and have been published in the meantime under the title *Measurement of the response of Silicon Photomultipliers from single photon detection to saturation* [112]. It shall explicitly be pointed out, that the result plots, which are presented in the following, have been created *in the course of this thesis*, and some also appear in the publication. A short reference is still added to the respective figures.

Systematic uncertainties on N_{fired} and N_{Seed} are estimated taking into account non-linearities of the direct circuit box (1 %), the preamplifier (2 %) and the reference diode (1 %), as well as the non-uniformity of the engineered diffuser (1.5 %) (cf. Section 6.2). The latter is assumed to add an asymmetric systematic uncertainty, because with a non-uniformity, only less of the sensitive area of the SiPM might get illuminated, never more. Also, another asymmetric systematic uncertainty arising from contributions of after-pulses is assumed to be of the order of 1 % [3]. The uncertainties are applied to the corresponding measurement observables and then propagated to N_{fired} and N_{Seed}. For instance, the uncertainty from the linearity of the reference diode is applied to I_{ref}, the uncertainty from the linearity of the direct circuit box or of the preamplifier to the QDC mean values $\overline{q_{qdc}}$ and the uncertainty from after-pulses and from the uniformity of the diffuser directly to N_{fired}.

As another source of uncertainties, temperature variations inside the dark box could vary the gain and noise (especially optical crosstalk) characteristics of a SiPM as measured before in another setup and presented in Ref. [78]: With rising temperature, the breakdown voltage U_{break} would increase because of a decreasing electron mobility and therefore the gain and the crosstalk probability would decrease. Because the gain directly affects the calculated number of pixels fired, N_{fired} (see Equation 6.12) a lower gain due to a higher temperature would falsely increase the resulting response of a SiPM. The lab is temperature stabilized, but possibly small variations of about $\pm 0.3°$C might occur. Nevertheless, inside the dark box, where the SiPM is placed, the variations should be even smaller, because with the exception of the direct circuit box or the preamplifier, all other heat producing electronics are outside the box.

6.5.1. Latest Generation SiPM with 2668 Pixels

First, the results of the latest generation SiPM MPPC S13360-1325PE with trenches is discussed. Compared to the other SiPMs, it has two obvious advantages: with the highest number of total pixels $N_{total} = 2668$ and the lowest correlated noise factor $\mu_C = 1.01$ (Table 6.2), saturation and correlated noise effects have the lowest impact on the SiPM response. The result is shown in Figure 6.15, top. Added systematic and statistic uncertainties are plotted as gray

---

[3]Figure G.1 in Appendix G shows the after-pulse probability for the S1336x series which is well below 1 % for over-voltages applied here. For the other SiPM types, no official data from the manufacturer is available. According to the manufacturer, the after-pulse probability of the S1257x series is comparable. [134] As discussed earlier, the signal integration window of the QDC is very short below 100 ns, thus the fraction of after-pulses is in any way reduced.

rectangles.

The response of the SiPM is close to linear for small values N_{seed} and then saturates for high N_{seed} as expected.

Before going into more detail, the additionally plotted functions and fits shall be introduced first to allow a better discussion of the measurement results.

The constant horizontal yellow dotted line $N_{fired} = N_{total}$ represents the physical total number of pixels of the SiPM. The second yellow fine-dotted line going through zero, represents a linear behavior $N_{fired} = 1 \cdot N_{Seed}$ if there was no saturation, nor correlated noise.

The light blue dotted curve is a plot of the simple exponential response model, as defined in Equation 4.16 in Section 4.3.3.1, which utilizes the physical number of total pixels.

In dark blue, a fit to the data points taking into account statistical uncertainties is shown, which corresponds to the simple exponential model as introduced in Equation 4.16, with only the total number of pixels N_{total} as a free parameter. This is sometimes referred to as the *effective* total number of pixels [107], which allows this model to handle lower responses on the one hand and over-saturation on the other hand.

A fit of the optical crosstalk-extended model (XT-ext), as presented in Section 4.3.3.2 in Equation 4.17, is is shown in red, while N_{total} and crosstalk, $\epsilon_C \approx \mu_C - 1$, are free parameters. Finally in green, a fit of the advanced SiPM response model, as discussed in Section 4.3.3.3 and given in Equation 4.21, is shown, including ϵ_C and the recovery and charge contribution parameters, α and β, respectively. The total number of pixels, N_{total}, is fixed to the physical number and the after-pulses factor is neglected here.

As already mentioned, the SiPM response saturates, which is clearly visible due to the deviation between the measured data and the linear slope of 1 (yellow fine-dotted line). Until $N_{seed} \lesssim 120$, the data is still reconcilable with linear response within uncertainties. Regarding high light inputs, the data follows an exponential behavior and it can be anticipated, that it converges towards the total number of pixels. Nevertheless, this is just a presumption, since the input light intensities (and the photon detection efficiency of the SiPM, remember $N_{seed} = N_\gamma \cdot \epsilon_{PDE}$) are not high enough to actually reach the level of $N_{fired} \approx N_{total}$.

In the high light region from approximately $N_{seed} \gtrsim 2000$ on, the data points are a bit below the light blue simulation of the simple exponential response model, while still compatible within uncertainties. This is also represented by the two fit results with a free N_{total} parameter, resulting in $N_{total} = 2552.6 \pm 3.5$ for the simple model and $N_{total} = 2544.0 \pm 3.8$ for the XT-ext. model. The discrepancy from the physical total number of pixels, $N_{total} = 2668$ and particularly the fact that the fitted parameters are lower, might be explained by the non-uniformity of the engineered diffuser or non-linearities of the readout electronics as discussed before.

Especially because this SiPM has the lowest probability for optical crosstalk, the differences between the simple exponential and the XT-ext. model are very low, which confirms that crosstalk plays a small role for this SiPM response. Concerning the crosstalk parameters, both fits including such a parameter (XT-ext. & advanced) result in $\epsilon_C = 0.01$, which is consistent with the expected value $\mu_C = 1.01$ within this resolution (remember that μ_C includes the triggering event and therefore the relation to ϵ_C is given by: $\mu_C \approx 1 + \epsilon_C$).

Concerning the fit results of the advanced model, $\beta = 0$ and $\alpha \approx 1$ is synonymous with no observed over-saturation, which is the case in this considered range. The small deviation of
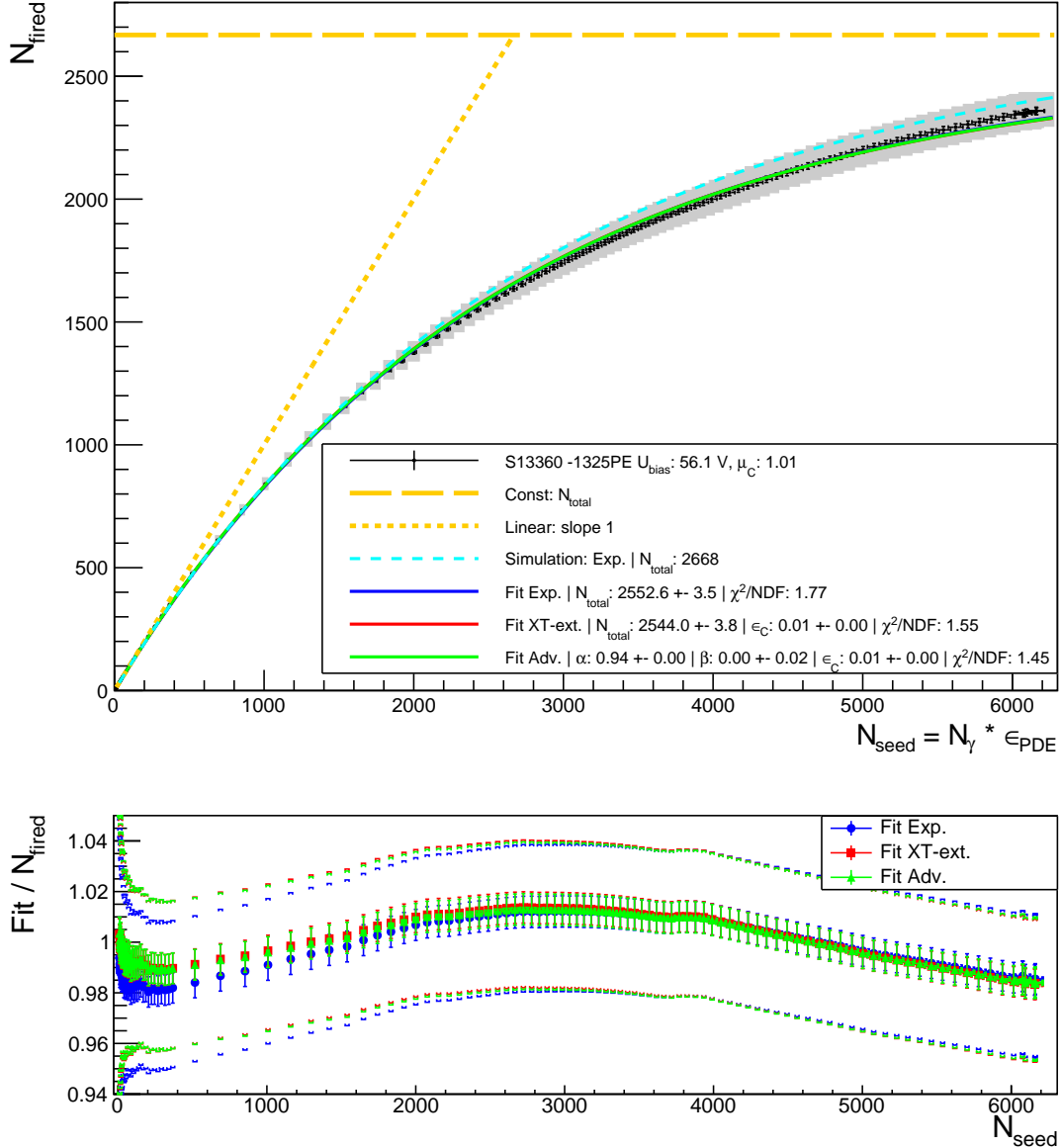
Figure 6.15.: Result showing the number of pixels fired N_{fired} (top) (also shown in [112]) and the ratio between the fit functions and the data fit/N_{fired} (bottom) as a function of the number of seeds $N_{seed} = N_\gamma \cdot \epsilon_{PDE}$ for MPPC S13360-1325PE with $N_{total} = 2668$ pixels at $U_{over} = (4.34 \pm 0.04)\,\mathrm{V}$. There are only small differences between the three fits, that's why they overlap.

α from 1 indicates only a small deviation from the simple exponential model, while these are described by NLO effects because of the recovery of pixels. As mentioned in Section 4.3.3.3, the advanced function would result in the simple exponential function $N_{adv} = N_{exp}$ in the case of $\alpha = 1$ and $\beta = 0$ and only correlated noise would make a difference.

With the fit parameters of the advanced and of the XT-ext model, no over-saturation is expected for larger N_{seed}.

Figure 6.15, bottom, shows the ratio between the three fit functions and the data. For a better viewpoint, statistic uncertainties are plotted as same-colored lines while added systematic and statistic uncertainties are plotted as square brackets. As already discussed on the upper plot, the three fits are more or less consistent with each other. Still, the simple exponential model shows the largest deviation from data, particularly for low to mid light intensities, where it deviates up to two percent.

To conclude, the response of MPPC S13360-1325PE with its low crosstalk probability is best described by the advanced SiPM model, but the XT-ext. model achieves a similar result. This statement is affirmed by the close χ^2/NDF of the two fits and the visible small deviations from each other.

6.5.2. SiPM with 1600 Pixels as Used on First Mainz SMD HBU

The behavior of MPPC S12571-25P with $N_{total} = 1600$ is expected to differ more from the simple exponential function (cf. Section 4.3.3.1), because its correlated noise factor $\mu_C = 1.26$ is not negligible compared to the previously discussed SiPM. The result is shown in Figure 6.16, top.

This SiPM response saturates comparable to the previously discussed SiPM. Again here, a presumption can be made, that the data converges towards the total number of pixels, but still and for the same reason as before, N_{seed} is not high enough to reach the level of $N_{fired} \approx N_{total}$.

As expected, optical crosstalk has an impact on the SiPM response, especially for low to medium light intensities. This impact is visible due to the fact, that N_{fired} is measured to be larger than the expectation from the simple exponential behavior (light blue curve) and even more obvious for low light intensities, where N_{fired} exceeds the fine-dotted yellow line, which refers to a response with a slope of 1, without correlated noise, nor saturation. For medium to high light inputs, the effect of crosstalk is reduced because it can only affect the decreasing number of non-fired pixels.

That is why the two models including crosstalk parameters (XT-ext. and advanced) can handle the range from low to medium N_{seed} much better than the simple exponential model, but at least for high number of seeds, the difference between the models decreases because of the reduced influence of crosstalk. This observation is confirmed in Figure 6.16, bottom, where the ratio between the three fits and the data is shown. Nevertheless, all of the three models show a deviation to the measured data.

Concerning fit parameters, the simple exponential model results in $N_{total} = 1559.3 \pm 1.7$ which is equal to the physical number of pixels (1600) within uncertainties, but since its shape differs that much from the data, especially in the low to medium range of N_{seed}, this result is disputable. The XT-ext. model results in $N_{total} = 1550.5 \pm 1.4$, which is lower than the expected value but comparable to the relative deviation that was already observed for the previously discussed SiPM. This deviation is supported due to the observation, that the measured number of pixels fired is even below the simulated simple exponential model (light blue) in the region around $N_{seed} \approx 3000$. This lower measured response might be introduced by possible small non-linearities of the readout electronics.

The resulting crosstalk parameters of the XT-ext. ($\epsilon_C = 0.19$) and of the advanced model ($\epsilon_C = 0.21$) are both below the expectation from the related and beforehand measured $\mu_C =$
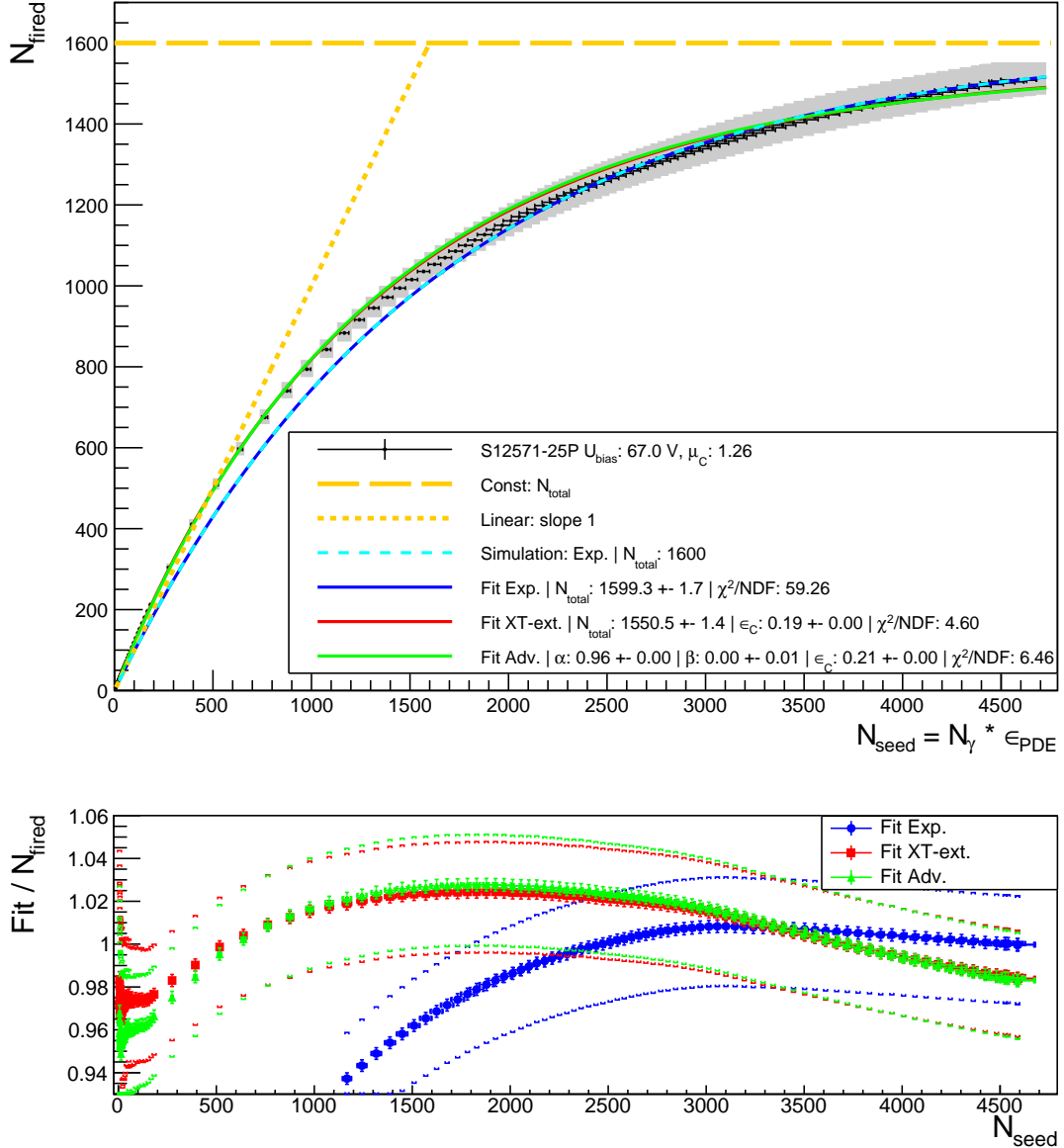
Figure 6.16.: Result showing the number of pixels fired N_{fired} (top) (also shown in [112]) and the ratio between the fit functions and the data fit/N_{fired} (bottom) as a function of the number of seeds $N_{seed} = N_\gamma \cdot \epsilon_{PDE}$ for MPPC S12571-25P with $N_{total} = 1600$ pixels at $U_{over} = (3.31 \pm 0.05)$ V.

1.26. This discrepancy is also visible in the ratio plot, where both fits have a ratio below 1 in the low region between approximately $0 < N_{seed} \lesssim 500$ and consequently underestimate the effect of crosstalk.

The fit parameters α and β of the advanced model are similar to the previously discussed results of MPPC S13360-1325PE and therefore expect no over-saturation for higher N_{seed}.

To summarize, the response of MPPC S12571-25P is affected by optical crosstalk and saturation. Therefore the two models including a description for crosstalk can handle the data way

better than the simple exponential model. In this specific case, the XT-ext. model achieves an even lower χ^2/NDF than the advanced model (but with only 3 free parameters). As a short outlook, the advantage of the XT-ext. model compared to the advanced model is, that it can be inverted. This is important for the use in the following CALICE analysis, where also this SiPM is utilized.

6.5.3. SiPM with 400 Pixels

The result for MPPC S12571-50P with $N_{total} = 400$ is shown in Figure 6.17. This SiPM has a high crosstalk probability at the applied bias voltage, resulting in $\mu_C = 1.47$. Also, since it consists of only 400 pixels, compared to MPPC S12571-25P, a lower amount of incoming photons is needed to reach a level of saturation, assuming that the PDE is in the same order of magnitude[4].

As an obvious contrast to the beforehand discussed results, over-saturation is observed here, meaning, that for a certain number of incoming N_{seed}, the SiPM response N_{fired} exceeds a value equal to its physical total number of pixels N_{total}. The number of pixels fired crosses the physical total number of pixels approximately at $N_{seed} \approx 900$. Over-saturation has been observed in other measurements with SiPMs of different series, too [106, 108]. In this case it is unclear, whether the response at the level of over-saturation converges to a specific maximum number of pixels fired, or continues to increase approximately linearly.

In any case, the difference between the simulated simple model (light blue curve) and the data is enormous, since it does not expect neither over-saturation nor optical crosstalk. Therefore it's not surprising that the fit of the simple exponential model is also not able to handle both effects, though it can to some extend take into account over-saturation by a high $N_{total} = 460.6 \pm 0.2$. The XT-ext. model manages to cope with the data much better, especially for low light intensities, $N_{seed} < 400$, but still is not able to reproduce the data for medium to high light intensities. That's why it does not surprise, that the crosstalk parameter $\epsilon_C = 0.31$ in this model is far too low compared to the related and expected $\mu_C = 1.47$. Only the advanced model, which is especially suited to describe combined effects of crosstalk and over-saturation, allows to reproduce the response for low and high numbers of seeds at once, which is reflected by the small χ^2/NDF. Especially, if one takes into account the ratio plot in Figure 6.17, bottom, only in the medium region around $N_{seed} \approx 350$, the model still diverges, while the majority of the fit remains well below 2% deviation from data.

The fit parameters of the advanced model provide a crosstalk parameter of $\epsilon_C = 0.46$, which practically matches the beforehand measured $\mu_C \approx \epsilon_C + 1$. Also, and in contrast to the previous results, the non-zero $\beta = 3.37 \pm 0.14$ and the small $\alpha = 0.29 \pm 0.01$ parameters reflect the observed over-saturation.

Yet, the origin of over-saturation is not completely understood (again refer to [106, 108]). Delayed photons could trigger partially recovered pixels and like this add up the charge measured with the QDC in a certain integration window and therefore increase the reconstructed number of pixels fired. This recovery of pixels can be described by the advanced SiPM response model

---

[4]This is reasonable by comparing the over-voltages applied in these measurements with the applied over-voltages for the PDE plots given in [101], p.3. The relative differences $(U_{over}^{here} - U_{over}^{Hamamatsu})/U_{over}^{Hamamatsu}$ between the applied over-voltages are: $\Delta U_{over}^{25P} = -5.7\,\%$, $\Delta U_{over}^{50P} = -5.4\,\%$ and $\Delta U_{over}^{100P} = +18.6\,\%$.
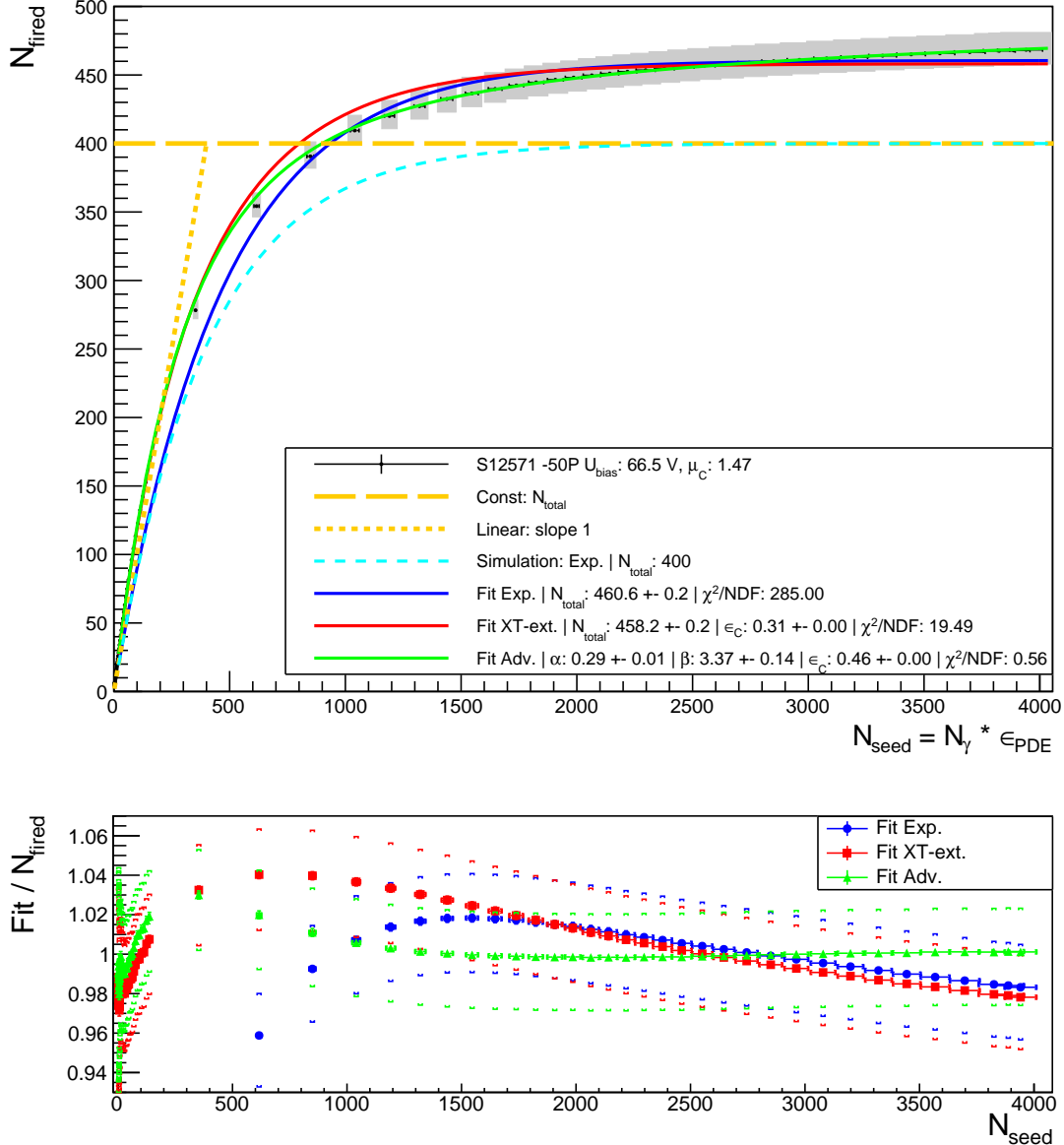
Figure 6.17.: Result showing the number of pixels fired N_{fired} (top) (also shown in [112]) and the ratio between the fit functions and the data fit/N_{fired} (bottom) as a function of the number of seeds $N_{seed} = N_\gamma \cdot \epsilon_{PDE}$ for MPPC S12571-50P with $N_{total} = 400$ pixels at $U_{over} = (2.46 \pm 0.04)$V.

as discussed in Section 4.3.3.3. But still, delayed photons, as they are described in this model, are not expected in this response measurement here, where the SiPM is directly illuminated. Because of the very short pulses of the laser diode (less 1 ns width), delayed photons from this source can be ignored.

Consequently, other effects must play a role and two possible candidates are discussed in the following: fast after-pulses and delayed optical crosstalk.

Because of the short integration window of the QDC (between 50 and 100 ns, matched to cover

around one complete SiPM signal), the contribution of after-pulses to the measured number of pixels fired is only taking into account as a systematic uncertainty as discussed in the beginning of Section 6.5. Still, the effect might be underestimated and increase the measured number of pixels fired. In contrast to optical crosstalk, after-pulses do not occur in time with the initial fired pixel, but have a delay profile. After-pulses do only contribute to the measured signal, if the pulse occurs after pixel recovery and before the integration window closes. In either way, the signal will never be completely integrated but cut off at the end of the integration window, which again minimizes the effect of after-pulses. Another difference to optical crosstalk is, that after-pulses only arise in the very same pixel of their origin. That is why after-pulses contribute constantly to the measured SiPM response in contrast to crosstalk, where the effect decreases with a rising number of pixels fired. Consequently, after-pulses might increase the measured number of pixels fired over the level of total pixels.

Delayed optical crosstalk, as for example explained in [99, 102, 103] might make up another source for over-saturation. If a crosstalk photon creates a free charge carrier not directly in a neighboring pixel, but in its vicinity, where still an electrical field is present, the charge carrier might diffuse to the avalanche region and trigger a delayed avalanche in this pixel. Therefore and in contrast to direct optical crosstalk, delayed crosstalk also increases the measured number of pixels fired, even in the case when all primary pixels fired already. Of course, delayed crosstalk is only possible, if the target pixel is at least partially recovered. As discussed already for after-pulses, the short integration window of the QDC prevents the complete integration of delayed avalanches.

In total, these two correlated noise effects are assumed to be at the level of a few percent and therefore might not completely explain the observed over-saturation. Especially, if one considers the still rising SiPM response at the level of over-saturation, for example for appoximately $N_{seed} > 2500$, and one remembers, that at this point about all of the pixels should have fired by the incoming primary photons and therefore the contributions from correlated noise should be at a maximum level, it might indicate, that other more complex effects increase the measured SiPM signal. Again, this assumption can only be made, as long as the initial photons are right in time.

Another possible explanation is given in Ref. [108], p. 16: "Another possible reason for the observed effect might be related to the region in-between the microcells. The trenches separating the individual pixels are coated with a thin reflective layer of aluminum and are supposed to be insensitive to incoming light. However, at very high light exposure, some photons may pass the layer, resulting in an additional signal." As also pointed out in this paper, this statement is questionable.

6.5.4. SiPM with 100 Pixels

Finally the response of MPPC S12571-100P, with the lowest total number of pixels $N_{total} = 100$ and the highest optical crosstalk probability of all four SiPMs, resulting in $\mu_C = 1.89$, is discussed by means of Figure 6.18.

As expected, the deviation from the simulated simple exponential model (light blue dotted curve) is huge because of the extremely crosstalk affected behavior of the SiPM response for
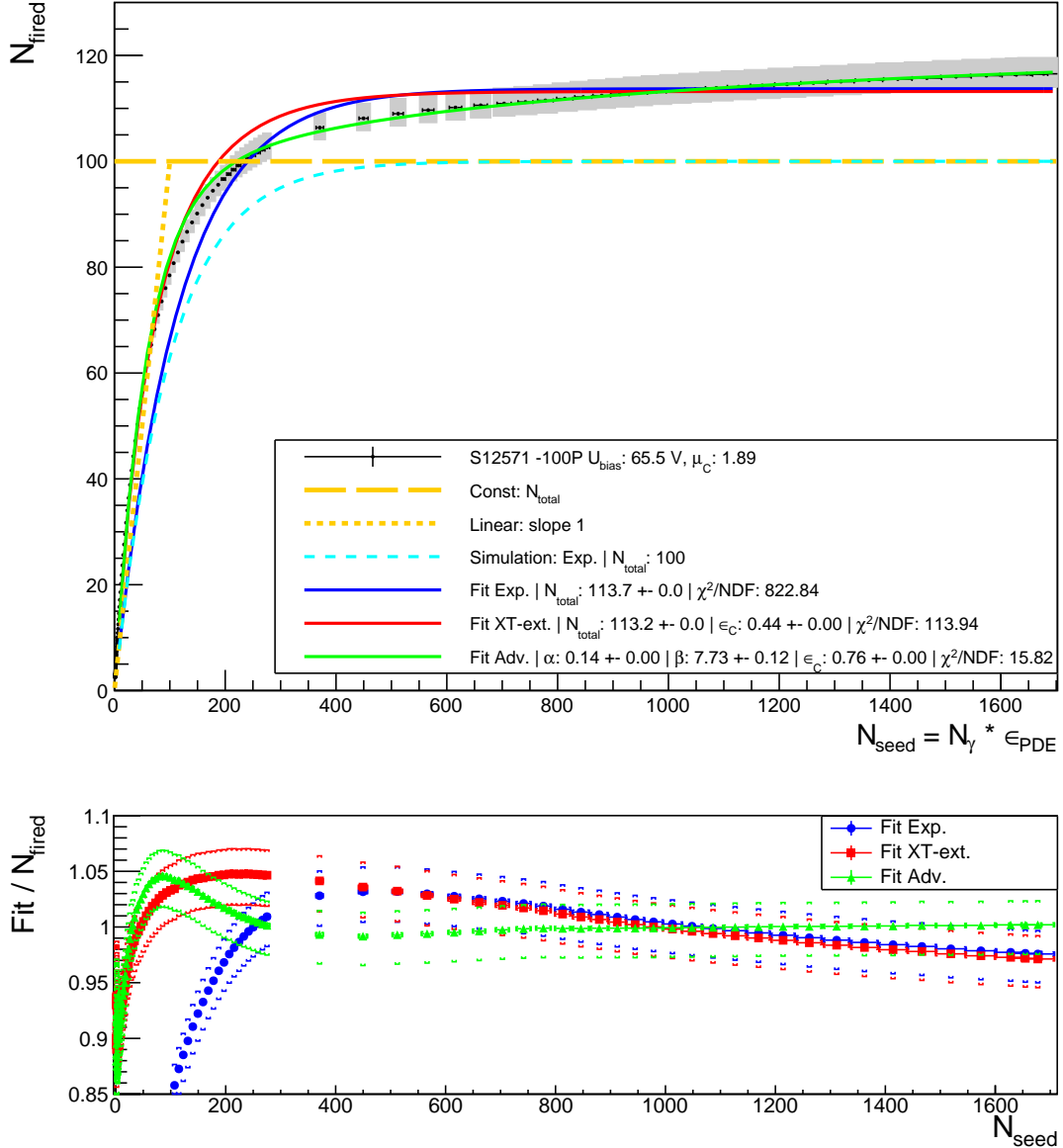
Figure 6.18.: Result showing the number of pixels fired N_{fired} (top) (also shown in [112]) and the ratio between the fit functions and the data fit/N_{fired} (bottom) as a function of the number of seeds $N_{seed} = N_\gamma \cdot \epsilon_{PDE}$ for MPPC S12571-100P with $N_{total} = 100$ pixels at $U_{over} = (1.66 \pm 0.06)$ V.

low to medium light intensities on the one hand, and because of the clear over-saturation on the other hand. Both impacts have also been observed and discussed for MPPC S12571-50P in the previous section. The number of pixels fired crosses the line of the physical total number of pixels at about $N_{seed} \approx 230$. The ratio between the crossing point, N_{cross}, and the total number of pixels, N_{total}, is comparable for both MPPC S12571-100P ($N_{cross}/N_{total} \approx 2.3$) and -50P ($N_{cross}/N_{total} \approx 2.25$). This might be by accident, because neither of the both 25 μm SiPM responses cross the level of N_{total}.
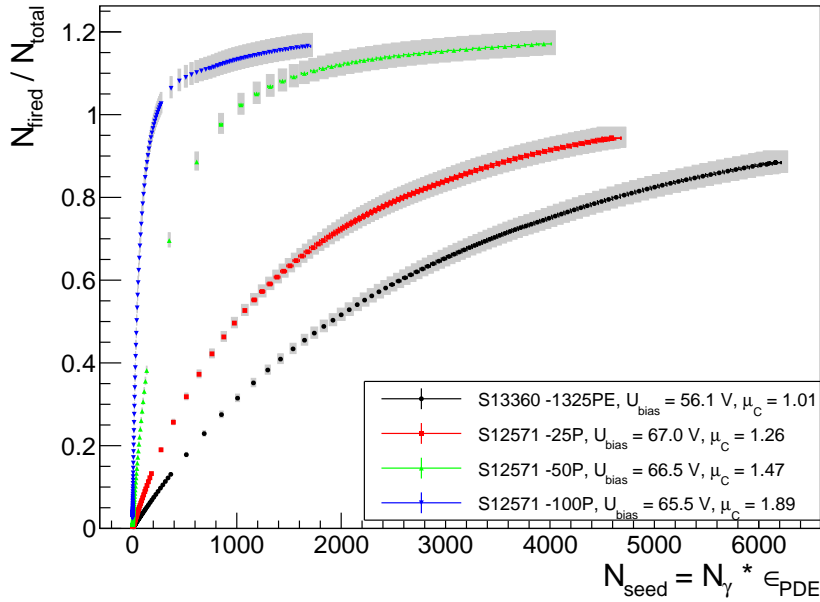
Figure 6.19.: Combined result showing the relative number of pixels fired N_{fired}/N_{total} vs. the number of seeds $N_{seed} = N_\gamma \cdot \epsilon_{PDE}$ for all four SiPMs.

Also in this result, the response at the level of over-saturation does still increase and it is uncertain, if it converges to a maximum or continues. Concerning the applied fits, the simple exponential model is far off the measured data, as it cannot describe crosstalk and struggles to handle a still rising over-saturation. The XT-ext. model has the same issue at handling the rising over-saturation, but is able to reproduce the low light input region $N_{seed} < 200$ much better - but still, as obviously visible in the ratio plot in the bottom of Figure 6.18, the model is not describing the data well. The fact, that the ratio is way lower than 1 in this low light region, indicates that the optical crosstalk parameter, $\epsilon_C = 0.44$, is underestimated in order to match the over-saturation, which this model is not intended to describe.

Also, the advanced model struggles to handle the complete range of N_{seed}. Though it is able to describe the rising over-saturation for around $N_{seed} > 230$, for low to medium number of seeds, it still shows deviations from data of more than 10%. This indicates, that non of the tested models are able to describe such high crosstalk impacts.

To complete the discussion, the advanced function still shows the best χ^2/NDF and recovers the high crosstalk impact better than the XT-ext model, but the crosstalk parameter $\epsilon_C = 0.76$ is still about 15% lower than the expected value. The small $\alpha < 1$ and high $\beta > 0$ parameters again describe the observed over-saturation. It has to be noted, that this SiPM at the applied bias and crosstalk conditions is an extreme case which will not be used in any further measurement.

6.5.5. Combined Results

For a direct comparison, Figure 6.19 shows a combined plot of the four SiPM response measurements. In this case, the relative number of pixels fired, N_{fired}/N_{total}, is plotted as a function of N_{seed}. Due to the definition of $N_{seed} = N_\gamma \cdot \epsilon_{PDE}$, which includes the PDE of each sensor, a
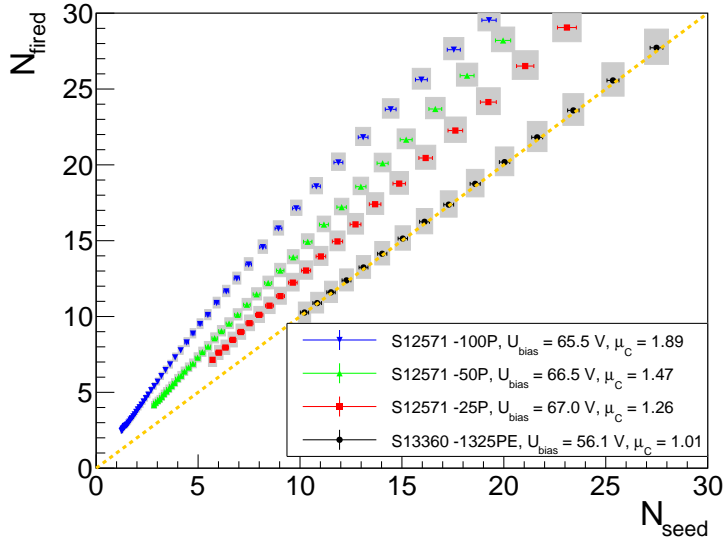
Figure 6.20.: Combined result showing the number of pixels fired N_{fired} vs. the number of seeds $N_{seed} = N_\gamma \cdot \epsilon_{PDE}$ for all four SiPMs for $N_{seed} \leq 30$. (Also similar shown in [112])

direct comparison of the responses is possible. Still, all of the sensors are biased with different over-voltages, U_{over}, which impedes a direct comparison for equal biasing conditions of the SiPM responses.

Nevertheless, more importance was assigned to study the SiPM response at the defined bias conditions as they are applied in the CALICE detector environment.

At the given conditions, MPPC S13360-1325PE with $N_{total} = 2668$ pixels shows the highest dynamic range, since it saturates slower compared to all other SiPMs. In general and under the assumption, that the differences between all four response curves are larger than the different over-voltages might influence, the higher the total number of pixels is, the slower the response saturates.

Figure 6.20 shows N_{fired} of the four SiPMs as a function of N_{seed} in the region $N_{seed} \leq 30$. The yellow dotted line $N_{fired} = 1 \cdot N_{seed}$ corresponds to a response without saturation, nor crosstalk effects. While MPPC S13360-1325PE follows this line within uncertainties, the three SiPMs with non-negligible optical crosstalk parameters lie above this line because of the impact of optical crosstalk. The larger the corresponding μ_C, the higher is the deviation from the yellow line.

6.6. Summary and Outlook

In the last three chapters a detailed description of the SiPM response measurement has been presented. Besides an introduction of SiPM properties, the measurement concept as well as the saturation behavior has been discussed, including different response models. One important characteristic of a SiPM, which affects the response of the sensor, is optical crosstalk. Therefore, a measurement of optical crosstalk has been presented. To verify the linearity of the readout devices and the uniformity of optics, separate measurements have been performed.

To study the SiPM response as a function of incoming photons times PDE, called N_{seed}, the calibration method is enhanced in order to correct for optical crosstalk. This is essential, because the reference measurement is directly calibrated to the response of a SiPM itself in the so called calibration region, where only a small number of photons hit the SiPM and no saturation is expected, but the SiPM signal is still crosstalk affected. Like this, the SiPM response can be studied at any over-voltage as far as the impact of crosstalk is known.

The results of the SiPM response measurement are summarized here.

Each of the sensors show a clear response saturation. Still, their behavior differs a lot: while MPPC S13360-1325PE with 2668 pixels is slowly saturating, SiPMs with lower total number of pixels lead to a faster saturation. This observation is expected and compatible with any underlying response model tested here.

The second mayor observation is that optical crosstalk has a large impact on the response, especially for low to medium light exposures. While MPPC S13360-1325PE has a tiny crosstalk probability of around 1% at the biasing conditions applied here, in particular because of the optical trenches placed between the pixels, MPPC S12571-25P with the same pixel pitch of 25 µm, but without optical trenches, has a non negligible crosstalk probability, which clearly increases the observed number of pixels fired and therefore modifies the response behavior. This modification is non-linear, since optical crosstalk only affects non-fired pixels, while this amount is decreasing for rising light exposures. These combined effects of saturation and optical crosstalk require a response model which handles both effects. As discussed in the results, the crosstalk-extended (XT-ext.) model and the advanced model are both able to reproduce the response of MPPC S12571-25P.

Concerning the response of MPPC S12571-50P and -100P, both of these sensors suffer from even higher optical crosstalk and lower total number of pixels, which increases the deviation of the response curves to the simple exponential response model. Especially for these two SiPMs, over-saturation is observed, which is most likely introduced by delayed photons triggering recovered pixels. The origin of these delayed photons is still open to question, because the light source provides photons within a few picoseconds and therefore primary photons can be neglected in this case. Secondary photons from fast after-pulses or delayed optical crosstalk might be an approach, as discussed in detail in Section 6.5.3.

In any case, the combined effect of optical crosstalk, saturation and over-saturation is best described by the advanced response model which is invented to especially handle all these effects.

As an outlook and in regards to the application of SiPMs in the subsequently discussed CAL-ICE detector prototype, where for instance MPPC S12571-25P is utilized in a combination with a scintillator tile, the influence of delayed photons from the scintillator, which could trigger recovered pixels, might increase. To study the response of the combined SiPM and scintillator system, a new setup is under investigation at the PRISMA detector lab at Mainz, Germany, including an UV laser capable of directly exciting the scintillator. The new setup can easily be integrated into the existing automation software, as the UV laser will provide similar communication tools.

Another difference in this planned setup is the way, photons are guided onto the sensitive area of the SiPM. In the setup presented here, an engineered diffuser is appropriated to uniformly

distribute incoming photons onto the whole surface of the SiPM. In the combined SiPM and scintillator design as used in CALICE, a dimple inside the scintillator is used to collect the light and focus it onto the SiPM. Thus, the intensity profile might not be that uniform anymore.

7

Data and Simulation Processing of the AHCAL Technological Prototype

This Chapter gives an overview of data and simulation handling and of the calibration of the CALICE AHCAL prototype. Raw data, for example recorded in a testbeam environment, has to be processed first in order to allow a further analysis. This processing is called *reconstruction* and is described in Section 7.1. Several *calibration* parameters enter the reconstruction procedure and have to be measured first, as discussed in Section 7.2.

In Section 7.3, the *simulation* of particle interactions is discussed, followed by a discussion of the *digitization* of simulated events in Section 7.4.

Various software tools are collected within a framework called ILCsoft [135], established by the Linear Collider community. It includes tools for the simulation, digitization and reconstruction of testbeam data. The data and simulation are processed with the Linear Collider I/O (LCIO) [136] data model, which is based on an event by event structure. MARLIN [137] is a C++ [111] framework which handles LCIO data and can be configured by XML steering files, which allows easy integration of self-developed modules into the complete framework.

In this study, these frameworks have been used for the simulation, digitization and reconstruction procedures presented next. The results of the ILCsoft tools are further analyzed as discussed in chapters 8 and 9. Therefore both, self-developed software in C++ and ROOT [131] is utilized, as well as adjustments are made to the ILCsoft software, for example if simulation parameters are tuned.

7.1. Data Reconstruction

The data recorded with the AHCAL technological prototype is initially made of analog SiPM signals from single channels. The signals are converted by an Analog to Digital Converter (ADC) to a digitized amplitude in units of ADC counts, similar to the QDC counts in the previous chapter. This value is assigned to a specific channel number, which it belongs to and stored in a raw data format.

After the data has been recorded, the data is reconstructed offline with the purpose to have a final easy readable and calibrated data format, which allows further processing and analysis. To achieve that, the amplitudes in units of ADC counts are converted to units of Minimum Ionizing Particles (MIP), which allows a physics reference of the energy as discussed in Section 7.2.

7.1.1. Data Handling Concept: From Raw to Reconstructed Data

The data reconstruction process within the ILCsoft is shortly presented here. As the digitized amplitude of the signal $A_{ADC}^{initial}$ in units of ADC counts of a SiPM includes a pedestal $A_{ADC}^{pedestal}$ due to the time integration of the ADC converter of a non-zero basis amplitude (for more details about pedestal see Section 5.2.7), this pedestal has to be subtracted from the initial amplitude. Also, as the SPIROC chips feature a low- and high-gain mode to digitize SiPM signals, the intercalibration factor IC between the two modes has to be taken into account as shown in Equation 7.1. If the signal is recorded in low-gain mode, the factor is $IC \approx 10$. Otherwise, if the signal is recorded in high-gain mode, the factor is $IC = 1$.

$$A_{ADC} = (A_{ADC}^{initial} - A_{ADC}^{pedestal}) \cdot IC \tag{7.1}$$

In a next step in Equation 7.2, the number of pixels fired N_{fired} is estimated by dividing the amplitude by the SiPM gain G, which is here also given in units of ADC counts.

$$N_{fired} = A_{ADC}/G \tag{7.2}$$

The response of the SiPM-tile system saturates and is modeled by a response function $f_{response}$, which is inverted to receive de-saturated numbers of seeds, N_{seed}, which corresponds to the number of photons times photon detection efficiency, (cf. Section 4.3.2). This is shown in Equation 7.3.

$$N_{seed} = f_{response}^{-1}(N_{fired}) \tag{7.3}$$

Finally, the conversion to energy in units of MIPs is done in Equation 7.4 by applying the light yield LY, which itself is defined by the measured MIP response, M in $\left[\frac{\text{ADC}}{\text{MIP}}\right]$, divided by the SiPM gain: $LY = M/G$

$$E_{MIP} = N_{seed}/LY \tag{7.4}$$

The light yield, defined like this, corresponds to the most probable number of SiPM pixels fired induced by a minimum ionizing particle, for example a high energy muon, which traverses the scintillator tile to which the SiPM is coupled. More details about the MIP calibration follow in the next section.

In a final step a MIP-cut is applied, which rejects all reconstructed energies below 0.5 MIP in order to prevent noisy channels and to reduce the amount of stored data.

Note, that as long as the response model is not optimized, the third step, where the inverted response function is applied, is skipped and N_{fired} is processed further in place of N_{seed} in the conversion to MIPs. Of course then, the reconstructed energies might be saturated.

So far, the energy reconstruction has been described, which is the most important part of the reconstruction procedure for this analysis. Besides, the reconstruction also applies the time calibration to convert the initial digital time in units of TDC ticks, digitized by the SPIROC chip, to a unit of nano seconds. As this feature has not been implemented completely by the time of this analysis, time of hits are not further taken into account.
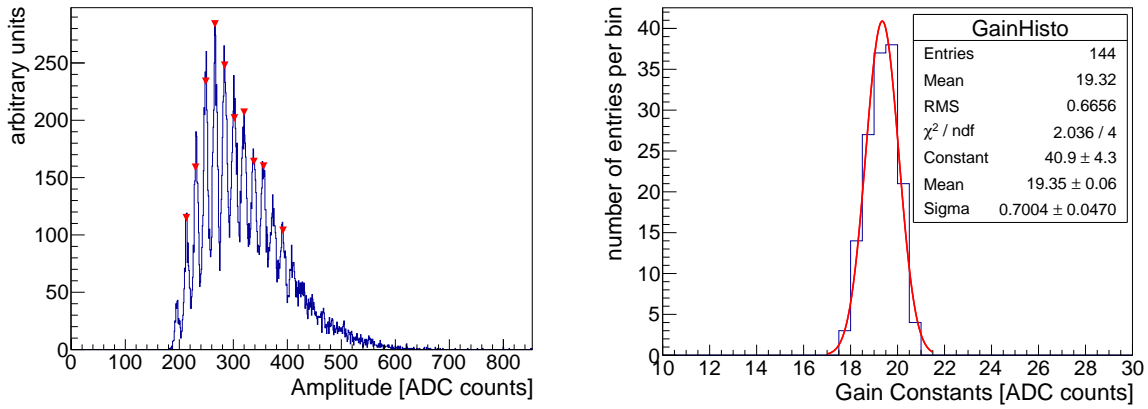
Figure 7.1.: Left: Typical ADC spectrum of a SiPM on the Mainz HBU in layer 3 during LED-measurement. Right: Histogram of gain values of all 144 channels of the Mainz HBU.

7.2. Calibration

For the calibration of the detector, dedicated measurements have been performed within the CALICE collaboration and this theses utilizes the constants calculated by [138, 139]. Nevertheless, the concept of the calculation shall be summarized in this section, showing the calibration steps required for the reconstruction of data as presented above. First, the pedestal and SiPM gain calibration and the high- and low-gain intercalibration are described, followed by the channel MIP calibration and the detection of inactive channels.

7.2.1. SiPM Gain and Pedestal

The measurement concept of the SiPM gain and of the pedestal has already been discussed in detail in Section 4.2.1 in the context of the SiPM characterization and response measurement. The calibration of the SiPM gain and pedestal works very similar in the application of the AHCAL technological prototype. In both cases, the SiPM signal is integrated over a certain amount of time, called the integration window, and digitized. For this purpose, all channels on the HBUs house a small LED, which supply the SiPMs with a pulsed light source in a dedicated LED measurement.

Due to a non-zero basis amplitude, the integrated amplitude is always larger than zero, which defines the pedestal (cf. Section 5.2.7). As discussed before, the integrated spectrum of a SiPM signal features single peaks as shown in the left of Figure 7.1, each representative for a specific number of pixels fired. The lowest peak to the left in this ADC spectrum corresponds to the pedestal, while the subsequent peaks correspond to 1, 2, 3, etc. pixels fired. This ADC spectrum belongs to a channel on layer 3 of the prototype, which is equipped with SMD SiPMs. Small red triangles indicate peaks which have been found by a peak finder algorithm supplied within the ROOT framework. [131] These positions are used as starting parameters for a multi-Gaussian function [1] which is fitted to this distribution and the gain value G is extracted from the mean difference of two consecutive peaks.

---

[1] The multi-Gaussian function is essentially a sum of Gaussian functions with the peak distance as a fit parameter.

On the right of Figure 7.1, a histogram of gain values of all 144 channels of layer 3 is shown. It shows a very narrow peak, which results in σ/mean $< 4\,\%$ for an applied Gaussian fit, which indicates a homogeneous behavior all over the layer.

The pedestal $A_{pedestal}$ is extracted from measurements with muons, while only those channels are considered, where the amplitude does not exceed a certain threshold of the SPIROC and thus do not correspond to the actual muon. Like this, only events with low amplitude are taken into account and the pedestal is extracted from the mean of the distribution which is estimated within a range of 3 RMS around the initial mean in order to minimize the impact of SiPM noise. A small side note: in contrast to all other calibration parameters introduced here, the pedestal is first estimated for all single memory cells (cf. Section 3.2.1) of each channel individually and thereafter averaged to one final parameter per channel, while the other parameters are directly estimated from the combined overlay of all memory cells.

7.2.2. High-gain and Low-gain Intercalibration

The SPIROC chip features a dual-range ADC to increase the dynamic range of the readout, similar to the QDC, which has been utilized before in Section 6.1.3 in the SiPM response measurement. The high-gain (HG) mode is used for small signals, while the low-gain (LG) mode is used for higher signals exceeding a certain threshold. The ratio between both gains should be 10:1, thus the intercalibration constant is expected to be $IC = 1$ in the high-gain and $IC = 10$ in the low-gain mode to accomplish the different gains and make both amplitudes comparable. Nevertheless, variations of capacities inside the SPIROC amplifiers require a separate measurement of the intercalibration factor channel by channel.

The HG/LG intercalibration is performed by storing LED data for both modes in parallel in the SPIROC, instead of storing only one of both modes and the time of the hit, which is dropped in that specific case.

A scatter plot of the two amplitudes allows to measure the actual intercalibration constant in the region of overlap, as similarly done in Section 6.1.3. Unfortunately, not enough intercalibration data has been recorded at the testbeam campaign in 2015, which has required to use constants of another testbeam measurement. This has only been possible for layers under similar conditions. For other layers, another method utilizing electron data has been applied as described in [139] and developed by [140]. In short, the method takes into account the ADC distributions of both, HG and LG entries. A wrong IC factor leads to an overlap or gap between both distributions. Two error functions are fitted to both edges of the distributions which allows the extraction of the ratio between the high-gain and low-gain factor.

7.2.3. MIP Calibration

The energy deposits in the prototype are calibrated to units of MIPs as already mentioned. Muon beams at $50\,\text{GeV}$ are used for this purpose, as they act as minimum ionizing particles. The energy, a muon deposits in one channel of the detector, can therefore be used as a reference for measurements with other particle beams.

As later described in more detail in Section 8.3.1, the muon beam used for this calibration is not completely pure and requires event selections to reject unwanted contamination. Besides
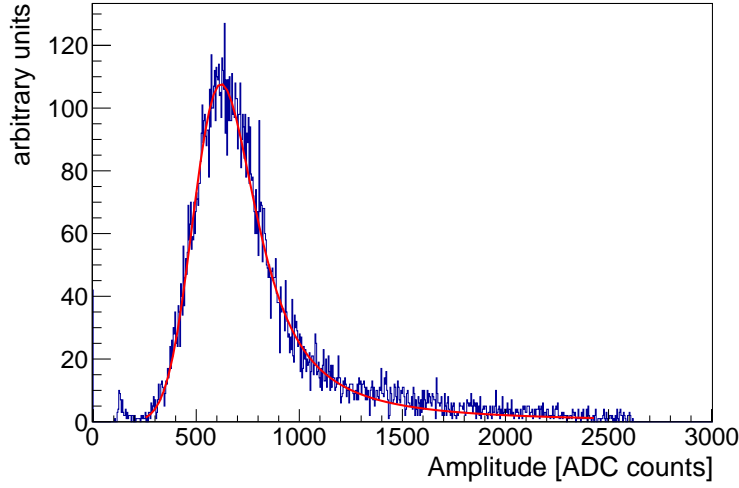
Figure 7.2.: Muon ADC spectrum of a single channel of layer 3 with applied event selections and fitted with a convoluted Landau Gaussian function.

the rejection of other particles, the muon has to be perpendicular traversing the tiles, as the distance traveled in a tile, which depends on the angle, is related to the number of generated photons and therefore related to the deposited energy. Therefore, a MIP track finder algorithm is utilized similar to [141]. In short, this algorithm counts all hits in the X-Y plane (transversal to the beam direction) without taking care of the layer (Z-axis) position. If the number of entries in a specific bin is larger than a certain threshold (for instance 6 hits), it is assumed as a track.

Though the actual MIP calibration of the prototype has been performed independent of this study [138], the procedure is shorty illustrated by means of a single exemplary channel of layer 3. The ADC spectrum of the single channel is shown in Figure 7.2 for muon data. Event selections and a track finder have been applied. A convoluted Landau Gaussian function is fitted to the data. The most probable value (MPV) is then subtracted by the pedestal, which results in the MIP constant M of this channel: $M = A_{MPV} - A_{pedestal}$.

7.2.4. Inactive Channels

A few channels in the prototype are either noisy, inactive or have not been able to be calibrated. In any case, these channels are marked as inactive and rejected in the data reconstruction procedure. Maps of layers with active and inactive channels are shown in Appendix Section H. Unfortunately, layer 6 and layer 10 have such a high number of inactive channels (approx 70 %), that they are completely rejected from the analysis.

7.3. Simulation

Simulations serve as a powerful tool in several applications, as they provide theoretical predictions and help to validate and interpret experimental results. Also, for example, a coincident simulation of a detector can be used to analyze implications arising from variations of detector

parameters, which allows to optimize the detector concerning performance and cost, without the need to actually build all variations first. Due to the advancements of computing power and memory technology in the recent years, simulations have become vital for high energy physics, as physical processes can be simulated with increasing detail and quantity. [142]

In particle physics, Geant4 [143] is a commonly used tool for the simulation of particle interactions. The CALICE technological prototype is simulated with Geant4 v10.1 along with the MOKKA [144] framework, which provides detailed detector geometry implementations and has been used for several CALICE AHCAL prototypes in the past (e.g. [38, 145, 146]). More details about the testbeam detector geometry, utilized in this study within MOKKA, are discussed in the next chapter in Section 8.1.4.1.

After a simulation with Geant4 has been performed, a digitization of the simulated events is required for several reasons, as discussed below in Section 7.4, for instance to allocate simulated hits in active volumes to related channels and to convert the energy deposits into a format which is required for the further reconstruction.

In this study, the main reason to use simulations is to define event selections for experimental data and to study different SiPM-tile response models by comparing modified simulations to data. Also, simulations are used to check the consistency to data and become aware of possible unforeseen discrepancies, as for example unexpected background in data (see Section 8.5).

The following subsections give an overview of the simulation of electromagnetic and hadronic particle showers in Geant4, while the structure of the overview is inspired by [38].

7.3.1. Simulation of Electromagnetic Showers

Because of the rather simple interactions between electrons, positrons and photons with matter (cf. Section 1.2), electromagnetic showers are assumed to be well understood. In Geant4, the electromagnetic interactions are simulated using the EM package, which has been validated in comparison to different calorimeter observables and reaches a precision within approximately 1 %. [147, 148] A detailed description of the utilized models is given in the Geant4 Physics Reference Manual [149].

7.3.2. Simulation of Hadronic Showers

In contrast to electromagnetic showers, hadronic showers are more complex as they involve the strong force and the projectile hadron is a composite particle, as well as the target nuclei is composed. Thus, the phase space of the final state of hadronic interactions can be large, as many particles are involved and inelastic strong interactions might lead to excitation of the nucleon for example (cf. Section 1.2.5). Because of this high complexity, different models that include parametrizations and approximations are used to simulate hadronic interactions. [149] These parametrizations are estimated from actual experimental measurements. In the context of a highly granular hadron calorimeter, the CALICE collaboration has contributed to the validation of several hadronic models within Geant4. [146]

With increasing particle momentum, the de Broglie wavelength $\lambda_B = h/p$ decreases, which generally defines the scale of hadronic shower interactions. As a consequence, smaller structures inside a nucleus have to be considered in the simulation, as they gain relevance for the interac-
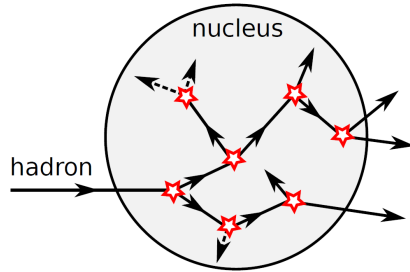
Figure 7.3.: Schematic of a cascade process of a hadronic projectile interacting with a target
nucleus, as it is modeled in Geant4. The projectile and the secondaries are tracked and interact
with nucleons inside the nucleus, potentially generating more secondaries. This process ends once
all secondaries leave the nucleus or are absorbed inside, when their energy drops below a certain
threshold. [40]

tion. Therefore, often different physics models are utilized to simulate hadronic interactions at
different energy scales. Like this, the simulation of hadronic interactions is split in a sequence
of reactions, which may begin with collisions inside a nucleus with a high energy hadron, fol-
lowed by the propagation of secondary particles within the nucleus and the de-excitation of the
nucleus, until it reaches its ground state. [142] An overview of the most relevant models for this
study is given in the following.

Intra-Nuclear Cascade Models

Following the de Broglie relation above, hadronic interactions can be described as a series of
interactions with nucleons within a nucleus, as long as the energy of the incident hadron is
within approximately $200\,\text{MeV} < E < 3\,\text{GeV}$ [150]. Within this energy range, the interactions
are mainly independent of the substructure of the nucleons. Such a series is is referred to an
intra-nuclear cascade as sketched in Figure 7.3.

Bertini Cascade
In the Bertini cascade [151] model, the nucleons are expected to have Fermi gas momentum
distributions inside the nucleus, which is modeled as a spherical shell with constant nucleon
density and all energy levels filled until the Fermi energy. As Pauli's exclusion principle prohibits
products of the interaction to enter occupied states, only secondary nucleons with an energy
larger the Fermi energy, $E_N > E_F$, are accepted. The model computes the type of the reactions,
the reaction products and the resulting four-momenta. Path lengths of nucleons and angels after
collisions are estimated from local densities and differential cross-sections based on experimental
data. After the calculation of the intra-nuclear cascade, the Bertini model also applies a pre-
equilibrium model for exited nuclei, as well as de-excitation models, taking into account Fermi
break-up, explosion, fission and evaporation.
The model has been extended to model hadron projectile interactions up to $20\,\text{GeV}$, while in
most cases, it is used until $10\,\text{GeV}$. [150]

Figure 7.4.: Schematic of a string model as implemented in Geant4. Left: A gluon string is formed between two quarks, one of the primary hadron and one from the nucleon. Right: Hadronization by string fragmentation due to the generation of quark-antiquark pairs. [40]

String Parton Cascade Model

For the simulation of inelastic interactions of high energy hadrons with nuclei, string parton models [152] are utilized in Geant4, which take into account quark substructures. The interaction between the initial particle and the nucleus is modeled by at least one or several excited strings and an excited nucleus. The two endpoints of a string are made by two quarks, one within the primary and another in the nucleon (see Figure 7.4, left). In the quark-gluon string model (QGS), the longitudinal strings transfer energy and momentum, while transverse strings are used for color exchange. [149] The generation of quark-antiquark pairs is modeled by a longitudinal string fragmentation model, as demonstrated on the right of Figure 7.4. The secondary particles and their interaction inside the excited nucleus are calculated by a cascade model (see above). Again, the de-excitation of the excited nucleus is modeled afterwards, utilizing default Geant4 models for nuclear fragmentation and de-excitation.

7.3.3. Physics List

In Geant4, various models for the simulation of hadron showers exist for specific energy ranges. A composition of such physics models builds a physics list, while each model is applied in the specific energy range for which is is best suited. [153] An overlap region between different models within one list is arranged by randomly selecting one of the eligible models. As the physics list QGSP_BERT_HP is assumed to be well tuned and suitable to simulate hadronic showers [154], it is utilized in this study of hadronic showers with Geant4. The physics list merges the following models:

- For energies below 9.9 GeV, the *Bertini* (BERT) cascade model is used.

- The *Quark-Gluon-String* model, QGSP, is used for energies exceeding 12 GeV.

- The gap between the two models is filled with the *Low Energy Parameterized* model, LEP, in the energy range between 9.5 and 25 GeV, generating some overlap. [154]

- The *High Precision Neutron Package* model, HP, is used to simulate neutrons below 20 MeV with higher precision [155].

7.4. Digitization

After a simulation has been performed, the generated hits have to be digitized in order to obtain a data format, which is directly comparable to measured data before reconstruction.

Simulated hits in Geant4 are located in active volumes and expressed in units of GeV. The active volumes for example represent a complete layer of the detector prototype. On the other hand, the real detector layer consists of several channels, composed of a SiPM and a scintillator tile, each. Therefore, geometrical allocations of hits in active volumes in the simulation to respective channels in the detector are performed in the digitization. While in the simulation, energy deposits in active volumes are stored in units of GeV, measured data signals are stored in units of ADC counts, which requires a conversion in the digitization.

Afterwards, both, data and simulation can be reconstructed using the same procedures. The conversion of energies from GeV to ADC counts is one major part of the digitization procedure, requiring a response model of the SiPM-tile system. Also other effects are taken into account in the digitization, as the simulation of optical tile-to-tile crosstalk for channels without reflective foil and the addition of noise.

7.4.1. Optical Tile-to-Tile Crosstalk

Several HBU layers feature tiles without individually wrapped reflective foil, but with edges that are chemically etched (cf. Figure 3.3a), which allows light to cross from one channel to a neighboring channel, called *optical tile-to-tile crosstalk*. Channels with wrapped reflective foil are assumed to have negligible crosstalk.

Instead of correcting this crosstalk effect within the reconstruction, it is added to the simulation during digitization. Like this, the MIP-calibration of the single channels is maintained, as within the MIP calibration, this effect is already included. A correction of the tile-to-tile crosstalk within the reconstruction would require an adjustment of the MIP calibration of these channels, which is not wanted.

The digitization of tile-to-tile crosstalk is done only taking into account the directly neighboring channels in the horizontal and vertical lane. A fraction of the deposited energy in the initial channel is then added to the energy of the (up to) four neighboring channels. In the past, this fraction has been measured to be within 2.5 to 4.5 % per neighboring channel [38, 156, 157], which sums up to a total value of 10 to 18 % tile-to-tile crosstalk. The tile-to-tile crosstalk value will later be tuned in Section 8.6.2.

7.4.2. Energy Conversion and SiPM-Tile Response

One of the main features of the digitization is the conversion from GeV to ADC counts. Therefore, beforehand measured calibration constants are applied.

In a first step, simulated energy depositions are converted from GeV to the MIP scale. For that purpose, a dedicated simulation of a muon traversing a tile is used from which the most probable value of 470 keV is estimated, similar to the procedure discussed in Section 7.2.3 by fitting a Landau-Gaussian function to the energy distribution. [76]

In the second step, a threshold of 0.5 MIP is applied to simulate the threshold of the SPIROC. At this point, the upper declared tile-to-tile crosstalk is simulated.

Thereafter, the SiPM-tile-system characteristic is simulated. First of all, the number of seeds, N_{seed} (cf. Equation 4.14), is estimated by multiplying the simulated energy E_{MIP}^{MC}, in units of MIP, with the measured light yield constant, LY, in units of MIP^{-1}, of the channel as shown in Equation 7.5.

$$N_{seed} = E_{MIP}^{MC} \cdot LY \tag{7.5}$$

Then, the SiPM-tile response model is applied to, in first order, model SiPM saturation. As introduced previously in Section 4.3.3 and as analyzed later in Section 9.2, the response is also affected by other effects, as SiPM crosstalk and the recovery of pixels. After applying a response model function $f_{response}$, the number of pixels fired, N_{fired}^{*}, is estimated as shown in Equation 7.6. The default response model is the simple exponential model as introduced in Section 4.3.3.1.

$$N_{fired}^{*} = f_{response}\left(N_{seed}\right) \tag{7.6}$$

Thereafter, the number of pixels fired is smeared by applying binomial smearing as shown in Equation 7.7, to take into account the statistical effects of the SiPM-tile system. This method has been validated in [38, 158].

$$N_{fired} = f_{smear}(N_{fired}^{*}, N_{total}) \tag{7.7}$$

In a final step in Equation 7.8, the number of pixels fired is converted to the amplitude A_{ADC} in units of ADC counts by multiplying the measured gain constant, G in units of ADC counts, of the channel.

$$A_{ADC} = N_{fired} \cdot G \tag{7.8}$$

7.4.3. Noise

As described before, several thresholds and rejections are included in the digitization and reconstruction procedures to reject noise. Like this, channels with pure noise can be discarded easily. Still, noise can play a role if, a real signal from an energy deposition of a particle is overlayed with noise. This can have two outcomes: either, the amplitude from the deposited energy is already higher than the threshold, then only the amplitude is increased by noise, or, in case the amplitude is smaller than the threshold, then a new hit with amplitude over threshold can be generated.

Noise is extracted from muon runs by rejecting the muon track itself and taking the remaining channels into account. These noise hits are stored in a separate file, provided by [159], which is repetitive overlayed over the simulation. On average, one noise hit is around 2 MIP [76].

Summary

This chapter has described the processing of data and simulation of the AHCAL technological prototype. Data and simulation have to be reconstructed in order to receive a data format which can easily processed further by offline data analysis. This includes the conversion of initial amplitudes in units of ADC counts to energies in units of MIPs with physical meaning. The channel-wise calibration is necessary for both, the reconstruction as well as the digitization

procedures. The SiPM gain, pedestal and the high-gain and low-gain intercalibration have been discussed, as well as the MIP calibration.

Thereafter, the simulation of electromagnetic and hadronic particle showers in Geant4 and within the MOKKA Framework has been discussed.

In the last section, the digitization procedure has been presented. The digitization is required, to convert the data format of the simulation to the data format of raw testbeam data. Within the digitization, noise and tile-to-tile crosstalk are simulated, as well as the conversion of the simulated energy in GeV to units of ADC counts is performed by taking into account a SiPM-tile response model. After digitization, data and simulation are comparable to each other.

<div style="text-align: right; font-size: 3em; color: gray;">**8**</div>

CALICE AHCAL Technological Prototype at CERN SPS in 2015

The CALICE AHCAL technological prototype has been operated in a testbeam campaign at the Super Proton Synchrotron (SPS) facility at CERN in July and August 2015. In this thesis, the experimental data taken in July are utilized.

This and the next chapter focus on the analysis of this data and on simulations, performed in order to reproduce the recorded data. With a comparison of simulation and data, the response models for the combined SiPM-scintillator tile system are evaluated and followed by a study on the linearity and energy resolution of the prototype.

The first section in this chapter depicts the setup of the prototype in the testbeam environment. This includes details about the installation of the prototype and a description of the beamline. Furthermore, it includes information about the implementation of the simulation setup.

Thereafter, the event selection procedure is discussed in Section 8.3, which includes studies about the implications of these selections. A comparison between data and simulation follows in Section 8.4.

Due to an unexpected low-energy background in electron data, additional event selections are added in Section 8.5.

Finally, some parameters of the simulation are tuned in Section 8.6, followed by a second comparison between data and simulation after optimization.

8.1. Testbeam Setup

In 2015, the CALICE collaboration performed several testbeam campaigns with the AHCAL technological prototype. Intensive preparations were done beforehand. Back in 2014, first tests were done in two testbeams at the Proton Synchrotron (PS) at CERN, followed by three testbeams at DESY in the first half of 2015 and long term stability tests without beam. Finally, the technological prototype has been shipped to CERN for two testbeam runs at the SPS in July and August 2015. In July, the steel absorber structure, as planned for the ILC detector barrel, has been used, whereas the tungsten absorber structure, as used before in the physics prototype, has been utilized in August. The testbeam setup of July 2015 is described in the following.

Layer	Slot	WLS-Fiber	Individually Wrapped Tile	Type of Readout	Number of Channels	Sensitive Area [cm^2]
1	1	-	-	SMD	144	18×18
2	2	-	-	Side	144	18×18
3	3	-	yes	SMD	144	36×36
4	4	-	-	Side	144	36×36
5	5	-	-	Side	144	36×36
6	6	yes	-	Side	144	36×36
7	7	yes	-	Side	144	36×36
8	8	yes	-	Side	144	36×36
9	9	yes	-	Side	144	36×36
10	10	yes	-	Side	144	36×36
11	11	-	yes	Side	576	72×72
12	13	-	yes	Side	576	72×72
13	21	-	yes	Side	576	72×72
14	31	-	yes	Side	576	72×72

Table 8.1.: Basic configuration of the setup of the AHCAL technological prototype at CERN SPS in 2015. The layer numbers and the slot numbers of the AHCAL absorber stack, into which the layers are inserted, are listed besides the number of channels and the sensitive area of the layers. Information about the layer-wise channel conditions are also listed, including the utilization of wavelength shifting (WLS) fibers, of individually wrapped tiles with reflective foil and the type of readout. [76, 89]

8.1.1. CALICE AHCAL Technological Prototype in 2015

The AHCAL technological prototype tested in July 2015, uses the EUDET steel absorber stack [160]. Each absorber plate, with a thickness of 1.7 cm, corresponds to about 1 radiation length and roughly 0.1 nuclear interaction length. The complete stack is placed on a movable stage, allowing for relative alignment to the particle beam to ensure that every channel of the detector can be calibrated with muon beam. The stack is equipped with 14 active modules, while 34 of the total 48 slots remain empty. The configuration of the prototype is listed in Table 8.1 and is as follows:

In the first two slots, two ECAL Base Units (EBUs, cf. Section 3.2) with horizontally oriented scintillator strips are installed. The first EBU features surface mounted (SMD) SiPMs with 10000 pixels, the second SiPMs with pins with 1600 pixels. The EBUs are built of four ASICs, each controlling 36 stripes with a size of $45 \times 5 \text{mm}^2$, covering a total active area of $180 \times 180 \text{mm}^2$. Single HCAL Base Units (HBUs) are placed in slots 3 to 10. All of them consist of four ASICS, including in total 12×12 square channels with a size of $30 \times 30 \text{mm}^2$ each (cf. Section 3.2). Like this, they provide an active area of $360 \times 360 \text{ mm}^2$. The HBUs have different configurations concerning scintillator tiles and readout SiPMs.

The first HBU in layer 3 is equipped with individually wrapped tiles (cf. Figure 3.3b), reducing optical tile-to-tile crosstalk to a negligible level. Also, it features the same SMD SiPMs (HAMAMATSU S12571 -25P) with 1600 pixels as discussed in Chapter 6. The next two layers 4 to 5 are equipped with 12000 pixel SiPMs and tiles without individual wrapping. In layers 6 to 10, HBUs with 800 pixel SiPMs and tiles with wavelength shifting (WLS) fibers and without

individual wrapping are used (cf. Figure 3.3a).

The last four modules consist of 2×2 HBUs, called big layers, to cover a larger area of $720 \times 720 \, \text{mm}^2$ with the aim to study broad pion showers in a certain depth. On all of them, individually wrapped tiles are utilized, while layers 11 and 12 house SiPMs with 2300 pixels and layers 13 and 14 house SiPMs with 1300 pixels. Very important is the placement of these last four layers. In order to be able to display the development of deep showers, they are placed into slots 11, 13, 21 and 31.

To summarize, the detector consists of 14 active layers with a total of 3744 channels, each read out with a single SiPM. Unfortunately it is important to note, that the two EBUs in layers 1 and 2 and two HBUs in layers 6 and 10 are not accessible in this analysis, because of issues which occurred during data taking in case of the EBUs and because of a large fraction of inactive channels in case of the two HBUs. Therefore, only 10 active layers remain.

Additional information about the utilized SiPMs are listed in Table 8.2.

For a picture of the absorber stack of the AHCAL technological prototype of July 2015 please refer to the previous Figure 3.5.

Layer	SiPM Manufacturer	SiPM Model	N_{total}	Pixel Pitch [μm]	Sensitive Area [mm²]
1	Hamamatsu	S12571-010P	10000	10	1×1
2	Hamamatsu	S10362-11-025O	1600	25	1×1
3	Hamamatsu	S12571-25P	1600	25	1×1
4-5	Ketek	-	12000	18	2.25×2.25
6-10	CPTA	CPTA	800	40	1.28×1.28
11-12	Ketek	PM1125NS-SB0	2300	25	1.2×1.2
13-14	SensL	MicroFB-10020-SMT	1300	20	1×1

Table 8.2.: Layer-wise SiPM properties including the physical total number of pixels, N_{total}, the pitch between pixels and the sensitive area of the SiPMs. Values taken from [76, 101, 161].

8.1.2. Beamline

The particle production for the H2 experiment zone is realized by the conversion of a primary proton beam of up to 400 GeV, provided from the SPS, to secondary and partially tertiary particle beams after collisions with dedicated targets. [87] Secondary beams consist of different particle types, like electrons and a variety of hadrons with various energies.

The extraction of wanted particle beams is described in [162] and shortly summarized here:

The production of pion beams is accomplished after a first rejection of the electron component of the mixed beam, by placing a thin lead absorber of 3 to 10 mm thickness inside the beamline. While this absorber is nearly transparent to hadrons, electrons loose a high fraction of their energy due to Bremsstrahlung and are not further transported. Pions are then selected with a set of dipole magnets and collimators, which allow a momentum selection.

Electron beams are produced by shooting a neutral photon beam onto a converter, which is a few millimeters thin lead plate. Due to gamma conversion, photons convert to electron and positron pairs. Only electrons are transported further, while positrons are guided apart due to dipole magnets and dumped. After the momentum selection, a very pure electron beam

remains.

The generation of muon beams requires first the production of a high-intensity pion beam. By stopping the beam with a beam dump or with a collimator, mainly muons remain. If the closed collimator is upstream of the last momentum selection with a group of dipoles, muons are also momentum selected.

Hadron beam energies within an momentum range of 10 to 360 GeV can be generated. [163] During the testbeam campaign in July 2015, pion beams between 10 and 90 GeV, electron beams between 10 and 50 GeV and muon beams of 50 and 150 GeV have been utilized. More information can be found in Section 8.1.3. The maximum momentum resolution of the beamline is $\Delta p/p = \pm 2\,\%$.

As an anticipation it should be noticed, that because of a poor steering, the electron beam touched some upstream material. [164, 165] Thus, a low-energy electron background is present in electron data, which requires additional offline data processing. More details follow later in Section 8.5.

The beamline is equipped with various tools to inspect particle beams, such as scintillators to count particles and wire chambers to estimate beam positions. Unfortunately, the wire chambers have not been compatible to the recording of the AHCAL prototype and thus cannot be used, which complicates the simulation of particle showers.

Directly in the front and in the back of the prototype, scintillator plates are placed, in order to use their signals as validation trigger signals. Two scintillator plates of $10 \times 10\,\text{cm}^2$ are both placed upstream, while two larger scintillator plates of $50 \times 50\,\text{cm}^2$ are placed one up- and the other downstream. The scintillator plates in front of the detector, which are covered in black tape, can be seen in the picture on the right of previous Figure 3.5. They are read out by photomultiplier tubes. The smaller plates are utilized for electron and pion beams, which aim at the center of the detector, while the larger plates are used for muon beams. As the detector is moved via the movable stage to allow a full calibration of the detector with muon beams, as mentioned above, these scintillator plates have to be larger to cover the complete area of interest. In case of coincidence between the two respective scintillator plates, the signal is directly transferred to specific channels of the detector. These channels are located at the edges of the big layers, where no significant signal from the particle shower is expected. Therefore, the trigger information has to be applied offline after data taking. This validation signal is labeled T_0-signal in the following, as it defines a time reference to when the particle traverses the scintillator plates.

A Cherenkov detector is included in the beamline around 90 m upstream of the detector. It is used to tag incoming particles and helps to reject unwanted beam contamination, for instance left over electrons in pion beams. Particles that traverse an optical medium emit light in case their relativistic velocity is larger compared to the speed of light in this medium, which is connected to its refractive index. The light is emitted in a cone with a characteristic angle proportional to the mass of the particle. [166] The detection of the emitted light in a specific angle therefore allows conclusions to the particle type. The signal of the Cherenkov detector is again directly fed into specific channels of the detector, similar to the validation trigger signals.

8.1.3. Dataset

During the testbeam campaingn at CERN SPS in July 2015, three different particle types were measured: muons, electrons and pions. For each particle, different beam energies were investigated. For each energy, different runs containing a number of measured events were taken. In this analysis, only preselected runs are taken into account in order to secure a high quality of the data. For example, the preselection covers tests about working external validation triggers and energy thresholds. In some cases, the particle beam during measurement has not been stable enough, which leads to a rejection of these runs.

Muon runs were taken in order to calibrate the detector to a MIP-scale. Electron runs were taken to analyze the performance of the detector to electromagnetic particles and, particularly in this analysis, to tune SiPM-tile response models. Pion runs were taken to examine the hadronic response of the detector. Table 8.3 lists the dataset used in this analysis, including particle type, beam energy and the number of reconstructed events.

Particle	Beam Energy [GeV]	#Reconstructed Events
μ^-	50	9 378 956
e^-	10	30 033 970
	15	10 397 770
	20	10 893 030
	30	4 315 385
	40	5 983 798
	50	5 600 677
π^-	10	18 023 150
	30	5 615 437
	50	7 284 255
	70	9 368 770
	90	4 369 228

Table 8.3.: Dataset of testbeam events used in this analysis, including particle type, beam energy and the number of reconstructed events.

8.1.4. Simulation Setup

8.1.4.1. Testbeam Geometry

The detector geometry of the AHCAL technological prototype is provided by the MOKKA framework, which is based on Geant4 and provides detailed descriptions of materials and geometry as introduced in Section 7.3. A picture of a visualization of the detector simulation is shown in Figure 8.1. With the exception of trigger scintillators and a Cherenkov detector, no beamline instrumentation is modeled. The Cherenkov detector, which is modeled as a helium volume, is 11 m long and centered 90 m upstream to the detector shown here. The steel absorber stack is not completely filled with active layers, as only a small number of layers is utilized in this prototype. The different sizes and positions of the active layers are visible, corresponding to two EBUs, eight HBUs and four 2×2 HBUs.

Active layers are surrounded by steel cassettes and consist of a PCB and cable mixture and
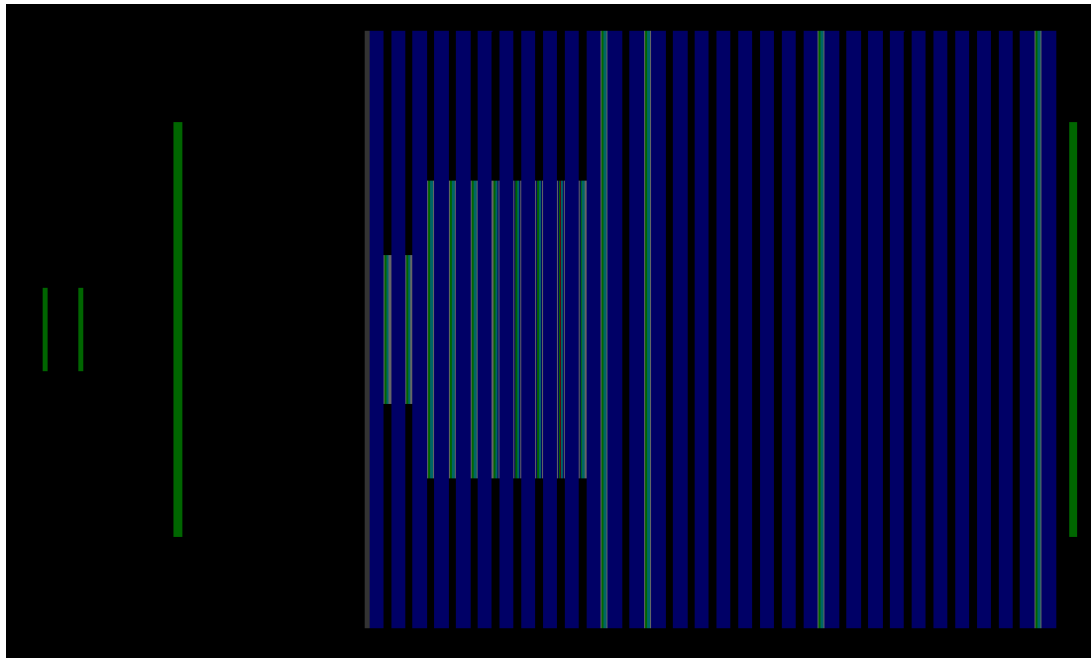
Figure 8.1.: Picture of the geometry of the simulated AHCAL technological prototype in July 2015 from bird's-eye view, including trigger scintillators (green), steel absorber plates (blue), active layers (mainly light blue and green) and empty slots with air (black). An additional iron absorber plate (grey) is also visible in front of the first steel absorber plate.

two small layers of reflective foil with the scintillator tile inside. Between the steel cassette and the steel absorber, a small layer of air remains. As discussed before, many slots remain empty and are filled with air.

Directly in front of the first absorber plate, an additional tunable iron layer is placed in order to account for unknown upstream material. Before further tuning of the additional absorber width, a default width of 12 mm has been selected in a rough optimization study, matching the center of gravity of electron showers between data and simulation [167].

8.1.4.2. Beam Profiles

After a detector model has been implemented in the simulation, the particle itself has to be generated. Particles are generated by a particle gun, which includes primarily parameters like its energy, starting position and direction. The energy and the starting position in x and y of a particle are presumed as Gaussian distributions, with the expected value μ and the variance σ. This accounts for the width of the beam and some inaccuracy (assumed to be approx. $\pm 2\%$ following [87]).

With the Cherenkov volume centered at $z = -90\,\mathrm{m}$ upstream to the detector, the particle gun is placed at $z = -100\,\mathrm{m}$. The detector itself starts at $z = 0\,\mathrm{m}$.

A direct measurement of the beam profile with beamline instruments, like wired chambers, would have been the easiest way to define the particle gun parameters in simulation, but since these instruments have not been combined with the detector readout and no external information about the profiles are accessible, another method is applied:

Particle	Energy [GeV]	σ_E [GeV]	μ_x [mm]	μ_y [mm]	σ_x [mm]	σ_y [mm]
μ^-	50	1.0	0.0	0.0	200.0	200.0
e^-	10	0.2	4.85	9.2	10.0	0.1
e^-	15	0.3	3.0	6.0	24.0	5.0
e^-	20	0.4	-2.0	2.0	23.0	19.0
e^-	30	0.6	-3.6	21.0	20.4	13.5
e^-	40	0.8	-0.5	1.0	15.0	30.0
e^-	50	1.0	-40.0	-11.0	29.0	20.0
π^-	10	0.2	-0.3	18.0	23.0	20.5
π^-	30	0.6	1.7	-2.0	25.0	22.5
π^-	50	1.0	2.0	1.4	19.0	15.0
π^-	70	1.4	11.25	-6.7	29.5	29.5
π^-	90	1.8	2.0	-4.8	25.0	17.5

Table 8.4.: Particle gun settings optimized to match the beam profile of recorded data.

The position parameters in x and y are iteratively adjusted to match the associated transverse center of gravity distributions of simulation and data. The parameter set of the first iteration is directly chosen from the mean and RMS of the distribution for data. The 100 meters between the starting position and the detector lead to an additional broadening of the beam because of scatterings in the air and in the Cherenkov volume. Another issue are inactive and noisy channels of the detector, which bias the mean and RMS of the center of gravity distributions. Therefore, the gun parameters have to be iteratively adapted to take these effects into account. This method is applied to electron and pion runs. Only for muon runs, where the beam profile is not expected to have an impact on the MIP-response of single channels, the parameters have been exceptionally customized to a broad beam in the center, $\mu_x = \mu_y = 0$ mm, and a variance of 200 mm. Like this, a large fraction of the detector is covered by the muon beam.

The final particle gun settings are listed in Table 8.4. Example transverse center of gravity distributions are presented later in Section 8.4.2.2, after event selections have been applied.

In the course of this analysis, muon, electron and pion runs at different beam energies have been simulated. Table 8.5 lists the beam energies and the corresponding number of simulated events per beam energy for each particle type. This first iteration of the simulation includes the default values of the additional absorber (12 mm) and of the tile-to-tile crosstalk (12 %, cf. Section 7.4.1). Note that later in Section 8.6, several additional simulations with adjusted parameters are performed with the aim, to further improve the agreement between data and simulation.

Particle	Beam Energy [GeV]	#Simulated Events
μ^-	10, 15, 20, 30, 40, 50, 70, 90	1 000 000
e^-	10, 15, 20, 30, 40, 50	1 000 000
	70, 90	100 000
π^-	10, 15, 20, 30, 40, 50, 70, 90	200 000

Table 8.5.: Dataset of simulated events including particle type, beam energy and the number of simulated events per beam energy.

8.2. Definitions & Nomenclature

Before starting with the actual data analysis, a short definition of frequently used nomenclature is given in Table 8.6. All values are defined for single events, while one event can have multiple hits with corresponding hit energies, but from these hits, only one layer-wise number of hits, one layer-wise hit energy and one layer-wise energy can be estimated for one event, similar to the total number of hits and the total energy.

nomenclature	acronym	description
hit channel		a channel with energy over threshold
layer-wise number of hits	N_l	sum of all hits in a layer l
total number of hits	$n_{hits} = \sum_l N_l$	total sum of all hits in all layers
hit energy	e_{hit}	energy in a single channel
layer-wise hit energy	e_l	energy in a single channel of layer l
layer-wise energy	$E_l = \sum_i e_l^i$	sum of all hit energies in layer l
total energy	$E_{total} = \sum_l E_l$	total sum of all hit energies of all layers

Table 8.6.: Frequently used definitions and nomenclature in context of data analysis of the AHCAL technological prototype.

8.3. Event Selection

Real data is not 100 % clean, it can rather be a superimposition of different particle types. To study the response of the detector for a specific particle type, selections have to be applied to recorded events. This section describes in detail the event selections applied to select muon, electron and pion data. Unfortunately, the true beam composition is not known. Thus, selections are estimated with simulated data, where the initial particle is well known. The simulation has been validated to match their representatives in real data (as discussed later in Section 8.4.2). In the following, event selection efficiencies η are defined as the ratio of the number of events which passed the selections, N_{passed}, divided by the number of simulated events before any selection, N_{sim}:

$$\eta = N_{passed}/N_{sim} \tag{8.1}$$

All event selections are applied to both, data and to simulation, later on in this analysis. No SiPM-tile saturation correction is performed either on data nor simulation at this point, because already after this selection, data and simulation can be compared to each other and saturation models can be tuned, as discussed later in Section 9.1.

The basic event selections and related event observables discussed in this section have been worked out in internal discussions and are thus related to selections presented in [76, 139]. Nevertheless, the selection cuts, the efficiencies and implications etc. have been studied independently within the course of this thesis as discussed below. There are many differences to the upper mentioned references, as for instance the generated simulations and selected datasets differ and also, the conditions for selection cuts are optimized differently here.
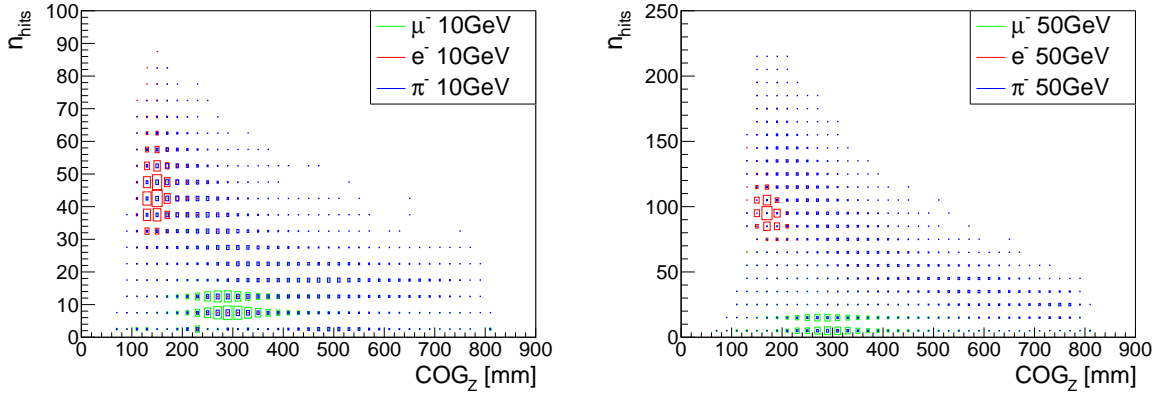
Figure 8.2.: Distribution of the total number of hits per event, n_{hits}, as a function of COG_Z for simulated muons, electrons and pions, each for 10 GeV (left) and 50 GeV (right). The size of the boxes represent the fraction of events in each bin. No previous selection is applied.

8.3.1. Muon Selection

The selection of muons is essential for a good energy and time calibration of the detector. Since the detector has already been calibrated by the CALICE collaboration before this analysis, the selection of muons and the calibration itself is not described in detail here. Still, a short overview on how to select muons is given.

First of all, minimum ionizing particles, like muons at 50 GeV, should pass straight through the detector without generating showers. The selection requires MIP-like particles to travel the detector perpendicular, hitting one channel per layer. In each hit tile, the mean value of the deposited energy should be equal as long as the channels are equal in material and dimension. One important event parameter is the center of gravity (COG). The center of gravity in z is defined as:

$$COG_Z \,[mm] = \left(\sum_i z_i e_{hit}^i \right) / \sum_i e_{hit}^i \tag{8.2}$$

The indicator i represents a specific hit within one event, z_i and e_{hit}^i are the corresponding position on the z-axis and energy of the hit, respectively.

To estimate the particle selections presented in this chapter, muons are forced to travel the detector within the sensitive area of the single HBUs (layers 3 to 10). This is done by rejecting muon events with a COG in x and y (similar to Eq. 8.2, but with x and y instead of z, respectively) larger than 150 mm. Otherwise, muons with a track outside the sensitive area of these layers but still inside the area of the 2x2 HBUs in the last four layers 11 to 14 would cause artifacts with a lower number of hits per events and a larger COG. In electron and pion runs with centered beams with small diameters, this is not expected to happen.

Figure 8.2 shows the total number of hits per event, n_{hits}, as a function of COG_Z, for simulated muons, electrons and pions of 10 and 50 GeV.

The shape of the distribution in COG_Z is strongly influenced by the technical alignment of the equipped and unequipped layers (cf. Section 8.1.1).

The accumulation around $n_{hits} \approx 10$ and COG_Z around 300 mm for 10 GeV can be explained

by the fact, that muons tend to pass the detector without showering, resulting in on average one hit per layer (remember, only 10 layers are active) and a center of gravity in the center of the detector, taking into account the alignment of the layers.

A cut of $n_{hits} <= 20$ is appropriated to select muons, taking into account one hit per layer and a maximum of one noise hit per layer.

This first selection on n_{hits} already leads to selection efficiencies of less than 10^{-2} % for electrons, 14.4 % for pions and remaining high with 99.5 % for muons for 50 GeV beam energy (which is the only one of interest, following Table 8.4).

To discard more pions, a MIP track finder, provided by the CALICE analysis tools, is utilized. In a nutshell, the MIP track finder algorithm creates collections of hits in the same x- and y-position. The number of entries in each collection must be higher or equal than a given threshold. The threshold is ideally identical to the number of active AHCAL layers, but to take into account inactive channels, a threshold of at least 7 hits in a track is chosen. This implements the predefined requirement of perpendicular traversing muons, rejecting any tilted tracks. To take into account the probability of a noise hit, a second threshold on the maximum number of hits per layer is set to 2, which allows for one noise hit per layer, as before.

With all muon event selections applied, the total efficiencies result in 89.7 % for muons, 0 % for electrons and 8.8 % for pions for a beam energy of 50 GeV.

With these selections, the full MIP-calibration of the detector using muon data has been performed within the collaboration [168]. This particularly allows to express measured hit energies in units of MIP.

8.3.2. Electron Selection

The selection of electron showers is described in the following. Electron data is utilized to study the electromagnetic-response of the prototype and to validate different SiPM response models (cf. Section 4.3.3). The latter is possible, because the energy, deposited by electron showers, is usually way higher compared to minimal ionizing muons. This allows to investigate further the parameters of the response models for the combination of the SiPM with the scintillator tile even in the saturation region of the SiPM, which is discussed later in Section 9.1. A clean sample of electron events, fully contained in the AHCAL and well described by simulation, is essential for further studies.

Two external event quality selections are applied to data only: the validation trigger tag (T_0) and the Cherenkov tag (see Section 8.1.2).

In order reduce transverse leakage and to secure that the beam passed the external upstream validation scintillator (T_0) with a size of 100×100 mm^2, a selection on the center of gravity in x and y (COG_X, COG_Y) is added such that -50 mm $\leq COG_{X/Y} \leq 50$ mm. For some beam energies, this selection is even hardened in order to align the simulations COG even more precisely to the COG of data. The efficiencies presented in the following exclude this $COG_{X/Y}$ selection, since it would falsely bias the estimated efficiencies due to the different beam alignments used for different particles and beam energies in simulation, as listed previously in Table 8.4. [1] This selection is handled in the same way for pions in the following subsection.

---

[1] Certainly, this selection could have been added, if the beam alignments would have been simulated equal for each particle type and energy, but a simulation describing the alignment of the data has more importance.
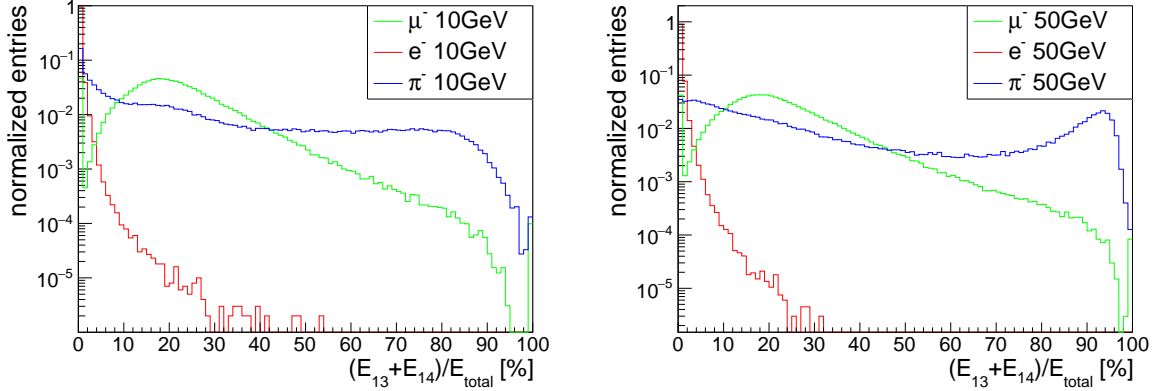
Figure 8.3.: Fraction of events as a function of the ratio between the energy of layer 13 and 14 and the total energy in the AHCAL $(E_{13} + E_{14})/E_{total}$, for simulated muons, electrons and pions, for 10 GeV (left) and 50 GeV (right). No previous selection is applied.
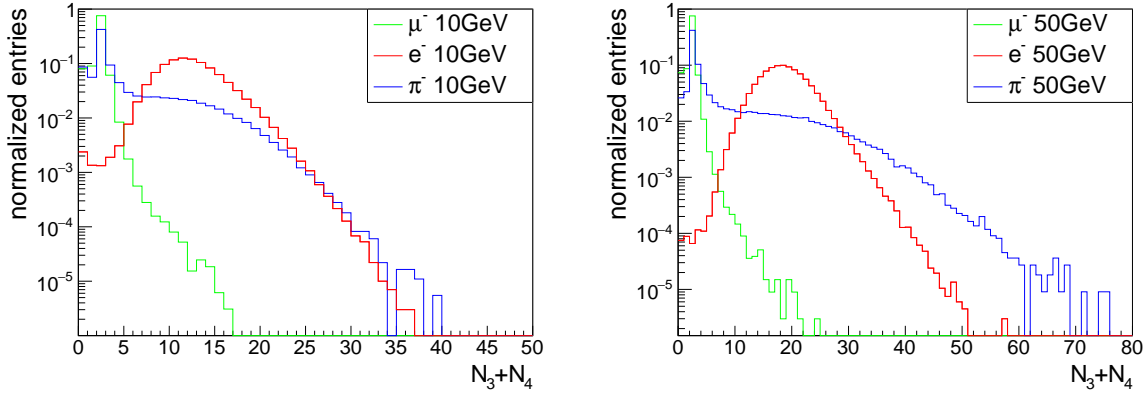

Figure 8.4.: Fraction of events as a function of the sum of the number of hits in layer 3 and 4, $N_3 + N_4$, for simulated muons, electrons and pions, for beam energies of 10 GeV (left) and 50 GeV (right). No previous selection is applied.

The first two electron selections can be derived from the information in the previous Figure 8.2, which shows the dependency of the total number of hits per event, n_{hits}, to the shower center of gravity in z, COG_Z, for simulated muon, electron and pion beams of 10 and 50 GeV. For other beam energies, refer to Appendix A. Most electrons are located in the region, where n_{hits} is in a specific range, depending on the beam energy, and $COG_Z \leq 250$ mm. Especially the selection on the number of hits reduces the fraction of muons, while the COG-selection includes early showering particles, like electrons.

To furthermore reduce the amount of late showering particles, a cut on the ratio between the deposited energy in the last two layers $(E_{13}+E_{14})$ and the total deposited energy in the AHCAL, E_{total}, is utilized on the basis of Figure 8.3 (see also Appendix A). As viewable, a large amount of pions and also muons can be rejected while keeping a high fraction of electrons, by requiring the sum of the last two layers to contain less or equal 1 % of the total Energy.

Additionally, the distribution of the sum of the number of hits in the first two AHCAL layers (layers 3 and 4), $N_3 + N_4$, allows another selection criterion. Figure 8.4 shows these distributions
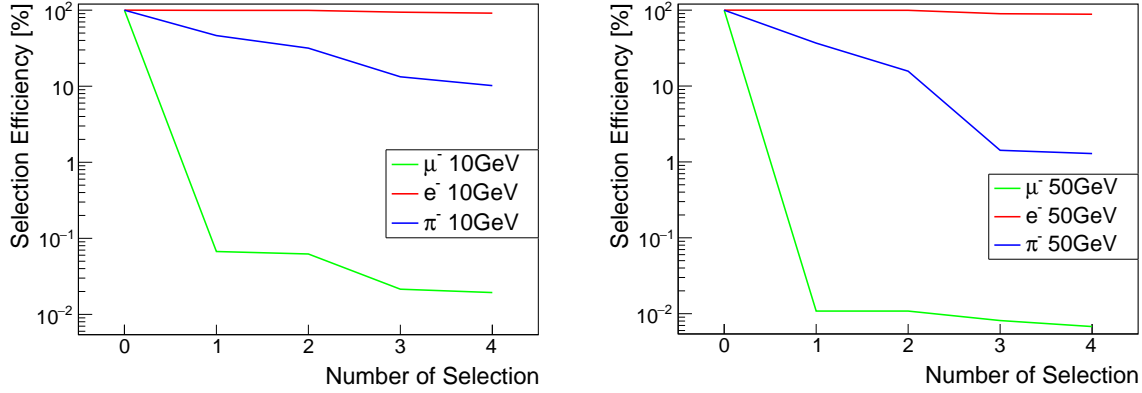
Figure 8.5.: Step by step electron event selection efficiencies η_{step} (cf. Eq. 8.1), based on one another, exemplarily shown for 10 GeV and 50 GeV. X-axis numbers correspond to selection numbers in Table 8.7.

#	Selection	Energy	primary effect
0	Cherenkov tag ON	all (data only)	include e$^-$
1	$25 \leq n_{hits} \leq 75$	10 GeV	exclude μ^-
	$35 \leq n_{hits} \leq 85$	15 GeV	
	$40 \leq n_{hits} \leq 100$	20 GeV	
	$50 \leq n_{hits} \leq 115$	30 GeV	
	$60 \leq n_{hits} \leq 125$	40 GeV	
	$70 \leq n_{hits} \leq 135$	50 GeV	
2	$COG_Z \leq 250$ mm	all	early showering
3	$(E_{13} + E_{14})/E_{total} \leq 1\%$	all	exclude late showering particles
4	$7 \leq N_3 + N_4$	10 GeV	early showering
	$8 \leq N_3 + N_4$	15 GeV	
	$8 \leq N_3 + N_4$	20 GeV	
	$9 \leq N_3 + N_4$	30 GeV	
	$10 \leq N_3 + N_4$	40 GeV	
	$11 \leq N_3 + N_4$	50 GeV	

Table 8.7.: Optimized event selections for electrons.

for simulated particles at 10 GeV and 50 GeV beam energies. Refer to Appendix A for more plots. Dependent on the beam energy, $N_3 + N_4$ has to be larger than a certain threshold, to reduce possible contamination from late showering particles, like pions and to select early showering particles, like electrons.

Other possibilities to select electrons have been studied, for instance a cut on the sum of the energies in the first few layers, but are finally dropped, because of low benefits to the reduction of pion and muon efficiencies, compared to the efficiency drop for electrons.

Step by step electron selection efficiencies η_{step} are plotted in Figure 8.5. Plots for other beam energies can be found in Appendix A. The number on the x-axis corresponds to the number of the selection, as indicated in Table 8.7, which lists detailed information about each electron selection step.
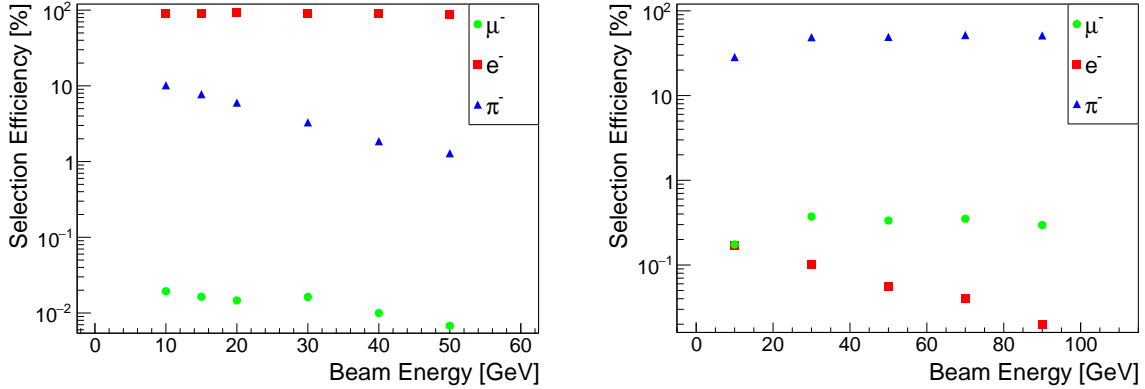
Figure 8.6.: Total electron (left) and pion (right) event selection efficiencies η (cf. Eq. 8.1) for all required beam energies. Estimated with simulation.

With the selection step 1 on n_{hits}, the muon efficiency is reduced by a factor larger of about 10^3, while the pion efficiency is reduced by more than $50\,\%$. The pion efficiency drops furthermore with each of the following steps 2, 3 and 4. While selections 2 and 3 reduce the pion efficiency throughout all beam energies, the impact of selection 4 leads to a relative reduction of the pion efficiency of around $23\,\%$ between selection step 3 and 4 for low beam energies, where the pion efficiency still remains significantly high after selection 3, but weakens for higher beam energies. Figure 8.6, left, shows the total electron selection efficiency as a function of the beam energy. Overall, the selection efficiency for electrons is well above 88%. The efficiency for pions decreases with the beam energy. Especially for low energies (10-20 GeV), still a significant efficiency of around $10\,\%$ to $6\,\%$, respectively, remains, which is due to the fact, that pions tend to shower earlier with lower energy and are hard to distinguish from electrons in that case. Nevertheless, the contamination of pions in data is expected to be negligible due to the production process of electrons (cf. 8.1.2). This assumption coincides with the observations presented later in Section 8.4.1. The efficiency for muons is $< 0.1\,\%$ throughout all energies. Total numbers are listed in Table 8.8.

Beam Energy [GeV]	η_{μ^-} [%]	η_{e^-} [%]	η_{π^-} [%]
10	$2 \cdot 10^{-2}$	91.3	10.2
15	$2 \cdot 10^{-2}$	90.9	7.8
20	$1 \cdot 10^{-2}$	92.3	6.0
30	$2 \cdot 10^{-2}$	90.9	3.3
40	$1 \cdot 10^{-2}$	89.8	1.9
50	$1 \cdot 10^{-2}$	88.4	1.3

Table 8.8.: Total electron event selections efficiencies η (cf. Eq. 8.1) for all three particle types. Estimated with simulation.

8.3.3. Pion Selection

To study the performance of the AHCAL prototype to hadronic particles, not only a clean sample of pion showers is needed. In addition, the pion showers must be contained inside the detector, that's why the data selections have to also reject pions which develop no or late showers inside the detector.

Similar as for electrons, two external event quality selections are applied to data only. The validation tag, T_0, and the Cherenkov tag. As opposed to electrons, the Cherenkov tag is used as a veto, in order to exclude electrons. For the same reasons as described above, the additional selection on the $COG_{X/Y}$ is not included in the estimation of efficiencies presented here.

For the selection of pion showers, the distribution of n_{hits} and $(E_{13} + E_{14})/E_{total}$ as shown earlier in Figures 8.2 and 8.3, respectively, are utilized again.

A cut on the minimum number of hits, $n_{hits} > n_{minimum}$, is used to reject possible muon contamination and non-showering pions. The minimum number of hits increases slightly with rising beam energy. In contrast to electrons, no selection on the center of gravity in z is performed, since the fraction of pions in the region, where electrons are dominant, is not negligible and represents early showering pions, which shall not be excluded from the analysis.

The former selection on the fraction between the energy in the last two layers and the total energy, $(E_{13} + E_{14})/E_{total}$, is inverted for pions: events with $(E_{13} + E_{14})/E_{total}$ larger a certain energy-dependent threshold are kept in order to select late showering particles only.

The former selection on the sum of the number of hits in the first two AHCAL layers is also appropriated for pions: in order to reduce possible electron contamination, $N_3 + N_4$ has to be lower than a certain threshold, dependent on the beam energy. All optimized pion event selections are listed in Table 8.9.

Figure 8.7 shows step by step pion selection efficiencies η_{step} for 10 and 90 GeV beam energies (cf. appendix Section A for other energies). Each x-axis bin corresponds to the indicator of the selections listed in Table 8.9. After applying selection 1 on n_{hits}, the efficiency for muons drops

#	Selection	Energy	primary effect
0	Cherenkov tag OFF	all (data only)	exclude e$^-$
1	$17 < n_{hits}$	10 GeV	exclude μ^-, non-showering π^-
	$18 < n_{hits}$	30 GeV	
	$19 < n_{hits}$	50 GeV	
	$20 < n_{hits}$	70 GeV	
	$20 < n_{hits}$	90 GeV	
2	$1\% < (E_{13} + E_{14})/E_{total}$	10, 30, 50 GeV	include late showering particles
	$3\% < (E_{13} + E_{14})/E_{total}$	70 GeV	
	$4\% < (E_{13} + E_{14})/E_{total}$	90 GeV	
3	$N_3 + N_4 < 5$	10 GeV	exclude e$^-$
	$N_3 + N_4 < 6$	30 GeV	
	$N_3 + N_4 < 6$	50 GeV	
	$N_3 + N_4 < 7$	70 GeV	
	$N_3 + N_4 < 7$	90 GeV	

**Table 8.9.:** Optimized event selections for pions.
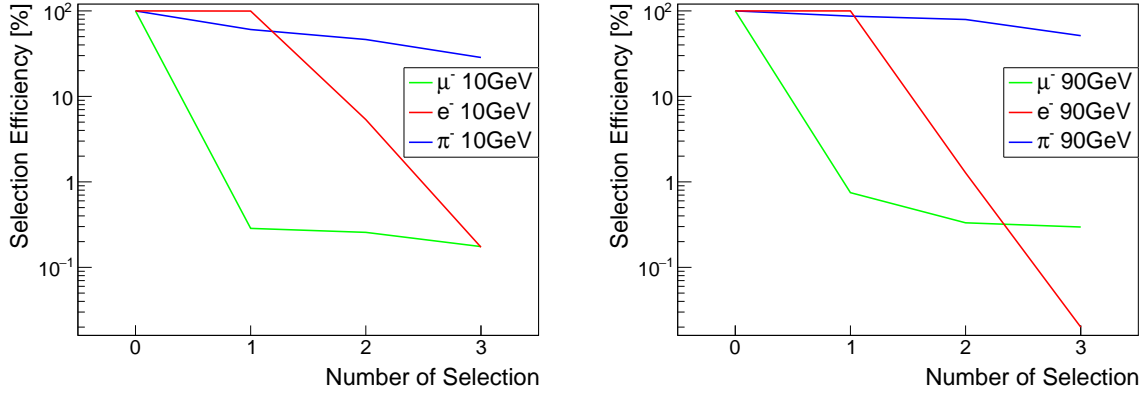
Figure 8.7.: Step by step pion event selection efficiencies η_{step} (cf. Eq. 8.1), based on one another, exemplarily shown for 10 GeV and 90 GeV. x-axis numbers correspond to selection numbers in Table 8.9.

Beam Energy [GeV]	η_{μ^-} [%]	η_{e^-} [%]	η_{π^-} [%]
10	0.2	0.2	28.5
30	0.4	0.1	48.9
50	0.4	0.1	49.9
70	0.4	$4 \cdot 10^{-2}$	51.8
90	0.3	$2 \cdot 10^{-2}$	51.3

Table 8.10.: Total pion event selections efficiencies η (cf. Eq. 8.1) for all three particle types. Estimated with simulation.

lower than 1% at all energies, while the electron efficiency nearly remains unaffected. Still, this first selection also affects pions, reducing the efficiency down to around 60% for 10 GeV, while remaining reasonable high around 87% for 90 GeV.

The second selection on the relative energy of the last two layers drops the electron efficiencies down to 5% for 10 GeV and 1% for 90 GeV. This selection reduces the efficiency for pions, too, down to 46% for 10 GeV and between 77% and 81% for 30 to 90 GeV.

The third selection on the number of hits in the first two AHCAL layers further reduces the electron efficiency and leads to the total selection efficiencies listed in Table 8.10 and also shown above in Figure 8.6, right.

The most attention is paid on the reduction of potential contamination from muons, electrons and non-showering pions. This results in a very good rejection leaving an efficiency of lower than 1% for all muons and significantly lower than 1% for electrons for all beam energies. The selection efficiency for pions is roughly around 50% for all energies, except 10 GeV, where it drops down to around 29%, since pions are difficult to distinguish from electrons or muons at this low beam energy.

The selection efficiency is expected to increase with more equipped active layers in the AHCAL for future prototypes, which will give more information on the shower depth and will thus increase the efficiency of a last-layers-energy-selection, comparable to selection 2. Also, with active layers in front of the AHCAL, a shower start finder algorithm can be used in the future in order to estimate the starting point of a shower.

(a) Selection 1 applied.

(b) Selection 1 and 2 applied.

(c) Selection 1, 2 and 3 applied.

(d) Selection 1, 2, 3 and 4 applied.
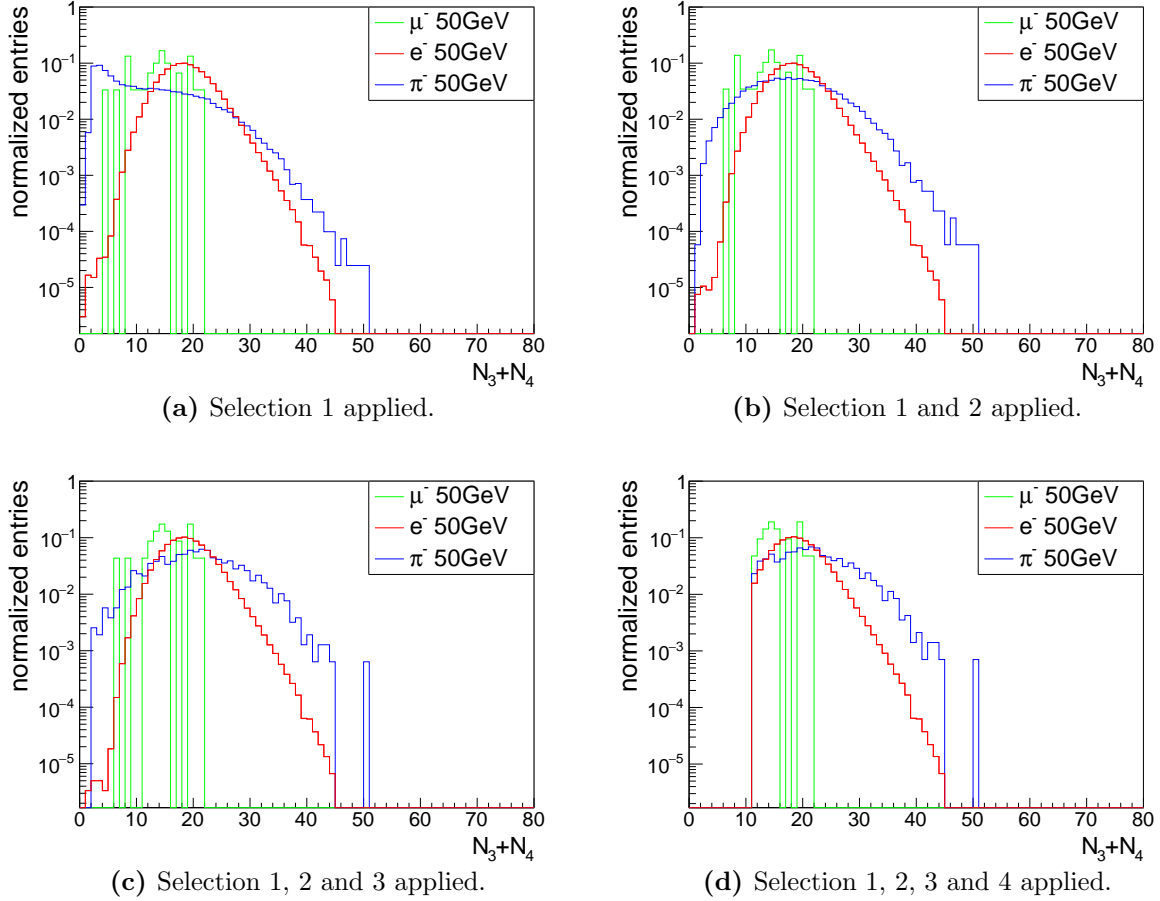
Figure 8.8.: Implications of electron event selections for $N_3 + N_4$ of simulated muons, electrons and pions of 50 GeV after applying selection 1 (a), 1 and 2 (b), 1, 2, and 3 (c) and all four (d) selections (cf. Table. 8.7).

8.3.4. Implications of Event Selections on Simulation and Further Studies

In the previous subsections, the chosen event selections and their impact on the efficiencies for different particles and beam energies have been discussed. Now, the impact of electron and pion event selections on simulated events is visualized and discussed in more detail in order to prove that the chosen event selections are reasonable.

Figure 8.8 illustrates the implications of the electron selections on simulated muons, electrons and pions of 50 GeV by means of the sum of the number of hits in the first two AHCAL layers, $N_3 + N_4$. For a better view, entries are normalized in each plot. The fraction of remaining events after each selection can be read from previous Figure 8.5.

Starting from the original non-selected distribution in Figure 8.4, right, Figure 8.8a shows the distribution after the first electron selection on n_{hits}. While the distribution becomes a bit sharper for electrons, a huge fraction of muons is rejected by the lower-edge criterion $70 \leq n_{hits}$, as well as a notable fraction of pions with $N_3 + N_4 \approx 2$, which might be associated with punch-through pions. Also, pion events with high $N_3 + N_4$ on the right falling edge of the distribution are reduced by the upper-edge criterion $n_{hits} \leq 135$ and can be associated with early showering

(a) Selection 1 applied.

(b) Selection 1 and 2 applied.

(c) Selection 1, 2 and 3 applied.
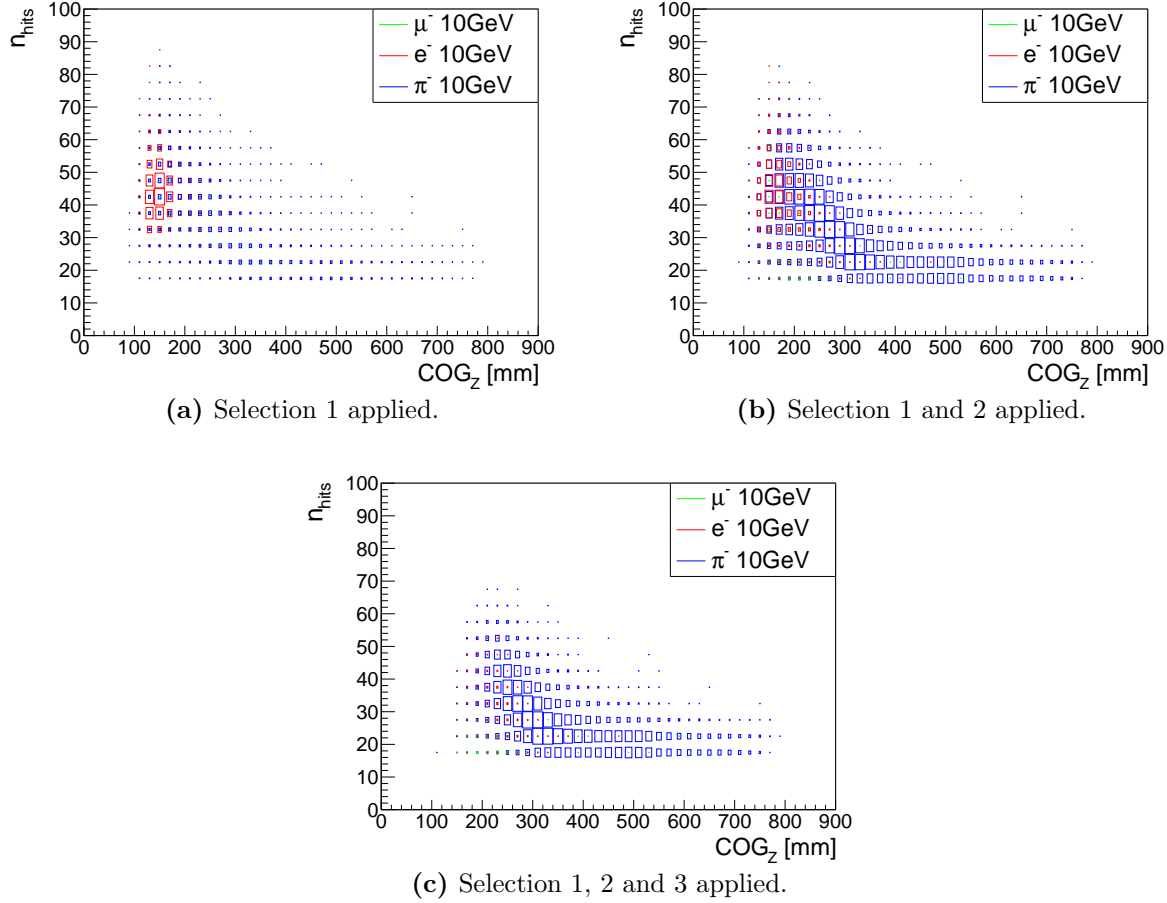
Figure 8.9.: Implications of pion event selections on the 2D distribution n_{hits} versus COG_Z for simulated muons, electrons and pions of 10 GeV after applying selection 1 (a), 1 and 2 (b), and all three (c) selections (cf. Table. 8.9).

pions.

After adding the second selection on COG_Z, the strong reduction of entries in the low region of the distribution, as shown in Figure 8.8b, demonstrates that with selection 2, early showering events are selected as expected. This leads to a strong reduction of late showering pions.

With the third selection on $(E_{13} + E_{14})/E_{total}$, the fraction of remaining pions is reduced as discussed above, without big changes to the shape of the remaining distributions, as shown in Figure 8.8c. It is safe to assume that this selection affects all remaining pions, independently of $N_3 + N_4$.

After adding the last selection on $N_3 + N_4$ itself, even more pions with a low number of hits in the first two layers are rejected. Besides, this effect is small at 50 GeV compared to lower beam energies, where a larger fraction of pions are cut off in this region.

The implications of the pion selections are presented in detail in Figure 8.9 on the basis of the 2D distribution n_{hits} versus COG_Z for simulated 10 GeV muons, electrons and pions. Here, entries are normalized to the initial number of events before the first selection has been applied. The original non-selected distribution, as shown in Figure 8.2, comprises a hotspot of electrons
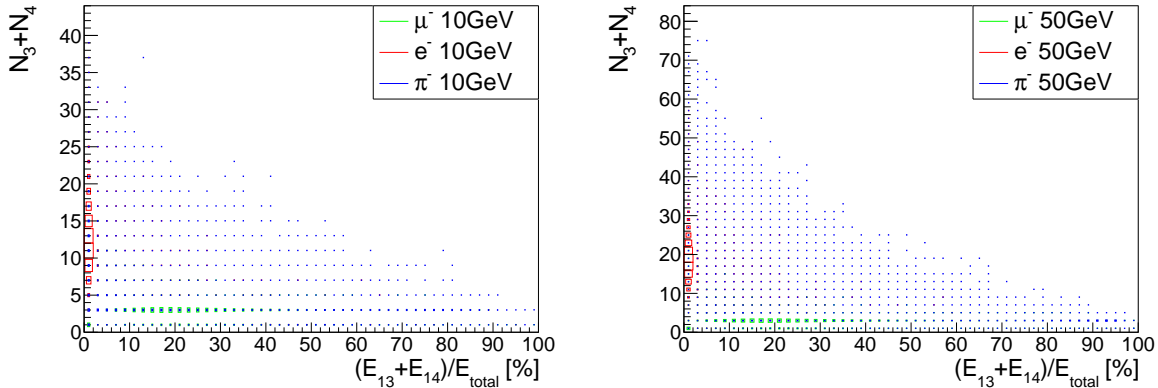
Figure 8.10.: 2D-distributions of $N_3 + N_4$ and $(E_{13} + E_{14})/E_{total}$ for simulated muons, electrons and pions of 10:GeV (left) and 50 GeV (right). No event selections are applied here.

and another hotspot of muons, while pions are spread all over the distribution. Electrons tend to shower early and deposit most of their energy in several channels in the first few layers, while muons tend to just punch through the detector and hit all active layers once.

With the first pion selection on n_{hits}, most of the muons are removed from the distribution in Figure 8.9a, while the electrons remain unaffected. Still, a few pions are rejected too, which do not shower broad or early enough to pass this selection. This is intended, since only pions showers fully contained in the detector are of interest.

Figure 8.9b shows the impact of the second pion selection on the ratio $(E_{13} + E_{14})/E_{total}$, applied in order to select late showering particles. The impact of this selection is clearly visible in the relative increase of pion entries compared to electron entries, which are strongly rejected. Previously not clearly visible, now a concentration of pions, starting in the electron hotspot and reaching further until a COG of around 550 mm, becomes apparent. The shape might indicate an anti correlation between n_{hits} and COG_Z for the remaining pions.

The last selection on $N_3 + N_4$ further rejects electron entries as shown in Figure 8.9c, making the pions the dominant particle nearly all over the distribution, especially also in the former electron hotspot region.

In addition, Figure 8.10 shows the distribution of $N_3 + N_4$ as a function of $(E_{13} + E_{14})/E_{total}$ for 10 and 50 GeV muons, electrons and pions before any event selection. Electrons are mainly located close to the y-axis where $(E_{13} + E_{14})/E_{total} \approx 1\%$ while muons are located close to the x-axis with $N_4 + N_4 \approx 2$, as discussed above. Pions don't show any exposed position. This proves that the simple cuts on the two variables of this distribution are reasonable in order to reject electrons and muons in the pion selection, or expressed the other way round, to selected them in the case of their own selection procedure.

8.4. Validation of the Simulation

Now, that the impacts of event selections on simulations have been discussed, a curiosity grows about how the data itself looks like and how good it can be expressed by the simulation. This section addresses both questions by showing implications of event selections on data in
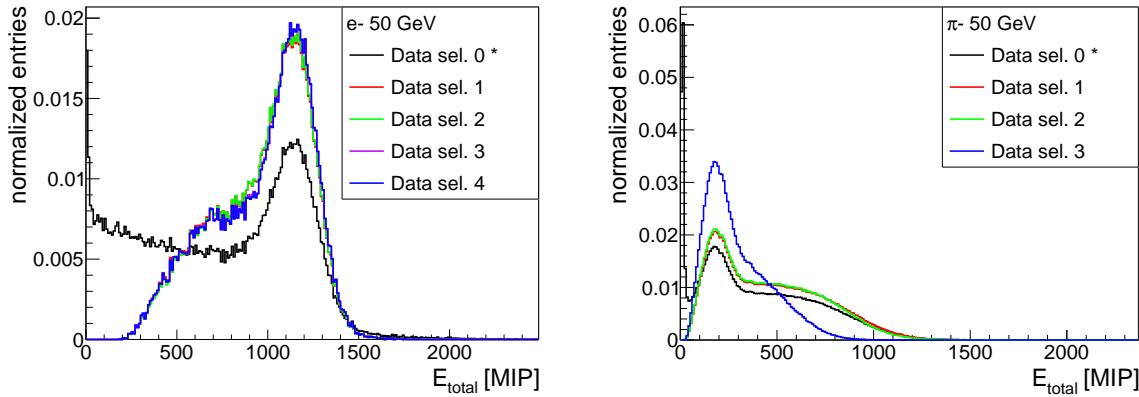
Figure 8.11.: Impact of consecutive event selections on 50 GeV electron (left) and pion (right) data, shown by means of the total energy E_{total}. For electron data, electron event selections are applied, while for pion data, pion event selections are applied.

Section 8.4.1 and by discussing the comparison between data and simulation in Section 8.4.2. The latter includes a short check of the MIP calibration using muons, followed by a detailed discussion for electron and pion showers. This includes transverse shower center of gravity profiles, as well as hit energy, total energy and number of hits distributions. The comparison of these distributions allows a first validation of the simulation.

8.4.1. Implications of Event Selections on Data

So far, all event selections have been discussed by means of simulations. Figure 8.11 shows the impact of the consecutive event selections on data on the total Energy, E_{total}, for 50 GeV electrons and pions.

The selections marked in the legends correspond to the consecutive event selections listed in Table 8.7 for electrons and 8.9 for pions, respectively, whereas the first entry (Data sel. 0 *) includes an additional selection on the center of gravity in x and y, in order to accept only events within the area of the validation trigger scintillator, as earmarked above.

The electron data in Figure 8.11, left, with only the positive Cherenkov tag and the *COG* in x and y in preselected boundaries (sel. 0) shows an accumulation of entries with a peak around 1100 to 1200 MIP, which becomes more significant with the following selections. Different to all following selections, the sel. 0 includes a high fraction of events with a total energy lower than 20 MIP and also a large low-energy tail which slowly decreases between 20 MIP and the above mentioned peak. A large fraction of this low-energy background is already rejected with selection 1.

All following electron event selections are not able to reduce the low-energy fraction any further, only the width of the peak itself might become a little thinner.

As previously visualized in Figure 8.5, the selections 2, 3 and 4 aim to reduce the fraction of pions in the beam. Since the impact of these selections on data is low, is can be concluded, that pion contamination is also low - or already suppressed by the previous event selections which include the pion discriminating positive Cherenkov tag.

Also the estimated efficiency, as previously shown in Figure 8.5 for simulation, suggests, that the first electron selection especially rejects muons which leads to the assumption, that the low energy entries between 0 and 20 MIP in data with seleciton 0 belong to muons or MIP-like particles, passing the detector without any shower development. The low-energy entries higher than 20 MIP might not arise from muons, since a most probable value of 1 MIP per layer leads to an expected value of 10 MIP plus noise for the 10 active layers. Thus, these events might rather arise from showering particles, like electrons or pions. The lower measured energy might be a result of the inactive EBUs in the first two slots of the detector, leading to a loss of information of the deposited energy of the shower, especially, if the initial particle showers early. This directly reduces the total reconstructed energy. Similar to the non-active EBUs, the loss of information of the inactive layers 6 and 10 also reduces the reconstructed energy.

On the other hand, the low-energy background could be a result of electrons with less than the intended beam energy, because these entries are not much affected by electron event selections, though their origin is not clear at this point.

Figure 8.11, right, shows the total reconstructed energy, E_{total}, for 50 GeV pion data. Here, the peak position is at a much lower total energy around 200 MIP and a higher-energy tail is visible, which slowly sinks with rising E_{total}.

Similar to above, the major difference between the selection 0 and 1 is the discrimination of entries in the lowest energy bins, which again can be identified as muons and non-showering pions. This assumption is strengthened by the impact of selection 1 on simulated pions, as visualized in Figure 8.7.

The differences between pion data with consecutive selections up to selection 1 compared to selections up to 2 are low. The last additional selection 3, which aims to rejects early showers often induced by electrons, reduces the high-energetic pion tail, which might correspond to early showering pions.

8.4.2. Data and Simulation after First Event Selections

In order to validate the simulation, a comparison to data is performed. This step is important to ensure a good description of the data by simulation and to be able to draw meaningful conclusions from simulations. To do this, all previously discussed event selections are applied to data and to simulation.

First the pre-existing channel-wise energy calibration is checked by a comparison of muon data and simulation. Then, the simulation is validated by a further comparison between data and simulation for electron and pion showers, including transverse center of gravity profiles, as well as hit energy, total energy and total number of hits distributions.

The simulations presented in this section utilize the default values for the additional absorber thickness of 12 mm and for the tile-to-tile crosstalk value of 12 % (cf. sections 8.1.4.1 and 7.4.1, respectively). Additionally, hit energies are saturated in simulation following the default method presented in Section 7.4.2, while data is obtained saturated. Both, simulation and data exclude a de-saturation of the SiPM-tile response.
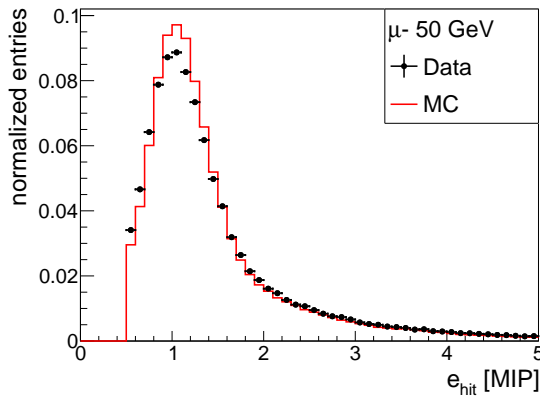
Figure 8.12.: Main part of the hit energy e_{hit} distribution as a composition of all channels for 50 GeV muons in data and simulation with muon event selections.

8.4.2.1. Energy Scale Calibration Check

The MIP calibration of the detector is briefly tested by means of a comparison of hit energies of muons in data and simulation. As the MIP calibration defines the energy scale of deposited energies, it is very important. The MIP calibration itself has been performed in another analysis by measuring the most probable value of the deposited hit energies of muons in single tiles [76], similar to the method described in Section 7.2.3.

Figure 8.12 shows distributions of the composition of hit energies e_{hit} of all AHCAL channels after the previously discussed muon event selections (cf. Section 8.3.1) for 50 GeV muons in data and simulation. The two shapes agree relatively well, while data looks a little wider. The reason for this widening in data might be found in small mis-calibrations of channels. Further studies have been done in [76], resulting in a validation of the simulation, which reproduces the data within 4 % deviation for small energies.

8.4.2.2. Electron and Pion in Data and Simulation

In order to validate the simulation for electromagnetic showers, a comparison of electron shower observables in data and simulation is performed. Compared to pion showers, electron showers have the advantage, that the underlying physics are well understood and thus can be simulated with high precision. That's the reason why electron showers are utilized to validate the detector geometry, the material composition and the calibration of the complete detector. Besides and for the same reason, electron showers are also used later on in this analysis for the optimization of simulation parameters and for the response tuning of the SiPM-tile system.

To prove that the same channels are hit in data and simulation and thus that the beam alignment and detector geometry are implemented correctly, first of all, transverse center of gravity distributions are compared. As described above in Section 8.1.4.2, particle beams are simulated by means of a particle gun with a Gaussian profile with tunable expected value and variance, defining the transverse position and width of the beam. As already described, these values have been optimized in order to match the data.

Figure 8.13 and Figure 8.14 show center of gravity distributions in x and y (similar to Equa-
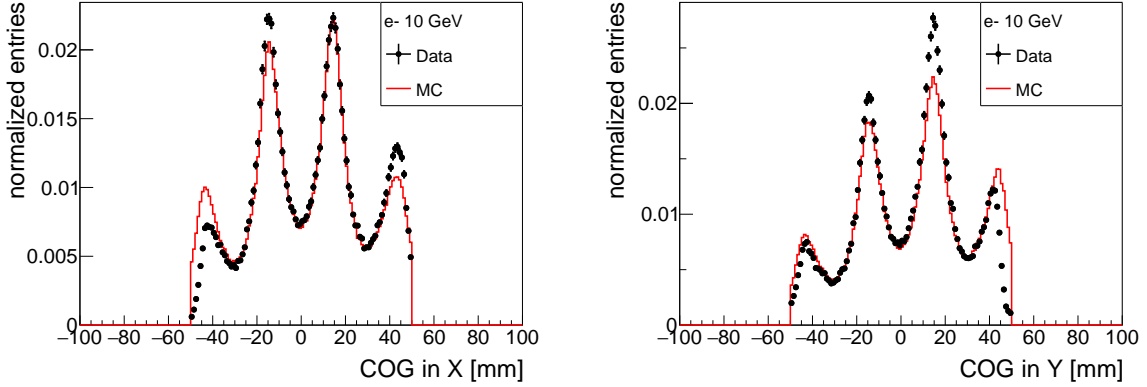
Figure 8.13.: Center of gravity in x (left) and y (right), exemplarily shown for 10 GeV electrons for both, data and simulation.
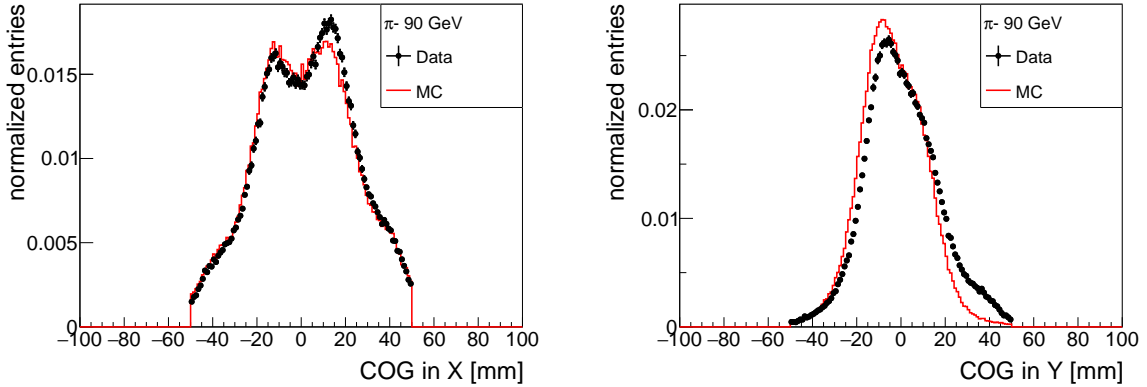

Figure 8.14.: Center of gravity in x (left) and y (right), exemplarily shown for 90 GeV pions for both, data and simulation.

tion 8.2) of electrons and pions, respectively, for data and simulation. More plots can be found in Appendix B, which show a similar agreement between data and simulation.

The shape of the electron distributions, with local maxima and minima alternating approximately every 15 mm, have their origin in the structure of the HBUs, which consist of tiles with 30 mm length and width. The position of a hit in a tile is defined by the middle of the tile. This minimum-maximum-shape is more pronounced for electrons, while the shape looks more blurred for pions. The cut on the transverse center of gravity $-50\,\mathrm{mm} \leq COG_{X/Y} \leq 50\,\mathrm{mm}$ is visible.

Differences in the shapes between data and simulation might be induced by non-Gaussian profiles and beams not perpendicular to the detector front in data. Also due to the variety of inactive channels, even small differences might have a large impact on the center of gravity. Still, the agreement between data and simulation is good enough to proceed.

Along with electron and pion showers come higher energy deposits in single tiles, in contrast to muons. The reconstructed energy mainly depends on the deposited energy, but also on noise,
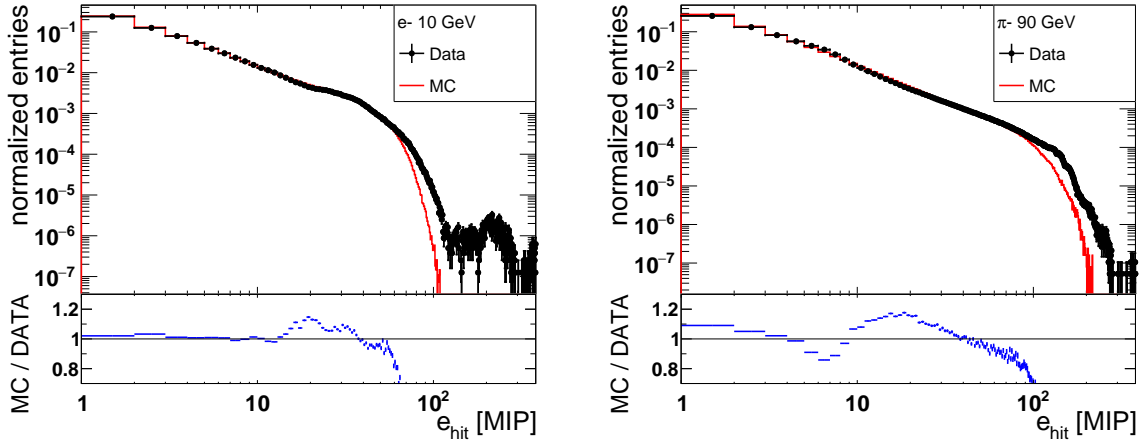
Figure 8.15.: Hit energy e_{hit} distributions of the complete detector for 10 GeV electrons (left) and 90 GeV pions (right) in data and simulation. On the bottom of each plot, the ratio between simulation and data is shown.

tile-to-tile crosstalk and not at least on SiPM response saturation, especially for high energy deposits. In particular for electrons, who tend to deposit a high fraction of the shower energy in only a few tiles, a proper SiPM response saturation model is essential. Though these effects are included in the simulation, they are not yet optimized. Therefore, discrepancies between data and simulation are expected, especially in the high energy region of single hits.

Figure 8.15 shows distributions of hit energies e_{hit} of single channels of the complete AHCAL for 10 GeV electrons and 90 GeV pions. Refer to Appendix B for additional beam energies. The highest fraction of entries are located at small hit energies and decreases with rising hit energy. At a certain hit energy, for 10 GeV electrons around 100 MIP, the distribution drops sharply, most probable because of SiPM saturation.

For 10 GeV electrons, the data is described well by the simulation within 15 % deviation of a ratio of 1 until approximately 60 MIP, for higher hit energies the discrepancy increases. The high deviation in the region around 20 MIP can be explained by mis-calibrations of the high- and low-gain intercalibration factors applied in data. This results in a shift of hit energies recorded in low-gain mode to slightly higher values. From 60 MIP on, the simulation underestimates the fraction of high hit energies, which is in all likelihood a direct consequence of an insufficient saturation model. Both data and simulation show a sharp falling tail as mentioned above, while in data also entries at higher hit energies are present. These entries are not expected and their origin might be found in not rejected noisy channels. Since the fraction of these events is very low, this issue is ignored.

The comparison between data and simulation for higher beam energies shows a similar behavior, where the simulation describes the data within 30% deviation for hit energies up to around 80 MIP, from where on the deviation increases even more due to the unsatisfactory saturation model applied in the simulation. On the side: Due to different shower depths dependent on the beam energies and due to the variety of different SiPM-types utilized in different layers of the prototype, the impact of SiPM saturation might change for different beam energies. The response saturation will be discussed in more detail in Section 9.1.
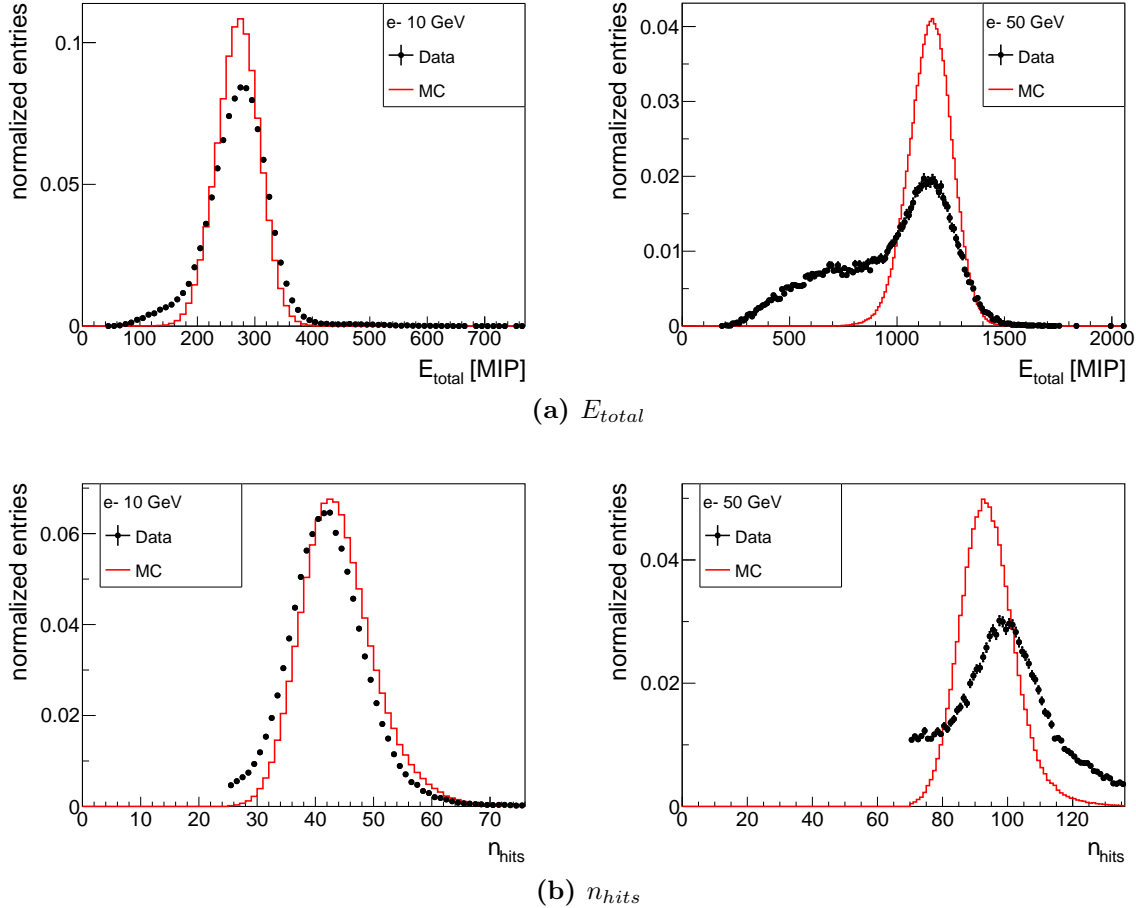
(a) E_{total}

(b) n_{hits}

Figure 8.16.: Distributions of the total energy, E_{total}, (a) and of total number of hits, n_{hits}, (b) for 10 and 50 GeV electrons in data and simulation.

The hit energy e_{hit} distribution for pions is also briefly discussed, which looks similar to the distribution of electrons with the highest fraction of entries at the lowest hit energies and decreasing fraction with rising beam energy. Also, the sharp falling edge is visible. For 90 GeV, the simulation describes the data well within less than 20 % deviation up to hit energies of around 80 MIP, from where on a large discrepancy is observed again. Also, the local increase of the deviation in the region around 5 to 35 MIP can be assigned to mis-intercalibrations. For all beam energies at a certain high energy, dependent on the beam energy, the deviation increases over 30 %, again most probable due to a insufficient response saturation model.

The distributions of data and simulation of the total energy, E_{total}, and of the total number of hits, n_{hits}, are shown for 10 and 50 GeV electrons in Figure 8.16. For 10 GeV, the agreement between data and simulation is way better than for 50 GeV. Compared to simulation, the total energy distribution of 10 GeV data exhibits a sooner smoothly rising flank and a slightly weaker falling flank resulting in a broader distribution, while in simulation, the flank is sharper to both edges and the distribution looks more Gaussian. A higher mean total energy is measured for 50 GeV compared to 10 GeV, as expexted. The simulation still looks Gaussian, while the data
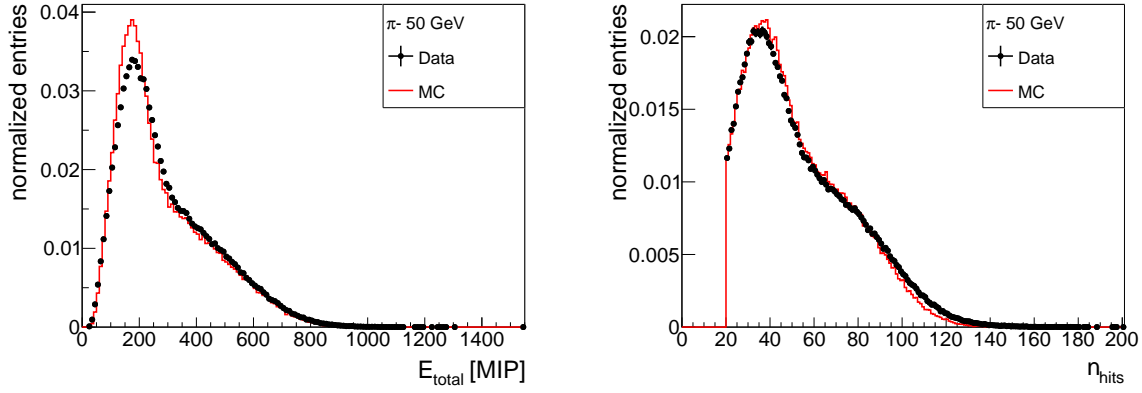
Figure 8.17.: Distributions of the total energy, E_{total}, (left) and of total number of hits, n_{hits}, (right) for 50 GeV pions in data and simulation.

exhibits a large fraction of lower E_{total} entries, which cannot be interpreted as a rising flank of the mean peak with a mean around 1200 MIP anymore.

This low-energy background cannot be explained by inefficiencies induced by inactive layers, because otherwise it would to some extend be visible in simulation, too. Instead, these entries most probably originate from contamination with electrons with lower energy, as already discussed above in Section 8.4.1. This low-energy background increases with rising beam energy. Since none of the previously discussed electron event selections manage to reject this low-energy background, there is a need for an additional data-based selection, which is presented below in Section 8.5. Nevertheless, the positions of the main peaks agree well between data and simulation at all beam energies.

The n_{hits} distributions again look Gaussian and feature a higher mean for higher beam energies, as expected. The distributions agree better for 10 than for 50 GeV electrons, while the simulation is a little overestimating the number of hits at 10 GeV and underestimating it more clearly at 50 GeV. For both beam energies, data features a higher fraction of entries at lower n_{hits}, which ends abruptly at each corresponding n_{hits} selection cut. This background, which is larger for higher beam energies, might also be related to low-energy electrons. For 50 GeV, a larger falling flank is visible, which is also cut at the maximum allowed n_{hits}.

The discrepancies between data and simulation of the mean positions of the peaks in the n_{hits} distributions can most probably be attributed to an inaccurate simulation of the tile-to-tile crosstalk and the upstream material in the beamline. Both parameters are optimized later in Section 8.6. Already at this point, it can be assumed that one global parameter for each tuned aspect will not improve the agreement for each single beam energy, because the mean positions of n_{hits} in simulations are once higher and once lower compared to data for different beam energies. Still, the overall agreement can be optimized.

Figure 8.17 shows distributions of E_{total} and n_{hits} for 50 GeV pions. Both distributions feature a Gaussian-like peak at low $E_{total} \approx 200$ MIP or $n_{hits} \approx 35$, followed by a lengthened falling tail to higher energies or number of hits, respectively. The shape is biased by the fact, that pions tend to shower in the region of the detector prototype, which is only rarely equipped with active layers, thus a large fraction of deposited energy and hits is not measured. In the number

of hits distribution, a strong selection cut on $n_{hits} > 19$ is visible, which is necessary to reject possible muon contamination.

In both cases, the shapes agree well between data and simulation. In simulation, a larger fraction of events is found in the peak around $E_{total} \approx 200\,\text{MIP}$ and the width of the peak is a bit shifted to the left and a bit narrower compared to data. The long falling edge to high E_{total} is a bit underestimated in simulation.

On the other hand, the main peak in the n_{hits} distribution is a little wider in simulation compared to data. There are also differences between data and simulation in the shapes of the falling flank, as the simulation first overestimates and from around $n_{hits} > 90$ on underestimates the fraction of events. Still, the mismatches are low and also might change with the following tuning of the simulation, while the impact of the tuning is expected to be lower for pions than for electrons. Though not shown at this point, higher beam energies lead shift the distributions of E_{total} and n_{hits} to higher energies or number of hits, respectively.

The distributions and the agreement between data and simulation for other electron and pion beam energies are comparable to the distributions shown here.

It can be concluded, that the simulation is already at this point in good agreement to data, but there is still room for improvements. The MIP calibration has been checked in order to prove, that the simulation is able to describe low-energy depositions in the detector. Electron showers have been investigated in order to study the agreement for higher energy depositions. Also with electrons, the detector geometry has been validated. A crosscheck with pion simulations has also shown a good agreement to pion data.

To further improve the agreement between data and simulation, first, additional event selections have to be applied to electron data in order to reject the observed low-energy background. This is not necessary for pions, as no remaining contamination is observed there. Afterwards, the simulation of the upstream material and the tile-to-tile crosstalk will be optimized.

8.5. Data Based Electron Event Selection due to Low-energy Background in Data

With the comparison between data and simulation presented in the last section, a low-energy background in electron data is discovered, which is not present in simulation. Since these events pass all electron event selections, it is most likely, that they actually belong to real electrons, but with less energy. The origin of these low-energy electrons lies presumable in upstream collisions of electrons with beamline infrastructure due to a bad tuning of the beamline parameters for the particle production. [164, 165]

A new data-driven electron event selection is investigated with the goal to reduce the low-energy background in data. The approach is to select events with a specific ratio between the deposited energy in the first active layer and the total energy, which is discussed in Section 8.5.1. This additional selection has been subject of internal meetings and is likewise applied in [139]. Nevertheless, the selection is optimized independently here.

Also, in order to give an adequate reason for this approach, an overlay of electron simulations
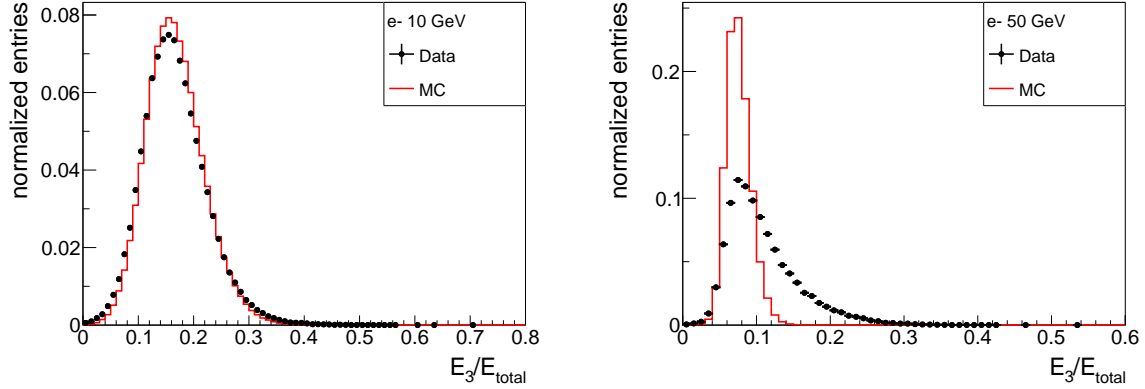
Figure 8.18.: Ratio E_3/E_{total} for event-selected electrons of 10 and 50 GeV for data and simulation.

of different beam energies is discussed in Section 8.5.2, allowing for another additional selection on the total energy, as described in Section 8.5.3.

8.5.1. Additional E_3/E_{total} Electron Selection

Figure 8.18 shows histograms of the ratio E_3/E_{total} between the summed energy in layer 3, E_3, which corresponds to the first active layer, and the total energy, E_{total}, for 10 and 50 GeV electron data and simulation. For other beam energies, see Appendix C. The mean of E_3/E_{total} decreases with rising beam energy. This means, that with rising beam energy, relatively more energy is deposited in layers behind layer 3. For 10 GeV, the two histograms for data and simulation agree better than for 50 GeV. While the shape looks like a symmetric Gaussian in simulation, independent of the beam energy, data features a slower falling edge at higher beam energies, as at 50 GeV. A slower falling edge is expected, if the actual beam energy is overlaid with events with lower electron energies. Like this, a selection cut on the ratio E_3/E_{total} can be instantiated in order to exclude events from electrons with lower energy.

Consequently, an energy-dependent threshold r_{E_3} is introduced such that events exceeding the threshold will be rejected and only events lower or equal the threshold are kept: $E_3/E_{total} \leq r_{E_3}$. The threshold is selected with the condition, that the fraction of rejected events is within 1 to 2 % for the simulation. Like this, only a small fraction of events with the actually aimed energy are rejected.

It is obvious that the impact of such a selection will be small for lower beam energies, because the falling edge in data does not differentiate too much from simulation, which might indicate, that lower beam energies are less affected by a low-energy background; while for higher energies, a larger low-energy background is expected to be rejected. This is in accordance with the results discussed before in Section 8.4.2.2.

Table 8.11 lists the threshold r_{E_3} on E_3/E_{total} and the related ratio $\kappa = N_{sel\,\&\,r_{E_3}}/N_{sel}$ between the number of selected events including the new cut, $N_{sel\,\&\,r_{E_3}}$, and the total number of selected events excluding it, N_{sel}.

As a consequence of the above defined condition of the new selection, the ratio κ remains withing 98 to 99 % for all beam energies for the simulation. For data, the impact of the
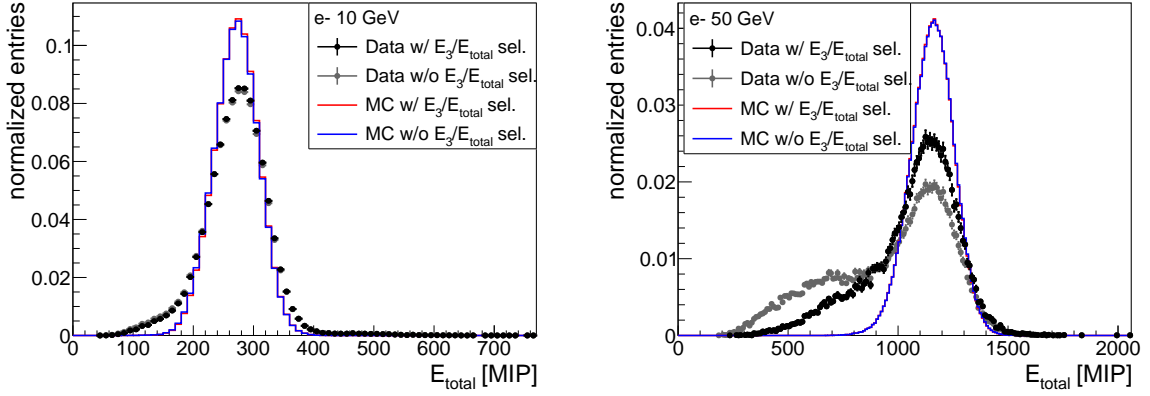
Figure 8.19.: Impact of E_3/E_{total} selection on the total energy distribution, E_{total}, for 10 and 50 GeV electrons for data and simulation.

Beam Energy [GeV]	r_{E_3}	$\kappa_{e^-}^{MC}$ [%]	$\kappa_{e^-}^{DATA}$ [%]
10	0.30	98.8	97.8
15	0.24	98.6	96.2
20	0.2	98.3	93.3
30	0.17	99.0	88.2
40	0.14	98.7	82.4
50	0.12	98.8	68.3

Table 8.11.: Additional data-based electron event selections on the ratio $E_3/E_{total} \leq r_{E_3}$ and efficiencies κ_{e^-} on simulation and data.

selection increases with rising beam energy, leading to lower ratios κ. This is consistent with the expectation, because the higher the beam energy, the higher is the fraction of low-energy events, which are suppressed now. The lowest ratio $\kappa = 68.3$ is found at 50 GeV.

 The impact of the the new selection on E_3/E_{total} is demonstrated by means of the total energy distribution, E_{total}, in Figure 8.19 for 10 and 50 GeV electrons. For additional beam energies, see Appendix C. Data and simulation with and without the new selection cut on E_3/E_{total} are shown. As expected, the impact is low for simulation. For data, the impact is also low at 10 GeV, but increases with the beam energy. For 50 GeV, a clear reduction of the low-energy part is visible, leading to a relative increase of the aimed high energy fraction and to a reduction of the discrepancy between data and simulation.

Unfortunately, the low-energy background cannot be rejected completely with this selection. Hence, the origin of this background is simulated in the next subsection in order to pave the way for a strong cut on the total energy E_{total} itself.

8.5.2. Overlaying Simulations

The preceding sections suggest, that electron data includes a relatively high fraction of electrons with less than the aimed beam energy. Since the highest fraction is found in 50 GeV electron data, only 50 GeV data is evaluated in this analysis. Therefore, simulations of different lower beam energies are utilized and combined with a 50 GeV simulation. In the course of this analysis,

two additional simulations have been generated with beam energies of 25 and 35 GeV. The goal of this analysis is explicitly not to nicely simulate the low-energy background itself, but to test, whether the observed low-energy background can be explained by a contamination of low-energy electrons.

To be consistent to the handling of 50 GeV data, the low-energy simulations have to pass the same event selections for 50 GeV electrons [2]. Before any event selection, the same number of $5 \cdot 10^5$ events are taken into account from each simulated beam energy. After the 50 GeV event selections, the remaining fraction of events $\eta_{e^- \, 50 \, \text{GeV}}$ are listed in Table 8.12. As expected, the selection efficiency is high with 88.4 % for 50 GeV (as before) and sinks with decreasing beam energy down to 0.1 % for 10 GeV.

Beam Energy [GeV]	$\eta_{e^- \, 50 \, \text{GeV}}$ [%]
10	0.1
15	3.0
20	13.1
25	35.3
30	58.6
35	78.1
40	85.7
50	88.4

Table 8.12.: Total 50 GeV event selection efficiency $\eta_{e^- \, 50 \, \text{GeV}}$ for different electron simulations.

After the 50 GeV event selections have been applied to the simulations, the remaining events are merged with an adjustable weight w for each beam energy. These weights have been tuned to approximately generate the low-energy background. Figure 8.20, left, shows the distribution of the total energy, E_{total}, without E_3/E_{total} selection for data, the merged simulation and the single simulations of different beam energies with the corresponding weights applied, as listed in the legend of the figure. Data and the merged simulation are normalized to their total number of entries. The single energy simulations are not normalized to the number of their entries, but to the number of entries in the merged simulation, N_{merged}, and scaled with the weight they contribute, resulting in a scaling of each bin content by a factor $s = w/N_{merged}$. Like this, their contribution to the merged simulation can be read easily.

The merged simulation now also includes entries within the low-energy region. Also, the rising flank at around 1000 MIP agrees better to data than before (see Figure 8.19, right). Though the merged plot does not contain enough simulations with different beam energies to fill the complete low-energy background as visible in data, it still demonstrates, that electrons with lower beam energy can actually generate such a background. Also because of the absence of additional beam energy simulations, which could fill the gaps in the merged low-energy background simulation, the main peak within 1000 and 1400 MIP is still overestimated in simulation, albeit the overestimation is already reduced a lot compared to the simulation of 50 GeV electrons as shown before in Figure 8.19, right.

---

[2]In this case and as before, the selection cuts on the transverse COG are not applied in order to not bias the selection efficiency.
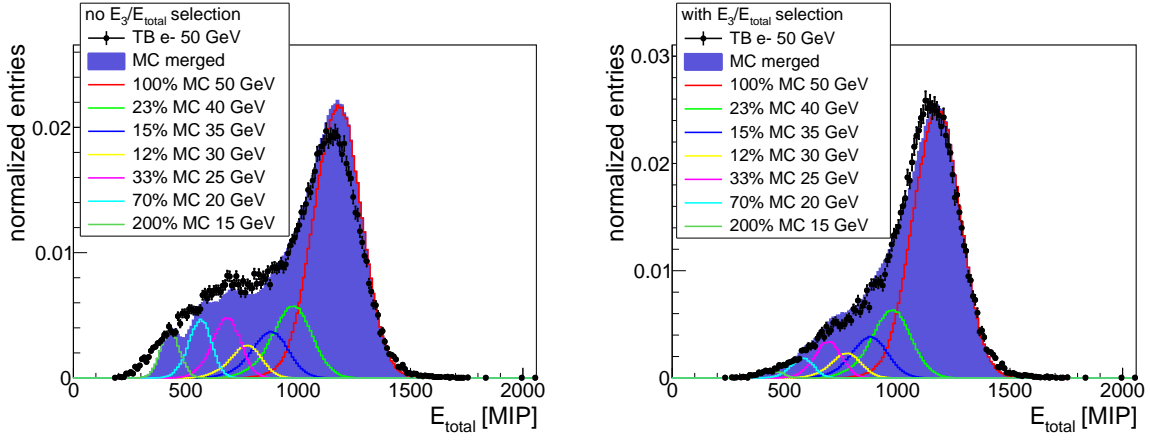
Figure 8.20.: Total energy distribution, E_{total}, for data, single simulations of different beam energies with applied weights and a merged simulation after applied 50 GeV electron event selection without E_3/E_{total} selection (left) and with E_3/E_{total} selection (right).

Another possibility to rebuild such a background would be to simulate electron beams with a steady energy distribution, that matches the observed background. The method used here is still reasonable and has the advantage, that the impact of the 50 GeV electron event selections can directly be read from the single energy simulations.

Lower beam energies of the single energy simulations lead to smaller means of the reconstructed total energy. Due to the 50 GeV event selection applied to all simulations, the weights have to increase for simulations with lower beam energies, in order to be consistent with the observed fraction of entries in the low-energy background of data. If the background in data is really caused by electrons, then it can be concluded, that it is generated by electrons with initial energy profiles with a maximum in the region somewhere within 0 to 20 GeV and decreasing fraction with higher energies. Only at around 40 GeV, where the weight has to increase again to rebuild the rising edge of the main peak in data, the fraction increases until it finally reaches 50 GeV, which is actually no background anymore, but signal. Also, from the absence of a considerable fraction of entries in data with total energies higher than what is expected from the 50 GeV simulation, it can be concluded, that no electrons with initial energies significantly higher than 50 GeV are present in the beam.

Still unclear is the discrepancy at the very first start of the background around 200 to 400 MIP. Here, not even 10 GeV electron simulations are capable to fill the gap between data and simulation within reasonable weights. Thus, no 10 GeV simulation is shown here. It is also questionable, whether such a large fraction of 200 % weighted 15 GeV electrons can be present in data, especially if compared to Figure 8.11. Most reasonable, also other additional unknown effects might contribute to the observed background.

Furthermore, Figure 8.20, right, shows the same distributions with the additional E_3/E_{total} selection applied to both, data and simulations.

With the E_3/E_{total} selection applied, which in this case allows some crosschecks, the merged simulation still agrees well with data, including the low-energy background. The fraction of events in the main peak agree better, which might be a result of the fact, that less gaps are visible in the simulated low-energy background, due to the additional selection.

Unfortunately, there are a few discrepancies: The mean position of the main peak in the merged simulation is, as before, a little shifted to higher total energies compared to data. This might be improved with the future tuning of the simulation parameters. Before the selection, there have been gaps in the simulated low-energy background due to the small number of single simulations merged, now, not only no gaps, but also a little higher fraction of events compared to data is present in this region. This might indicate, that also other effects might contribute to the observed background, as already mentioned.

The impact of the E_3/E_{total} selection on the single low-energy simulations is also visible in the reduction of entries of each corresponding peak. The impact is larger for lower beam energies, as already learned in Section 8.5.1.

All things considered, the agreement between data and the merged simulation is good enough to conclude, that at least a large fraction of the low-energy background can actually be a result of a contamination with low-energy electrons in data. In order to reject those events, an additional selection on the total energy itself is introduced next in Section 8.5.3.

8.5.3. Additional Cut on the Total Energy

The previously introduced E_3/E_{total} selection already reduces the fraction of low-energy events, but especially for high beam energies, a large fraction remains. The overlay of different low-energy electron simulations in Section 8.5.2 has suggested, that these events can to some extend actually be interpreted as real electrons with lower than intended energy. Thus, to finally reduce the remaining low-energy contributions, a cut on the total energy is performed, requiring $r_{E_{total}} \leq E_{total}$ with the minimum threshold $r_{E_{total}}$. Only a minor bias on the intended full energy electron is expected.

The thresholds $r_{E_{total}}$ are chosen such that the efficiency of this additional selection remains just above 99 % in simulation with low impact on the expected distribution and are listed in Table 8.13. Also included are the implications of this additional cut, expressed by the ratio $K = N_{incl.}/N_{excl.}$ between the number of selected events including all previously discussed selections and the new cut on E_{total}, $N_{incl.}$, and the total number of events excluding the latter, $N_{excl.}$.

Beam Energy [GeV]	$r_{E_{total}}$ [MIP]	$K_{e^-}^{MC}$ [%]	$K_{e^-}^{DATA}$ [%]
10	180	99.3	95.0
15	280	99.1	94.4
20	370	99.3	93.3
30	540	99.1	90.7
40	710	99.2	87.7
50	900	99.1	81.1

Table 8.13.: Additional event selection on the total energy, E_{total}, and efficiencies K_{e^-} on simulation and data.

While the ratio K is above 99 % for all simulations as required, it decreases with rising beam energy for data. While it is still high with 95 % at 10 GeV, K drops down to 81.1 % at 50 GeV. This again demonstrates, that the fraction of low-energy background increases with rising beam energy, which is accordingly rejected with this cut.
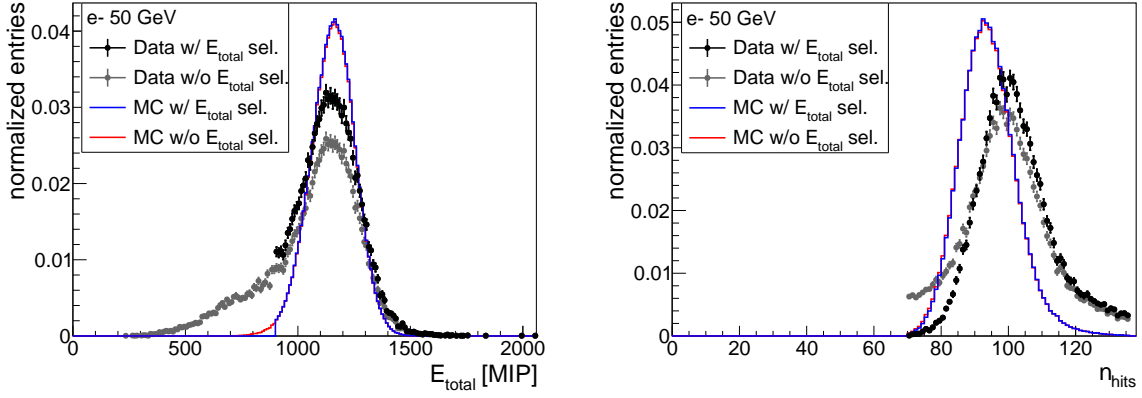
Figure 8.21.: Impact of the E_{total} selection cut on the total energy, E_{total}, itself, and on the total number of hits, n_{hits} for 50 GeV electrons in data and simulation.

Figure 8.21 shows the impact of the new selection cut on E_{total} by means of the total energy distribution itself (left) and of the total number of hits distribution, n_{hits}, for 50 GeV electron data and simulation with and without the new cut. While the selection is inefficient on the simulation and only a small part of the rising edge is cut off, the impact is larger for data. In the E_{total} distribution, a large fraction of the rising edge, including the low-energy background, is cut off with the new cut. This results in a significant increase of the relative fraction of events within the main peak and reduces the deviation between data and simulation. Still, the distribution in data remains wider than in simulation. This can have different reasons, most reasonably still a small fraction of low-energy electrons remains in the region around 50 GeV. Other reasons might be connected with not simulated mis-calibrations of single channels or an overestimated accuracy of the beam energy in simulation (cf. σ_E in Table 8.4). Altogether, the agreement between data and simulation is improved with the selection cut on E_{total}.

With regard to the distribution of n_{hits}, the mean positions in data and simulation do not agree well. The simulation underestimates the total number of hits, leading to a global shift between data and simulation as observed before (see Figure 8.16b). Actually, this discrepancy is dealt with later in Section 8.6 by tuning the simulation parameters, especially of the tile-to-tile optical crosstalk value, which directly influences the n_{hits}.

Thus, the main focus ought to be on the impact on the E_{total} selection on the n_{hits} distribution. While the impact is tiny as expected for the simulation, the new selection reduces the fraction of events with a low n_{hits} in data. Consequently, the relative fraction of events in the main peak increases and, apart from the global shift, agrees better to the shape in simulation. The fraction of events with $n_{hits} > 120$ in data remains nearly untouched and is not represented in simulation.

In this section, two additional data driven event selections for electrons have been discussed: a selection of the ratio of E_3/E_{total} and a selection of events, exceeding a certain total energy, E_{total}. Both selections reduce the low-energy background that has been observed in data. A comparison between data and a merged simulation, which includes different low-energy electron simulations, has verified, that the observed background can actually to some extend be a result of low-energy electron contamination. This permitted to apply a selection cut on the total

energy without major biasing the observation of the actually aimed electron with full intended energy.

8.6. Simulation Tuning

Now, that the first iterations of the simulation are done and validated with data, further improvements to the simulation are investigated. As previously mentioned in Section 8.1.2, the simulation can be adjusted with an additional upstream absorber placed directly in front of the detector in order to correct for unknown beamline material to some extent. The tuning of the thickness of this additional absorber is discussed in Section 8.6.1.

Subsequent in Section 8.6.2, the optical tile-to-tile crosstalk, which is included in the digitization procedure as described in Section 7.4.1, is tuned to improve the agreement between data and simulation.

As these two tunings have been part of several internal discussions, they are to some extend also discussed in [139]. Nevertheless, there are large differences between the reference and this thesis. For instance here, different and larger data and simulation sets are utilized and different event selections have been applied as discussed before. While in [139], the tuning of the absorber thickness is done by means of an energy weighted center of gravity (COG), here, a not energy weighted COG is utilized besides other observables, as discussed in the following. Concerning the tile-to-tile crosstalk tuning, the total number of hits is utilized as observable for the optimization in the reference, while here, hits from layers with and without tiles with reflective foil are distinguished, as discussed in a moment.

In the course of the simulation tuning presented here, additional 10^5 events per energy and per set of parameters have been simulated.

8.6.1. Additional Material Tuning

The material inside the beamline, upstream to the detector, is not well known. First comparisons between electron data and simulation have shown, that low-energy background is visible in electron data. This background might be introduced by upstream collisions with beamline infrastructure, thus material is missing in the simulation to describe the observed data.

First hints for this low-energy background have been found within the collaboration (see for instance [169]) due to a deviation between the center of gravity distributions in z, COG_Z, in data and simulation, while the latter did not include any additional upstream absorber at that point. It has been observed, that the incoming electron starts to shower earlier in data, resulting in a lower COG_Z, compared to the expectation. In order to verify that the geometry of the detector is well implemented in the simulation, data and simulation of a preceding electron test beam at DESY in June 2015 have been considered. [169] There, a similar detector prototype setup has been operated, but at a different beamline. A good agreement between data and simulation has been found, which leads to the result, that the detector geometry is in fact well simulated.

This gives rise to the presumption, that the mismatch arises from upstream beam collisions, which can to some extend by simulated by additional absorber in the beamline upstream to the detector. The decision to place the additional absorber directly in front of the detector has been
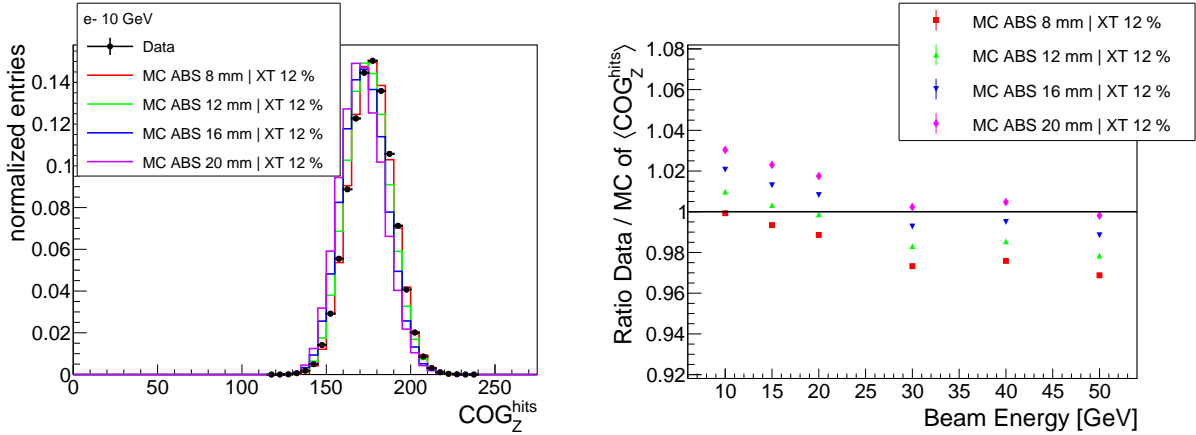
Figure 8.22.: Left: Not energy weighted center of gravity in z, COG_Z^{hits} for 10 GeV electron data and simulations. Right: Ratios between data and simulations of the mean of each corresponding COG_Z^{hits} vs. beam energy. The simulations include 12 % tile-to-tile crosstalk (XT) and different absorber thicknesses (ABS).

made in order to still be able to tune the transverse beam profiles. If the absorber would be split into different parts or placed further upstream away from the detector, the transverse profile measured in COG_X and COG_Y becomes wider and wider and independent of the initial setting, because of scatterings and too early showering. Like this, the transverse profiles couldn't be simulated well anymore. Maybe this issue could to some extend be bypassed by adding beam guiding systems in the simulation, but this would exceed this analysis.

To help out, an iron plate of additional absorber is added in front of the detector absorber structure in the simulation, right in front of the first ECAL layer (cf. Section 8.1.4.1). Like this, the additional widening of the transverse shower profile is harmless and can still be tuned with the particle gun parameters (cf. Table 8.4). A default additional iron absorber of 12 mm thickness has previously been chosen before this study and has already been included in the above analysis so far. This value has been selected after a first comparison between data and simulation beforehand, where only light event selections have been applied.

Now, that specific event selections for different particles and energies are estimated, a second analysis can be performed by more accurately testing absorber thicknesses of 8, 12, 16 and 20 mm.

The first approach to estimate the best thickness of the additional absorber is to optimize shower observables that are less affected by SiPM saturation or tile-to-tile crosstalk, because both of them still have to be optimized.

Figure 8.22, left, shows the not energy weighted center of gravity in z, COG_Z^{hits} (with $e_{hit}^i = 1$ in Equation 8.2), for 10 GeV electrons in data and simulations, the latter with different absorber thicknesses and fixed default 12 % tile-to-tile crosstalk. The hit energies are not taken into account in COG_Z^{hits} to be independent of any saturation effect. Still as always, the energy of the hit has to exceed the default 0.5 MIP cut in order to be counted. However, COG_Z^{hits} is still influenced by tile-to-tile crosstalk, which could increase the number of hit channels.

The mean of COG_Z^{hits} is around 170 to 180 in data. In simulation, the mean depends on the additional absorber thickness and decreases with rising thickness, as expected. The shapes of
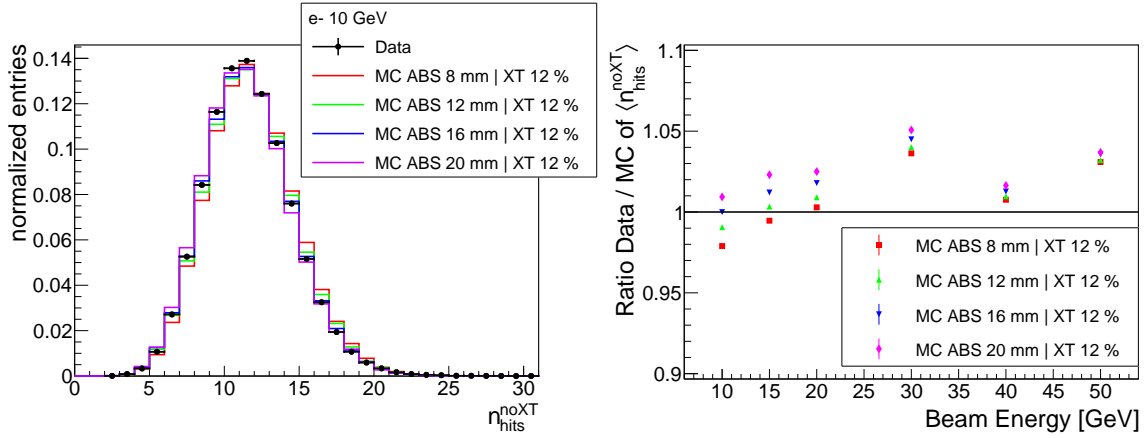
Figure 8.23.: Left: Total number of hits in all layers that are not affected by tile-to-tile crosstalk, n_{hits}^{noXT}, for 10 GeV electron data and simulations. Right: Ratios between data and simulations of the mean of n_{hits}^{noXT} vs. beam energy. The simulations include 12 % tile-to-tile crosstalk (XT) and different absorber thicknesses (ABS).

the simulations look similar, thus only the mean is analyzed in the following.

Figure 8.22, right, shows the ratio between data and simulation for the mean of COG_Z^{hits} for different absorber thicknesses and beam energies.

A remark: in order to improve the readability, the arithmetic *mean* is expressed here by surrounding *angular brackets* instead of the typical bar on top.

By comparing all absorber thicknesses it can be concluded, that independent of the beam energy, higher absorber thicknesses lead to lower $\langle COG_Z^{hits} \rangle$ in simulation, resulting in higher ratios. This just shows the wanted effect: by adding additional absorber material, the shower center of gravity is shifted to lower values, which implies an earlier start of the shower. For example, 8 mm absorber thickness results in a ratio of about 1 for 10 GeV, while a thickness of 20 mm leads to a ratio of about 1.03.

The ratio of the upper example of 8 mm absorber thickness becomes worse for higher energies. With rising energy, the ratio for all absorber thicknesses decreases between 10 and 30 GeV and remains approximately stable between 30 and 50 GeV. A thickness of 12 or 16 mm shows the best overall accordance concerning the maximum deviation from a ratio of 1 (which is approximately ≈ -0.02 at 50 GeV for 12 mm and $\approx +0.02$ at 10 GeV for 16 mm).

To decide between an absorber thickness of 12 or 16 mm, a second variable is taken into account. Figure 8.23, left, shows the total number of hits in all layers with individual tile-wrapping, which are thus not affected by tile-to-tile crosstalk, n_{hits}^{noXT}, for 10 GeV electrons in data and simulations. Again, the simulations include 12 % crosstalk and vary in different absorber thicknesses. In n_{hits}^{noXT} only hits in layers 3 and 11 to 14 are taken into account. Layers with tile-to-tile crosstalk are ignored here, since the number of hits strongly depends on the simulated tile-to-tile crosstalk, which is discussed in the next section.

The mean of n_{hits}^{noXT} in data is around 11 hits for 10 GeV. In simulation, higher absorber thicknesses shift the mean to lower values and vice versa. For this beam energy, an absorber thickness of maybe 16 mm agrees best with data. How does it look for the other beam energies?
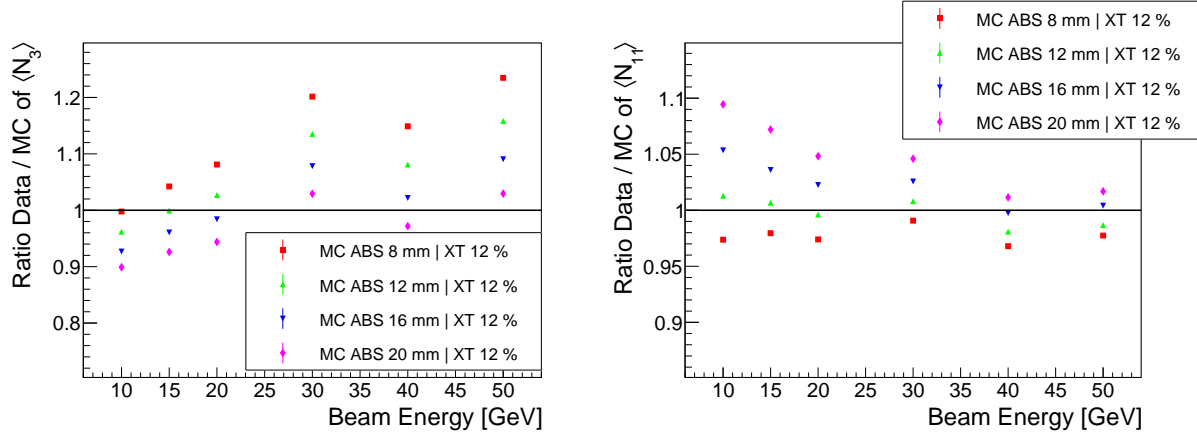
Figure 8.24.: Ratios between data and simulations for the mean of the number of hits in layer 3, $\langle N_3 \rangle$, (left) and layer 11, $\langle N_{11} \rangle$, (right) as a function of the beam energy, for different absorber thicknesses (ABS) and 12 % tile-to-tile crosstalk (XT).

Figure 8.23, right, shows the ratios between data and simulations of the mean of each corresponding n_{hits}^{noXT} for different beam energies. As similar seen before, higher absorber thicknesses lead to lower $\langle n_{hits}^{noXT} \rangle$ in simulation, resulting in higher ratios within a fixed beam energy. This can be seen for all energies except for 50 GeV, where the ratios of 20 and 16 mm are nearly the same. This can be explained by the above observation, that more absorber thickness leads to an earlier shower center of gravity, which results in more hits in early layers and in a reduction of hits in late layers. Since n_{hits}^{noXT} only takes into account the first and the four last layers, the impact of shifting the shower center of gravity results in less hits in the last layers and more hits in layer 3.

In order to study the impact of the absorber thickness in more detail, Figure 8.24 shows the ratio between data and simulation of the mean number of hits in layer 3, $\langle N_3 \rangle$, (left) and layer 11, $\langle N_{11} \rangle$, (right). Both of these layers are not directly [3] affected by tile-to-tile crosstalk. The number of hits in the early layer 3 displays the effect of an earlier start of shower much better than a late layer 11, where only the tail of the shower is recorded. Therefore, the information from layer 3 is weighted higher for the choice of the additional absorber thickness.

The ratio between data and simulation for $\langle N_3 \rangle$ and $\langle N_{11} \rangle$ shows the above expected behavior. In layer 3, an increase of the absorber thickness in simulation results in more hits and therefore a lower ratio. As expected, the opposite is the case for layer 11, where a higher absorber thickness leads to a lower number of hits and a higher ratio.

The impact of different absorber thicknesses is more crucial for layer 3, as the ratios even exceed 1.2, while remaining lower than 1.1 for layer 11, which supports a higher weight for layer 3 concerning the choice of the absorber thickness.

With rising energy, the ratio of $\langle N_3 \rangle$ increases within 10 to 30 GeV, then is reduced at 40 GeV and again increased at 50 GeV and behaves similar but mirrored to the ratio of $\langle COG_Z^{hits} \rangle$ above. For both layers it can be concluded, that for low energies, a small absorber thickness leads to

---

[3]Not directly affected by tile-to-tile crosstalk means, that no crosstalk is foreseen in these layers, but still there could be small differences due to applied event selections, taking into account information from layers with crosstalk.

good ratios close to 1, while for higher energies, higher absorber thicknesses work better. For layer 11, this is not the case for 30 GeV, but still at higher energies, a thicker absorber also leads to better ratios, while it remains stable and good for 12 mm within 10 to 30 GeV.

It is apparent, that the best agreement between data and simulation of $\langle N_3 \rangle$ and $\langle COG_Z^{hits} \rangle$ could be reached by energy-dependent absorber thicknesses. This could be explained by different applied settings of beam steering parameters for the beamline with different beam energies during data taking.

Nevertheless, the information from Figure 8.22, right and Figure 8.24, left, are utilized to chose a final global iron absorber thickness of 16 mm.

With 16 mm thickness, the maximal deviation from a ratio of 1 is minimal over all energies with the highest deviation of approximately +0.09 at 50 GeV for $\langle N_3 \rangle$ and approximately +0.02 for $\langle COG_Z^{hits} \rangle$. Checking the two other plots, the maximum deviation for $\langle n_{hits}^{noXT} \rangle$ is smaller than +0.05 and for $\langle N_{11} \rangle$ smaller than +0.06 and can therefore be verified.

8.6.2. Optical Tile-to-Tile Crosstalk Tuning

With the new iron absorber thickness of 16 mm applied to the simulation, the tile-to-tile crosstalk can now be optimized. As a reminder, layers 4 to 10 are equipped with tiles without individual wrapped foil, which might lead to optical crosstalk from one tile to a neighboring tile.

In the digitization of simulated events, a first order tile-to-tile crosstalk correction is applied, as described in Section 7.4.1. A default crosstalk value of 12 % has been selected as a first estimate and has been applied in the upper analysis. For this preselection, a comparison between data and simulation of the total number of hits, n_{hits}, with only light event selections applied, has been utilized before this study.

Now, that precise event selections are applied to data and simulation, the tile-to-tile crosstalk value can be optimized. Therefore, simulations with five different crosstalk values are generated with 8 %, 12 %, 14 %, 16 % and 20 %. These values are global for all tiles within one simulation. Still in reality, there could be minor differences from channel to channel, because of variances in the gluing process of the tiles to the boards or in the chemical etching of the tile edges.

To estimate the impact of different tile-to-tile crosstalk values, the total number of hits of all layers, which include tiles without individual wrapped foil, where crosstalk is expected, n_{hits}^{XT}, is compared between data and simulation. The ratios between data and simulation of the associated means, $\langle n_{hits}^{XT} \rangle$, are plotted in Figure 8.25, left, for different crosstalk values.

An increase of the crosstalk value results in a higher number of hits in simulation and therefore in a lower ratio, as expected. This observation is the case for all beam energies. With rising beam energy, the ratios increase between 10 and 30 GeV, then decrease slightly at 40 GeV and increase again at 50 GeV.

For small beam energies, lower crosstalk values lead to better ratios, while for large beam energies, higher crosstalk values do. To some degree, this can be explained by the fact that tile-to-tile crosstalk is only simulated in first order, by only taking into account the four direct neighbors (top, bottom, left, right). Especially for high energy hits (whose rate increases with higher beam energy), the second order becomes more and more relevant, where neighbors of direct neighbors have to be considered, too. A hit is only counted, if the energy in a tile exceeds the 0.5 MIP cut.
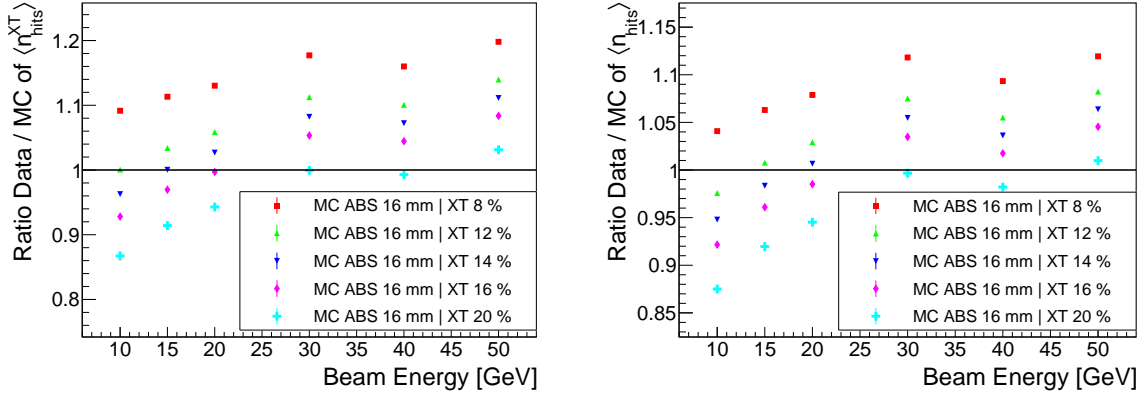
Figure 8.25.: Ratios between data and simulations of the mean of the total number of hits in all layers with tile-to-tile crosstalk (layers 4-10), $\langle n_{hits}^{XT} \rangle$, left, and of all layers, $\langle n_{hits} \rangle$, right, as a function of the beam energy, for different tile-to-tile crosstalk values (XT) and 16 mm additional absorber thickness (ABS).

If new hits, created as consequences of first order crosstalk corrections, include enough energy to generate themselves a new hit in a neighboring tile, the first order correction is not sufficient anymore. Another reason might be the neglected crosstalk to diagonal tiles, which, especially in combination with second order corrections, would increase the probability to trigger a new tile, too.

There are three apparent possibilities to proceed. First, a second order crosstalk correction could be added to the digitization software, second, to compromise the next order effects, different crosstalk values could be chosen for different beam energies, and third, one single crosstalk value could be chosen such that the ratio between data and simulation is described in an acceptable way over all beam energies.

As it turns out, Figure 8.25, left, shows a good agreement if the second approach is followed such that different energy-dependent crosstalk values are chosen. Still, in order to keep the amount of free parameters as small as possible, only one fixed crosstalk value is chosen, finally following the third approach. The lowest maximum deviation from a ratio of 1 is achieved with a crosstalk value of 16 %, resulting in a deviation from a ratio of 1 of less than -0.08 at 10 GeV and less than $+0.09$ at 50 GeV.

The crosstalk value of 16 % has been chosen from the hit information of layers equipped with tiles *without* individual wrapping, exclusively. To estimate the impact of the choice for *all* active layers, the ratio between data and simulation of the mean of the total number of hits, $\langle n_{hits} \rangle$, is plotted in Figure 8.25, right.

The shape of this plot is similar to the shape of Figure 8.25, left, apart from a few shifts. It now contains the hit information of all layers, including those without tile-to-tile crosstalk (cf. Figure 8.23, right). It turns out that for 10 GeV, the deviation from a ratio of 1 is less than -0.08 comparable to before, while for 50 GeV, the deviation becomes a bit smaller with less than $+0.05$. Though for $\langle n_{hits} \rangle$, a tile-to-tile crosstalk value of 14 % shows even a bit lower maximum deviation from a ratio of 1, this is influenced by additional effects not introduced by crosstalk itself and therefore the 16 % crosstalk remains the best choice.
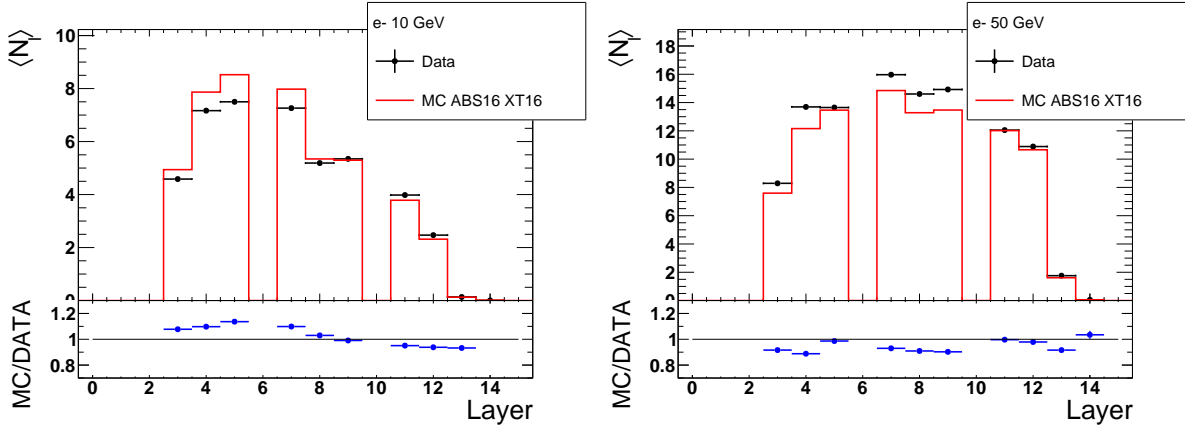
Figure 8.26.: Shower profiles of the mean number of hits per layer, $\langle N_l \rangle$, for data and simulation of 10 and 50 GeV electrons. On the bottom of each plot, the ratio between simulation and data is shown.

8.6.3. Data and Simulation after Simulation Tuning

After the final event selections have been applied and the additional absorber thickness and tile-to-tile crosstalk value have been optimized in the previous subsections, the resulting shower profiles are now compared between data and simulation.

Electrons

Shower profiles of the mean number of hits for each layer, $\langle N_l \rangle$, are plotted in Figure 8.26 for electron data and simulation. Layers 1, 2, 6 and 10 are inactive and include no entries. Following Table 8.1, the distances and the numbers of absorber plates in the last four layers 11 to 14 increase from layer to layer.

The hits shower profile increases in data and simulation from layer 3 to layer 5 for 10 GeV, and from layer 3 to 8 for 50 GeV, respectively. After reaching the maximum, the mean number of hits decreases until the last layer 14 for both energies, with an exception in layer 9 for 50 GeV and for 10 GeV, the latter only in data. The exception in layer 9 can be explained by a large fraction of inactive channels in layer 8 (for maps of inactive channels refer to Appendix H), resulting in less reconstructed hits there. Figure D.1 in the appendix includes the hits profiles for the other beam energies, where a similar behavior is found.

A rising beam energy results in an increasing total number of hits and in a deeper hits shower profile, with an increasing amount of hits, especially in the second half of the detector.

Due to the choices of energy independent additional absorber and tile-to-tile crosstalk values, it is expected, that for lower beam energies, an on average larger total number of hits is simulated compared to data, while for higher beam energies, the situation is reversed. This is visible in the hits shower profiles, too, where especially the mean number of hits in layers 3 to 9, where most of the shower energy is deposited as shown soon, follow this assumption.

Except layer 14, where hits are mostly suppressed due to the electron selection (cf. Section 8.3.2), the simulation describes the data well within less than 20 % deviation from a ratio of 1 for all beam energies.

The shower profiles of the mean energy in layers, $\langle E_l \rangle$, are shown in Figure 8.27 for 10 GeV
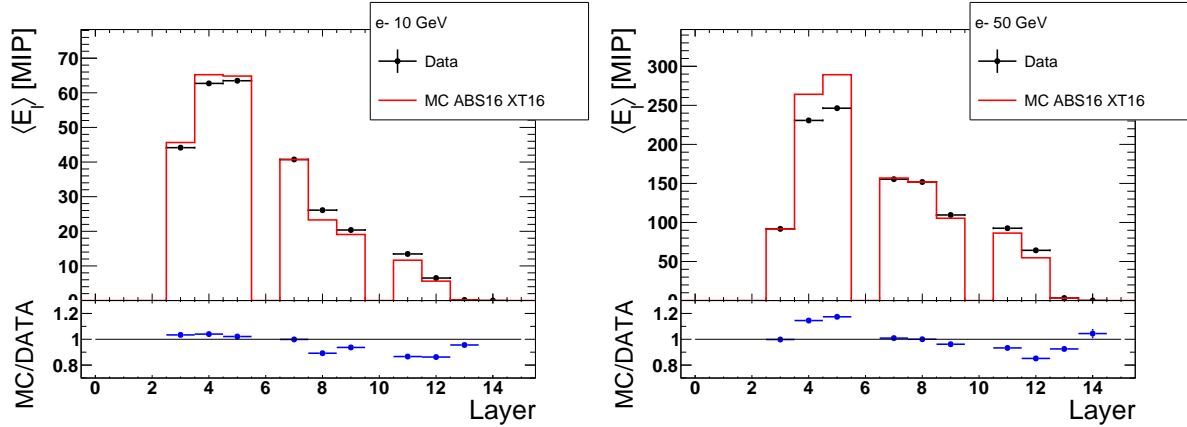
Figure 8.27.: Shower profiles of the mean energy in layers, $\langle E_l \rangle$, for data and simulation of 10 and 50 GeV electrons. No de-saturation is applied. On the bottom of each plot, the ratio between simulation and data is shown.

and 50 GeV electrons and additional beam energies are shown in the appendix in Figure D.1. For data and simulation, the energy profiles also increase from layer 3 to 5 for all beam energies, with one small exception in simulation for 10 GeV, where the maximum is already reached at layer 4; and decrease behind layer 5, with again one small exception for simulation at 30 GeV in layer 9. As discussed above, this exception has its origin in the inactive channels of layer 8. Still, the effect of less hits in layer 8 is not as dominant on the mean energy of this layer, compared to the related mean number of hits. The reason is, that most of the inactive channels are located outside the inner channels of the layer. While most of the energy of the shower is deposited in the inner channels, the outer channels include less energy.

Similar as above, a rising beam energy results in an increasing total energy in generally all layers, especially in the front.

The impact of the choice of the *constant* additional absorber and tile-to-tile crosstalk values cannot be directly estimated from these plots, since the amplitude depends not only on the number of hits, but significant on the energy of each hit. Therefore also response saturation of the SiPM-tile system matters here.

Compared to data, the conspicuous too high amplitudes in layers 4 and 5 over all beam energies in simulation might originate from an underestimated saturation behavior of the response in simulation, while a too high tile-to-tile crosstalk value might not be the reason if compared to Figure 8.26, where the mean number of hits in simulation lies above data for low and below data for high beam energies, respectively. The tuning of the channel response saturation is discussed next in Chapter 9.

Again, except for layer 14, where energy depositions are mostly suppressed due to the electron selection, the simulation describes the data well within less than 20 % deviation from a ratio of 1 for all beam energies.

Pions

Now that the comparison between electron data and simulation with the new parameters of the additional absorber thickness of 16 mm and the tile-to-tile crosstalk of 16 % have been discussed,
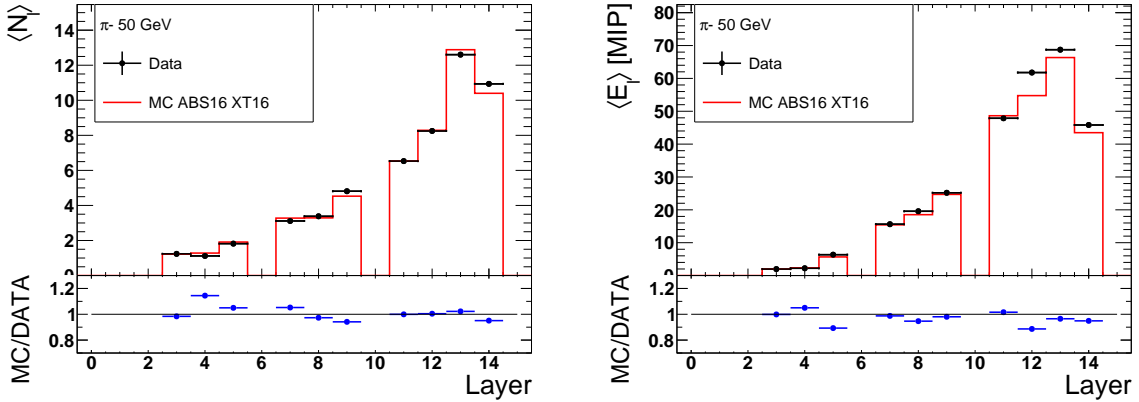
Figure 8.28.: Shower profiles of the mean number of hits per layer, $\langle N_l \rangle$, (left) and of the mean energy per layer, $\langle E_l \rangle$, (right) for data and simulation of 50 GeV pions. No de-saturation is applied. On the bottom of each plot, the ratio between simulation and data is shown.

the comparison for pion data and simulation follows briefly.

It should be mentioned, that it is unclear, whether the pion beam is also influenced by upstream material, as pions generally penetrate iron further before showering. In any case, the thin additional absorber does not have a large impact on the pion shower shape and as shown next, data and simulation with the additional absorber are in rather good agreement.

The shower profiles of the mean number of hits per layer, $\langle N_l \rangle$, and of the mean energy in layers, $\langle E_l \rangle$, are shown in Figure 8.28 for 50 GeV pions in data and simulation. Profiles for additional beam energies can be found in the appendix in Figure D.2.

For all beam energies, the mean number of hits per layer, $\langle N_l \rangle$, increases on average with proceeding layers, until the maximum is reached at layer 12 or 13, depending on the beam energy. Small discrepancies from this trend can be found in layers 4 and 8. At 90 GeV, the maximum in data is even found in the last layer 14. By the way, this has a direct impact on the expectable energy resolution for pions of the prototype, since it shows, that the shower is not completely covered within the active layers. But of course, this is anyway not the case due to the empty slots and inactive layers within the prototype.

With increasing beam energy, the mean of the hits shower profile increases for both, data and simulation, suggesting an increase of the pion shower depth itself. Compared to electron hits profiles, pion showers show less hits in the first half of the detector but penetrate the detector much further, which results in many more hits in the last layers.

The pion energy shower profiles are similar to the hits profiles in many ways. Also here, in spite of a few minor deviations, the mean energy increases with proceeding layers, until a maximum is found at layer 12 or 13, depending on the beam energy. The mean energy sinks between layer 13 and 14 for all beam energies. Still, a significant fraction of energy is reconstructed in this last active layer, which also supports the upper assumption concerning the expected loss of resolution of the prototype.

The agreements between simulation and data of the shower profiles of both, the mean energy and the mean number of hits, are again well within 20 % deviation from a ratio of 1 for all beam

energies.

Finally a short comparison between electron and pion shower profiles is given. While electrons tend to shower early and deposit a large fraction of their energy within the first layers, pion showers penetrate the detector further and deposit high fractions of their energy in the last active layers. Comparing the maximum energy deposition in single layers at 50 GeV, electron showers deposit much more energy within single layers than pion showers do. While the maximum for pions at 50 GeV can be found in layer 13 with around 65 to 70 MIP in data and simulation, for electrons it is much larger with around 250 to 290 MIP in layer 5, depending on whether data or simulation is chosen.
Therefore, the impact of SiPM response saturation is expected to be very much larger for the reconstruction of electron than for pion showers.

8.6.4. Short Summary

In this section, the tuning of two simulation parameters has been discussed. The additional absorber thickness and the tile-to-tile crosstalk value especially influence the number of hits in the simulation. Different values have been investigated and 16 mm absorber thickness and 16 % crosstalk have shown the best overall results and thus have been selected. Comparisons of shower profiles have shown, that the simulation describes the data well within less than 20 % deviation. Particularly high energy depositions have been recognized for electrons, coming along with discrepancies between data and simulation, underlining the need for an improved response saturation handling of the SiPM-tile system, which is discussed in the following chapter.

9

Channel Response Studies, Uncertainties and Linearity & Resolution

The linearity of the response of the detector prototype depends primarily on the linearity of the response of the single channels, which the detector modules are equipped with. One channel comprises a scintillator tile and a SiPM. Therefore, a good knowledge and modeling of the response of the SiPM-tile system is key to handle and correct for possible non-linearities induced by SiPM saturation. Unfortunately, no direct measurement of the response of the combined SiPM-tile system is available. Therefore, different response models are applied to the simulation and compared to data.

Section 9.1 first describes the method utilized to study the SiPM-tile response, including necessary modifications in the digitization and reconstructions procedure. Particular attention is payed to the handling of light yield in order to maintain the MIP calibration of the detector prototype. In the following Sections, the results of the response study are discussed in detail.

Thereafter from Section 9.8 on, dominant systematic uncertainties are discussed and a final comparison between data and simulation with inverted optimized SiPM-tile response models, implying de-saturation, is presented.

Using these final results, a short study of the linearity and energy resolution of the detector prototype is presented in Section 9.9.

9.1. Tuning the SiPM Response Saturation

Saturation of the SiPM response directly reduces the reconstructed energy of the detector. This non-linearity is more sufficient, the higher the deposited energy in a single channel is. On the other hand, optical crosstalk within the SiPM itself (not to be mistaken with tile-to-tile crosstalk) increases the observed number of fired pixels, N_{fired} and therefore the reconstructed energy especially at low deposited energies. With increasing deposited energy, the impact of SiPM crosstalk decreases because of the concurrently reduced number of un-fired pixels of the SiPM. A model which handles both, saturation and crosstalk effects, is therefore essential for the AHCAL prototype to manage the reconstruction of the full energy scale from a few to thousands of MIPs.

So far, all presented data has shown saturated and crosstalk affected responses of each SiPM.[1] To compare to data and to validate the simulation, the simple exponential SiPM response model, as discussed in Section 4.3.3.1), has so far been utilized within the digitization of the simulation

---

[1]Note that other SiPM noise like afterpulses might also play a role but are not considered here.

(cf. Section 7.4.2). This model includes the effective total number of pixels, N_{total}^{eff}, or short N_{total}, but can also be tuned to higher or lower values. Like this, different saturation behaviors of the SiPM can to some extend be simulated.

The simulation presented so far uses the simple exponential SiPM response model with N_{total} being the physical total number of pixels of each SiPM as they are already listed in Table 8.2. Previously in Section 6.5, different SiPM response models have been discussed. In contrast to these measurements, now in the AHCAL detector prototype, the SiPM is within a combined system with a scintillator tile. Thus, it is not illuminated directly by an external light source, but illuminated by photons generated from traversing particles due to the scintillation process. In this combined SiPM-tile system photons usually have a broader time distribution, because of the scintillating process itself and due to different paths (including reflections) the photons take, until they reach the SiPM. This can lead to over-saturation ($N_{fired} > N_{total}$), mainly because of the recovery of the SiPM pixels within the integration time window. Also, the SiPM itself might imply some over-saturation, depending on the SiPM-type (cf. Section 6.5.3).

The simple exponential model can to some extend compensate over-saturation by increasing the parameter N_{total}. Though, it does not handle SiPM crosstalk at all.

In order to account for response saturation and SiPM crosstalk, different response models are analyzed and tuned in this chapter. The method is explained in Section 9.2 and key observables are discussed in Section 9.3. Thereafter, the results for two different response models are discussed in Section 9.5 and Section 9.6 and a conclusion is given in Section 9.7.

9.1.1. Clarification: Response Model vs. Inverted Response Model

First, some clarification is given about the difference between the *response model* and the *inverted response model*.

A **response model** $f_{response}$ is used to model the response of the SiPM-and-tile system within the digitization process of the simulation (cf. Section 7.4.2). The model simulates saturation and crosstalk effects of this SiPM-tile system. Therefore, it converts the initial signal into a saturated and crosstalk affected signal. Like this, the simulation should comply the state of data, which is affected by saturation and crosstalk when measured.

On the other hand, the **inverted response model** $f_{response}^{-1}$ inverts the saturation and crosstalk effects of the SiPM-tile system and can be applied within the reconstruction procedure for data and simulation (cf. Section 7.1.1). Therefore, is converts a saturated and crosstalk affected signal (as it is for pure data and digitized simulation) back to the (expected) initial signal.

9.2. The Method

In this subsection, the method applied to study and optimize the handling of response saturation is explained in detail. First of all, it is important to keep in mind that all measured data, presented so far, includes saturation and crosstalk effects of the combined SiPM and tile system. As a reminder, the simulation so far utilizes the simple exponential SiPM response model within the digitization procedure to saturate simulated energies.

There are two different approaches to tune and compare different models: First, one could apply an inverted response model to data, which de-saturates energies and takes into account SiPM crosstalk (and other) effects and compare the results to a non-saturated simulation. This approach has the disadvantage, that digitized simulation would no longer be directly comparable to raw data, which would miss the initial aim of simulation and digitization. Also, other digitization perspectives, as pixel smearing, could not be covered easily, if the energy would not have been saturated first. In the second approach, which is taken in the following, a model is applied to the simulation in order to match it with pure data - which intrinsically includes all saturation and crosstalk effects. Following the second approach, the digitized simulation will, as it should, be comparable to data already before the reconstruction procedure (c.f. Section 7.1), in which no inversion of the response model is applied in the first step.

Once different models have been compared and a preferred one is optimized, the inversion of this response model can then be utilized to invert the effects of saturation and crosstalk in both, data and simulation. This inverted model is then applied within the reconstruction procedure.

Now that an overview of the method is given, the procedure of the model optimization itself is discussed. As pointed out, different response models $f_{response}$ are tested and applied to the simulation within the digitization procedure, as introduced in Section 7.4.2. Within the digitization, many different aspects are covered. In the following, a short wrap-up of the digitization and reconstruction steps is given, highlighting important steps where the response model has an impact. For a detailed description, refer to Section 7.4 and 7.1. First consider the **digitization** procedure:

1. Simulated energy deposits are converted from GeV scale to MIP scale, utilizing a MIP-to-GeV factor from simulation.

2. A minimum MIP threshold of 0.5 MIP is applied. The position where this cut is performed is moved to the end of the digitization procedure, in order to allow a response model to increase the initial energy from lower to above 0.5 MIP threshold, because of the impact of SiPM crosstalk.

3. Tile-to-tile crosstalk is estimated and added.

4. The simulated deposited energy within one tile, E_{MIP}^{MC}, is converted from MIP scale to a number of seeds scale: $N_{seed} = E_{MIP}^{MC} \cdot LY$. Here, the number of seeds, N_{seed} (c.f. Section 4.3.2), is defined by the number of photons on the SiPM, n_γ, multiplied with the SiPM photon detection efficiency, ϵ_{PDE}: $N_{seed} = n_\gamma \cdot \epsilon_{PDE}$. Therefore, N_{seed} is a direct representative of the number of photons that would trigger an avalanche and fire a pixel in case of no saturation. The light yield, LY, will be important in the following study, because it is determined in a measurement, which is affected by saturation and crosstalk itself. More about this follows below.

5. The number of pixels fired is estimated by applying a response model function, $f_{response}$, on the number of seeds: $N_{fired}^* = f_{response}(N_{seed})$. This is the main point of this study, where different response models can be applied and tested.

6. The number of pixels fired is smeared by applying binomial smearing:
   $N_{fired} = f_{smear}(N^*_{fired}, N_{total})$.

7. The number of pixels fired is converted to the scale of ADC counts and noise is added.

At this point, data and simulation are comparable to each other. Afterwards, the **reconstruction** procedure converts back the amplitudes from ADC counts to energies in units of MIP:

1. For data only: the pedestal is subtracted and low- to high-gain intercalibration is applied.

2. Amplitudes in ADC counts are converted to the number of pixels fired scale.

3. In case it is wanted (not so far), the inverted response model is applied to convert from number of pixels fired to number of seeds: $N_{seed} = f^{-1}_{response}(N_{fired})$.

4. Final conversion to MIP-scale: $E_{MIP} = N_{seed}/LY$. The role of light yield is discussed below.

As a final step, events are selected offline utilizing the previously defined event selections for electron or pion showers (for example see Section 8.3).

With the overview of the digitization and reconstruction steps given above, next, needed adaptations are discussed. The most obvious modification is the response model itself. By applying different response models with various parameter combinations in the digitization, the resulting agreement between data and simulation can be studied and compared.

As indicated above, the **light yield** itself has to be taken care of. The light yield LY is a *measured value* which represents the number of pixels fired (and to be precise: not photons) for one minimum ionizing particle perpendicular traversing a tile. Because the light yield is a measured value, it depends on the response of the SiPM-tile system itself, and therefore is affected by possible saturation and crosstalk. Thus, in order to really estimate N_{seed}, the light yield has first to be corrected for these effects. The converted light yield, LY_{seed}, does not represent the number of pixels fired anymore, but the number of photons times PDE, induced by a minimum ionizing particle. To achieve that conversion, the light yield has to be applied to an inverted response function, as shown in Equation 9.1.

$$LY_{seed} = f^{-1}_{response}(LY) \tag{9.1}$$

Thus, LY_{seed} depends on the response model itself. A side note: In case of the advanced response model, an analytic inversion of the function is not available. Therefore, another approximation method is applied, as discussed later in Section 9.6.1.

This step of converting the light yield from units of pixels to seeds is crucial, because any response function needs N_{seed} as an input parameter. Does that mean, all previously presented results are wrong? No, because LY and LY_{seed} only differ if, on one hand, saturation decreases the number of pixels fired for one MIP, which is negligible, and on the other hand, if crosstalk is taken into account within the response model, which has not been the case so far. Thus, the light yield only has to be converted, if SiPM crosstalk (or large saturation also at small numbers of pixels fired) is taken into account in the response model.

An important note: With the light yield conversion applied, the *MIP calibration* of the detector *is still valid* after applying different response models. Step 4 of the digitization procedure listed above is adjusted to $N_{seed} = E_{MIP}^{MC} \cdot LY_{seed}$.

In the reconstruction procedure, first of all, no inverted response model is applied here and has been applied in the previous results. This is simply because a comparison between data and simulation should be done with the minimum needed steps applied to the observed data, in order to minimize subsequent uncertainties. In case no inverted response model is applied in the reconstruction, the default light yield LY without conversion is applied to both, data and simulation, in step 4, because then the light yield in units of pixels fired is the intended one. In this case, step 3 is skipped and the equation in step 4 is adjusted to $E_{MIP}^{sat} = N_{fired}/LY$. Whenever an inverted response model is applied in the reconstruction, and if this model includes crosstalk effects, the converted light yield, LY_{seed}, has to be taken into account instead of the default light yield, because the result of the inverted response function is N_{seed} (rather than N_{fired}). Therefore, $E_{MIP} = N_{seed}/LY_{seed}$ has to be applied in step 4 of the upper reconstruction list.

9.2.1. Inverted Response Model Application with Event Selections

In this study, an additional adjustment is performed in the reconstruction procedure. Event selections, which involve selections on energies, would not be sufficient anymore, but need adjustments in case the inverted response model is applied. To bypass this issue, the reconstruction procedure is adjusted as follows:

Instead of directly applying the inverted response model in step 3, first, this step is skipped and saturated energies are converted to E_{MIP}^{sat} as described above. Then, event selections can be applied as usual. Afterwards, the last step is inverted to receive back the number of pixels fired: $N_{fired} = E_{MIP}^{sat} \cdot LY$, explicitly utilizing the default (crosstalk and saturation affected) light yield. Then, the inverted response model can finally be applied just as described in step 3: $N_{seed} = f_{response}^{-1}(N_{fired})$ and converted to $E_{MIP} = N_{seed}/LY_{seed}$, utilizing the converted light yield.

9.2.2. Example

To visualize the method and to explain the need for a light yield conversion, an example is discussed in the following.

Let's assume, a high energetic muon traverses a tile. The most probable deposited energy in this tile is the definition of 1 MIP. Due to the scintillation process, a number of photons n_{scint} is generated. The final number of photons which hit the SiPM, n_γ, depends on the efficiency for the generated photons to hit the sensitive area of the SiPM, ϵ_{tile}:

$$n_\gamma = n_{scint} \cdot \epsilon_{tile} \tag{9.2}$$

This efficiency ϵ_{tile} mainly depends on the uniformity of the tile and on the effectiveness of the guidance of photons onto the sensitive area of the SiPM. Ideally, the whole sensitive area of the SiPM is illuminated uniformly. In reality, there might be hot spots on the SiPM on one hand, and the illuminated area might be larger or smaller than the sensitive area of the SiPM on the

other hand. This might affect the SiPM response in the first case and lead to lower ϵ_{tile}.

Let's assume, after efficiencies, most probable $N_{seed} = n_\gamma \cdot \epsilon_{PDE} = 20$ photons are generated by an incoming muon. If the SiPM features 1600 total pixels and a crosstalk factor of $\epsilon_C = 0.2$, than this initial $N_{seed} = 20$ will result in approximately $N_{fired} = f_{response}\left(N_{seed}\right) \approx 23.8$ [2] pixels fired, which represents the most probable value of the measured light yield. Here, effects like saturation, which lowers the number of recorded pixels fired, and crosstalk, which, on the other hand, increases it, are taken into account. Since here $N_{fired} > N_{seed}$, crosstalk plays a larger role at these low numbers of pixels fired. To estimate the initial N_{seed}, which is needed to apply any response model, this light yield value is now converted as intended above in Equation 9.1: $LY_{seed} = f_{response}^{-1}\left(23.8\right) = 20\,\mathrm{MIP}^{-1}$.

Now assume the case where an electron shower deploys 10 MIP in a tile. Following the adjusted step 4 of the upper digitization procedure, $N_{seed} = 10 \cdot LY_{seed} = 10 \cdot 20$. This leads to $N_{fired} = f\left(200\right) \approx 221.2$ pixels fired. [2]. In the purpose of this example, smearing and conversion to the scale of ADC counts is skipped.

Afterwards, we could either not apply the inverted response function and receive a saturated and not crosstalk corrected $E_{MIP}^{sat} = N_{fired}/LY \approx 9.29$ MIP, as it is done in the purpose of this response optimization study. Or once a reasonable model is found, the inverted response function can be applied, which returns the initial energy $E_{MIP} = N_{seed}/LY_{seed} = f^{-1}\left(221.2\right)/\left(20\,\mathrm{MIP}^{-1}\right) = 200/20\,\mathrm{MIP} = 10\,\mathrm{MIP}$.

9.3. Response Model Observables

The method and the needed adjustments to the digitization and reconstruction processes have been explained. Each response model utilizes different parameters, which can be tuned to optimize the agreement between data and simulation. To evaluate the different parameter combinations, specific observables are needed to reduce the large amount of information to a single significant value. These observables will help to classify the advantages and disadvantages of each response model.

As pointed out previously, the response models are applied to simulation only and the results are compared to data. To study the impact of different parameter combinations, three initial observables are considered for each beam energy and separately for each layer:

1. The deviation from one of the ratio of the two means of the energy distributions of each considered layer l of simulation and data : $|1 - \langle E_l \rangle_{MC}/\langle E_l \rangle_{DATA}|$.

2. The chi-squared, $\chi^2_{E_l}$, divided by the number of degrees of freedom, NDF_{E_l}, calculated using Pearson's chi-squared test with the two distributions of the energy, E_l, in each considered layer l of simulation and data (comparable to Figure 8.16a, but for one layer only).

3. The chi-squared, $\chi^2_{e_l}$, divided by the number of degrees of freedom, NDF_{e_l}, calculated using Pearson's chi-squared test with the two distributions of the hit energies, e_l, in each

---

[2]Values estimated with the advanced response model.

considered layer l of simulation and data (comparable to Figure 8.15, but for one layer only).

As a reminder and as listed in the previous Table 8.6, the energy in layer l is the sum of the hit energies in layer l: $E_l = \sum e_l$. In order to improve the readability, the arithmetic *mean* is expressed here by surrounding *angular brackets* instead of the typical bar on top.

Pearson's chi-squared test is applied in observables 2 and 3 to test the goodness of the response model in simulation in comparison to data. As described for example in [170], χ^2 can be approximately calculated from:

$$\chi^2 = \sum_{i=1}^{k} \frac{(n_i - Np_i)^2}{Np_i} \ , \tag{9.3}$$

with n_i the in data observed number of entries in bin i of a distribution with k non-empty bins and with $\sum n_i = N$, while N is the total number of observation, which equals the total number of entries in the distribution. p_i is the probability of an event to occur in bin i, estimated from simulation, with $\sum p_i = 1$. The connection to the default definition of $\chi^2 = \sum_{i=1}^{k} \frac{(x_i - \mu_i)^2}{\sigma_i^2}$, with the observed value x_i, the expected value μ_i and the variance σ_i, can be made with the assumption, that the entries in each bin are distributed according to a Poisson distribution, which allows to write the variance as $\sigma_i^2 = \sqrt{\mu_i}^2 = \mu_i$.

The first initial observable is the most important one, since it directly indicates the agreement of the mean energy of each considered layer. If the mean is off too far, than even a possible good agreement of the shapes of the rising and falling edges don't really matter. On the other hand, the second observable gives more detailed information about the agreement of the shapes - and therefore also the edges of the distributions. This information is useful to validate the result of observable 1. The third observable, which rates the agreement of the shapes of the hit energy distributions of each considered layer, gives even more detailed information on the single hit level.

It has to be pointed out, that generally this third information is the most pregnant one, if it comes to response saturation, because this hit energy level is the lowest level of energy information and closest to the SiPM response itself. But this is only true, as long as the simulation and data agree well in all other aspects, for instance the description of the beam profiles and the detector model. Especially the first point is questionable, because, as discussed in detail in Section 8.5, the electron beam includes components of low-energy electrons. Other inconsistencies, like deviations between data and simulation in the layer-wise number of hits distributions (for instance see Figure 8.26) reduce the significance of this observable. For example, if the electromagnetic shower is not simulated well enough and the shower is wider in data than in simulation, more channels are hit compared to simulation and the energy of the shower is allocated differently between single channels, which makes it hard to compare the resulting hit energy shapes. This observable would be the most important one in a scenario, where it is secured, that the incoming energy into a tile is well known, for instance if each channel of the detector would be under test individually, with a well known beam focused on each of the single tiles. Since this is not the case in our scenario, this third observable has the lowest sensitivity
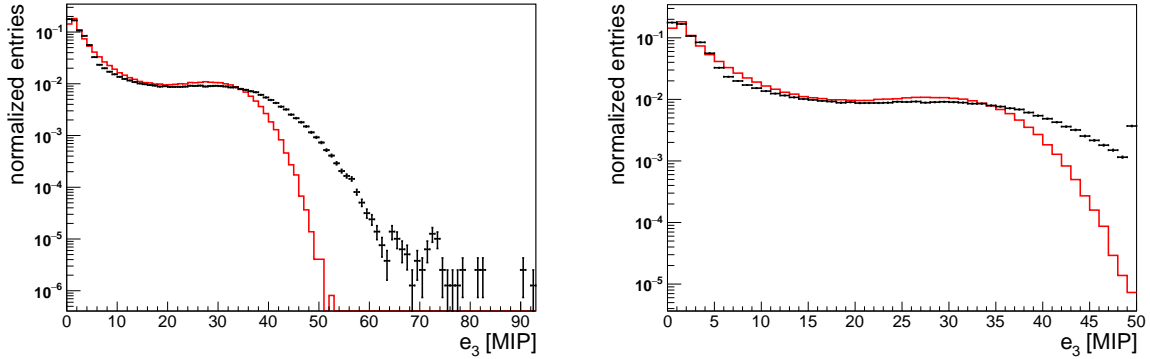
Figure 9.1.: Exemplary hit energy distributions of layer 3, e_3, of data (black) and simulation (red) with normalized entries. On the right plot, the bin merging procedure is applied as discussed in the text.

in terms of tuning the response models, but can on the other hand indicate the agreement of the beam and detector tuning in simulation compared to data.

Bin merging

Pearson's chi-squared test only works for non-empty bins and the number of entries in any bin should not fall below 5 entries to be reliable. Especially when two distributions of data and simulation are compared, it is most likely, that the bin entries in one of the two distributions is still above 5, while in the other there are less or even zero entries. For example, consider the distributions of hit energies in layer 3, e_3, for data and simulation in the left of Figure 9.1, where in data, many more bins are filled compared to the simulation. Additional modifications are applied to the distributions, to merge the entries of these bins, following the subsequent steps:

- Starting from the left edge of the distribution, the first bin, containing a minimum of five entries, is found for both, data and simulation. If this bin differs for data and simulation, the highest bin is chosen. Bin entries of all preceding bins are summed up and added to the chosen bin, while resetting all preceding bins to zero entries.

- The same procedure is repeated, but starting from the right edge of the distribution and finding the last bin, containing a minimum of five entries in both, data and simulation. Also here, entries from bins higher that chosen bin are summed and added to the chosen bin, while resetting all higher bins to zero.

This bin merging procedure allows to perform a Pearson's chi-squared test, even if one of the two compared distributions are wider than the other. The number of degrees of freedom of the Pearson's chi-squared test is $NDF = k - r$, which takes into account the number of bins, k, and the number of constraints r used to estimate p_i. It is then calculated from the new number of bins with a minimum of five entries after merging.

The already mentioned Figure 9.1 shows two example plots of e_3 distributions of data and simulation. The left plot shows the two distributions without any modifications, while the right plot includes the bin merging modifications listed above. On the left edge of the distributions,

no modifications are applied in this case, while on the right edge, bins are merged.

Combined Observables

The three initial observables can be calculated for a fixed beam energy, but the response models should be optimized for *all beam energies at once.* To take into account all available data at once and therefore a bunch of six different beam energies, for electrons reaching from 10 to 50 GeV, the three initial observables are combined to three *combined observables* as follows:

1. The first combined observable, M_{E_l}, which takes into account the mean energy of each considered layer l, $\langle E_l \rangle$, is estimated from a product over all beam energies:

$$M_{E_l} = 1 - \prod_{beamenergies} (\langle E_l \rangle_{MC} / \langle E_l \rangle_{DATA})^* \qquad (9.4)$$

   The * indicates, that all ratios $r = \langle E_l \rangle_{MC} / \langle E_l \rangle_{DATA}$ of single beam energies, which turn out to be larger than 1, are mirrored at 1 to be lower than 1, but *maintain the actual difference to 1.* This is done by a simple if-condition: if the ratio r is larger 1, the ratio is converted to $2 - r$. This is important, because otherwise the product could result in a value which is closer to 1, than are the single ratios for different beam energies[3]. With this conversion, the main aspect of the observable M_{E_l} remains, which is a rating of the difference between r and 1.

2. The second combined observable, X_{E_l}, taking into account $\chi^2_{E_l}$ of the distributions of the energy of each considered layer, E_l, is estimated from a sum of the $\chi^2_{E_l}$ of each beam energy, divided by the sum of the number of degrees of freedom of each beam energy:

$$X_{E_l} = \sum_{beamenergies} \left(\chi^2_{E_l} \right) / \sum_{beamenergies} (NDF_{E_l}) \qquad (9.5)$$

3. Similarly, the third combined observable, X_{e_l}, of $\chi^2_{e_l}$ and NDF_{e_l} of the hit energy distributions e_l is estimated by:

$$X_{e_l} = \sum_{beamenergies} \left(\chi^2_{e_l} \right) / \sum_{beamenergies} (NDF_{e_l}) \qquad (9.6)$$

These combined observables have the advantage, that they reduce the number of observables from initial three times six to a final of three, which helps to make decisions easier later in the evaluation of the results.

Now that the observables are introduced, next, two different response models are tested: the crosstalk-extended exponential model in Section 9.5 and the advanced model in Section 9.6.

---

[3]Example: If the ratios are 0.9, 0.95 and 1.15, than the product of all three would be approximately 0.98, which is closer to 1 than any of the single ratios. With the conversion, the final product is approximately 0.73.

9.4. Crosstalk-Extended Response Model Adjustment and Inversions

The crosstalk-extended exponential response model (XT-ext) has been introduced earlier in Section 4.3.3.2. For the application in the AHCAL prototype, an adjustment has been made in order to allow for a reasonable inversion of the model, as discussed here.

The known XT-ext model function is repeated here in Equation 9.7 (compare to Equation 4.17),

$$f_{response} = N_{fired}^{XT-ext} = N_{total} \cdot \frac{1 - X}{1 - (\epsilon_C \cdot X)} \;, \tag{9.7}$$

with the exponential part wrapped in $X = \exp(-N_{Seed}/N_{total})$, the total number of pixels N_{total} and the crosstalk parameter ϵ_C.

Equation 9.8 gives the inverted function :

$$f_{response}^{-1} = N_{seed}^{XT-ext} = -N_{total} \cdot \ln\left(\frac{N_{fired} - N_{total}}{\epsilon_C N_{fired} - N_{total}}\right) \tag{9.8}$$

The maximum value of the XT-ext function 9.7 cannot exceed N_{total}. For data, this can lead to an issue, once the inverted model is utilized to de-saturate data by utilizing the inverted response model in the reconstruction procedure. Given a hit energy in data that corresponds to a saturated $N_{fired} > N_{total}$, the inverted XT-ext function cannot be used to estimate the de-saturated value, because Equation 9.8 is not defined for $N_{fired} > N_{total}$.

To bypass this issue, the XT-ext model is extended by a linear extension. A similar approach is used in the reconstruction procedure of the CALICE analysis tools, with the distinction, that there the approach applies to the simple exponential model [139]. It aims to take into account *over-saturation* of the SiPM-tile system, which is, to emphasize it, the definition of $N_{fired} > N_{total}$.

As long as Equation 9.9 is fulfilled,

$$R < N_{fired}/N_{total} \tag{9.9}$$

, with R being a new parameter smaller 1, the inverted XT-ext function (Equation 9.8) remains as before. As soon as $N_{fired} \geq R \cdot N_{total}$, the inverted function instead continues with a linear behavior with the slope of the inverted XT-ext function at $N_{fired} = R \cdot N_{total}$. After the estimation of the slope and of the axis intercept, followed by simple transformations, this leads to Equation 9.10 for the response function and Equation 9.11 for the inverted response function. Note, that due to the transformation, the condition for the response function changes to $N_{fired} > -N_{total} \cdot \ln(\frac{R-1}{\epsilon_C R - 1})$:

$$\text{if } N_{seed} > -N_{total} \cdot \ln(\frac{R - 1}{\epsilon_C R - 1}) \;, \text{ then:}$$
$$N_{fired}^{XT-ext} = RN_{total} - (N_{seed} + N_{total} \cdot \ln(1/Y)) \frac{(\epsilon_C - 1)Y}{(\epsilon_C - Y)^2} \tag{9.10}$$
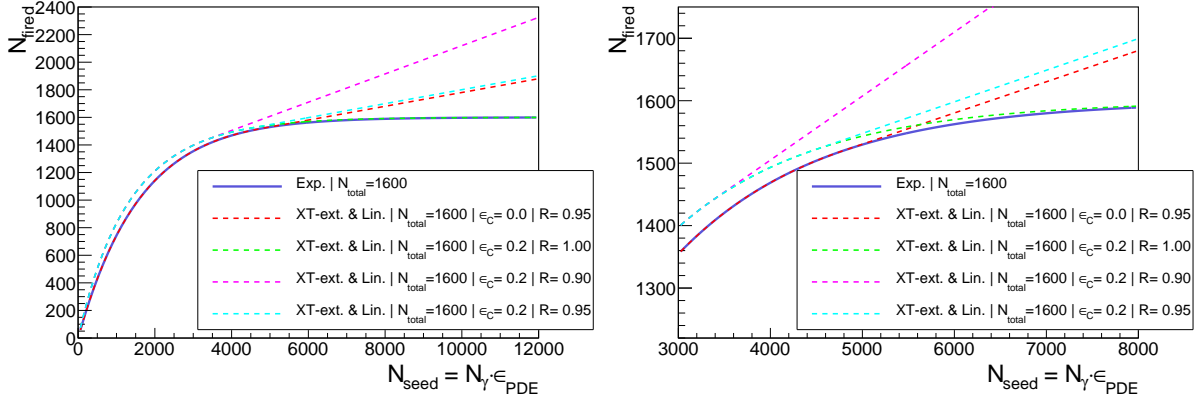
**Figure 9.2.:** Plots of the crosstalk extended model with linear extension, for a fixed $N_{total} = 1600$ pixels, various crosstalk parameters ϵ_C and ratios R. The right plot gives a zoomed view.
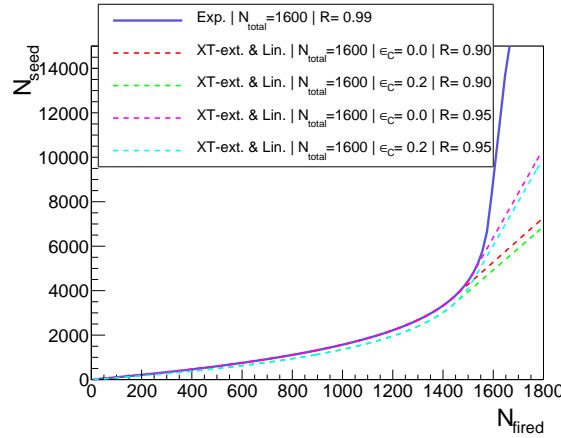

Figure 9.3.: Plots of the inverted crosstalk extended model with linear extension, for a fixed $N_{total} = 1600$ pixels, various crosstalk parameters ϵ_C and ratios R.

with $Y = (\epsilon_C R - 1)/(R - 1)$. For the inverted model follows:

if $N_{fired} > R \cdot N_{total}$, then:

$$N_{seed}^{XT-ext} = \frac{(\epsilon_C - 1)(N_{total} R - N_{fired})}{(R - 1)(\epsilon_C R - 1)} - N_{total} \ln \left(\frac{R - 1}{\epsilon_C R - 1} \right) \tag{9.11}$$

Whenever from now on the crosstalk-extended model is referred to, than the model with the extensions of R is meant, if not stated otherwise.

Figure 9.2 shows plots of the XT-ext response model with a fixed $N_{total} = 1600$, which corresponds to a SiPM of Layer 3, various SiPM crosstalk parameters ϵ_C and ratios R. The default exponential model (cf. Equation 9.7), which is similar to the XT-ext model for $\epsilon_C = 0.0$ and $R = 1$, is plotted as comparison. An $\epsilon_C > 0$ leads to an increased N_{fired}, especially for low to medium N_{seed}, while for large N_{seed}, the impact of SiPM crosstalk eases. As stated before, this is expected, because SiPM crosstalk can only trigger a new pixel to fire, if this pixel has not already fired. Thus, the SiPM crosstalk itself saturates. Also visible is the impact of R. The

smaller R is, the lower N_{seed} needs to be, until the linear extension begins. Thus, the slope of the extension increases, the lower R is.

Figure 9.3 shows simulations of the inverted XT-ext response model, also with a fixed $N_{total} = 1600$ and various SiPM crosstalk parameters ϵ_C and ratios R. Though this figure does not show any new information, it helps to point out the need for the appended R parameter: by adding the linear extension, now also $N_{fired} > 1600$ and therefore over-saturation can be handled by this model without increasing N_{total}.

9.5. Crosstalk-Extended Response Model Studies

The first considered response model is the crosstalk-extended exponential model with linear extension (XT-ext), as discussed before. As the name suggests, this model is based on the simple exponential model, but also includes a mechanism to model the impact of optical crosstalk of a SiPM. This model includes two initial and one additional parameter: the total number of pixels, N_{total}, the crosstalk parameter, ϵ_C and the ratio R (cf. Eq. 9.9).

This response model study is mainly done using electron data and simulation, primary because the reconstructed deposited energy of electron showers is usually higher compared to pion showers, as seen in Section 8.6.3. This is important, because the impact of response saturation increases with higher energy depositions. Only for layers 13 and 14, pion showers are utilized to study and optimize the response model. Electron showers do not penetrate the detector far enough, to deposit high enough energies in these last two layers, but pions do. Still, the procedure applied, to study the impact of different response model parameter combinations, is similar for both particle showers.

In the following, the study of the XT-ext response model is discussed in detail by means of layer 3. The other layers 4 to 14 are thereupon discussed in less detail, focusing on the main aspects and results. Refer to Table 8.2 for details about the equipped SiPM type of each layer.

Whenever XT-ext model parameter combinations are written, the following structure is applied: $(N_{total}|\epsilon_C|R)$. In case only two parameters are written, R is considered to be 1: $(N_{total}|\epsilon_C)$.

9.5.1. Layer 3

As a reminder, layer 3 comprises a combination of a scintillator tile and SiPM S12571-25P with a physical total number of 1600 pixels with 25 μm pixel pitch. The SiPM crosstalk factor ϵ_C is expected to be roughly in the range between 20 to 26 %.

Excursion concerning the expected SiPM crosstalk factor

While the dedicated crosstalk measurement in Section 6.3 resulted in a crosstalk factor of around 26 % [4] (cf. Table 6.2), the analysis of the dedicated SiPM response measurement (without tile and with pulsed laser as light source) concluded a lower crosstalk factor $\epsilon_C \approx 19$ with the fitted XT-ext response model (without R extension), or approximately 21% with the fitted advanced response model (cf. Figure 6.16). This gives a range for an uncertainty of these values.

---

[4]The probability is measured to be $P(\geq 1XT) \approx 21\,\%$, while this accounts only for the number of all crosstalk events, not taking int account multiplicities of pixels fired by such events. On the other hand, the average factor of crosstalk $\mu_C \approx 1.26$ is comparable to the crosstalk factor $\epsilon_C \approx \mu_C - 1 = 26\,\%$. This factor takes into account the probability, that more than one pixel can fire as a consequence of crosstalk.
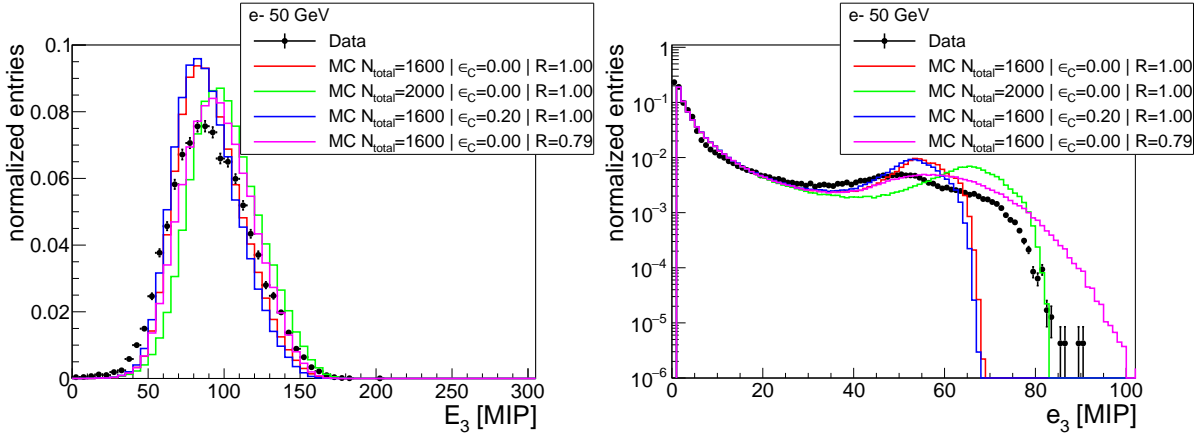
Figure 9.4.: Impact of different XT-ext response model parameter combinations for 50 GeV electron simulation in comparison to 50 GeV electron data, shown by means of the energy distribution in layer 3, E_3, (left) and the related hit energy distribution, e_3, (right).

As discussed in a previous work [78], the SiPM crosstalk probability decreases indirectly with increasing temperature. Indirectly, because the crosstalk probability is coupled to the effective voltage (here: over-voltage) of the SiPM, which itself depends on the temperature. Further studies (cf. a previous work [77] and Reference [171]) have shown, that if the effective over-voltage is kept constant by taking countermeasures with the bias voltage of the SiPM, SiPM crosstalk probability only has a weak or no dependency to temperature. Since no countermeasures have been done and only bias voltages are consistent between the two measurements, it is reasonable, that the crosstalk factor might be lower, roughly around 20 %, at the testbeam at CERN, because of higher temperatures around 31°C (measured directly on the HBUs during run time [172]) compared to measurements in the lab at around 22°C (cf. Chapter 6).

Impact of response model parameters on the E_3 and e_3 distributions

Before taking a closer look into the outcome of the combined observables for different parameter combinations of the XT-ext response model, first, the impact of the different parameters on the shapes of the energy distribution of layer 3, E_3, as well as for the hit energy distribution of layer 3, e_3, are discussed. Because the combined observables aim to quantify the compliance of data and simulation by a reduction of information to only one final value each, lots of information is lost. Hence it is important to understand, what actually happens in the underlying distributions.

The distributions of the energy in layer 3, E_3, and of the hit energy of layer 3, e_3, are shown in Figure 9.4 for 50 GeV electron data and simulations, the latter with different parameter combinations. The default parameter combination $(N_{total}|\epsilon_C|R) = (1600|0|1)$ is plotted in red, and obviously there are many disagreements to data which will be discussed in a minute. Each other parameter combination only changes one of the three parameters, as green changes to $N_{total} = 2000$, blue to $\epsilon_C = 0.2$ and purple to $R = 0.79$, while maintaining the two other parameters as default. A beam energy of 50 GeV is presented here, because the impact of SiPM saturation is expected to be at a maximum, because the reconstructed energy in layer 3 is the highest at 50 GeV, compared to lower beam energies (cf. Figure 8.27).

In the layer 3 energy distribution, E_3, data is in any case wider compared to any simulation.

In the hit energy distribution of layer 3, e_3, the right flank of the distribution in data looks different to any simulation, because it features some kind of double edge. This might indicate, that data features at least two different saturation behaviors. Since all channels in a single layer consist of the same SiPM-type and tile combination, it is not expected and the origin is unclear. Because only a small number of channels of a single layer, especially in an early layer 3, are hit by the 50 GeV electron shower, and such high hit energies are only deposited in a small number of channels (for instance one or two), these two tails might be related to only a few individual channels. Still, the saturation behavior should be similar in all channels and this observation requires further inspections in the future. Different other parts of the shapes also disagree, which indicates, that this difference cannot be addressed completely by this response model within these parameter ranges or, not even by any response model, since there might be other effects.

Dependance on N_{total}

Compared to the default combination, a larger N_{total} (green) leads to higher energies and increases the mean of the E_3 distribution from initially 91.3 MIP to 100.8 MIP, while the RMS of the distribution also increases from initially 21.5 to 23.0, though it relatively to the mean decreases. As expected, a higher N_{total} lowers saturation and increases reconstructed energies. This is also visible in the hit energy distribution, where more entries are in the high energy region, which shifts the right edge to higher energies.

Dependance on ϵ_C

A higher SiPM crosstalk parameter $\epsilon_C = 0.2$ slightly reduces the mean of E_3 and also sharpens the peak, as the mean becomes 89.0 MIP and the RMS becomes 21.0. In the e_3 distribution, an $\epsilon_C = 0.2$ shifts the distribution to slightly lower values, too. Usually one would not expect that SiPM crosstalk reduces the high-energy entries, for example in the right falling edge of the e_3 distribution, because the impact of SiPM crosstalk also saturates with rising input energies, as discussed before.

The origin of this effect lies in the way, crosstalk is handled in the digitization and reconstruction procedure:

As discussed above in Section 9.2, LY_{seed} is a converted light yield, which is corrected mainly to the impact of SiPM crosstalk at 1 MIP, where saturation only plays a minor role. As a consequence of applying the converted light yield LY_{seed} instead of the default light yield LY, the input, $N_{seed} = E_{MIP}^{MC} \cdot LY_{seed}$, of the response model function is shifted similar to the shift between of LY_{seed} and LY. Because an $\epsilon_C > 0$ leads to a smaller LY_{seed}, as long as saturation is negligible at 1 MIP, the LY_{seed} is smaller than LY. Hence, the input N_{seed} of the response function is lessened by applying LY_{seed}, which results in a smaller output of the response function $f_{response}(N_{seed})$ itself. This is actually correct, as the crosstalk affected LY falsely leads to too high responses at high energies. Because of this mechanism, the MIP calibration of the detector is maintained, as already discussed.

Dependance on R

A lower ratio $R = 0.79$ increases the mean of the E_3 distribution to 95.8 MIP and the RMS to 22.7. Though the impact on the energies looks smaller compared to the green curve, the e_3 distribution shows, that this parameter allows to actually reach very high energies (in this case up to 100 MIP) by widening the high energy edge and reducing the height of the right peak in
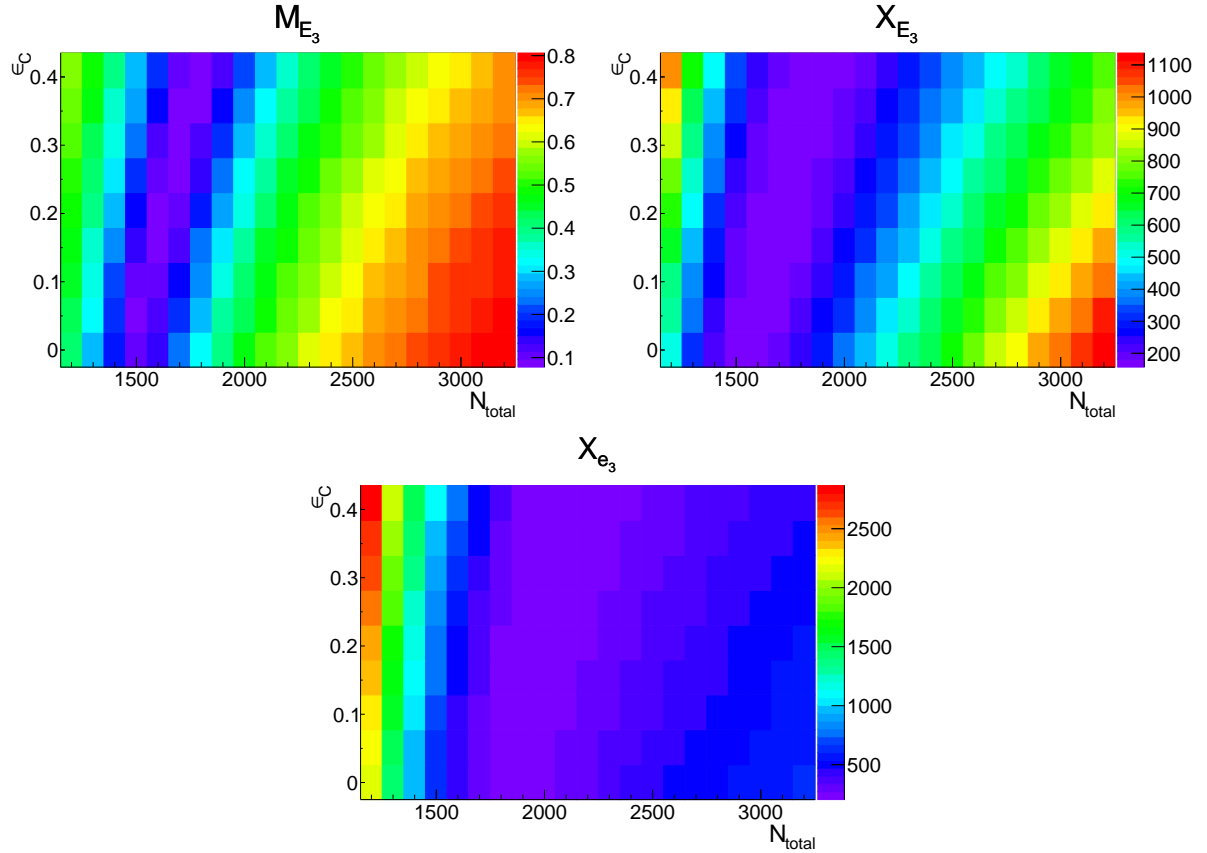
Figure 9.5.: The three combined observables M_{E_3}, X_{E_3} and X_{e_3} (cf. equations 9.4, 9.5 and 9.6), for the crosstalk-extended response model as two-dimensional histograms as a function of N_{total} and ϵ_C for layer 3. The parameter R is fixed to 1. Estimated with electron data and simulation.

the distribution. This allows the assumption, that the right peak just before the falling flank in all simulations actually is a direct consequence of saturation. As the simulations of the XT-ext response model function in Figure 9.2 have shown, a wide range of high inputs N_{seed} results in a small range of outputs N_{fired}, because of the exponential functionality, which finally leads to the observed high energy peaks in the hit energy distribution. Because the ratio R defines the point, from where on the linear behavior replaces the exponential behavior, both, higher output energies are possible and the right high energy peak is reduced.

9.5.1.1. Layer 3 Combined Observables Discussion

With the illustrated and discussed impact of the XT-ext response model parameters and the expected N_{total} and ϵ_C in mind, the combined observables of the response analysis, as introduced in Section 9.3, are presented in the following.

Figure 9.5 shows the three combined observables M_{E_3}, X_{E_3} and X_{e_3}, as two-dimensional plots with the axes corresponding to the model parameters ϵ_C and N_{total}. The additional parameter R is fixed to 1 here, which means, that the linear extension is not taken into account. The lower the observables are, the better is the agreement between data and simulation.

Observable M_{E_3}

As indicated above in Section 9.3, the first combined observable, M_{E_3}, in Figure 9.5 with Equation 9.4 is the most relevant in this study, because it is a measure of the agreement of the means of the layer-wise energy distributions of data and simulation at all beam energies simultaneously. A low-value valley is visible in purple in the region from about $(N_{total}|\epsilon_C) = (1500|0)$ to $(1800|0.4)$, indicating a better agreement than outside of this area. Within this valley, no clear minimum can be found, which might indicate some possible correlation between N_{total} and ϵ_C.

At first glance, no direct correlation is expected, because ϵ_C affects the shape of the response function mainly for low inputs, while on the other hand, N_{total} mainly affects high inputs. For medium energies, the two aspects overlay, which might be the reason for the observed plateau. But at a second glance, another reason for this valley has already been discussed above by means of Figure 9.4: It lies in the the way, SiPM crosstalk is handled in the digitization and reconstruction procedure, which requires the light yield LY to be converted to LY_{seed}, which takes into account mainly the impact of crosstalk at 1 MIP. Because this LY_{seed} is applied to all input energies of the response model, it also affects high energies. Still, both N_{total} and ϵ_C have their reason for existence, because the mechanisms are different.

M_{E_3} increases and therefore the agreement deteriorates, the further away the parameter combination of N_{total} and ϵ_C gets.

Comparing the previously applied parameter combination of $(1600|0)$ (equal to the standard exponential model) to the expected $(1600|0.2)$, M_{E_3} can be improved from around 0.135 to 0.084, which corresponds to a reduction of around 62 %. Still, there are a few parameter combinations with even lower values in the observed ranges.

Observables X_{E_3} and X_{e_3}

The second combined observable, X_{E_3} (cf. Equation 9.5), in Figure 9.5 shows a broader valley of relatively small values, which does not completely match the valley of M_{E_3}. Similar to before, the observable increases, the more the parameter pair walks away from the valley. The values within the purple valley actually are still high, which suggests, that the shapes of the two underlying distributions of data and simulation don't agree well, apart from a possible agreement of the main.

In the case of the third combined observable, X_{e_3}, the purple valley is even wider and moved to higher N_{total}. The values of X_{e_3} are even higher, which indicates that the hit energy distributions of layer 3, e_3, agree even less between data and simulation than the related energy distributions, E_3.

Impact of ratio R

Figure 9.6 shows the three combined observables as a function of the ratio R and N_{total}, with a fixed $\epsilon_C = 0.2$. For M_{E_3}, the lowest values are in the region around $N_{total} = 1600$ and $R > 0.75$. For lower R, the values increase and the agreements of the means decrease. At lower $R < 0.75$, the blue low-value region bends to smaller N_{total}. Because a small R negates more and more saturation, it can to some extend compensate a lower N_{total}. Compared to M_{E_3} in Figure 9.5, the value of $(1600|0.2)$ can be improved from 0.084 to 0.068 for a ratio $R = 0.79$.

For X_{E_3} and X_{e_3}, a broader shape of the 2D-distribution is visible, for the latest even more.
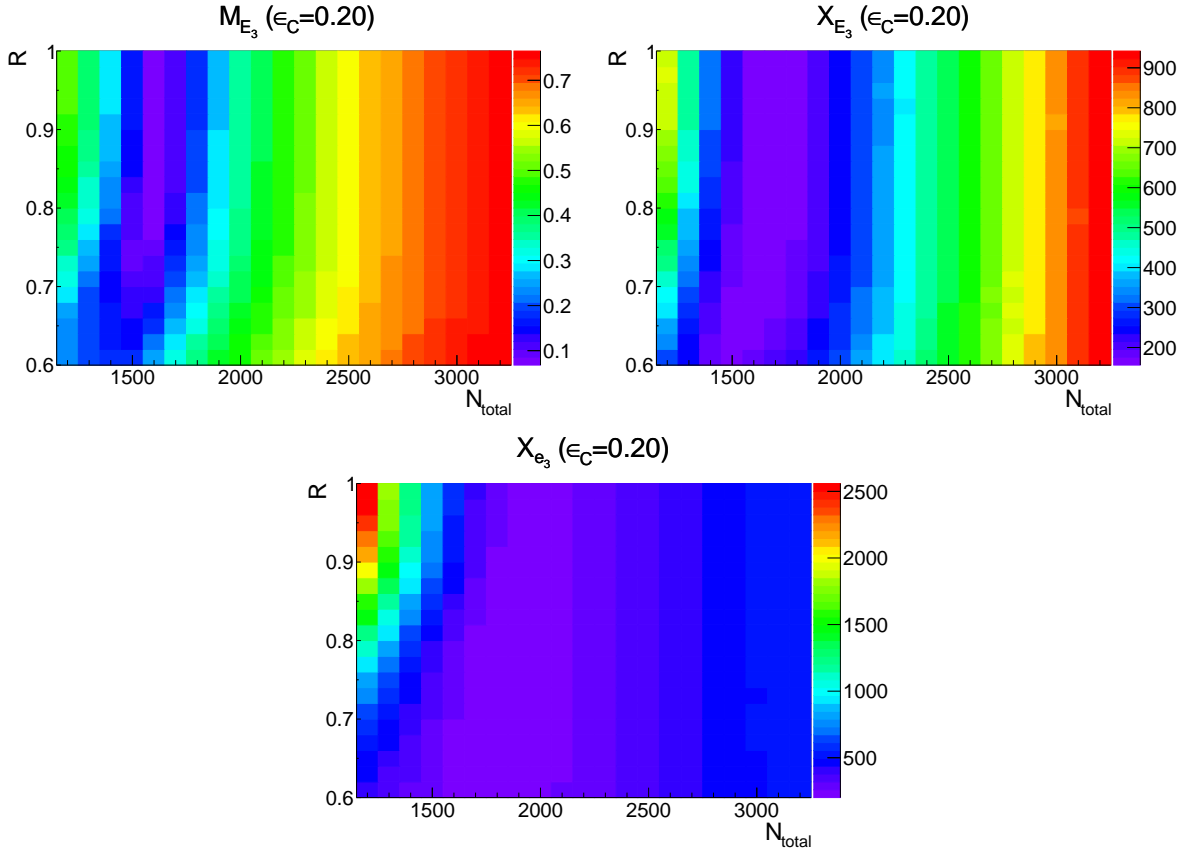
Figure 9.6.: The three combined observables M_{E_3}, X_{E_3} and X_{e_3} (cf. equations 9.4, 9.5 and 9.6), for the crosstalk-extended response model as two-dimensional histograms as a function of N_{total} and R for layer 3. The parameter ϵ_C is fixed to 0.2. Estimated with electron data and simulation.

The relative impact of R, on improving the results of the X_{E_3} and X_{e_3}, is lower than for the first combined observable M_{E_3}.

Conclusion

To sum up, no clear optimum can be found. For any observable taken on its own, there is no single parameter combination with a minimum, but an area with equal low results. Especially in case, where chi-squares are estimated, the results are noticeable high, which already tells, that the shapes of data and simulation do not agree well and that this situation cannot be improved further by the response model within the observed parameter ranges. A larger parameter range is not expected to give better results, as the observable values systematically increase to both, lower and higher N_{total}. Concerning ϵ_C, even larger values than 0.4 are expected to follow the shape and give similar results and no further improvements. For the ratio R, only values ≤ 1 make sense and as R already increases for values approximately larger 0.7, there is no obvious need to increase the range any further.

As discussed at Section 9.3, M_{E_3} is most essential, followed by X_{E_3} and last X_{e_3}. Because the preferred combination with $N_{total} = 1600$ and $\epsilon_C = 0.2$ leads to one of the best results in M_{E_3} and to relatively good results for the two other observables, this combination is selected as

optimum. For the ratio, an even value of $R = 0.8$, close to the minimum of M_{E_3} in Figure 9.6, is chosen, which finally leads to the combination (1600|0.2|0.8).

Now that the study of the XT-ext response model has been discussed in detail by means of layer 3, the remaining layers are discussed briefly in the following.

9.5.2. Layer 4-14 Combined Observables Discussion

Similar to the study of the XT-ext response model in layer 3 in the previous section, the other layers have been studied in detail. The following layers can be aggregated in several groups, as they feature similar SiPM and tile combinations and thus similar response behaviors are expected. For reasons of space, plots of only one layer of each group are presented here and the remaining plots are moved to Appendix E.

9.5.2.1. Layer 4 and 5

Layers 4 and 5 feature the same combination of SiPM and tile (cf. tables 8.1 and 8.2) and are therefore analyzed together. The SiPM has 12000 physical pixels on a sensitive area of 2.25×2.25 mm^2. Thus, this SiPM features the largest number of pixels on the largest sensitive area. It is important to keep this in mind. The tiles are not wrapped with reflective foil, which allows some tile-to-tile crosstalk. This tile-to-tile crosstalk is modeled within the digitization procedure for the simulation and the parameter has been optimized in Section 8.6.2. Nevertheless, as pointed out earlier, this model might not be significant for high energies.

With these notes in mind, lets continue with the combined observable discussion. The combined observables of layer 4 are presented here in Figure 9.7, while the corresponding plots for layer 5 can be found in the appendix in Figure E.1.

Observables M_{E_4} and M_{E_5}
Concerning the first combined observables M_{E_4} and M_{E_5} it is conspicuous, that the regions with low values, which indicate a good agreement of the mean of the layer-wise energy distributions of data and simulation of layer 4 or 5, respectively, are at rather low N_{total}, approximately around 4000 to 7000 pixels. What has already been observed before for layer 3 is the valley of low results, which in case of layer 4 and 5 spans approximately between (5000|0.0) and (7000|0.4). A higher ϵ_C requires a larger N_{total} to give similar results for M_{E_l}. The valley of low values is shifted a little to higher N_{total} for layer 5 compared to layer 4.

Observables X_{E_l} and X_{e_l}
The observables X_{E_4} and X_{E_5} again show a broader valley of low values, which is shifted to higher N_{total} compared to M_{E_4} and M_{E_5}, respectively. The valley of low X_{E_l} does not directly correspond to the valley of the related M_{E_l} and gives a hint, that the shape of the underlying distributions are not described well in simulation compared to data, though the mains might be consistent.
The observables X_{e_4} and X_{e_5} show low values at very high N_{total}, which is not consistent anymore with the respective M_{E_l}. As pointed out earlier, the information of X_{e_l} should not be overestimated, since this observable relies on a good description of the shower profile and the
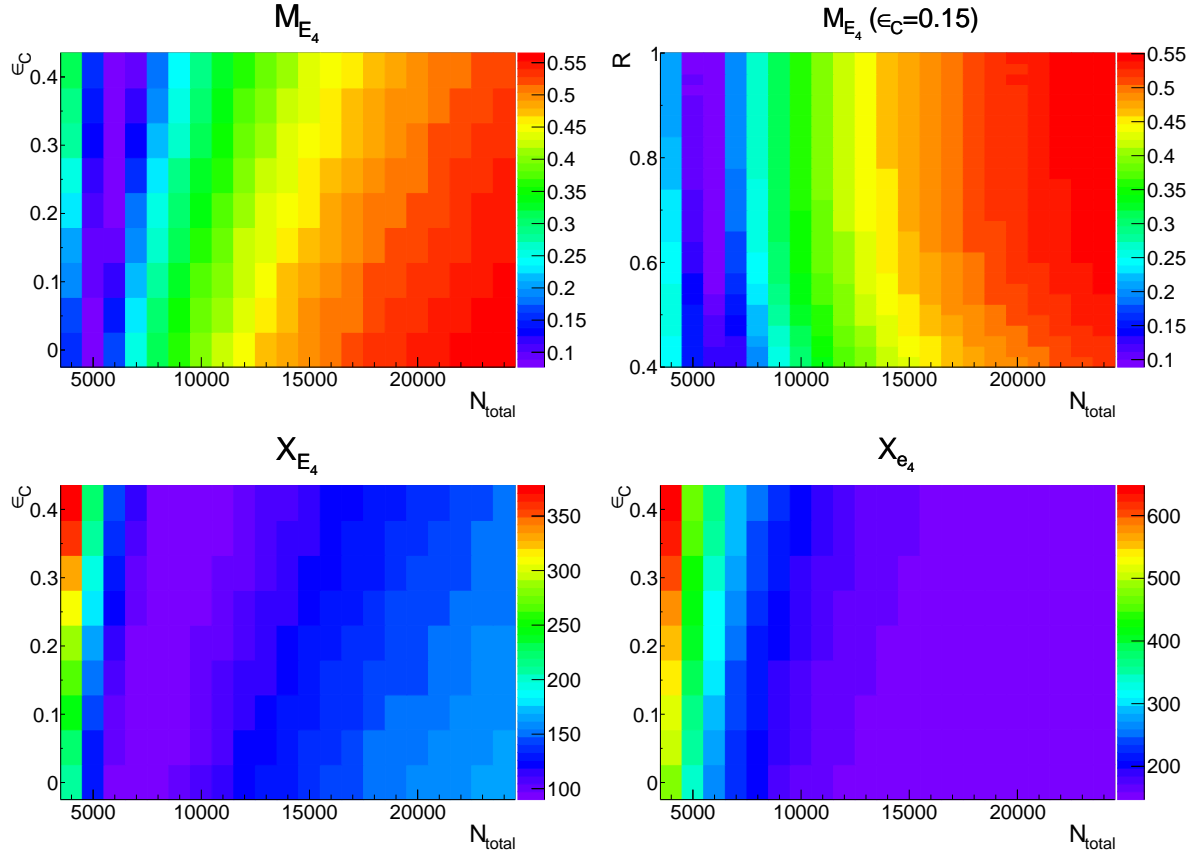
Figure 9.7.: The combined observables M_{E_4} (top left and right), X_{E_4} (bottom left) and X_{e_4} (bottom right) for the XT-ext response model as two-dimensional histograms as a function of N_{total} and ϵ_C or R for layer 4. Except for the top right plot, the parameter R is fixed to 1. Estimated with electron data and simulation. The corresponding plots for layer 5 can be found in Figure E.1.

number of hit channels, which cannot be granted in this analysis. Therefore, as a reminder, a dedicated measurement of each single channel would enhance the significance of this observable.

Dependance on R

Also, M_{E_4} and M_{E_5} are shown as functions of the ratio R for a fixed $\epsilon_C = 0.15$. The lowest values can be found for $N_{total} \approx 6000$ and $R \approx 0.6$ for layer 4 and $R < 0.55$ for layer 5. Higher or lower N_{total} result in higher values.

Conclusion

Taking into account M_{E_l} and X_{E_l} of both layers 4 and 5, a reasonable combination of N_{total}, ϵ_C and R is (6000|0.15|0.6), which will be applied later in this analysis. The underlying distributions have also been checked and found to be reasonable at this combination. It is obvious, that there are other possible combinations, which would also give similar results. This combination has been selected, because the SiPM crosstalk factor is expected to be within 10 to 20 %[5].

---

[5]No direct information or measurement of crosstalk of this specific SiPM type is available. Thus, the expected range has been calculated from the general crosstalk information of the manufacturer at [173] for an over-voltage of approximately 4 V.
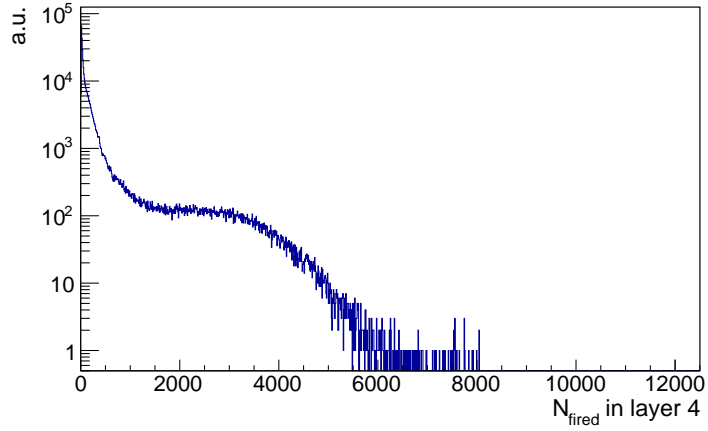
Figure 9.8.: Distribution of the reconstructed number of pixels fired, N_{fired}, in layer 4 at 50 GeV electron data.

How can such a low $N_{total} = 6000$ compared to the physical 12000 be explained?
Consider Figure 9.8, which shows the reconstructed number of pixels fired, N_{fired}, in 50 GeV electron data of layer 4. Only a small number of events exceeds 6000 pixels fired, which supports this number as an optimized N_{total}. The question arises, if only parts of the sensitive area of the SiPM have been illuminated by the scintillation light to explain the observation. In layers 4 and 5, a SiPM is placed in the middle of one edge of a tile, where parts of the scintillator is removed for the SiPM to fit in. A hollow is added in front of the SiPM to allow some guide of the scintillation light onto the sensitive area of the SiPM. In case there is a geometrical mis-alignment, for example a focus of the light onto a smaller area on the SiPM, this could very well be the origin of a low N_{total}. There are some hints in other studies, which also report some possible mis-alignment of the tile-SiPM system, like in [174] and [175], though they report on other SiPM-tile combinations, which are not utilized in this detector prototype anymore.
Another source for this large difference between the physical and optimal N_{total} might be found in the way, tile-to-tile crosstalk is modeled in the digitization of the simulation. As discussed previously, tile-to-tile crosstalk is modeled in first order only, which is fine for low to medium deposited energies, but might not be significant anymore at high energies, which are considered here. Additional investigations would be necessary to analyze the impact of tile-to-tile crosstalk on the channel response. But because this SiPM-tile combination, and also any SiPM-tile combination without wrapped reflective foil is not considered anymore in future AHCAL detector prototypes, such a study has low priority.

9.5.2.2. Layer 7, 8 and 9

Layers 7, 8 and 9 consist of the same SiPM- and tile-type combination and are thus analyzed simultaneously. In difference to all other layers, these SiPMs have the lowest amount of physical pixels, which is 800. The pixel pitch is with 40 µm the largest, while the sensitive area is in the midfield with $1.28 \times 1.28\,\text{mm}^2$ (cf. Table 8.2). The expected SiPM crosstalk probability is negligible with about 1 % as specified in [176]. The tiles are not wrapped with reflective foil,
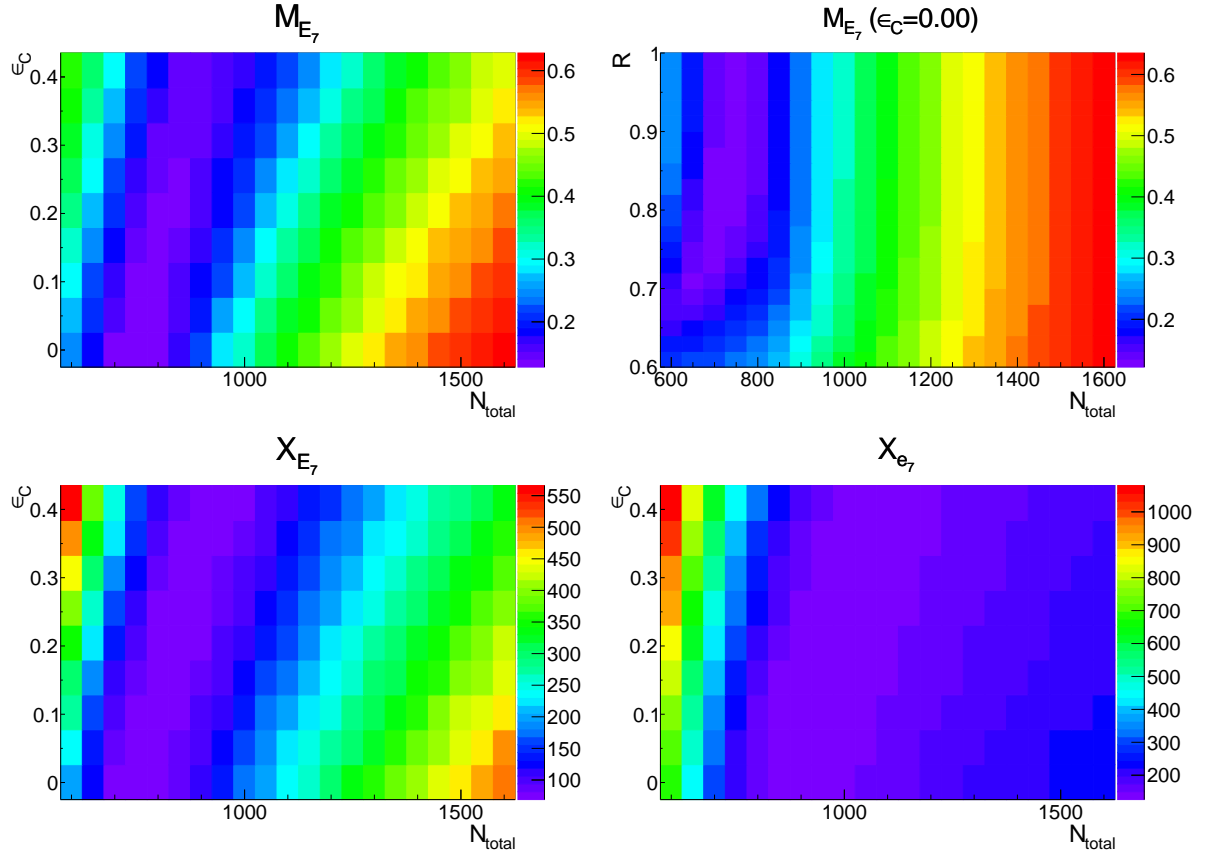
Figure 9.9.: The combined observables M_{E_7} (top left and right), X_{E_7} (bottom left) and X_{e_7} (bottom right) for the XT-ext response model as two-dimensional histograms as a function of N_{total} and ϵ_C or R for layer 7. Except for the top right plot, the parameter R is fixed to 1. Estimated with electron data and simulation. The corresponding plots for layers 8 and 9 can be found in appendix Figure E.2.

thus optical tile-to-tile crosstalk has an impact.

Figure 9.9 shows the three combined observables for layer 7, while again, the corresponding plots for layers 8 and 9 can be found in the appendix in Figure E.2. The shape of the distributions look similar to the previously discussed related distributions of layer 3.

Observable M_{E_7}, M_{E_8} and M_{E_9}

Starting with the first combined observable M_{E_l}, for layer 7, a low-value valley (purple and dark blue region) starts around $N_{total} \approx 700$ and $\epsilon_C = 0$ and reaches up to $N_{total} \approx 1000$ and $\epsilon_C = 0.4$. For layer 8, this valley of low observable values is moved to the right at higher N_{total} and the area of the purple and dark blue region is wider. This shift is extended for layer 9, where the lowest values for $\epsilon_C = 0$ are around $N_{total} \approx 1000$. If the smallest results are compared between the three layers, layer 7 shows the best results. There, the lowest value is around 0.13, while for layer 8 and 9, the smallest values are 0.33 and 0.2, respectively. This indicates that, though the layers are similar concerning the SiPM-tile combination, the degree of accordance between simulation and data differs from layer to layer. A tuned response model can improve the agreement between data and simulation only within these boundaries, thus other effects

might be the origin for these discrepancies, for example the previously discussed unsatisfactory tile-to-tile crosstalk model and a possible remaining contamination with low-energy electrons in data.

Observables X_{E_l} and X_{e_l}

The area of the low-value valley with purple and blue cells of the second combined observables X_{E_l} increases from layer 7 to 8 and even further for layer 9. There is some overlap of the low-value areas compared to M_{E_l} of each layer. However, the areas are wider and in case of layer 8 and 9 favor higher N_{total}.

The third combined observables X_{e_l} show even broader low-value areas, preferring even higher N_{total}.

Dependance on R

M_{E_l} is also shown as a function of N_{total} and R for a fixed $\epsilon_C = 0.0$ for layers 7, 8 and 9. For layer 7 and 9, the lowest values can be found for $R > 0.7$, while for layer 8 they are approximately within $R > 0.8$. No clear improvement can be found compared to the CALICE-default value of $R = 0.95$, thus this value is selected.

Conclusion

Again it is obvious, that there is not that single perfect parameter combination. As before, M_{E_l} is handled with the highest weight. The combination of $(850|0.0|0.95)$ is selected for the further analysis, because with this combination, the observables give reasonable results for all layers. In contrast to the default $N_{total} = 800$, the chosen 850 especially takes into account the observables of layer 9. A crosstalk of $\epsilon_C = 0.0$ is comparable with the expected crosstalk of about 1 %.

9.5.2.3. Layer 11 and 12

Layers 11 and 12 feature SiPMs with 2300 pixels on a sensitive area of $1.2 \times 1.2 \, \mathrm{mm}^2$. The expected crosstalk probability is around 5 % [176]. The tiles are wrapped with reflective foil, therefore tile-to-tile crosstalk is negligible. Compared to the previously discussed layers, the deposited energies of electron showers are lower (cf. Figure 8.27), thus the visible impact of saturation might be smaller.

Observables M_{E_l}, X_{E_l} and X_{e_l}

Figures 9.10 and E.3, the latter in the appendix, show the three combined observables for layer 11 and 12, respectively. Different to the observations of the previous layers, this time, the shapes of the three combined observables agree mostly, not only within one layer, but also for both layers. The lowest observables can be found at very high $N_{total} \approx 6000$, which is approximately 2.6 times the physical total number of pixels of the SiPM, thus it looks like saturation doesn't play a role at all. If saturation is negligible, than it is not surprising anymore, that all three observables look similar, preferring very high N_{total}. Even larger N_{total} have been analyzed too, but the results of the observables don't improve any further but remain stable.

Dependance on R

Also shown is M_{E_l} as a function of R and N_{total} with a fixed $\epsilon_C = 0.0$. While the impact of R is very small for layer 11, the values improve for $R < 0.8$ in layer 12, but the gain is very small.
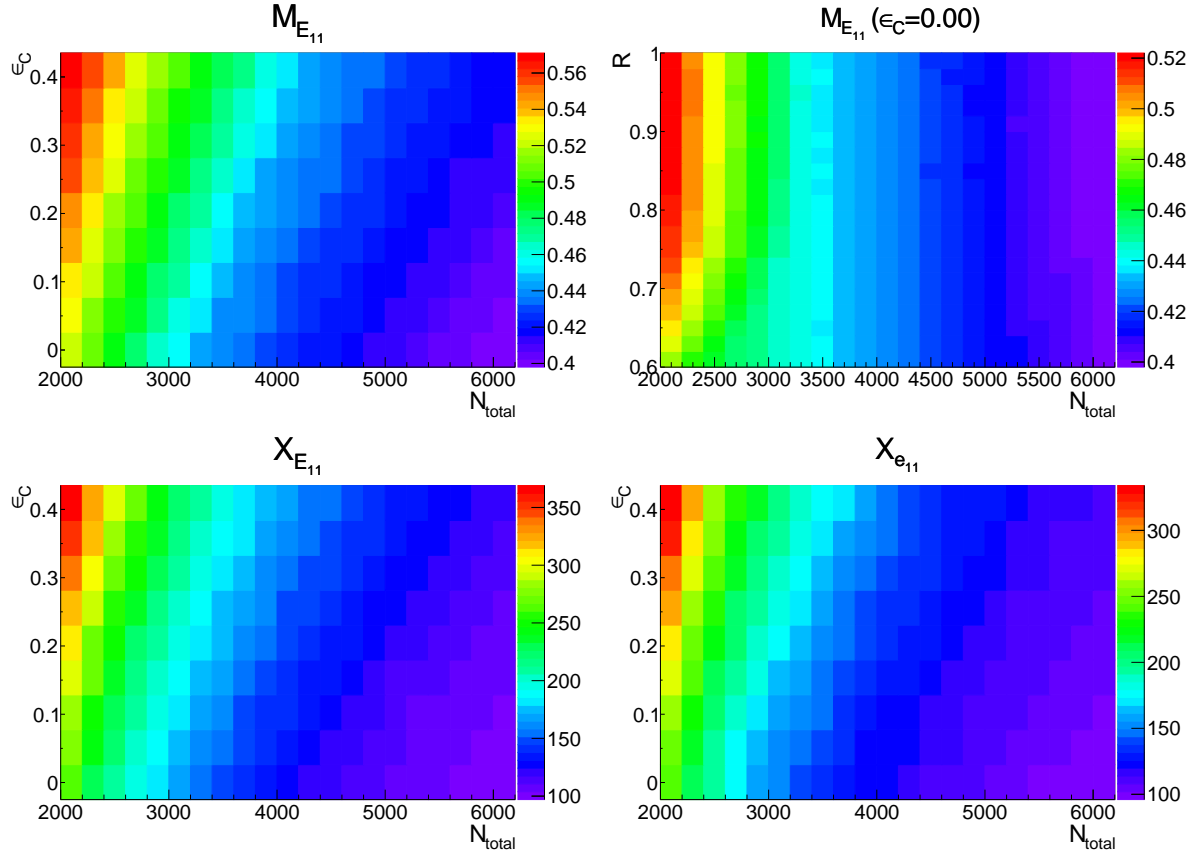
Figure 9.10.: The combined observables $M_{E_{11}}$ (top left and right), $X_{E_{11}}$ (bottom left) and $X_{e_{11}}$ (bottom right) for the XT-ext response model as two-dimensional histograms as a function of N_{total} and ϵ_C or R for layer 11. Except for the top right plot, the parameter R is fixed to 1. Estimated with electron data and simulation. The corresponding plots for layer 12 can be found in appendix Figure E.3.

This indicates again, that nearly no saturation is present in layer 12, which has already been noted above. Even lower R have been studied, but the results do not improve significantly.

Conclusion

With these observations, a final parameter combination of $(6000|0.0|0.95)$ is chosen. Because layer 11 includes more deposited energy than layer 12, the information of this layer has more worth for the optimization. Thus, a default $R = 0.95$ is reasonable. A crosstalk value of $\epsilon_C = 0.0$ is lower than the expected crosstalk of 5%, but there is no obvious need to increase the value larger than 0. The high N_{total} indicates no observed saturation. One possible explanation, besides the fact, that saturation only plays a minor role because of the low deposited energies in these two layers, is recovery of pixels. As a reminder, if a fired pixel recovers within the integration window of the readout, a delayed photon could trigger the same pixel to fire once more. This mechanism allows not only to lead to over-saturation ($N_{fired} > N_{total}$), but also counteract saturation at all. Still, it is not clear, why this effect is only observed in these two late layers. Because these layers are not at the center but at the end of the shower, different arrival times of parts of the shower into the same channels might favor the role, that pixel recovery plays. This might be reasonable for pion showers with larger time developments as
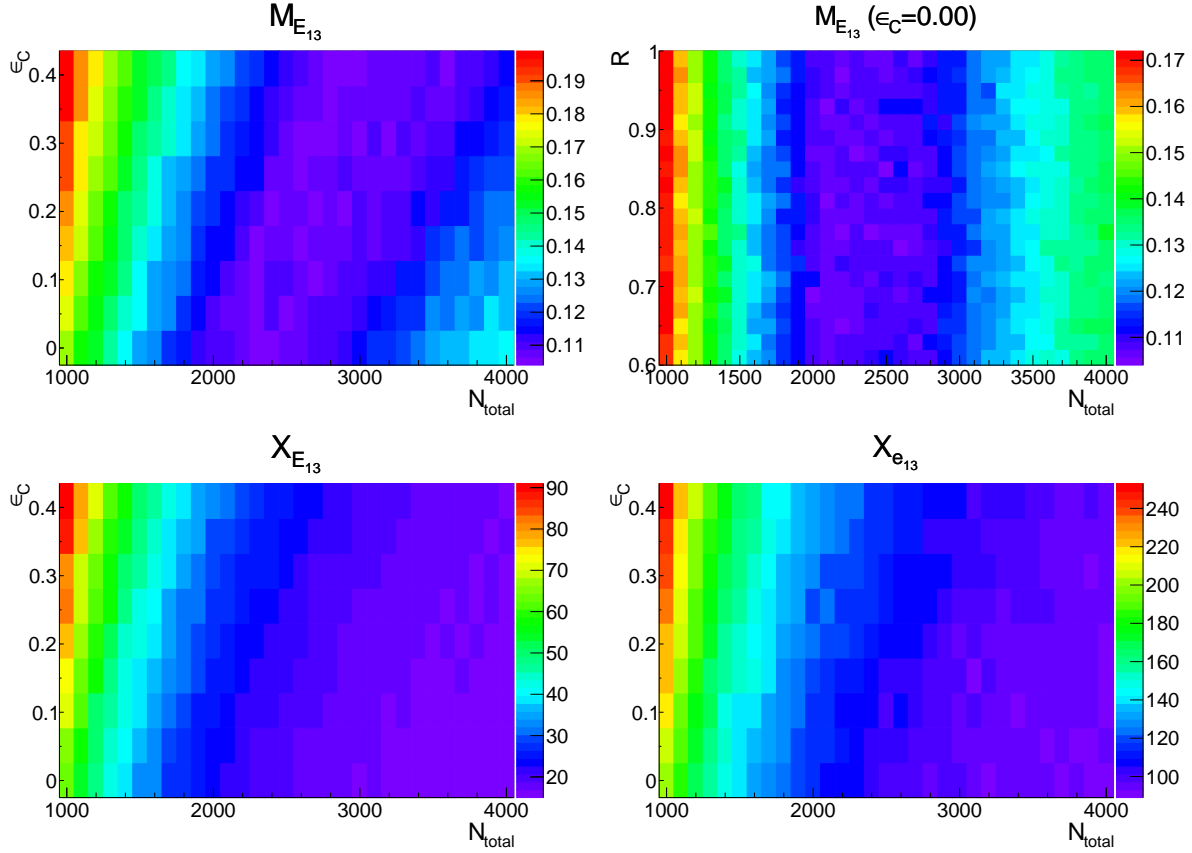
Figure 9.11.: The combined observables $M_{E_{13}}$ (top left and right), $X_{E_{13}}$ (bottom left) and $X_{e_{13}}$ (bottom right) for the XT-ext response model as two-dimensional histograms as a function of N_{total} and ϵ_C or R for layer 13. Except for the top right plot, the parameter R is fixed to 1. Estimated with pion data and simulation. The corresponding plots for layer 14 can be found in appendix Figure E.3.

discussed earlier in Section 1.2.5, but is not expected for electron showers, as utilized here. Future additional dedicated response measurements of these layers would again be helpful to study the response with more credibility. For now, $N_{total} = 6000$ is selected, because it provides the best agreement between data and simulation.

9.5.2.4. Layer 13 & 14

Finally, layers 13 and 14 are equipped with SiPMs featuring 1300 pixels on a sensitive area of $1 \times 1 \, \text{mm}^2$. These layers are the last two layers and have a large distance of 10 slots between each other (cf. Table 8.1). Electron showers do not penetrate the detector far enough to deposit high-enough energy in these two layers to allow any conclusions concerning response saturation. Thus, pion showers are utilized to study the response of layers 13 and 14, though the simulation of pion showers compared to electron showers is commonly more difficult. But because electron showers measured at CERN in 2015 suffer from low-energy electron contamination in data, both shower types are challenging.

Figures 9.11 and Figure E.3 in the appendix show the three combined observables of layers 13

and 14, respectively.

Observables $M_{E_{13}}$ and $M_{E_{14}}$

For layer 13, $M_{E_{13}}$ shows a low value valley comparable to what has been observed before. The lowest values are around a broad area between roughly (2000 to 2600|0.0) and (2800 to 3600|0.4). For layer 14, the observable favors lower N_{total} around 1400 at $\epsilon_C = 0.0$. If the actual values are compared, layer 13 has lower minimums around 0.1, while layer 14 only reaches roughly 0.3. Therefore, and because layer 13 includes more deposited energy than layer 14 (cf. Figure 8.28), the information from layer 13 is more important for the saturation recovery optimization.

Observables X_{E_l} and X_{e_l}

The second combined observables X_{E_l} look similar for layer 13 and 14 and favor higher N_{total} than M_{E_l} do, which also has been observed before in other layers. Similar is the case for the third combined observable, X_{e_l}, where high N_{total} are even more preferred.

Dependance on R

The results of $M_{E_{13}}$ and $M_{E_{14}}$ seem to be more or less independent of R and allow no additional improvement of the results, thus the default $R = 0.95$ can be chosen.

Conclusion

Finally, a combination of (2300|0.0|0.95) is chosen, taking into account the weights that have been applied before to the different observables and focusing on the information of layer 13. Concerning crosstalk $\epsilon_C = 0.0$, no expected values are available to compare to. Similar to layers 11 and 12, the chosen N_{total} is much higher (about 1.8 times) than the physical number of pixels of the SiPM and similar reasons apply.

9.5.3. Summary of Final Parameter Combinations

As a short summary, Table 9.1 lists the final optimized parameters of the crosstalk-extended response model for all active layers of the detector prototype, as discussed in the previous subsections. A relative variation of the three optimized parameters of $\pm 5\,\%$ shows, that the variation of N_{total}^{eff} has the highest impact on the observable M. Therefore, only N_{total}^{eff} is taken into consideration concerning uncertainties. The uncertainty of N_{total}^{eff} is assessed to be of the order of 5 %, which in most cases roughly compares to one bin variation around the optimum in the M distributions. Such a variation already shows a significant difference in the observable M in most layers, as for example in Figure 9.5. For the discussion about uncertainties, please refer to Section 9.8.1 below.

Layer	$N_{total}^{physical}$	N_{total}^{eff}	ϵ_C	R
3	1600	1600	0.2	0.8
4-5	12000	6000	0.15	0.6
7-9	800	850	0.0	0.95
11-12	2300	6000	0.0	0.95
13-14	1300	2300	0.0	0.95

Table 9.1.: Final parameters of the crosstalk-extended response model. Besides the layer information and the physical total number of pixels of the SiPM, $N_{total}^{physical}$, the corresponding total number of effective pixels after optimization, N_{total}^{eff}, the crosstalk parameter ϵ_C and the ratio R are listed.

9.6. Advanced Response Model Studies

The advanced response model has been introduced already in Section 4.3.3.3. Different to the crosstalk-extended response model as discussed before, this model includes several parameters to account for the recovery of SiPM pixels and charge contributions of multiple photons, which both allow to model over-saturation. It also includes parameters for the total number of pixels, N_{total}, for SiPM crosstalk and an additional parameter for SiPM after-pulses. The factor of after-pulses, ϵ_A, is implemented as a scale factor. In this study, the after-pulse factor is fixed to $\epsilon_A = 0$ in order to reduce the amount of free parameters. Also, N_{total} is fixed to the physical number of pixels on the SiPM. With these adjustments, three free parameters remain, which are: α, β and ϵ_C.

So far, no direct inversion of the advanced model is available. Still, an inversion could be approximately implemented by a look-up table for example.

The advanced response model is studied in a similar way as done with the XT-ext model, but only utilizing electron data. Thus, only results for layers 3 to 12 are discussed here, as energy depositions of electron showers are too low in layers 13 and 14, to allow a significant study of response saturation. In case of the advanced model, the study has not been pursued with pion data, as will be declared later.

9.6.1. Approximate Method for LY_{seed} Estimation

The method of the response model application has been explained above in Section 9.2. Thereby, the need to estimate the converted light yield, LY_{seed}, has been discussed and a method has been presented, to estimate LY_{seed} from the default light yield LY. LY_{seed} represents the number of photons, generated by a minimum ionizing particle (MIP) and hitting the active area of the SiPM, times the photon detection efficiency of the SiPM - which is needed as an input parameter for the response model. On the other hand, LY represents the number of pixels fired by a MIP, which is a measured value and therefore affected by the response of the SiPM-tile system itself, including crosstalk and saturation. With Equation 9.1, LY_{seed} can be estimated by applying the inverted response model $LY_{seed} = f_{response}^{-1}(LY)$. As stated above, no inversion of the advanced model is available, thus an approximated method has been developed:

As a first order correction and similar to the method applied in Section 4.3.2 (for example Equation 4.15), the light yield is first corrected to crosstalk by means of $\mu_C \approx 1 + \epsilon_C$ in Equation 9.12.

$$LY_{XT} = LY/\mu_C \tag{9.12}$$

Thereafter in Equation 9.13, the ratio R_{LY} between the saturated and the initial 1 MIP signal is estimated. Here, the advanced model is applied.

$$R_{LY} = \frac{f_{adv}(LY_{XT})}{LY} \tag{9.13}$$

Finally in Equation 9.14, a second order correction is applied, using the previous equations leading to an approximate LY_{seed}:

$$LY_{seed} \approx LY_{XT}/R_{LY} \tag{9.14}$$
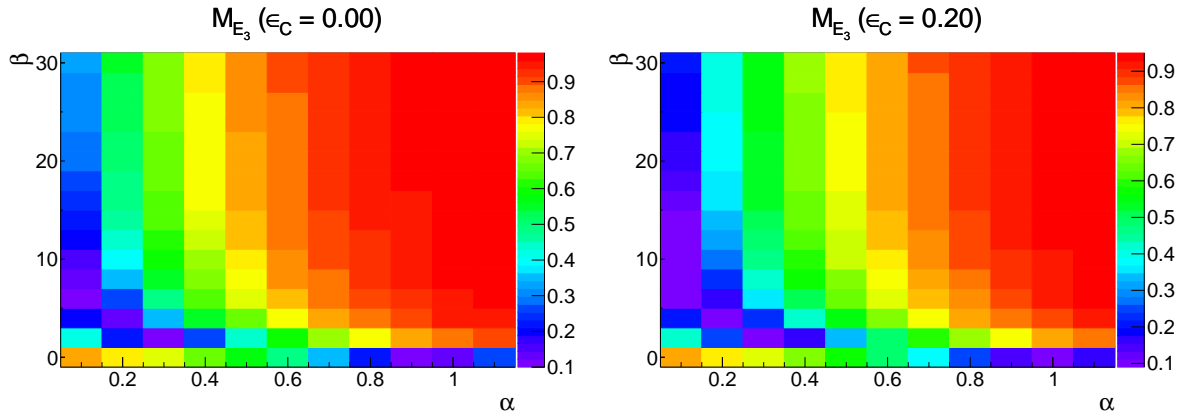
Figure 9.12.: The first combined observable, M_{E_3} (cf. Equation 9.4), for the advanced response model as two-dimensional histograms as a function of α and β for layer 3 for fixed crosstalk parameters $\epsilon_C = 0.0$ (left) and $\epsilon_C = 0.2$ (right).

The differences between this approximated method and the default method have been studied by means of the XT-ext model, where the inverted model known. In the full range of interest, $0 \leq \epsilon_C \leq 0.4$ and for an exemplary $LY_{seed} = 20$, the maximum deviation between the two methods is smaller 3 ‰.

With the preconditions for the study of the advanced response model now given, the next section discusses the combined observables of the advanced model for layer 3.

9.6.2. Layer 3 Combined Observables Discussion

Similar to the study of the combined observables M_{E_l}, X_{E_l} and X_{e_l} of the crosstalk-extended response model, the results are discussed in detail by means of layer 3 and with less detail for other layers.

Observable M_{E_3}

Figure 9.12 shows two maps of the first combined observable, M_{E_3}, for the advanced response model as a function of α and β for fixed $\epsilon_C = 0.0$ and $\epsilon_C = 0.2$. For $\epsilon_C = 0.0$, a large fraction of the map is filled with high values marked in red, mainly for $\beta \geq 4$ and $\alpha > 0.6$. On the other hand, for $\alpha = 0.1$ and $\beta \geq 4$, the observable becomes relatively small, as well as in the region around $\alpha \approx 1$ and $\beta = 0$. With this resolution it is hard to tell, whether the two low-value regions are connected or separated. Thus, Figure 9.13 shows a detailed view with higher resolution in a smaller range, from which becomes clear, that it is actually one connected low-value valley, which indicates some correlation between α and β, as already mentioned before in Section 4.3.3.3.

Low value region

What actually is the meaning of this valley? If the advanced model is inspected, there are several
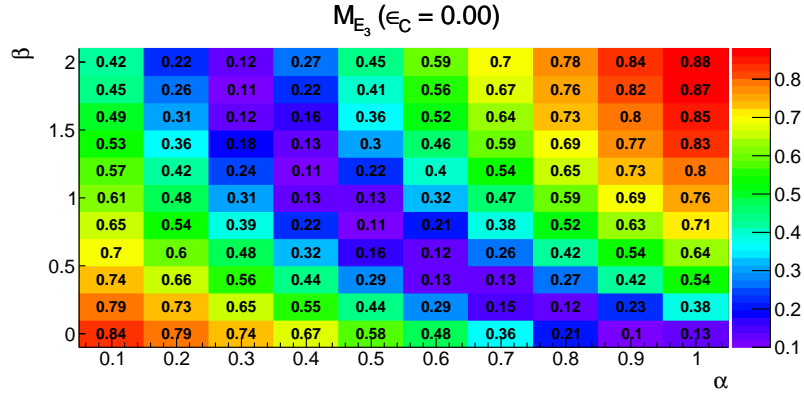
Figure 9.13.: Detailed view of the first combined observable, M_{E_3}, for the advanced response model as two-dimensional histogram as a function of α and β for layer 3 for a fixed crosstalk parameter $\epsilon_C = 0.0$.

parameter combinations for which the advanced model, N_{adv}, results in the simple exponential model, N_{exp}, in case $\epsilon_C = 0.0$. A few examples are listed in Equation 9.15.

$$N_{adv}(\alpha = 1.0,\ \beta = 0) = N_{exp}$$
$$N_{adv}(0.75,\ 1/3) = N_{exp}$$
$$N_{adv}(0.5,\ 1) = N_{exp} \tag{9.15}$$
$$N_{adv}(0.25,\ 3) = N_{exp}$$
$$N_{adv}(0.1,\ 9) = N_{exp}$$

If these parameter combinations are compared to the results shown in Figure 9.13, the lowest results of M_{E_3} are actually in the region, where the advanced model equals the simple exponential model. This leads to the assumption, that the simple model is already sufficient enough to describe the response of layer 3 channels.

Impact of ϵ_C

Figure 9.12, right, shows M_{E_3} for $\epsilon_C = 0.2$. This crosstalk value is shown here, because it has been selected within the crosstalk-extended response model studies before. There is a small shift in the distribution, which slightly broadens the low-value region at low α compared to M_{E_3} with $\epsilon_C = 0$. M_{E_3} can be reduced to 0.09 at some spots, which is a small improvement to 0.1, which is the lowest result at $\epsilon_C = 0.0$. This indicates that also in case of the advanced response model, an $\epsilon_C = 0.2$ is reasonable. Other ϵ_C up to 0.4 have been analyzed but do not improve the result any further.

Observables X_{E_3} and X_{e_3}

Figure 9.14 shows X_{E_3} and X_{e_3} of the advanced response model for layer 3 and $\epsilon_C = 0.0$. X_{E_3} looks similar to the M_{E_3} with a similar shape preferring the region around $N_{adv} \approx N_{exp}$. The lowest values of X_{e_3} are shifted to higher β. This indicates, that the underlying distributions of the energy (E_3) and of the hit energies (e_3) of layer 3 behave a little differently, as seen already above within the study of the crosstalk-extended model.
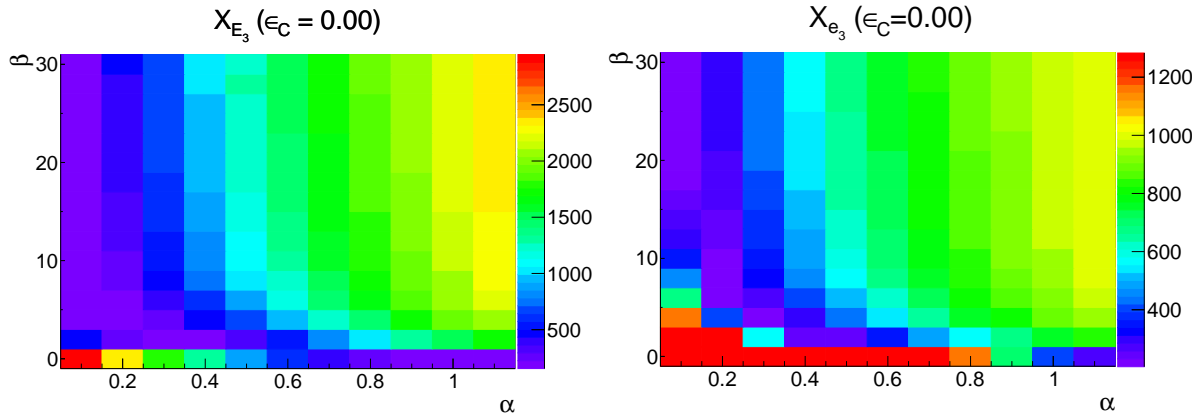
Figure 9.14.: X_{E_3} (left) and X_{e_3} (right) for the advanced response model as two-dimensional histograms as a function of α and β for layer 3 for a fixed crosstalk parameter $\epsilon_C = 0.0$.

In both, X_{E_3} and X_{e_3}, the lowest results are of the same order compared to the results from the crosstalk-extended model shown before in Figure 9.5.

Conclusion and comparison to XT-ext model

To summarize shortly, the advanced model does not improve the agreement between data and simulation on the basis of the combined observables compared to the crosstalk-extended model in layer 3 (cf. Figures 9.5 and 9.6). On the contrary, the crosstalk-extended model allows even better results for M_{E_3} around 0.07. In both models, the results can be slightly improved by taking into account crosstalk with $\epsilon_C = 0.2$. Because the advanced model needs more computing power and the converted LY_{seed} and the inverted advanced response model can only be estimated approximately, the crosstalk-extended response model is preferred for the future analysis of layer 3. What about the other layers?

9.6.3. Other Layers Combined Observables Discussion

The remaining layers are only discussed by means of the first combined observable M_{E_l} and the other two observables are dropped here, because they only would bring a small information yield.

9.6.3.1. Layers 4 and 5

Because layers 4 and 5 carry the same type of SiPM and tile, they are analyzed together.
Figure 9.15 shows M_{E_4} and M_{E_5} as functions of α and β for a fixed $\epsilon_C = 0.0$ for layers 4 and 5. Different to layer 3, the lowest results are found for $\beta = 0$, with a minimum at $\alpha = 0$ for both layers. Still, the shapes which are expected from the simple exponential function, as discussed for layer 3, are also visible but do not compete with the lowest results. Crosstalk values up to $\epsilon_C = 0.4$ have been studied, but neither the shape nor the values change significantly.

 Figure 9.16 shows a detailed view of M_{E_4} with higher resolution. The impact of a small α and β has been sketched by Figure 4.11, which has shown that both, small α and small β, decrease the output of the advanced function. This lowered result of the model has the same tendency as a smaller N_{total}, for example in the XT-ext model, would have. Therefore, the observation
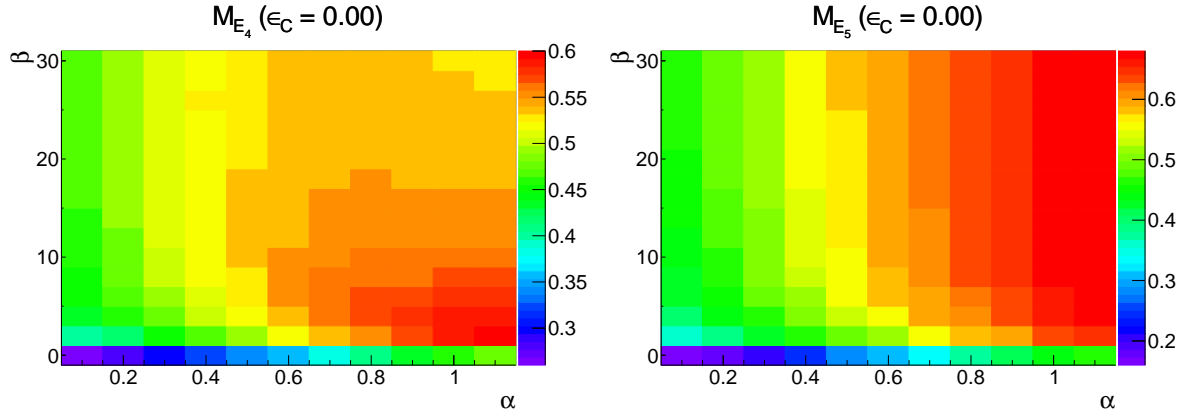
Figure 9.15.: The first combined observables M_{E_4} and M_{E_5} for the advanced response model as two-dimensional histograms as a function of α and β for layer 4 (left) and layer 5 (right) for a fixed crosstalk parameter $\epsilon_C = 0.0$.
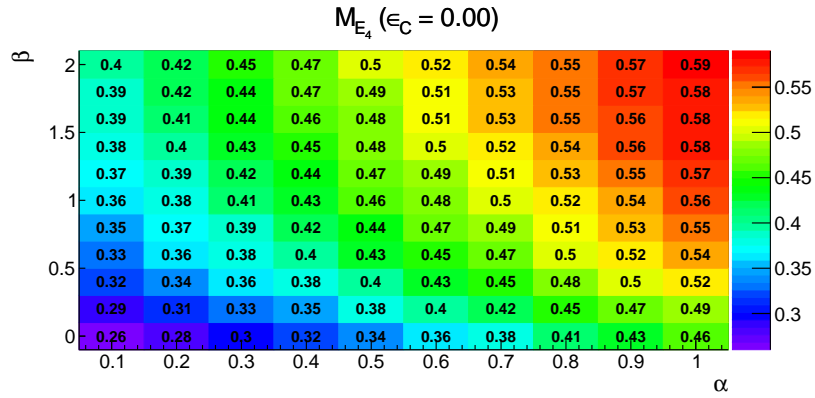

Figure 9.16.: Detailed view of M_{E_4} for the advanced response model as a function of α and β for layer 4 for a fixed crosstalk parameter $\epsilon_C = 0.0$.

is in agreement with the result of the XT-ext model studies in Section 9.5.2.1, where instead of the physical 12000 pixels, a N_{total} of only 6000 pixels has been preferred. As already discussed there, this indicates, that parts of the sensitive area of the SiPM might not have been illuminated completely, thus reducing the effective number of pixels.

9.6.3.2. Layers 7, 8 and 9

Layers 7, 8 and 9 are discussed in the following. Figure 9.17 shows M_{E_7}, M_{E_8} and M_{E_9} of these layers. In this case and in difference to layers 4 and 5, the shape looks similar to the shape of layer 3. The lowest values are in the region, where a simple exponential functionality is expected. From layer 7 to 8 to 9, the low-values walk a little from left to right to higher α. A higher α, which represents the recovery of SiPM pixels, leads to higher results of the advanced model, thus reduces the impact of saturation. This is similar to the results of the XT-ext response model study in Section 9.5.2.2, where from layer 7 to 8 to 9, the preferred N_{total} has increased. Because these three layers consist of the same SiPM and tile combination, this difference from
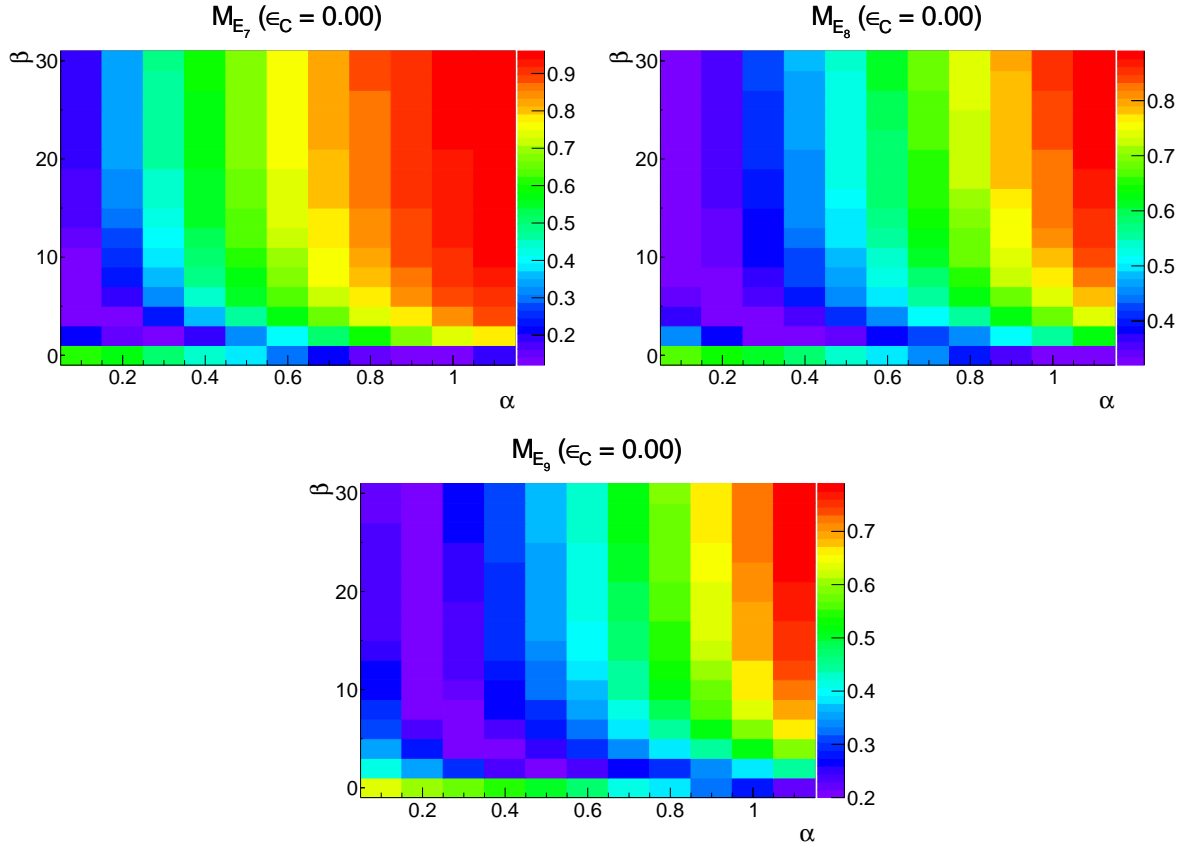
Figure 9.17.: The first combined observables M_{E_7} (left), M_{E_8} (right) and M_{E_9} (bottom) for the advanced response model as two-dimensional histograms as a function of α and β for a fixed crosstalk parameter $\epsilon_C = 0.0$.

layer to layer is not expected and may have its origin in other discrepancies between data and simulation. For instance, previous optimizations of the additional absorber in Section 8.6.1 or of the tile-to-tile crosstalk in Section 8.6.2 have already revealed some remaining discrepancies, for example caused by the presumable contamination of low-energy electrons in the electron beam (cf. Section 8.5).

9.6.3.3. Layers 11 and 12

Finally, layers 11 and 12 are discussed briefly. The 2D-distributions of $M_{E_{11}}$ and $M_{E_{12}}$ of the advanced model are shown in Figure 9.18. While the shapes of the low-value entries look familiar to the shape of layer 9 in Figure 9.17 for example, it is even more shifted to the right, preferring higher α. Again, a high α indicates higher SiPM pixel recovery, thus less saturation. This is in agreement with what the XT-ext model study already proposed in Section 9.5.2.3: There, instead of the physical 2300 total pixels, a N_{total} of 6000 showed the best result. As discussed there, this can be interpreted by low SiPM saturation or very high pixel recovery effects. Together both results indicate, that the latter might be the case and that layers 11 and 12 are affected by high pixel recovery.

For layer 12, the shift away from the simple exponential functionality is a bit lower compared
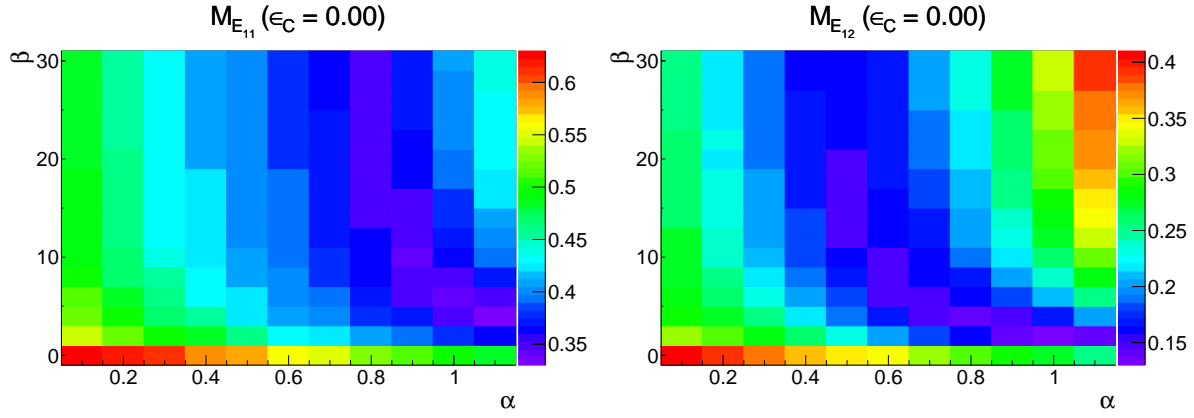
Figure 9.18.: The first combined observable $M_{E_{11}}$ (left) and $M_{E_{12}}$ (right) for the advanced response model as two-dimensional histograms as a function of α and β for a fixed crosstalk parameter $\epsilon_C = 0.0$.

to the shift for layer 11. This difference is interesting, because no such difference between the two layers has been observed before in the XT-ext response model study. This might indicate, that the advanced model is capable of modeling the recovery procedure in a finer way, which it is actually made for. Also if the values of the minimums are compared between the two models, the advanced model has a small advantage: while for example the lowest value of $M_{E_{11}}$ with the XT-ext model is approximately 0.4, the advanced model reaches approximately 0.33, which corresponds to a reduction of around 17.5 %.

Impact of ϵ_C

The impact of the crosstalk parameter ϵ_C has been studied for all previous layers, but because the impact is very small, it is not discussed in detail. There is nearly always a small shift of the low-value region to higher α. Because a higher α is to some degree comparable to a higher N_{total} in the XT-ext model, this observation is compatible to the observation at the XT-ext model study, where higher ϵ_C also requires higher N_{total} to keep the result of M_{E_l} alike.

9.6.4. Summary of Final Parameter Combinations

Table 9.2 lists reasonable parameter combinations of the advanced response model in consideration of the discussed combined observables. This list is in particular used to compare these results to those of the optimized XT-ext response model in the following section.

Layer	$N_{total}^{physical}$	α	β	ϵ_C
3	1600	0.1	8	0.2
4-5	12000	0.1	0	0.0
7-9	800	0.4	2	0.0
11-12	2300	1.0	2	0.0

Table 9.2.: Chosen parameters of the advanced response model. Besides the layer information and the physical total number of pixels of the SiPM, $N_{total}^{physical}$, the corresponding parameters α, β and the crosstalk parameter ϵ_C are listed.

9.7. Response Study Conclusions

The previous two sections 9.5 and 9.6 have discussed the optimization of two response models, the crosstalk-extended and the advanced response model, respectively. On the basis of three combined observables, M_{E_l}, X_{E_l} and X_{e_l} (cf. Section 9.3), the agreement between data and simulation with a dedicated set of response parameters has been studied.

For both response models, significant minimums in the combined observables can be found, which allow an optimization of the response parameters. Having said this, the observed minimums often vary between the three different observables, which makes it hard to identify an optimal parameter combination. While the minimums of M_{E_l} and X_{E_l} are often in more agreement to each other, X_{e_l} often shows the minimum at a significantly different region. This is most probable related to the fact, that M_{E_l} and X_{E_l} both result from the layer-wise energy distributions, while in contrast X_{e_l} is estimated from the hit energy distributions of each layer. As pointed out in Section 9.3, the hit energy distribution is generally more vulnerable to distinctions between data and simulation, concerning the exact reproduction of the detector geometry and the particle shower shape. Unfortunately, these requirements cannot completely be ensured in this analysis, especially because electron showers in data are most probably contaminated by low-energy electrons due to possible upstream collisions, induced by a bad steering of the beam parameters during data taking. Thus, the information of M_{E_l} and X_{E_l} are counted as more significant, as they are assumed to be less vulnerable, because their underlying layer-wise energy distributions aggregate the single hit energies to one total energy per layer, which is less affected by variations of the shower shapes between data and simulation.

Still, the often different results between the first two (M_{E_l} and X_{E_l}) and the third combined observable, X_{e_l}, which often has much worse results, indicate that the agreement between simulation and data is not perfect, as expected. Especially the response models are not capable of improving the agreement between data and simulation in such a way, that all observables and therefore both underlying distributions agree well. That indicates, that the remaining disagreement arises from another source, which cannot be addressed by any of the two response models. The deviations between M_{E_l} and X_{E_l} indicate, that respectively the mean and the shape of the layer-wise energy distributions also do not behave similar to response parameter variations. Though the mean might be in good agreement, the shape might still differ.

9.7.1. Impact on the Underlying Distributions

The impact of the implementation of the XT-ext and advanced response models in simulation on the layer-wise energy distributions, E_l, and on the layer-wise hit energy distributions, e_l, is discussed in the following. These are the underlying distributions of the three combined observables, which have been optimized previously. Optimized parameter combinations for the two response models have been listed before in tables 9.1 and 9.2.

Figures 9.19 and 9.20 show both distributions E_l and e_l exemplarily for layers 3, 5, 9 and 11 for 50 GeV electrons and layer 14 for 90 GeV pions. Like this, one layer for each SiPM-tile combination is presented at the highest available beam energy, where saturation effects are

expected to be high and impacts of different response models are expected to be significant. The following content is shown in each plot:

- Data without any applied saturation model,

- simulations with applied XT-ext response model with

  - default parameters,

  - optimized parameters,

  - and two variations of N_{total} originating from the optimized parameters and

- simulation with applied advanced response model with selected parameters (except for layers 13 to 14).

The variation of N_{total} is of the order of one bin size in the plots shown in the study of the XT-ext response model (e.g. Figure 9.5). These variations are included here in order to study the impact of possible variations of this parameter, also in regards to systematic uncertainties arising from the response model.

The E_l and e_l plots of different layers are discussed briefly one after the other.

Layer 3

Starting with E_3 in the top of Figure 9.19, the distribution looks Gaussian and the shape of data is a little wider than any simulation. There is no significant difference between the various models and parameters, though the simulation with the XT-ext optimum model (blue) features a better agreement of the mean compared to the default (red) and is a little broader and therefore a little closer to data. A higher N_{total} shifts the distribution to little higher energies. The simulation with the advanced model is a little off to a smaller mean.

The shape of the hit energy distribution e_3 in data features some kind of double edge around 50 GeV and 70 GeV (as previously mentioned by means of Figure 9.4), which is not present in any simulation and might indicate, that there are small differences in the responses of different channels on layer 3. The simulations show a much clearer difference between the various response models. While the default and the advanced models show a too early falling edge compared to data, the simulations with the optimized XT-ext model agree much better at the highest hit energies. The impact of the variations of N_{total} are also visible at the highest hit energies, where larger N_{total} result in little larger hit energies, as expected.

Layer 5

For E_5 in the bottom of Figure 9.19, the distributions again look Gaussian and the simulation with the default response model features too high energies compared to data. On the other hand, all optimized response models agree better to data, as their distributions are shifted to lower energies because of a lower N_{total} in the case of the XT-ext model (6000 for the optimized) and because of a small $\alpha = 0.1$ in case of the advanced model. Still, the shape of data is not reproduced well in any simulation, as the shape of the simulations are much sharper. Only the agreements of the means of the distributions are improved.

The shape of the distribution of e_5 (as well as e_4, which is not shown here) in data features a longer plateau in the region between approximately 80 and 170 MIP, which is not emulated in any simulation, which themselves feature a bump before the falling flank, induced by saturation
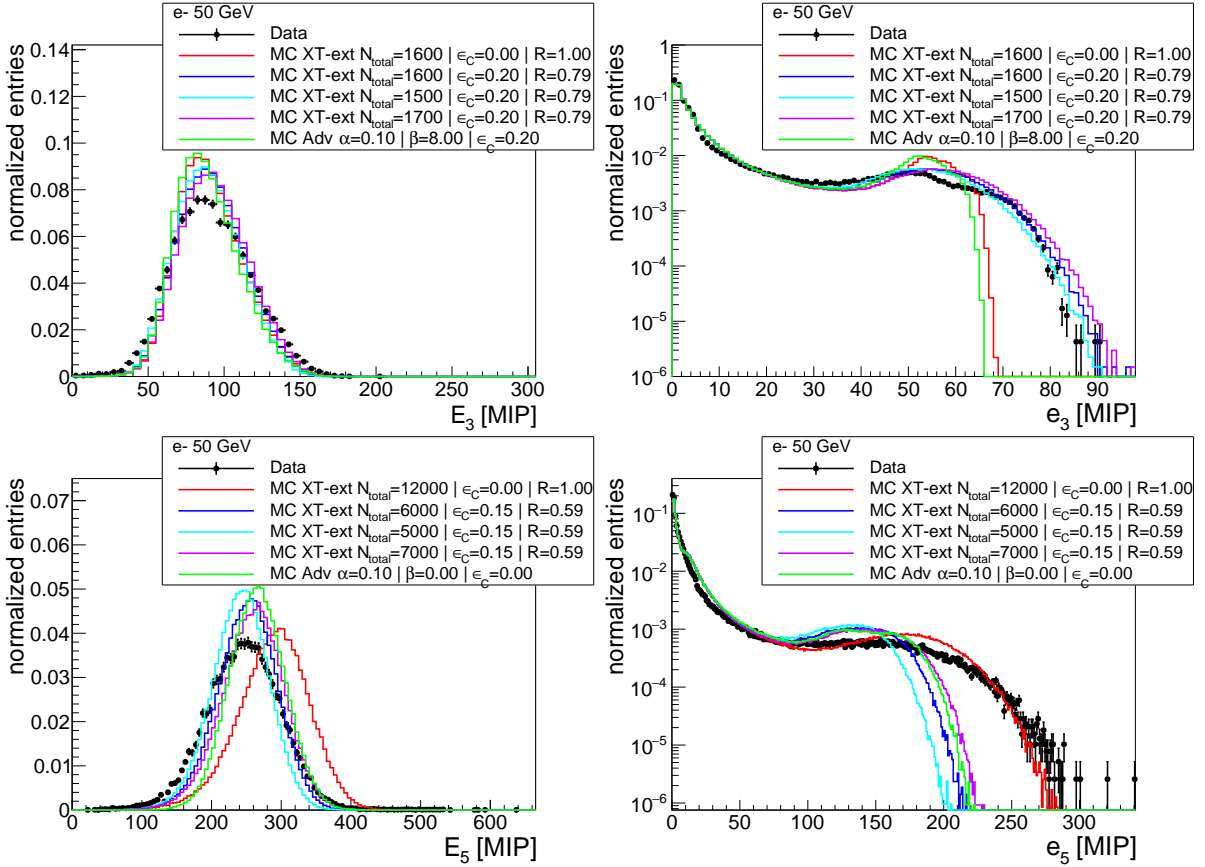
Figure 9.19.: Layer-wise energy E_l (left) and layer-wise hit energy e_l (right) distributions of layers 3 (top) and 5 (bottom) of 50 GeV electron data (black) and different simulations after applying the XT-ext response model with the default (red) and the optimized parameter combination (blue) and two variations of N_{total}, originating from the optimized parameters to indicate the impact of this parameter (cyan and violet). The advanced model has been applied in green. Entries are normalized.

in the model. The e_5 distribution is an exception to all other layer-wise hit energy distributions, as the simulation with the default response model agrees better to data at high energies, compared to the optimized response models. This does not surprise, as the observable X_{e_5} in Figure E.1 already indicated an optimum at high N_{total} in difference to the optimum at small N_{total} for X_{E_5}. As the response parameters are mainly optimized to improve the agreement between the means of data and simulation within the layer-wise energy distributions, E_l, the simulations with optimized response parameters feature shapes whose falling flanks finish too early. The result of the advanced model lies within the variation of the XT-ext model.

As discussed before, the simulation cannot generate a good agreement between data and simulation in both distributions, E_5 and e_5, at the same time. Most probable, this is due to the combination of very high energy depositions and the tile-to-tile crosstalk, which is only simulated in first order. This issue would require further investigations, in case layers without individual tile wrapping would be used in future measurements, but it is not foreseen.

Layer 9

In the E_9 distribution in the top of Figure 9.20, data and simulation are roughly of the same

width but the shape differs at the maximum. While data features a relative broad plateau at the maximum, the simulations show an additional maximum to higher energies at around 120 MIP. The origin of this shape might be related to inactive channels in layer 9, which differently influence the reconstructed energy of this layer in data and simulation, depending on the exact shower shape and whether the shower deposits parts of its energy in an active or inactive channel. As plotted in Figure H.1, there are two inactive channels in the center of layer 9. The differences between the simulations are relatively small, there is only a very small shift to higher energies for the simulations with optimized XT-ext and advanced models.

For e_9, the differences between the different simulations are also small, but the simulations with optimized XT-ext and advanced models agree better to data at high energies. Still, the shape of data is not in good agreement with any simulation at low to medium hit energies.

In both distributions, the simulation with the advanced model is embraced by the simulations with the variations of the XT-ext model parameters.

Layer 11

For layer 11 and 12, a very high $N_{total} \approx 6000$ instead of the default 2300 pixels has been selected as optimum for the XT-ext model and on the other side, a high $\alpha = 1$ in combination with $\beta = 2$ has been chosen for the advanced model. In E_{11} in the middle of Figure 9.20, the simulations with optimized response models are in much better agreement to data compared to the default model, which strengthens the validity of the optimization results.

The agreement between data and simulation of the e_{11} distribution can also be significantly improved with the optimized response models, especially concerning the long falling edge at high energies.

In both distributions, the differences between the simulations with the XT-ext and with the advanced model are very small.

Layer 14

For layer 13 and 14, only the XT-ext model has been optimized by means of pion data. The agreement between data and simulation in E_{14} in the bottom of Figure 9.20 can to some extend be improved with the optimized response model in comparison to the default model, which is a little more off at the falling flank. Generally speaking, all simulations are in rather good agreement to data and the differences between the models are small.

In e_{14}, a more obvious improvement from the default to the optimized response model is visible, as the shape at high energies agrees better for the latter.

Short conclusion

To summarize, in all distributions except for e_5, the simulations with the optimized response models are in better agreement to data than the simulations with the default response model. This is the case for both, the XT-ext as well as the advanced response model. The deviation in e_5 is expected from the optimization study.

The differences between the XT-ext and the advanced response models are generally small. Some deviations to the shape of data in both distributions remain, no matter which response models are applied.
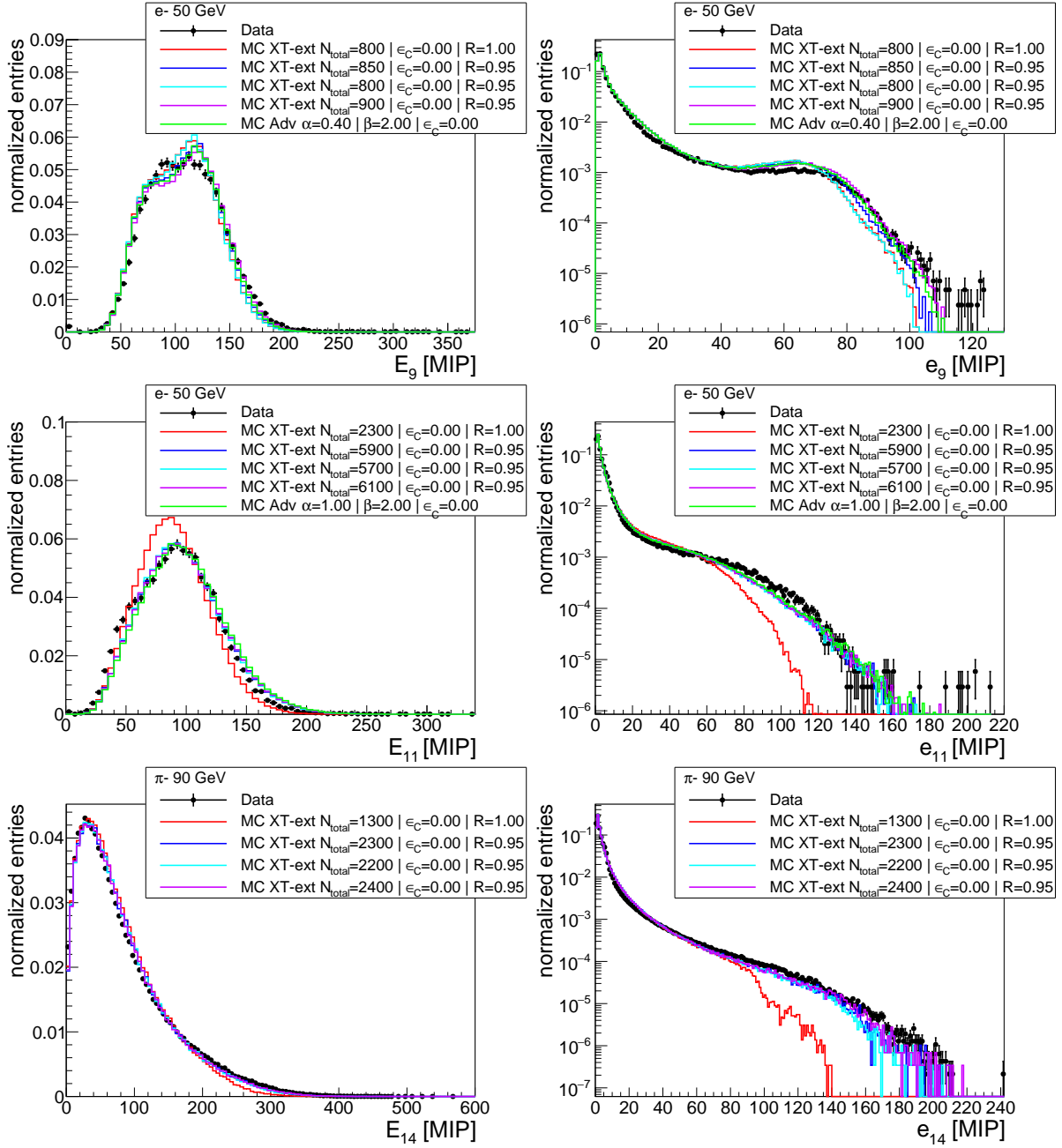
Figure 9.20.: Layer-wise energy E_l (left) and layer-wise hit energy e_l (right) distributions of layers 9 (top) and 11 (middle) for 50 GeV electrons and for layer 14 (bottom) for 90 GeV pions, each for data (black) and different simulations after applying the XT-ext response model with the default (red) and the optimized parameter combination (blue) and two variations of N_{total}, originating from the optimized parameters to indicate the impact of this parameter (cyan and violet). Except for the bottom figures, the advanced model has been applied in green. Entries are normalized.

9.7.2. XT-ext versus Advanced Model

The comparison between the XT-ext and the advanced model shows that in most cases, the XT-ext model reaches similar or even slightly better results than the advanced model, for instance

in layer 3, as discussed before. Layers 11 and 12 are a small exception, where the advanced model is capable of realizing better M_{E_l} observable results, most probable because in these layers, the SiPM pixel recovery mechanism is more dominant compared to other layers. The advanced model has an advantage there, as it takes into account pixel recovery, while the XT-ext model can only do this indirectly by increasing the effective total number of pixels. Still, if the underlying distributions E_{11} and e_{11} are investigated as above (cf. Figure 9.20), the differences between the two models are actually very small.

Nevertheless, the XT-ext model is selected to be applied to the further analysis. This has two main reasons: First, as written above, the results of the XT-ext model are of the same order compared to the advanced model, for some layers even better and for others little worse. The shapes of the distributions of the simulations with the advanced and the XT-ext models do not show any significant difference to each other. Second, the implementation of the XT-ext model is much easier to realize, because for the advanced model, an inversion is not available. As previously mentioned, this could be bypassed by means of a look-up table, but the solution with the XT-ext model is much leaner. Because mixing two different response models is not an option here, the XT-ext model is finally chosen with the parameters already listed in Table 9.1.

9.8. Systematic Uncertainties and Final Comparison

After the parameters of the response models of the SiPM-tile system have been studied and optimized in the previous sections, it is time to take a closer look at the final comparison between data and simulation. First of all, Section 9.8.1 deals with the systematic uncertainties, which arise from different aspects in which data and simulation are handled. The knowledge of systematic uncertainties is important to estimate the significance of any result. Thereafter in Section 9.8.2, a final comparison between data and simulation is presented, where the inverted response model is applied in order to receive de-saturated results. These results include information about the impact of systematic uncertainties.

9.8.1. Systematic Uncertainties

To estimate the significance of simulation and data, systematic uncertainties are taken into account. Some of these uncertainties have been calculated in other studies and if so, are referenced as such.

The following sources are taken into account for data:

- Gain calibration: To estimate the systematic uncertainty introduced by the gain calibration, two different gain calibrations have been performed using LED measurements of two different days. The distribution of the ratio of the two different gains, G_1/G_2, for each channel, has been fitted by a Gaussian, resulting in a standard deviation of $\sigma_{Gain} \approx 0.05$ which corresponds to 5 % relative uncertainty on the gain. [177]

- MIP calibration: For the estimation of systematic uncertainties introduced by the MIP calibration, the same set of calibration constants has been applied to two different sub-samples of muon data, separated in samples of even and odd run number. Due to the same set of calibration constants applied to both sets, the most probable value (MPV) of

the hit energy distributions of both sub-samples should be 1 MIP. Estimated MPVs are plotted into one histogram for each sample and Gaussian fits are applied, from which two σ are extracted. The mean of these two values is $\sigma_{MIP} = 0.015$ and corresponds to 1.5 % relative uncertainty on the MIP calibration. [139]

- High- and low-gain (HG/LG) intercalibration: Two different datasets from LED scans and from electron data have been used to measure two sets of HG/LG intercalibration values. The final chosen set of intercalibration constants is a best-fit combination of these both measurements [178]. A comparison of these two individual calibration sets leads to a difference in the two means of around 0.15 [177]. Following [179], this is considered as a maximum tolerance and leads to a standard deviation of the HG/LG intercalibration of $\sigma_{IC} = 1/\sqrt{12} \cdot 0.15 \approx 0.05$, appropriate to 5 % relative uncertainty.

- SiPM-tile response model parameters: The finally chosen SiPM-tile response model is the XT-ext model which includes three parameters: the total number of effective pixels, N_{total}^{eff}, the SiPM optical crosstalk parameter ϵ_C and the ratio R, which controls the start of the linear extension. The impact arising from a relative variation of $\pm 5\%$ on the three parameters has been studied leading to the result, that N_{total}^{eff} is the most dominant parameter. Thus, to minimize the number of values taken into account for the systematic uncertainty estimation, only N_{total}^{eff} is considered. Because the chosen N_{total}^{eff} differs from layer to layer, a relative $\sigma_{N_{total}} = 5\%$ has been evaluated (see Section 9.5.3) in order to cover about one bin in the previously discussed saturation scans (for example Figure 9.5).

The following sources are taken into account for simulation:

- Beam line simulation - additional absorber: In order to simulate the beamline, additional absorber material has been added upstream to the detector, as discussed in Section 8.6.1. An optimum thickness of 16 mm has been found, which prevails against other studied thicknesses of $\pm 4\,mm$. To estimate the systematic uncertainty, it is appropriate to take into account a variation of the absorber thickness of $\pm 2\,mm$, which corresponds to a relative uncertainty of $\sigma_{abs} = 12.5$ %.

- Tile-to-tile crosstalk: The tile-to-tile crosstalk of layers 4 to 10 has been tuned in Section 8.6.2 for the simulation, resulting in an optimum of 16 %. To evaluate the systematic uncertainty arising from this parameter, an absolute variation of ± 2 % is considered, similar as above, tantamount to $\sigma_{XT} = 12.5$ %.

- SiPM-tile response model parameters: Similar to data, the systematic uncertainty arising from the response model optimization is taken into account by a variation of $\sigma_{N_{total}} = 5\%$ on the effective total number of pixels, N_{total}^{eff}. The effect on the uncertainty in the simulation is rather small, as the de-saturation in the reconstruction procedure utilizes the inverted response model of the saturation in the digitization procedure. Still, as discussed in Section 9.2, small differences might occur because of the smearing of the number of pixels fired, which takes place between saturation and de-saturation. Like this, the uncertainty of the response model is mainly expressed by data.

The resulting systematic uncertainty for data and simulation is estimated from the upper listed sources. For each source S, representative for Gain, MIP, etc., the complete data or simulation, dependent on the source, is reproduced with the varied parameter $S^* = S \cdot (1 \pm \sigma_S)$. For data, this leads to 9 complete data sets, including one data set with optimized parameters and four times two sets with varied gain, MIP, IC and N_{total}. For the simulation, this results in a total number of seven simulation sets analogically. In each set, only one parameter is varied.

The resulting data and simulation sets are then processed as discussed in detail in Section 9.2.1, where first, event selections are applied before any inverted response model is utilized. This is important because otherwise, the event selections, which involve selections on energies, would not be sufficient anymore but need adjustments. After the event selections are performed, the inverted response model is applied in order to receive saturation and SiPM crosstalk corrected energies.

To estimate the final systematic uncertainty for each distribution, a symmetrization of the uncertainties is performed by selecting the maximum deviation for each bin and for each source, so that afterwards, only 1 symmetric uncertainty remains for each bin and source.
In a final step, the uncertainties (four for data and three for simulation) are added in quadrature for each bin, assuming no correlation, resulting in the final systematic uncertainty for data and simulation, respectively.

9.8.2. Final Comparison between De-saturated Data and Simulation

After the the inverted response model has been applied in order to receive energies which are corrected for saturation and SiPM crosstalk effects, the systematic uncertainties have been estimated. A final comparison between data and simulation is presented in this section. In the following, distributions of a limited number of beam energies are shown, for other beam energies, please refer to Appendix F. The agreement between data and simulation is rather similar compared to the presented plots shown here.

9.8.2.1. Electron Showers

First, electron showers are compared. Figure 9.21 shows the shower profiles of the mean number of hits per layer, $\langle N_l \rangle$, for both, data and simulation of 10 and 50 GeV. In comparison to the previously presented results in Figure 8.26, where the inverted response model has not yet been applied, both results look very similar and the shape has been discussed already there. That is the case, because $\langle N_l \rangle$ is not directly affected by the response model, which itself only affects energies, not hits. But because of the 0.5 MIP cut, which is applied after the inverted response model, there might be small variations. Still, the impact of the response model is very weak at these small energies.
The agreement between simulation and data is within around 20 % deviation from a ratio of 1 throughout all beam energies for all layers except layer 14, where nearly no hits are present. There still remain some notable deviations between data and simulation within systematic uncertainties which might indicate, that some source for systematic uncertainties might be
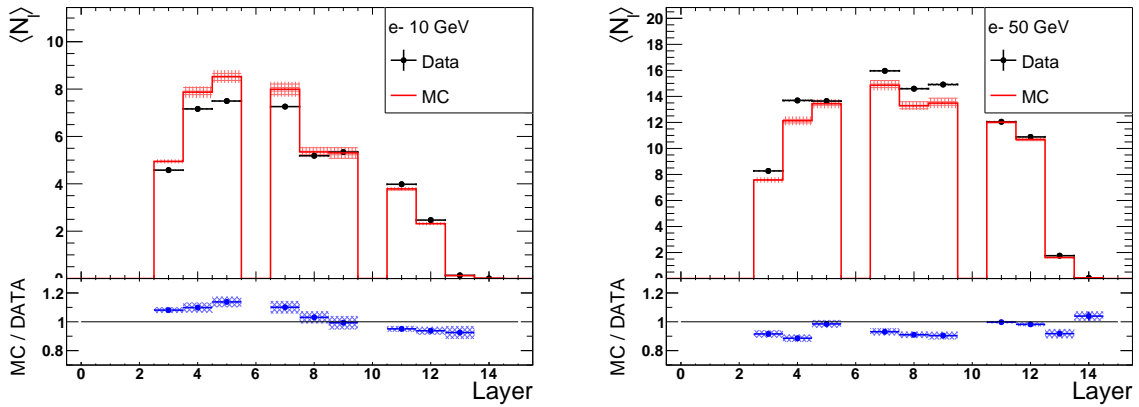
Figure 9.21.: Shower profiles of the mean number of hits per layer, $\langle N_l \rangle$, for data and simulation of 10 and 50 GeV electrons. The inverted response model is applied and systematic uncertainties are estimated. On the bottom of each plot, the ratio between simulation and data is shown. Additional plots for other beam energies can be found in Appendix F.

underestimated or that other sources are still not considered at all. Especially variations of the additional absorber and of the tile-to-tile crosstalk in the simulation affect the number of hits per layer. The additional absorber is used to take into account low-energy electron contamination, most probable because of a poor steering of the beam and therefore upstream beam collisions with beamline infrastructure. Still as discussed in Section 8.6.1, the additional absorber does not completely solve this issue, which is not surprising, as it is placed directly in front of the detector, instead of being included more upstream, as it is reasonable in data. Unfortunately, because no beam steering is implemented in the simulation, a further upstream placed absorber would cause early electron showers, which would widen the width of the shower in the simulation and would thus not be comparable to data anymore. The tile-to-tile crosstalk simulation is only performed in first order as discussed in Section 8.6.2. It is also not sufficient enough to reproduce data hit profiles. Further increasing the variations σ_{abs} and σ_{XT} might improve the agreement between data and simulation within uncertainties. Still, because both aspects are only an attempt to simulate more complicated processes and unfortunately have issues to do so, it is questionable, whether a further increase would improve the accuracy of the results.

The shower profiles of the mean energy in layers, $\langle E_l \rangle$, presented in Figure 9.22 for 10 and 50 GeV, show some significant differences compared to the results before response inversion in Figure 8.27. Obviously, the mean energies are increased due to the response inversion. Most of the shower energy is deposited in layers 3 to 5 at 10 GeV, while for 50 GeV, a clear maximum is in layer 5. At 10 GeV, data systematically has higher energies than simulation, while at 50 GeV, is is more mixed. This might indicate, that the response model overestimates the saturation at low beam energies which results in systematically too high energies in data.

The agreement between simulation and data in consideration of the uncertainties is within around 20 % deviation from a ratio of 1 throughout all beam energies for all layers except layer 14, where nearly no energy is deposited. Systematic uncertainties relatively increase for larger beam energies, which indicates that at high energies, the uncertainty of the response model
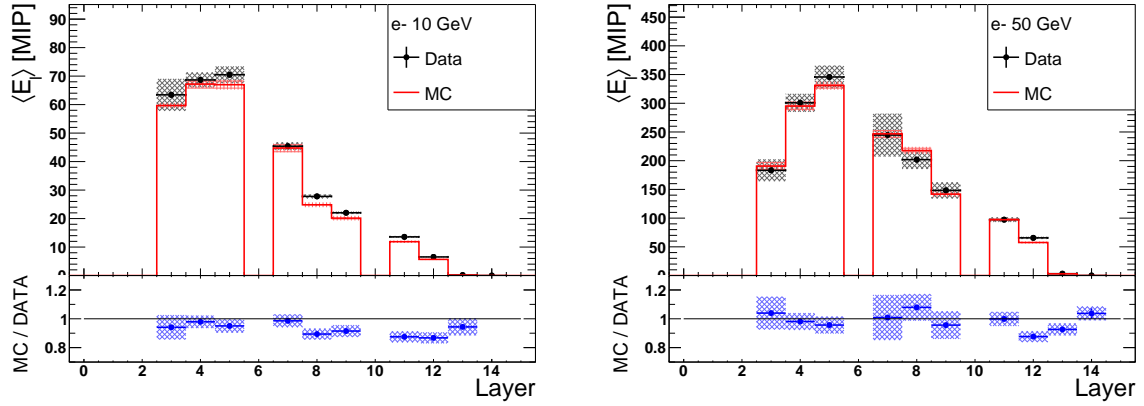
Figure 9.22.: Shower profiles of the mean energy in layers, $\langle E_l \rangle$, for data and simulation of 10 and 50 GeV electrons. The inverted response model is applied and systematic uncertainties are estimated. On the bottom of each plot, the ratio between simulation and data is shown. Additional plots for other beam energies can be found in Appendix F.

becomes more dominant. Some mean energies of several layers, as for example $\langle E_3 \rangle$, are continuously in agreement between data and simulation within uncertainties, while other layers, especially layers 11 and 12, are always off. Interestingly, the mean energy of these layers in data is always too high compared to simulation, which indicates, that saturation has been overestimated in the applied response model. As discussed in Section 9.5.2.3, these layers have shown a conspicuous behavior, leading to a very high N_{total} because of missing observed saturation, most probable because of high SiPM pixel recovery. Now that data is still showing too high mean energies in these layers after the inverted response model has been applied, this signifies, that the response model is not capable to describe the true response in any way for these layers, because even higher N_{total} also do not improve the agreement as discussed in Section 9.5.2.3.

For a more detailed comparison, Figure 9.23 shows the total energy distribution, E_{total}, for electron data and simulation of 10 and 50 GeV. The means of the distribution agree between data and simulation within around 4 % for 10 GeV and within 0.6 % at 50 GeV. The improvement of the agreement of the mean at 50 GeV shows, that the response model is fairly good in reproducing mean energy at high beam energies, as it aims for.
In both cases, the simulation is much sharper than data. The width of data increases for larger beam energies. The origin of the larger widths of data might lay in two aspects:
First, the broader edge at low energies at high beam energies might be introduced by low-energy electron contamination, as discussed many times before. Though several attempts have been made to simulate it with additional upstream absorber and suppress the contamination in data by applying additional selections (cf. Section 8.5.3), a fraction of low-energy electrons still remains, specifically within close range to the actual beam energy and therefore widens the distribution to smaller energies (see previous Figure 8.20, where the FWHM of the total energy distribution for 50 GeV electrons is increased by roughly 30 % to lower energies).
Second, the broader edge at high energies might be introduced by the applied inverted response model, as such a shape has not been present before applying the inverted model (comparable
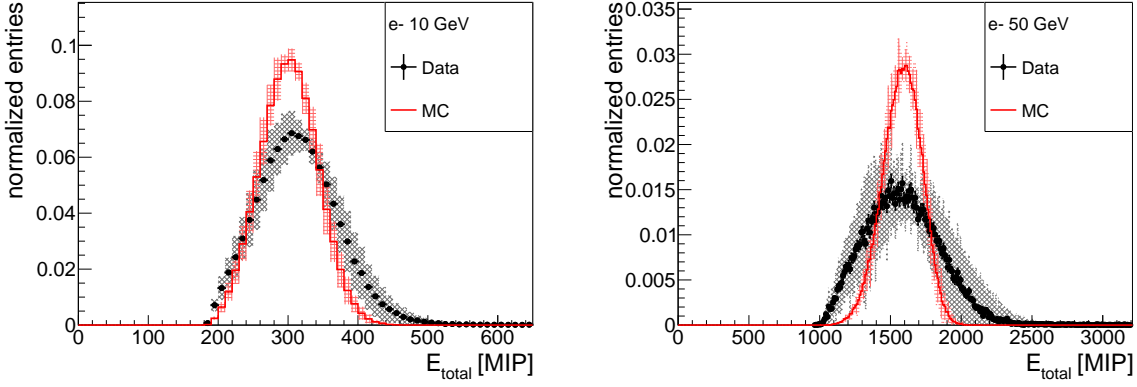
Figure 9.23.: Total energy distribution, E_{total}, for data and simulation of 10 and 50 GeV electrons. The inverted response model is applied and systematic uncertainties are estimated. A minor fraction of entries of less than 1 % exceeds the shown energy range. Additional plots for other beam energies can be found in Appendix F.

to Figure 8.21). Especially for high hit energies, which correspond to N_{fired} close to N_{total}, the response model features an exponentially increasing behavior, as plotted in previous Figure 9.3. Due to the linear extension triggered by the parameter R, this exponential shape migrates to a linear behavior from a certain point on. Small variations in the input parameter N_{fired} result in high variations of the output N_{seed} of the inverted response function, which compares to the here observed energies. Thus, the large tail to high energies in Figure 9.23 is introduced by the utilization of the inverted response model.

Because the width of the total energy distribution is related to the resolution of the detector, it can be anticipated, that the resolution of data will be much less compared to what is expected from simulation.

9.8.2.2. Pion Showers

Next, pion shower profiles are discussed. Figure 9.24 shows shower profiles of the mean number of hits per layer, $\langle N_l \rangle$, and of the mean energy per layer, $\langle E_l \rangle$, for data and simulation of 50 GeV pions. The hits profile again looks very similar to the profile before response inversion in Figure 8.28, for the same reasons as discussed above. The mean number of hits increases with small deviations from early to late layers with a maximum at layer 13, after which it decreases. The deviation from a ratio of 1 between simulation and data is less than 20 % throughout all beam energies. Again, estimated uncertainties are too small to indicate a good compatibility between data and simulation in several layers, as also discussed above. In this case though, pion beams are not expected to be contaminated by low-energy particles, as it is the case for electrons, as they generally penetrate iron further before showering. In any case though, the thin additional absorber does not have a large impact on the pion shower shape. On the other hand, pion showers are generally more complicated to simulate because of hadronic interactions. The mean energy shower profile features a similar shape as the hit profile with a maximum of the deposited energy in layer 13. Compared to the profile before response inversion in Figure 8.28, the energies have increased. Compared to the energy increase at electrons above, here, the effect
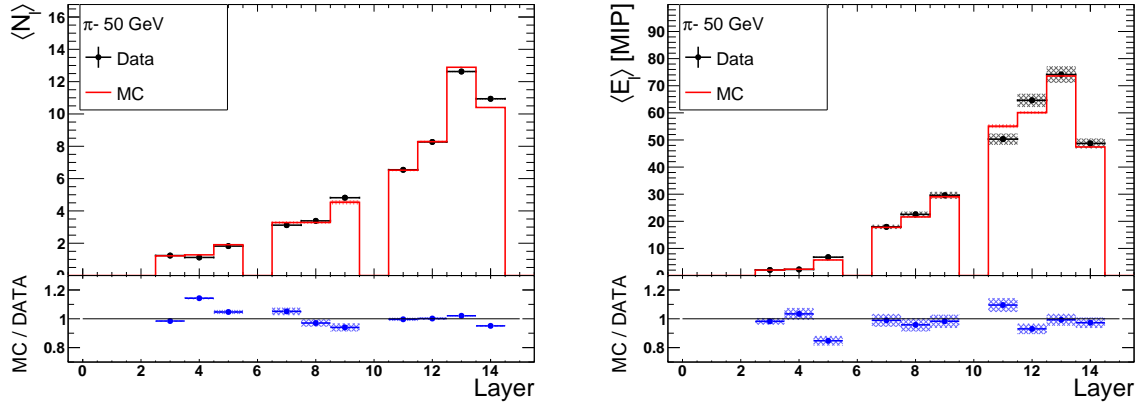
Figure 9.24.: Shower profiles of the mean number of hits per layer, $\langle N_l \rangle$, (left) and of the mean energy per layer, $\langle E_l \rangle$, (right) for data and simulation of 50 GeV pions. The inverted response model is applied and systematic uncertainties are estimated. On the bottom of each plot, the ratio between simulation and data is shown. Additional plots for other beam energies can be found in Appendix F.
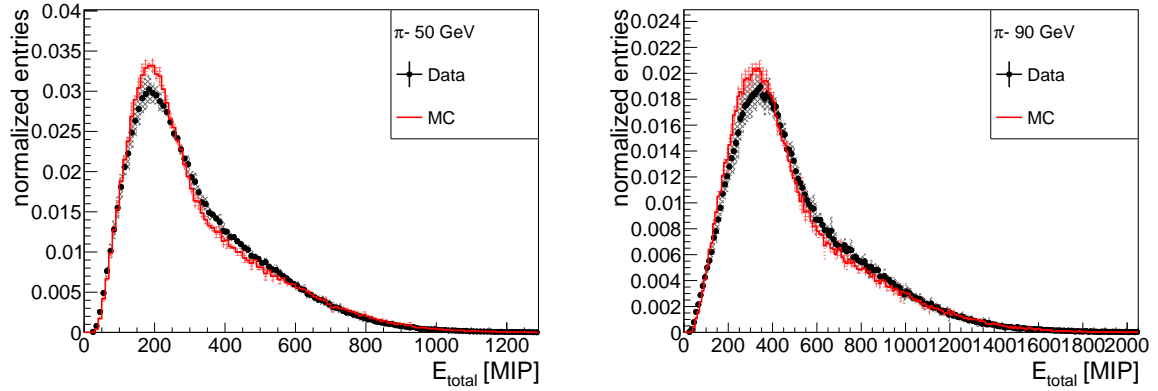

Figure 9.25.: Total energy distribution, E_{total}, for data and simulation of 50 and 90 GeV pions. The inverted response model is applied and systematic uncertainties are estimated. A minor fraction of entries of less than 1 % exceeds the shown energy range. Additional E_{total} distributions for other beam energies can be found in Appendix F.

is lower. This does not surprise, because the reconstructed energies of pion showers are way lower compared to electrons and thus response saturation plays a subordinate roll. Simulation deviates less than 20 % from data throughout all beam energies. Similar as discussed before for electrons, the systematic uncertainty increases slightly for higher beam energies, most probable because the impact of the inverted response model and therefore its uncertainty increases.

Figure 9.25 shows the total energy distribution, E_{total}, for data and simulation of 50 and 90 GeV pions. The shape looks different to the shape of electron showers in Figure 9.23 as it features a lower maximum and a larger high energetic falling edge, as observed before in Figure 8.17. As discussed already, this shape is a consequence of the setup of the detector prototype, with many unequipped slots from the center to the back of the detector. The shape of simulation is in better agreement to data than it is the case for electrons, most probable

because the pion shower is not affected that much by thin upstream material, which in case of electrons implies a high fraction of low-energy particles. Still, the simulation overestimates the fraction of events in the peak and underestimates a little the falling edge to high energies, which might result in a little too optimistic resolution in the simulation.

9.9. Energy Response Linearity and Energy Resolution

In this and in the previous chapter, the calibration of the detector prototype, the applied event selections and the modifications in the simulation have been discussed. The response model has been optimized, which allows to reverse saturation and crosstalk effects. Finally in this section, the linearity of the energy response and the energy resolution of the detector prototype are studied, which are both significant parameters of a detector and have been introduced in Section 1.3.1.

Beforehand it should be mentioned, that only a *poor energy resolution of the prototype is expected*. The reason for this expectation does not relate to the performance of the equipped layers, but mainly to the fact, that many slots of the detector are unequipped or inactive. Therefore, a lot of information is missing, which makes an energy measurement more complicated. In the following Section 9.9.1, the X_0-scaling method is applied in order to take this issue into account. Thereafter in Section 9.9.2 and 9.9.3, the energy linearity and resolution of the prototype are discussed.

9.9.1. X0-Scaling

The detector is a sampling calorimeter prototype with alternating steel absorber plates and slots for active readout layers. Ideally, the reconstructed energy is proportional to the sum of all measured energy depositions of an incoming particle. Unfortunately, not all slots are equipped with active layers (cf. Section 8.1) and therefore the measured energy is inchoate. To account for the missing information from unequipped slots, the X_0-scaling method is applied. The radiation length X_0 is a material characteristic for the energy loss of traversing particles with high energy and therefore best suited to weight the reconstructed energies of active layers. The method works as follows: For each active layer l, the X_0 of all material in front of the SiPM of each layer is added, as long as it has not been added already for any preceding layer. For example for layer 1, the X_0 of the very first steel plate, a small layer of air, the front of the first steel cassette, the PCB and cable-fiber-mix, the M3-reflective foil and the scintillator of the first EBU is added, which results in a total scaling (or sampling) factor $S_1 \approx 1.01$. For layer 2, the X_0 of the M3-reflective foil on the bottom side of the scintillator of the first EBU, the back of the first steel cassette and another small layer of air is added, as well as the X_0 of the second steel absorber plate until the second scintillator from EBU 2, similar as before. This results in $S_2 \approx 1.04$. The same procedure is repeated for all following layers.

Because layer 1 and 2 are not active, the first active layer is layer 3, which contains the Mainz HBU. To compensate the missing information of the preceding EBUs, the scaling factors of layer 1 and 2 are added to the specific scaling factor of layer 3, which results[6] in $S_3 \approx 3.10$, while

---

[6]The stand alone scaling factor of layer 3 would be roughly 1.05.

the S_1 and S_2 are set to 0. The similar procedure is applied to layer 7 and 11, because both of these layers have inactive preceding layers. Layers 12, 13 and 14 have each a different number of empty preceding slots (cf. Table 8.1), and their scaling factor is calculated analogically with the difference, that in empty slots, only air is present. The resulting layer-wise scaling factors, S_l, are listed in Table 9.3. With the scaling factors S_l and the layer-wise energy E_l of each layer

Layer l	scaling factors S_l
1	0
2	0
3	3.10
4	1.05
5	1.05
6	0
7	2.09
8	1.05
9	1.05
10	0
11	2.09
12	2.02
13	7.88
14	9.83

Table 9.3.: Layer-wise scaling factors, S_l, estimated from the X_0 of the preceding material and used to weight energies of separate layers l.

l, the scaled total energy of an event, $E_{total}^{X_0}$, is estimated with Equation 9.16.

$$E_{total}^{X_0} = \sum_l E_l \cdot S_l \tag{9.16}$$

Exemplary $E_{total}^{X_0}$ distributions for 10 and 50 GeV electron and 50 and 90 GeV pion data and simulation are shown in Figure 9.26. Obviously, pion simulations agree much better to data than it is the case for electrons, as observed before. Most significantly, the distributions for pions now look more Gaussian, because the X_0-scaling takes into account the invisible energy depositions in unequipped layers to some degree, which otherwise resulted in long falling edges, as observed before in Figure 9.25. Still, there is a small shift to higher mean energies in the pion simulations compared to data. In comparison to E_{total} in the previous Figure 9.23, the electron distributions are shifted to higher energies because of the applied scaling factors. To check, if there is any significant bias on the reconstructed energy resolution due to the X_0-scaling, Gaussian fits are applied to data and simulation on the initial E_{total} and on the evolved $E_{total}^{X_0}$ distributions. The relative resolutions are estimated with σ/μ from the fit parameters and compared before and after X_0-scaling. No bias has been observed, as the relative resolutions show no specific trend, but remain stable within small fluctuations to both directions.
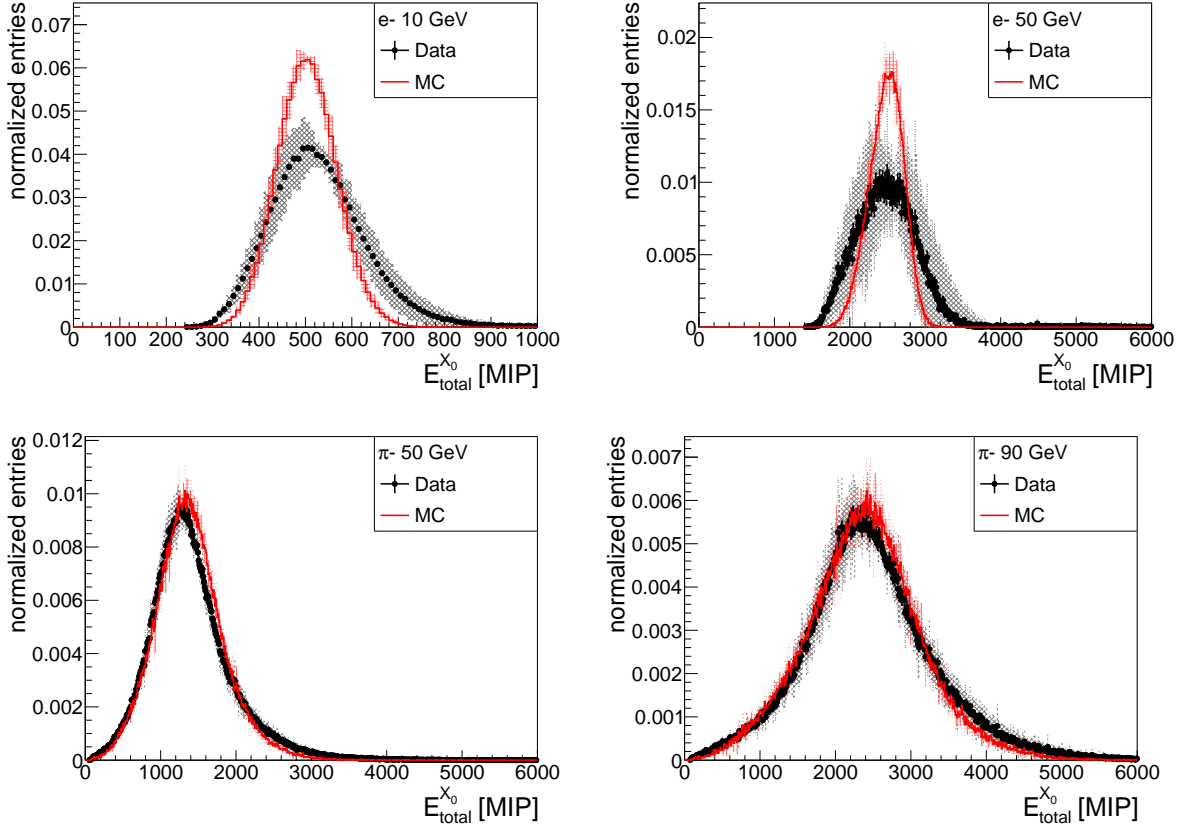
Figure 9.26.: $E_{total}^{X_0}$ distributions of data and simulation of 10 and 50 GeV electrons and 50 and 90 GeV pions. A minor fraction of entries of less than 1 % exceeds the shown energy range.

9.9.2. Response Linearity

The reconstructed energy, E_{rec}, of a specific beam energy is estimated by two consecutive Gaussian fits on the X_0-scaled total energy distribution, $E_{total}^{X_0}$. First, a rough Gaussian fit is applied to the distribution within a range given by the mean of the distribution plus or minus the RMS. The fit parameters are extracted and a second Gaussian fit is applied to the same distribution, but this time within a range defined by the mean plus or minus the sigma of the first fit, multiplied by a constant factor, depending on the particle type. For electrons, a factor of 1.5 and for pions a factor of 1 is applied. These factors are chosen such that the Gaussian fit can be performed well and the fit range does not include the higher energetic tail in pion data. Though the tail might have an impact on the mean position as well, this impact is assumed to not be significant in this case.

The mean of the second Gaussian fit corresponds to the reconstructed energy, E_{rec}, while the sigma σ_{rec} is a measure of the energy resolution. Generally, the energy resolution is given as the relative energy resolution σ_{rec}/E_{rec} (see Section 1.3.1).

The reconstructed energies, E_{rec}, are plotted as a function of the beam energy, E_{beam} in Figure 9.27 for electrons and pions. The visualized uncertainties are the quadratic sum of statistic and systematic uncertainties, while the systematic uncertainties are dominant. For both particle
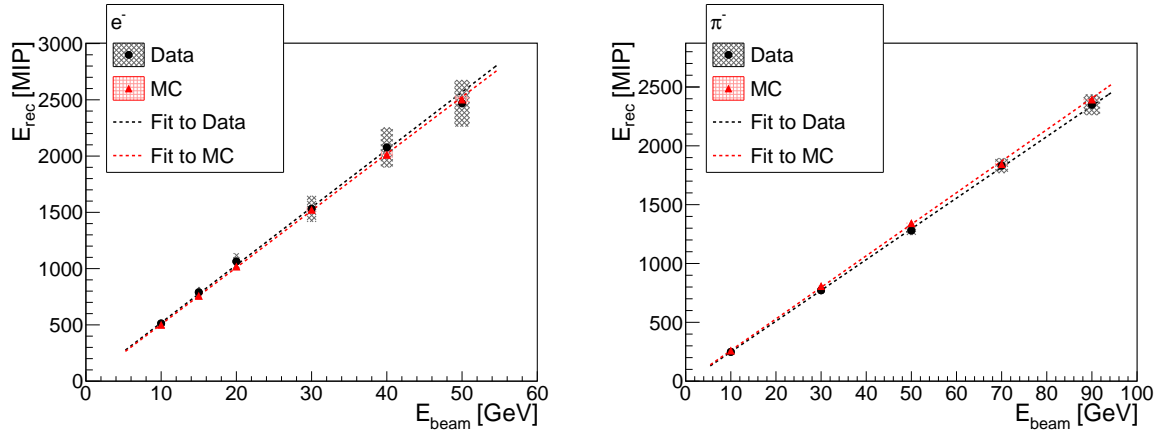
Figure 9.27.: Reconstructed energy vs. beam energy of electron (left) and pion (right) data and simulation. The uncertainties are the quadratic sum of statistic and systematic uncertainties. A linear fit is applied to both, data and simulation. The resulting fit parameters are listed in Table 9.4.

types, a linear behavior is observed. The uncertainty increases for higher beam energies and this effect is stronger for electrons. This is most probable related to the systematic uncertainty of the response saturation model applied in the reconstruction procedure. Because saturation increases with rising deposited energies, the uncertainty increases as well. The reconstructed energy of the electron simulation agrees well to data within uncertainties, while for pions, this is only the case for beam energies larger 50 GeV. The linear function in Equation 9.17 is applied,

$$f(E_{beam}) = m \cdot E_{beam} + o \tag{9.17}$$

where m is the energy scale factor in $\frac{\text{MIP}}{\text{GeV}}$ and o is the offset in MIP, which takes into account noise and threshold effects. Table 9.4 lists the results of these fits to both, electron and pion showers.

particle	type	$m \left[\frac{\text{MIP}}{\text{GeV}}\right]$	o [MIP]
e^-	data	51.2 ± 3.2	6.5 ± 47.5
e^-	simulation	50.5 ± 1.0	-0.5 ± 18.5
π^-	data	26.1 ± 0.6	-12.9 ± 9.9
π^-	simulation	26.8 ± 0.4	-7.3 ± 7.4

Table 9.4.: Linear fit parameters of Equation 9.17, estimated with Figure 9.27 with convoluted statistic and systematic uncertainties.

For electrons, m deviates less than 2 % between data and simulation and both results are consistent within uncertainties. The offset o on the other hand is larger for data than for simulation, but the uncertainties are a magnitude larger than the values for both, data and simulation. For pions, the deviation of m between data and simulation is lower 3 %. The offset o of data is a factor 1.8 larger than in simulation. In most cases, with the exception of pion data, the offset o is consistent with 0 MIP within uncertainties. Large differences in the offset parameters have been observed before in similar analysis of the AHCAL prototype [38].
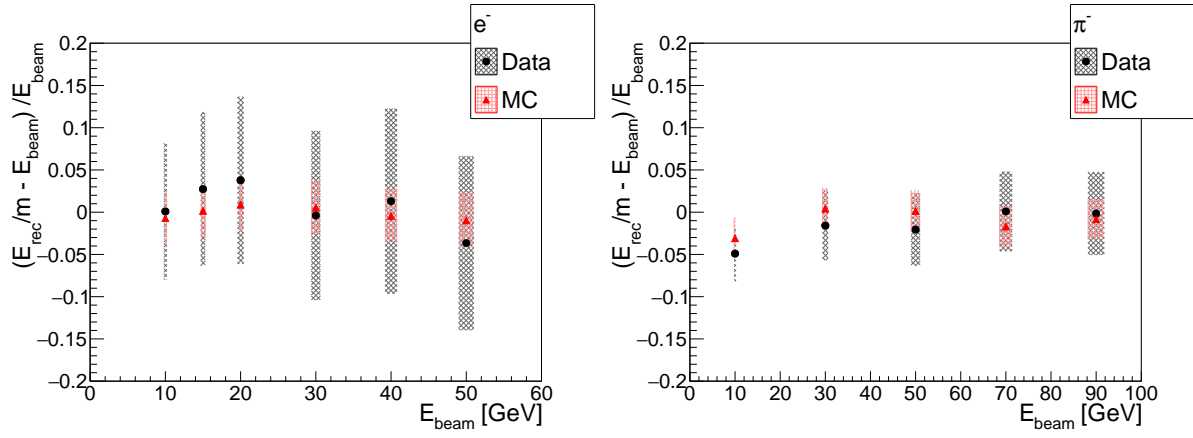
Figure 9.28.: Residuals of fits to data and simulation of the reconstructed energy in Figure 9.27, for electrons (left) and pions (right).

The m of pions is only approximately half the size of electrons. This points to a lower response of the calorimeter to hadronic than to electromagnetic showers, as it is expected for a not compensating calorimeter [35], which means, that only a fraction of the hadronic decay can be measured as discussed before in Section 1.3. Also, the large amount of unequipped slots of the calorimeter from which no shower information can be extracted, reduces the response and the X_0-scaling method can only take this into account to some extend. This is more dominant for pion showers than it is for electrons, because the front part of the detector, where electron showers deposit most of their energy, is more equipped than the main and back part, where pions tend to deposit a large fraction of their energy.

Residual

Figure 9.28 shows the residual $(E_{rec}/m - E_{beam})/E_{beam}$ of the linearity fits and the related data and simulation entries for electrons and pions. Note that the constant o is not considered here. The deviation of the electron data points from linearity is within $\leq 4\,\%$, while for simulation, the deviation is smaller within only $1\,\%$. The electron simulation is contained completely within data uncertainties, which are large and of the order of up to $11\,\%$. The higher deviation for data might be a sign that there are saturation effects, which are still not described well by the response model of the SiPM-tile system, as especially for $50\,\text{GeV}$, the deviation from the linear fit is significant and the reconstructed energy of data less than expected.

For pions, the deviation from linearity is $\leq 5\,\%$ for data and $\leq 4\,\%$ for the simulation. For all beam energies, simulation points are contained within data uncertainties, which are about half the size compared to uncertainties of electrons. Especially for data, the residual is mostly negative as the offset o is not considered. Interestingly, here the largest deviation is found at the lowest beam energy of $10\,\text{GeV}$. This might indicate, that for pions, saturation is less dominant because of on average lower hit energies in single channels, while other effects, like SiPM crosstalk increase in importance for the energy resolution.
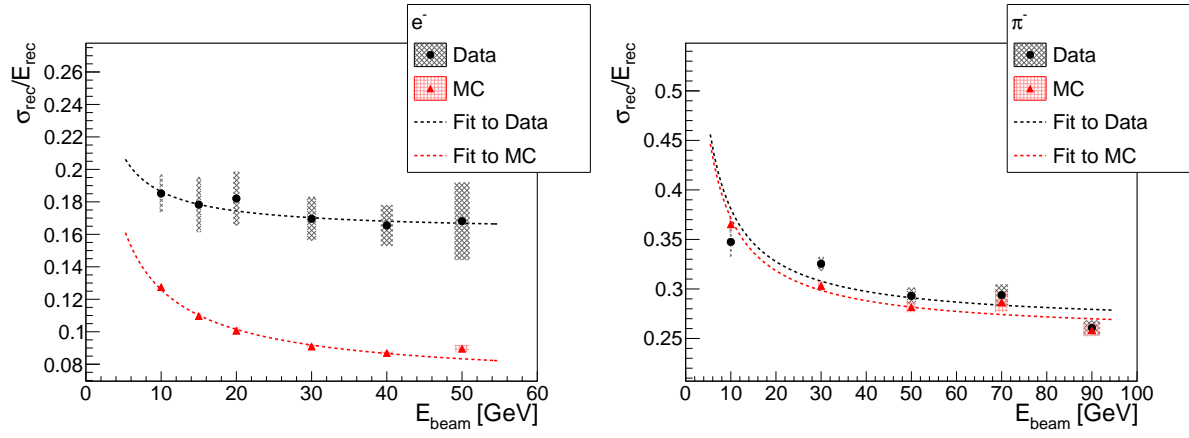
Figure 9.29.: Relative energy resolution of electron (left) and pion (right) data and simulation as a function of the beam energy. The uncertainties are the quadratic sum of statistic and systematic uncertainties. A fit following Equation 9.18 is applied to data and simulation and resulting fit parameters are listed in Table 9.5.

9.9.3. Response Resolution

Finally, Figure 9.29 shows the relative energy resolution σ_{rec}/E_{rec} of electron and pion showers in data and simulation. Generally, the relative resolution improves from low to high beam energies, as expected. A fit to the relative energy resolution is performed using Equation 9.18

$$\frac{\sigma_{rec}}{E_{rec}} = \frac{A}{\sqrt{E_{beam}/\mathrm{GeV}}} \oplus \frac{B}{E_{beam}/\mathrm{GeV}} \oplus C \tag{9.18}$$

where the parameters A, B and C are the stochastic, noise and constant contributions, respectively, similar to Section 1.3.1. Because the measured noise contribution in the prototype is 0.9 MIP, the noise term B is extracted from the in units of GeV converted value $0.9\,\mathrm{MIP}/m$, separately for each particle type. This results in approximately $B = 0.017$ for electron and $B = 0.034$ for pion showers.

Electron data shows a poorer resolution and larger systematic uncertainties compared to simulation. For the simulation, the relative resolution improves from 10 to 40 GeV, where it reaches its minimum and impairs again at 50 GeV. For data, more fluctuation is observed, especially at 20 GeV. The deviation between data and simulation is also expressed by the fit parameters listed in Table 9.5.

particle	type	$A\,[\%]$	$C\,[\%]$
e^-	data	29.3 ± 12.1	16.2 ± 1.3
e^-	simulation	33.4 ± 0.8	6.9 ± 0.2
π^-	data	86.8 ± 8.3	26.4 ± 0.8
π^-	simulation	85.7 ± 4.9	25.4 ± 0.5

Table 9.5.: Fit parameters A and C of Equation 9.18, estimated with fits in Figure 9.29 with convoluted statistic and systematic uncertainties.

The stochastic parameter A is 14% larger in simulation than in data, while the constant term C is around 2.3 times larger for data than in simulation. Unfortunately, the uncertainty of A in data is very large with approximately 41%, because of the large initial systematic uncertainties. Especially the difference in the constant term is visible in the deviation between the two resolution curves.

For pions, the relative resolution between data and simulation is generally in better agreement than for electrons. Still, there are some deviations, especially at low beam energies of 10 and 30 GeV. For higher beam energies, the deviations between data and simulation reduce.

Different to electron showers, the stochastic contribution A in pion showers agrees well within data and simulation. The deviation is only around 1%. The uncertainty on the other hand is of the order of 10% for data and 6% for simulation. Therefore it is again larger for data, but not as huge as it is the case for electrons. The constant term C also agrees better and is around 4% higher for data than for simulation.

9.9.4. Discussion

As expected, the relative resolution of the non-compensating calorimeter prototype is better for electron showers than for pion showers. At a beam energy of 50 GeV for example, the resolution σ_{rec}/E_{rec} for pion showers in data is around 74% larger compared to electrons. This deviation is also expressed in the three times larger stochastic parameter A for pions, whereas also the constant parameter C increases about 63% from electron data to pion data. The high constant parameter C is not that much surprising, as constant contributions to the relative resolution are expected due to inhomogeneities (cf. Section 1.3.1) of the detector, which are induced by the significant fraction of undetected energy in unequipped slots and by the large fraction of inactive channels on active layers. Therefore, C is expected to increase for pion showers, which deposit more fraction of their energy in areas of the detector, which are not fully equipped.

What are the reasons for the poor resolution for electron data and for the high deviation to simulation?

Impact of de-saturation

One possible candidate is the impact of de-saturation by the applied inverted response model, as outlined before in Section 9.8.2.1. The higher the deposited energies in single channels are, the higher is the effect of SiPM saturation and the stronger becomes the impact of the response function. The previous Figure 9.3 has demonstrated, that for high saturated energies (there, high N_{fired}), the values of the inverted response model, which are de-saturated energies, increase exponentially. The inserted linear extension in the XT-ext model reduces this effect, since the slope reaches a maximum gradient at a certain point, defined by the parameter R, from where on the slope is constant. Still, in this high energy region, small variations in saturated energies result in large variations in de-saturated energies. Therefore, the total energy distributions, E_{total}, after the applied inverted response model become broader to higher energies.

The impact of the inverted response model on the resolution extracted from the E_{total} distributions is investigated. Figure 9.30 shows the E_{total} distributions of data and simulation before and after applying the inverted response model (de-saturation) for 10 and 50 GeV elec-
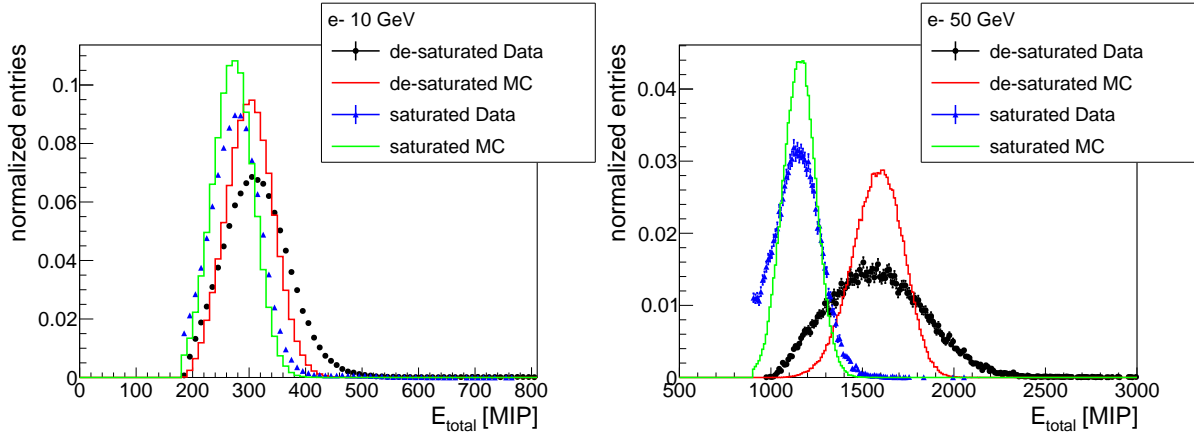
Figure 9.30.: E_{total} distributions of 10 (left) and 50 GeV (right) electron data and simulation, before and after applying the inverted response model. A minor fraction of entries of less than 1 % exceeds the shown energy range.

trons. De-saturated energies are shifted to higher energies as expected, reversing the effect of saturation. Obviously, the impact is larger for the higher beam energy of 50 GeV. Thereby, the width of the distribution increases. This effect is most significant for 50 GeV data, while simulation is not affected that much. This is the case, because data features already a broader distribution before de-saturation. The broader falling edge to high energies and occasionally high energy entries are most affected by the inverted response model and result in an even broader falling edge afterwards. The mean positions of the related distributions of data and simulation might still agree, which has been one major objective of the response model optimization in Section 9.1, but the shapes are often not very well described, as also discussed there.

The resolutions $\sigma/\mu_{E_{total}}$ before and after de-saturation are extracted from Gaussian fits to the distributions. Note that no X_0-scaling is applied here. Table 9.6 lists the results. The resolution in simulation improves for both beam energies, while the impact is larger at 50 GeV. For data, the opposite is the case. For both beam energies, the resolution gets worse due to the impact of de-saturation and is very large at 50 GeV with a deterioration of around 86 %.

type	$\sigma/\mu_{E_{total}}$ [%] (saturated)	$\sigma/\mu_{E_{total}}$ [%] (de-saturated)
10 GeV data	16.1	17.1
10 GeV simulation	13.8	13.2
50 GeV data	8.2	15.3
50 GeV simulation	11.3	8.5

Table 9.6.: Relative resolutions extracted from E_{total} distributions before and after applied inverted response model to data and simulation of 10 and 50 GeV electrons.

Impact of Other Sources

Not only is the resolution in electron data worse than in simulation at high beam energies, but also at lower beam energies. Therefore, the de-saturation feature of the inverted response model is not the only origin, as saturation effects are relatively small at low beam energies.

Also as shown in Figure 9.30, the distribution of 50 GeV data before de-saturation is broader not only in the falling edge at high, but also in the *rising edge* at low energies, compared to simulation. Other sources for the broader E_{total} distributions in data and therefore poorer response resolutions can be found in other aspects that have been mentioned before:

Low-energy Electron Contamination
The unfortunately present low-energy electron contamination in electron data has been cut off as far as possible as described in Section 8.5.3. Still, the cut on the total energy is not capable to reject all electrons with lower energy, especially those with energies close to the intended energy of the particle. This results in an increased width of E_{total} to low energies, as simulated in previous Figure 8.20. The subsequent simulation adjustment of additional upstream absorber material aims to take into account the low-energy contamination due to collisions with upstream material in the simulation, but though it improves the agreement to data, unfortunately disagreements remain as learned in Section 8.6.1.

Incompletely Equipped Detector Prototype
Finally, a main reason for a poor response resolution, also for pion showers, is the fact that most of the shower interaction takes place in areas, where the detector is not or only partially equipped. As a reminder, the absorber stack consists of a total of 48 slots from which only 10 are equipped with active layers, with most of them located in the first part. Like this, a lot of the shower information is missing and the low amount of available information is scaled using the X_0-scaling method to compensate it. On the one hand this does work to some extend, as the linearity of the response is fine within less than 5 % deviation. But on the other hand, the constant term C in the parametrization of the relative energy response, as listed in Table 9.5, is significantly large for both, electron and pion showers. While for the reconstruction of electron showers, the information of the first layers is important and the first two slots are not active, for pions the middle of the detector plays a large role, where even less slots are equipped. This parameter C allows conclusions towards sources that scale with the energy, as energy leakage due to inhomogeneities in hardware and intercalibration errors [35]. This underlines the impact of unequipped slots within the detector prototype. As mentioned, intercalibration errors, as the intercalibration between high- and low-gain (cf. Section 9.8.1), might also increase C in data.

9.9.4.1. Comparison to previous studies of AHCAL physics prototypes

Now that the incompleteness of the prototype has been identified as one source for lower energy resolution, a comparison to previous studies with completely equipped AHCAL physics prototypes shall be given. The AHCAL physics prototype utilizes a different kind of layers, each consisting of three different tile sizes and circular wavelength shifting fibers to guide the light onto a SiPM with approximately 1200 pixels [180]. Unfortunately, no direct comparison to a similar AHCAL prototype is available so far.
In Reference [181], data of a combined calorimeter system consisting of a scintillator electromagnetic calorimeter (ScECAL), an complete AHCAL physics prototype and a tail catcher and muon tracker (TCMT) has been studied. The data has been measured at CERN SPS in 2007. The hadronic response has been measured to be linear within ± 2 %, while the hadronic energy resolution results in $57.6 \% / \sqrt{E/\mathrm{GeV}} \oplus 1.6 \%$ with the standard energy reconstruction. This result can even be improved by means of software compensation, reaching a stochastic term

of approximately 45 % [4]. Similar results have been achieved in another study [38] with data that has been measured at the Fermilab Testbeam Facility in 2009, whereas in the latter, the response has been linear within ± 3 %.

These results show, that a fully equipped AHCAL, with access to additional information of the ECAL in front and to the tail catcher and muon tracker in the back of the detector, good hadronic energy resolutions can be achieved. These additional detector sections allow a finer selection of pion showers and therefore improve the resolution of the AHCAL, for example by the use of an algorithm to detect the layer with the first hadronic interaction [38]. Without these specialized detector sections it is not surprising, that the results reached with an incomplete detector prototype here stay behind. While the stochastic parameter A for pion showers here is about a factor 1.5 times larger compared to the measurements with the standard reconstruction in 2007 and 2009, the constant parameter C is around 16 times larger with $C = 26.4$ % which, as just discussed, is dominantly related to the inhomogeneities of the prototype. The maximum deviation from linearity reached for this prototype is not surprisingly absolute 2 % higher, as with increasing beam energy, more shower energy is deposited in the mostly unequipped rear half of the detector (cf. Figure F.3).

The electromagnetic energy resolution of the AHCAL physics prototype has been studied with data from 2007 at CERN SPS in a measurement without preceding ECAL to be approximately $21.9\%/\sqrt{E/\text{GeV}} \oplus 1.0\%$, with a response linearity deviation of less than 3 % [180]. The stochastic parameter A achieved here is approximately 1.34 times higher, while the constant parameter C is again about 16 times larger. The deviation from linearity is only absolute 1 % higher in comparison to 2007.

In any case, the validity of the stochastic parameters A and the deviation from linearity is questionable for both particles, as the uncertainties are high.

9.10. Conclusion and Outlook

This Section gives a conclusion of the main results obtained with the CALICE AHCAL technological prototype at CERN SPS in July 2015.

After the previous Chapter 8 paves the way by preparing data and simulation sets, which are in rather good agreement to each other with less than 20 % deviation, the final Chapter 9 finally ends in a study of the response of the AHCAL prototype. As the response of the detector depends mainly on the response of its single sensors, which are SiPMs in combination with a scintillating tile, it is key to first analyze them.

SiPM-tile response saturation

Two response models for the SiPM-tile system are investigated: the crosstalk-extended (XT-ext) model and the advanced model. Both models include features to take into account SiPM crosstalk, saturation and pixel recovery. SiPM crosstalk mainly affects the SiPM response at low energies, but it also affects the MIP calibration of the detector, which is responsible for the complete energy range. On the other hand, SiPM saturation directly affects the response at high energies, as the SiPM features only a finite number of pixels. Over-saturation is a consequence of SiPM pixel recovery within the signal integration time. Due to the pixel recovery, the same pixel can fire multiple times, if delayed photons hit it. One major source for the delay is the

scintillator tile; due to the scintillation process itself and due to the different paths the photons take until they reach the SiPM. Therefore, the pixel recovery affects not only the response at high energies, though there it is clearly recognizable when the number of pixels fired, N_{fired}, exceeds the physical number of total pixels, N_{total}, but also in the complete energy range.

The XT-ext model does not specifically consider pixel recovery, but the effect can to some extend be compensated by the parameter N_{total}. In contrast, pixel recovery is an intrinsic feature of the advanced model, as it is designed for the application of a SiPM-tile system.

Both response models have been applied to the simulation and compared to data. To test the applicability of both models and identify which model to apply later in the reconstruction of data and simulation of the AHCAL prototype, different observables M_{E_l}, X_{E_l} and X_{e_l} have been defined in Section 9.3. These observables translate the agreement between data and simulation of the layer-wise total energy distribution, E_l, and the layer-wise hit energy distribution, e_l, of a specific layer l to one single significant value. By the minimization of these observables, the parameters of both response models can be tuned, as discussed in Sections 9.5 and 9.6.

For both models, the study shows that no explicit optimum can be identified in many cases, as a wide range of parameter combinations result in equivalent observable values. Also, the different observables do not always coincide concerning their minimums, which indicates discrepancies between data and simulation, which cannot be addressed by the response models, but originate from other unsolved issues. Nevertheless, good parameter combinations for both models have been identified, which improve the agreement between data and simulation significantly, as discussed in Section 9.7.

A comparison between the two response models shows, that both achieve similar results. It should be mentioned, that the advanced model is constructed with six parameters, but within this study, the number of free parameters of both response models has been fixed to three in order to keep the number of variations manageable and the results comparable under similar conditions. Finally, the XT-ext model is chosen to be applied in the reconstruction procedure in this study, mainly because it is easier to implement because of the available inversion of the model, in opposite to the advanced model.

Data and simulation

After the optimized SiPM response model has been inverted and applied in the reconstruction procedure, a final comparison with de-saturated energies between data and simulation is presented in Section 9.8, including estimated systematic uncertainties. The following sources of systematic uncertainties have been identified: For data, the MIP calibration, high- and low-gain intercalibration, SiPM gain calibration and uncertainties from the SiPM response model optimization have been taken into account. For the simulation, uncertainties arising from the tuning of the additional absorber in the beamline, of the tile-to-tile crosstalk and of the SiPM response model optimization have been considered.

For both, electron and pion showers, simulation is in good agreement to data with less than 20 % deviation. Notable is, that for pion showers, the simulation agrees better to data as it is the case for electrons. Two main reasons have been identified: First, the electron beam is contaminated by low-energy electrons due to upstream collisions with beam instruments [164, 165], which despite event selection results in a broadening of the energy distribution of data to lower energies. Second, the broadening of the distribution to higher energies is a result of the inverted

response model, because of its exponential[7] translation of saturated to de-saturated energies.

Response of the prototype

Finally in Section 9.9, the response linearity and resolution of the AHCAL 2015 prototype has been studied for electron and pion showers. The X_0-scaling is applied as a simple method to compensate missing information from unequipped slots and inactive layers.

Thereafter, the electromagnetic and hadronic response is extracted from Gaussian fits to the scaled total energy distributions, $E_{total}^{X_0}$. The linearity of the response is obtained to be better than 5 % deviation for both particles. For electron data, an energy scale factor of $(51.2\pm3.2)\frac{\text{MIP}}{\text{GeV}}$ and for pion data a smaller factor of $(26.1 \pm 0.6)\frac{\text{MIP}}{\text{GeV}}$ has been obtained. The notable smaller factor for hadrons ($e/h \approx 1.96$) is not only related to the fact, that the detector prototype is a non-compensating sampling calorimeter, but also to the incompletely equipped prototype (refer to [181], where $e/h \approx 1.19$ for a fully equipped physics prototype). As pion showers penetrate the detector further than electron showers and as the front part of the detector is more equipped than the main and rear part, this effect is stronger for pions.

The electromagnetic and hadronic resolution of the prototype is $(29.3 \pm 12.1)\,\%/\sqrt{E/\text{GeV}} \oplus (16.2 \pm 1.3)\,\%$ and $(86.8 \pm 8.3)\,\%/\sqrt{E/\text{GeV}} \oplus (26.4 \pm 0.8)\,\%$, respectively. The rather high uncertainties are arising from systematic uncertainties mentioned before. Conspicuous are the large constant parameters, which can most probable be attributed to the inhomogeneities of the prototype. Besides this, other sources have been identified for the poor resolution as seen before: the de-saturation of very high hit energies and the low-energy electron contamination in electron showers.

Classification of the results and outlook

First it should be noticed that this iteration of the AHCAL technological prototype, which has been at testbeam at CERN SPS in 2015, never aimed for a good energy resolution. New electronic readout and control hardware as the LDA and CCC cards are tested at the same time as various layers are equipped with different HBUs with various generations of readout electronics and SiPM and tile combinations in order to examine advantages and disadvantages. Conclusions drawn from studies of this testbeam campaign are employed for the construction of following AHCAL prototypes.

Though a good resolution has never been the point of this prototype, what can be concluded from the response resolution study and other performed studies for future prototypes and applications? The following points are found to be key for a good resolution:

- SiPMs should have a reasonable high total number of pixels, N_{total}, such, that the deposited energy in a single channel does not reach the full saturation level. Otherwise, the de-saturation of saturated energies will increase the width of the reconstructed energy distribution, E_{rec}, and also the systematic uncertainties arising from the SiPM response model.

---

[7]The functionality is exponential until the energy reaches a certain point from where on it is linear, see Section 9.4.

- Low SiPM crosstalk $< 1\%$ is required to not affect the MIP calibration of the detector. Though this crosstalk can be taken into account by the SiPM response model, it still increases the uncertainties.

- Tile-to-tile crosstalk should be prevented ($< 1\%$ to all sides) by wrapping the single tiles into reflective foil, for example. Otherwise, the simulation of tile-to-tile crosstalk adds a large uncertainty to the results and also reduces the effective high granularity of the detector. The latter is needed for the energy reconstruction with the Particle Flow Approach (PFA). With lower granularity, the so called confusion between individual particle contribution increases, which limits the effectiveness of the algorithm [4].

- The detector should be fully equipped so that the complete shower is contained and no leakage appears. Otherwise, the linearity of the response and the energy resolution is reduced, reflected mainly in a higher constant contribution C to the energy resolution. In order to compensate the lower response to hadronic showers, software compensation techniques can be used to separate electromagnetic from hadronic components in a shower event to improve the hadronic resolution, as proven several times [4, 38, 181], which also requires the information of all layers of the detector.

- The particle beam should be as pure and mono-energetic as possible. Of course, upstream beam collisions due to wrong beam steering must not happen. Otherwise, the beam is no more mono-energetic due to the contamination of for instance low-energy particles from parts of early showers, which can also be interpreted as a kind of leakage. As these particles are of the same type as the intended one, they can pass most of the event selections which makes it hard to reject them. If they occur, it has a direct negative impact on the energy resolution.

Several of the upper named proposals are already considered in the composition of a new generation of an AHCAL technological (also called engineering) prototype. In April 2018, the new large prototype with 38 active layers equipped with 21888 channels of the same SiPM-tile combination has been built [75]. The SiPMs (MPPC S13360 -1325PE) meet the requirements above as the total number of pixels is rather high with $N_{total} = 2668$ and the SiPM crosstalk probability is small with less than 1% (cf. Table 6.2). The tiles are individually wrapped, which inhibits tile-to-tile crosstalk, and automatically placed onto identical HBUs with a pick-and-place machine. [90] This automation procedure secures the homogeneity of the detector and allows to prove the scalability of the prototype to a full detector for the ILC. With these adjustments made, everything is prepared for the new large prototype to realize an excellent response linearity and resolution.

Final Summary

The International Linear Collider (ILC) is a planned linear e^+e^- collider with high luminosity and designed for experiments at mainly 250 to 500 GeV center of mass energy. One of the main purposes are precision measurements of Standard Model parameters as well as the potential discovery of new physics beyond it. One major goal is to precisely measure the couplings of the Higgs boson [3]. To achieve this, a jet energy resolution of 3 to 4 % is required. With a classical approach of hadronic calorimeters, this precision is unreached. The Particle Flow Approach (PFA) has been developed in order to solve this issue.

The PFA combines the information of tracking and calorimeter sub-detectors to optimize the resolution and requires a high granularity of the calorimeter in order to distinguish between different nearby particles.

Within the CALICE Collaboration, several high granular sampling calorimeter prototypes have been developed over the past few years. A design combining novel Silicon Photomultipliers (SiPMs) with small plastic scintillator tiles is an integral part of the Analog Hadron Calorimeter (AHCAL). Several AHCAL prototypes have been constructed and tested in various testbeam campaigns, proofing the concept of a high granular calorimeter and the scalability to a full size calorimeter.

In July 2015, the AHCAL technological prototype with a steel absorber stack has been operated at CERN SPS H2. This prototype is not fully equipped and comprises various layer configurations. During the testbeam campaign, data has been recorded for muon, electron and pion beams.

This thesis comprises two main studies. The first focuses on the characterization of response saturation of SiPMs and is self-contained. The second concentrates on the analysis of data and simulation of the AHCAL technological prototype in 2015 and reuses some of the learned SiPM response features. The main challenge in the SiPM response characterization study is to measure the large range between single photons and saturation in one. In the AHCAL analysis, the main object is to optimize the agreement between data and simulation, followed by further studies of the response of the SiPM-tile system and of the linearity and energy resolution of the prototype.

SiPM response characterization

SiPMs are small solid state semiconductor photo detectors which consist of an array of pixels. If a pixel detects an incoming photon and fires, it is insensitive to other incoming photons within its recovery time, thus the SiPM response saturates. Four different SiPMs with 100 to 2668 pixels have been measured. While three are of the same type, the latter is an evolved type with lower crosstalk due to optical trenches between pixels.

In the SiPM response study, three models are investigated: the simple exponential model, the crosstalk extended model (XT-ext) and the advanced model. While the simple model only includes one free parameter for the description of saturation, the XT-ext model also handles the effect of SiPM crosstalk. The advanced model additionally includes parameters for the pixel recovery and after-pulses.

As part of this study, a present SiPM test stand has been extended to measure the response of

SiPMs from single photons to saturation. Therefore additional components have been selected, built up and put into operation in the PRISMA Detector Lab at Mainz. Within the setup, a laser diode shoots a tunable number of photons onto a reference diode and onto a SiPM. The operation has been automated. In parallel, other small setups have been utilized to study other SiPM characteristics and the linearity of the readout devices.

All measured SiPMs show a clear response saturation, but still differ a lot. While the latest generation SiPM with 2668 pixels is rather slowly saturating and because of its tiny crosstalk probability even well described by the simple response model, the SiPMs with less pixels saturate much faster. For the two SiPMs with the lowest numbers of pixels, over-saturation has been observed, most probable introduced by delayed photons, related to delayed optical crosstalk.

Within the presented study, crosstalk is found to be a crucial parameter of the SiPM response, as it has a high impact, especially for low to medium light exposures. It requires a response model that takes into account both effects, SiPM crosstalk and saturation. In most cases the XT-ext model shows good results. This observation is reused later in the study of the AHCAL prototype. Still, the advanced response model is best suited to describe the combined effects of optical crosstalk, saturation and over-saturation in the case they occur.

The results of the single SiPM response measurements are not directly transferable to the application of a SiPM coupled to a scintillator tile, as used in the AHCAL. Therefore, a future setup is under investigation to measure the response of a SiPM-tile system, which requires only small adjustments to the existing setup.

CALICE AHCAL technological prototype

The presented analysis of the testbeam measurements at CERN SPS H2 in 2015 of the AHCAL technological prototype aims to first optimize the simulation according to the measured data and second to analyze the response saturation of the SiPM-tile system and the impact of different response models for a variety of different layer configurations. Though the incompletely equipped prototype is not expected to be particularly suited for it, the electromagnetic and hadronic response linearity and energy resolution are analyzed.

Event selections for muon, electron and pion showers are utilized to select pure showers. The selections have been optimized with the simulation and efficiencies have been estimated. The electron selection efficiencies are high as intended for electron showers with $\eta_{e^-} \geq 88.4\%$ and still at $\eta_{pi^-} \leq 10.2\%$ for pion showers, which is fine because the beam is expected to be reasonably pure due to the electron generation procedure. The pion selection efficiencies to pion showers is comparatively small with $\eta_{pi^-} \leq 51.3\%$, but the efficiency for electron showers is rather good with $\eta_{e^-} \leq 0.2\%$.

A difficult task arises from the observation of unexpected low-energy background in electron data, which passes the event selections for electrons. Further studies and simulations have found, that this background is related to low-energy electrons. Therefore, two additional selections have been applied to electron showers. Later indeed, the origin of this issue has been identified to be caused by a wrong steering of the electron beam, resulting in upstream collisions.

As a consequence of the low-energy electron background, additional absorber is added in the simulation to take into account the upstream beam collisions and energy leakage. The additional material has been tuned to a width of 16 mm iron by means of several distributions, taking into account the number of channel-hits and the center of gravity.

Another optimization has been performed on the optical tile-to-tile crosstalk parameter, which is applied in the digitization procedure. This accounts for layers 4-9, which comprise tiles without individual wrapping which leads to tile-to-tile crosstalk. For this optimization, again distributions of number of channel-hits are considered, resulting in a tile-to-tile crosstalk factor of 16 %.

After these enhanced event selections and optimization studies, a comparison of shower profiles shows a rather good agreement of less than 20 % deviation of simulation from data.

Next, the response saturation of the SiPM-tile system is analyzed layer-wise, as the response of the single channels has a high impact on the electromagnetic and hadronic response of the complete detector. Two response models are investigated: the XT-ext and the advanced model, while the XT-ext model is adjusted with a linear extension for high energies to take into account over-saturation. The response models are applied to the simulation with a variety of different parameter combinations and compared to data.

As the previous study has shown a large impact of SiPM crosstalk on the response, this learned information is reused to adjust the channel-wise MIP calibration of the prototype for the impact of SiPM crosstalk. Like this, the MIP calibration of the detector is maintained after an inverted response model is applied.

Three observables are defined, which classify the agreement of major layer-wise energy and hit energy distributions between data and simulation. For both response models, good parameter combinations are estimated by means of the observables, improving the agreement between data and simulation. Still, no clear optimum can be identified for the parameters of the models, as often a wide range of parameter combinations leads to similar observables. Also, differences in the shapes of data and simulation remain, which cannot be solved by any of the tested response models.

None of the two models wins the upper hand as they accomplish similar results. Still, it has to be noted that the advanced model is trimmed to only three free parameters and might have some advantage in case more parameters are freed. The XT-ext model is utilized in the further study, because it is easier to implement, as an analytic inversion exists.

After de-saturating energies by applying the inverted response model, the agreement is still good within less than 20 % deviation of simulation from data. Main sources for systematic uncertainties arise from the calibration of the channels and from the performed optimization studies. Especially at high beam energies, the uncertainty arising from the SiPM-tile response model has a high impact on the reconstructed energy.

The study of the response linearity and resolution struggles mainly because of the incompletely equipped prototype, which can to some degree be covered by the X_0-scaling method. While the linearity of the response is within 5 % deviation, a rather high constant parameter of $C \approx 16.2$ % for electron and $C \approx 26.4$ % for pion showers remains in the parametrization of the response. Further studies show, that both, the de-saturation of high hit energies and the low-energy background in electron data worsen the energy resolution significantly.

Many of the challenges faced in this study will not be present in future prototypes, for example the incompletely equipped detector, tile-to-tile crosstalk and not-mono-energetic particle beams. These aspects, as well as the variety of different layers and the large fraction of inac-

tive channels, have in particular complicated the data analysis of the prototype. Besides the mentioned aspects the study shows, that a good energy resolution requires SiPMs with a high number of pixels and low crosstalk probability. All of these aspects are covered in the next generation of the AHCAL technological prototype, which has been built in 2017.

A

Appendix: Event Selections - Additional Plots

This appendix includes additional plots used for the estimation of event selections, as discussed in Section 8.3. Please refer there for additional information.

Main observables for event selections are the center of gravity in Z, COG_Z, the total number of hits per event, n_{hits} (both shown in Figure A.1), the ratio between the energy of layer 13 and 14 with the total energy in the AHCAL, $(E_{13} + E_{14})/E_{total}$ (as shown in Figure A.2) and the sum of the number of hits in layer 3 and 4, $N_3 + N_4$ (as shown in Figure A.3).

Additional cumulative step by step event selection efficiencies are shown in Figure A.4 for electrons and in Figure A.5 for pions.

All plots are shown for various beam energies.
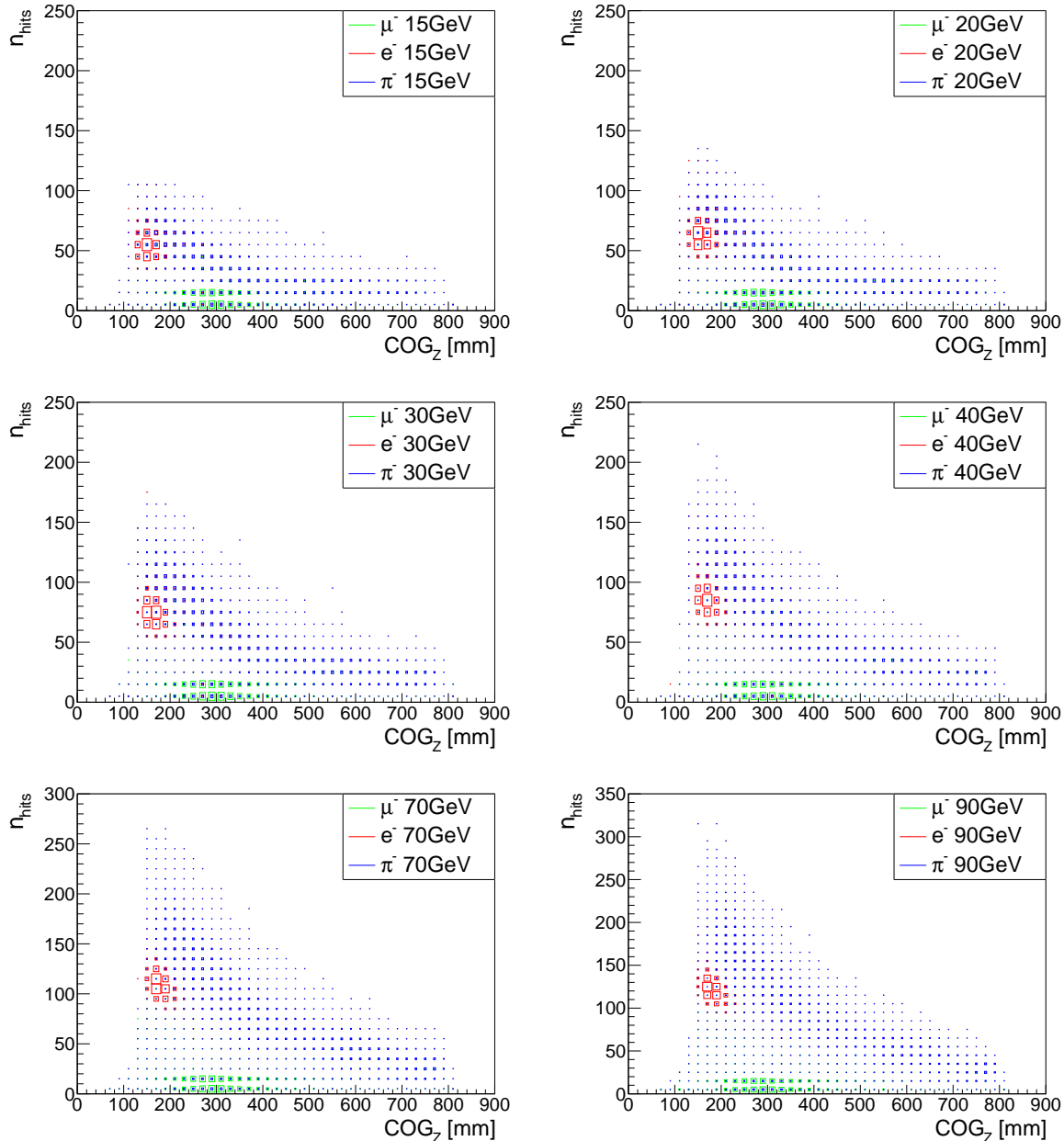
Figure A.1.: Additional distribution of the total number of hits per event, n_{hits}, as a function of COG_Z for simulated muons, electrons and pions. The size of the boxes represent the fraction of events in each bin. No previous selection is applied.
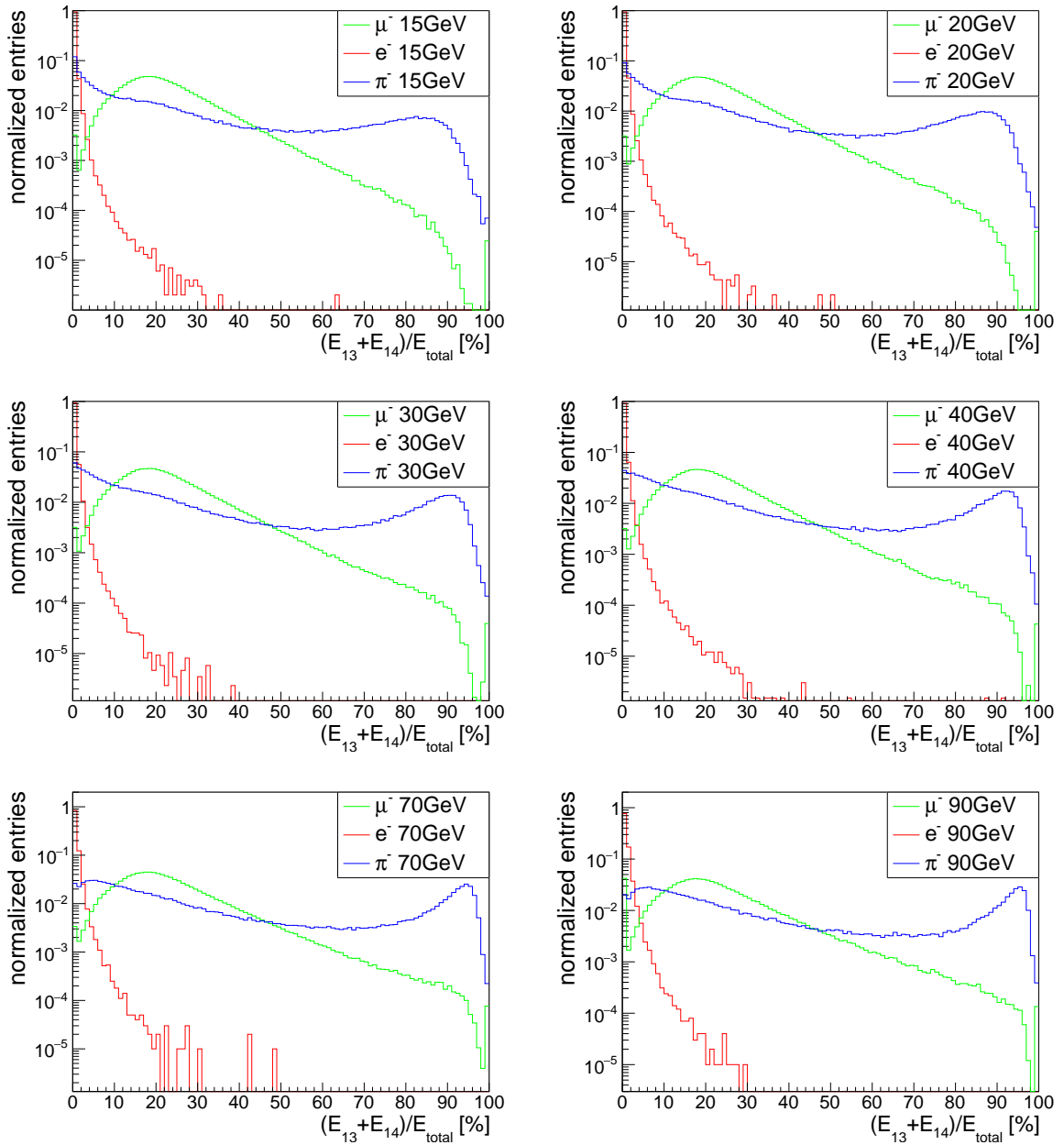
Figure A.2.: Fraction of events as a function of the ratio between the energy sum of layer 13 and 14 and the total energy in the AHCAL $(E_{13} + E_{14})/E_{total}$, for simulated muons, electrons and pions. No previous selection is applied.
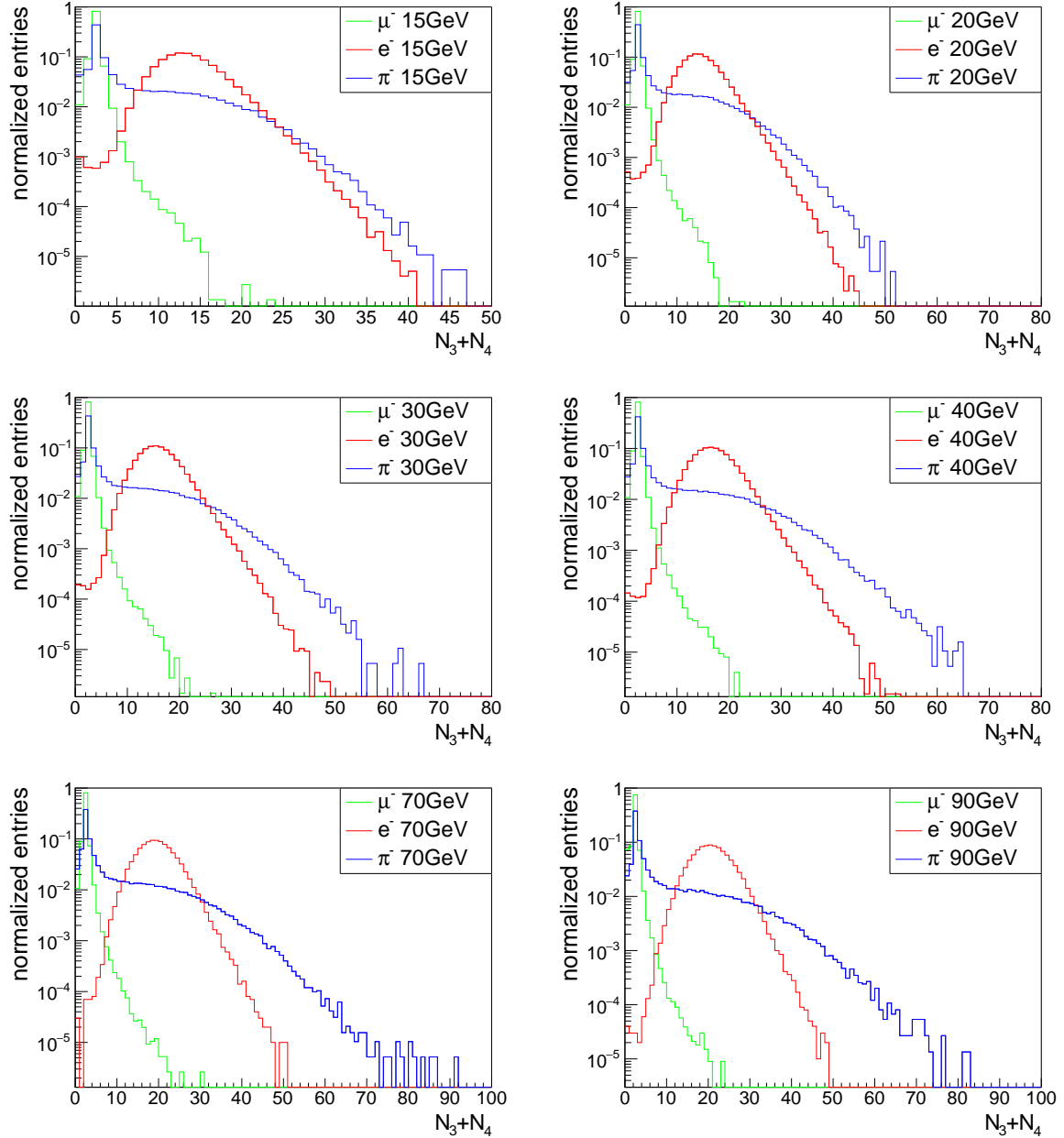
Figure A.3.: Fraction of events as a function of the sum of the number of hits in layer 3 and 4, $N_3 + N_4$, for simulated muons, electrons and pions. No previous selection is applied.
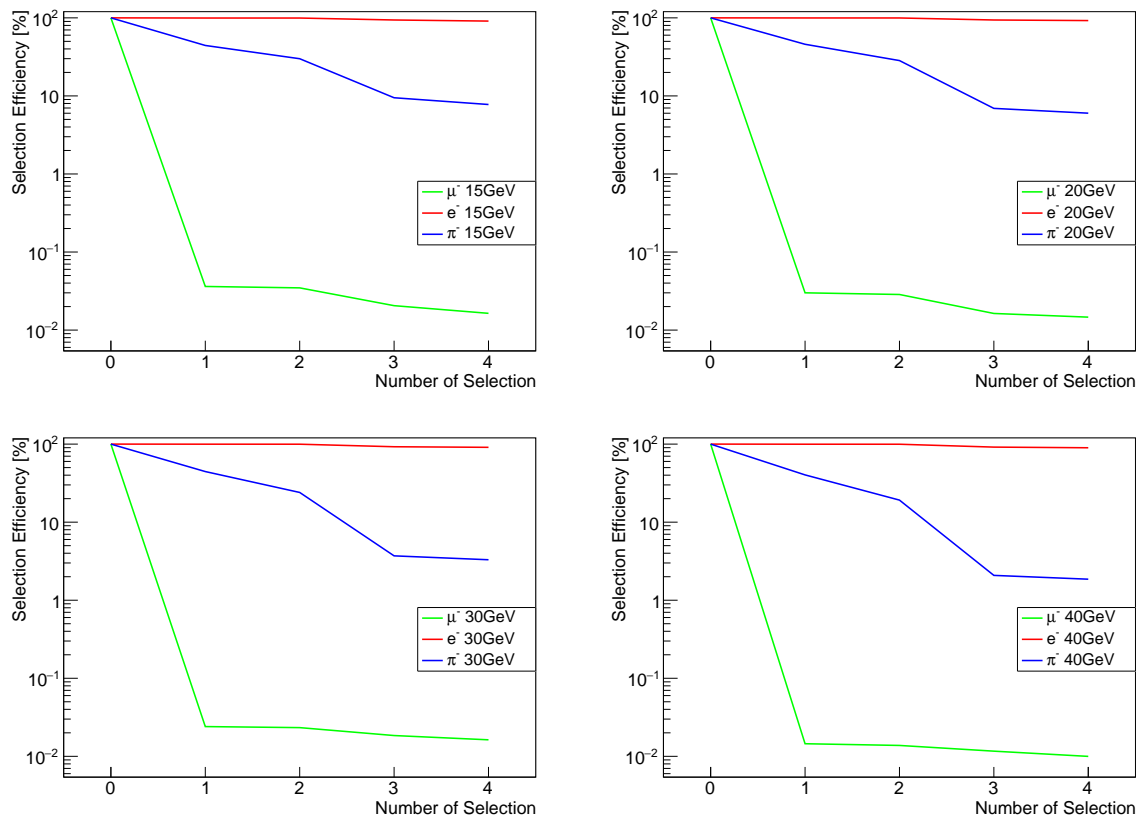
Figure A.4.: Additional step by step electron event selection efficiencies based on one another.
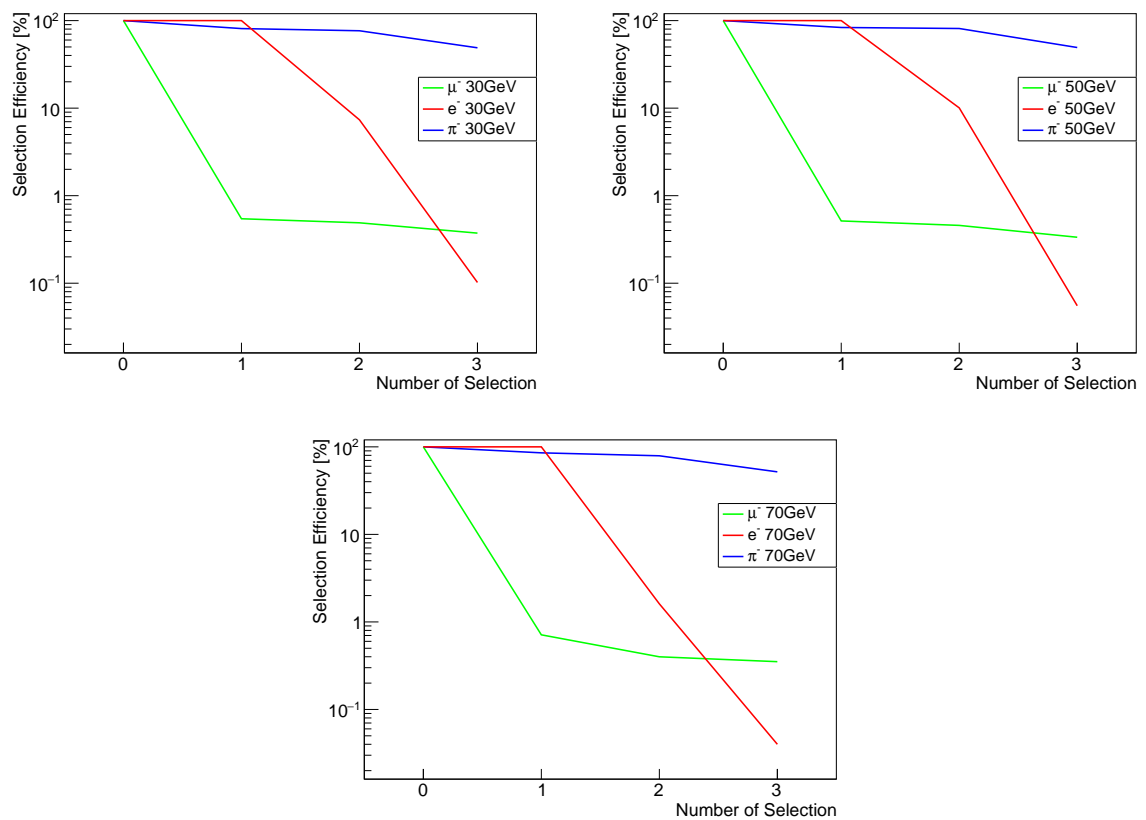
Figure A.5.: Additional step by step pion event selection efficiencies based on one another.

B

Appendix: Data and Simulation after First Event Selections - Additional Plots

In this appendix, additional plots concerning the comparison between data and simulation after the first event selections are shown. For detailed information and discussion, please refer to Section 8.4.2.

The following observables are shown for both, data and simulation and for various beam energies. For pions, the center of gravity in X direction (COG_X) is shown in Figure B.1 while for electrons, the center of gravity in Y direction (COG_Y) is shown in Figure B.2. The shape of these distributions is affected by the channel dimensions of $30 \times 30 \times 3\,\mathrm{mm}^3$. Though the COG_X for electrons and COG_Y for pions are not shown here, the shapes and the agreement between data and simulation is very similar.
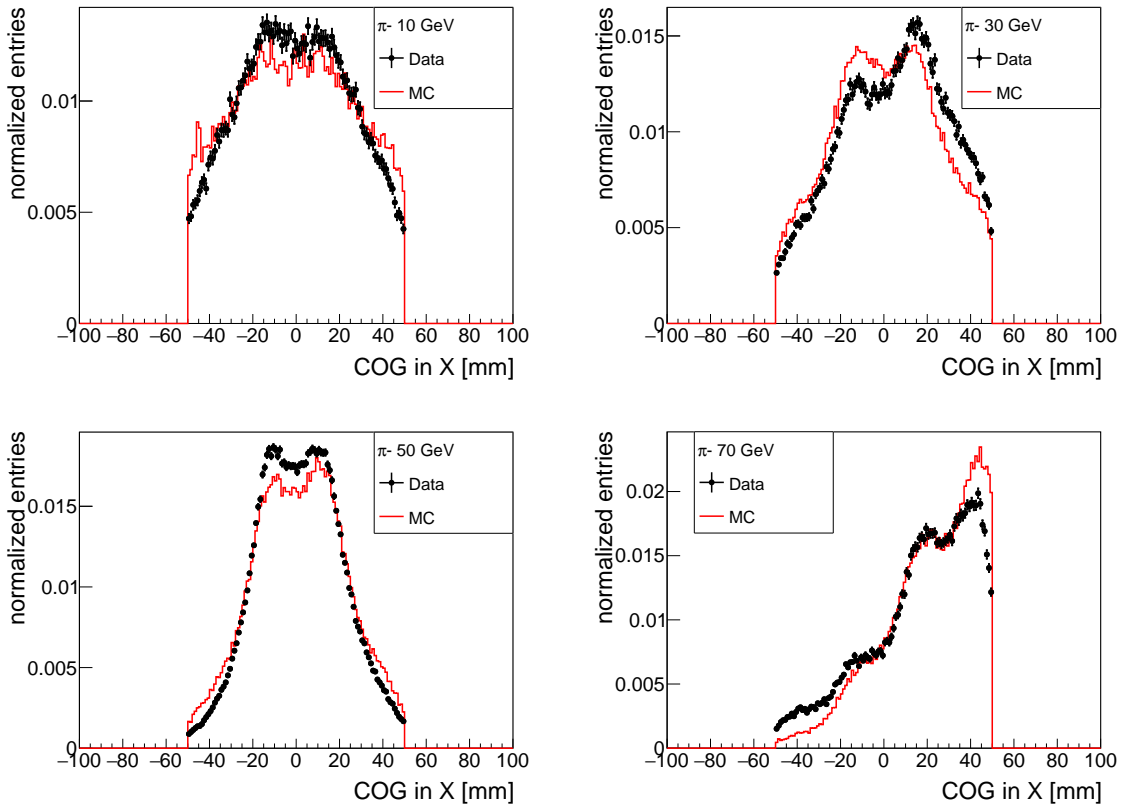
Figure B.1.: Center of gravity in x for 10, 30, 50 and 70 GeV pions for both, data and simulation.

Also, hit energy e_{hit} distributions of the complete detector are shown for electrons in Figure B.3 and for pions in Figure B.4. On the bottom of each plot, the ratio between simulation and data is shown.

For additional plots of total energy E_{total} distributions, please refer to Figure C.2 in Appendix C.
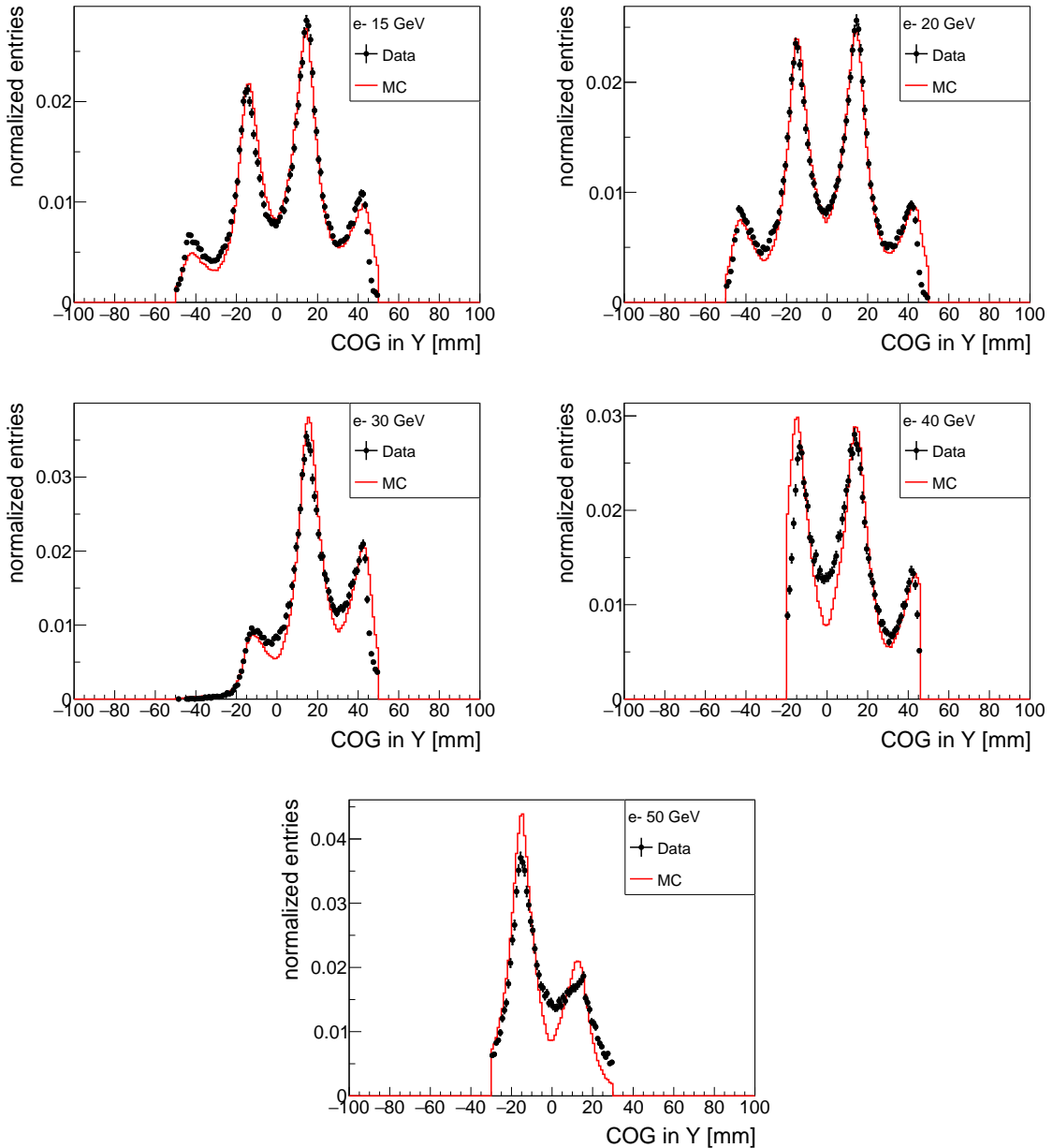
Figure B.2.: Center of gravity in y for 15, 20, 30, 40 and 50 GeV electrons for both, data and simulation.
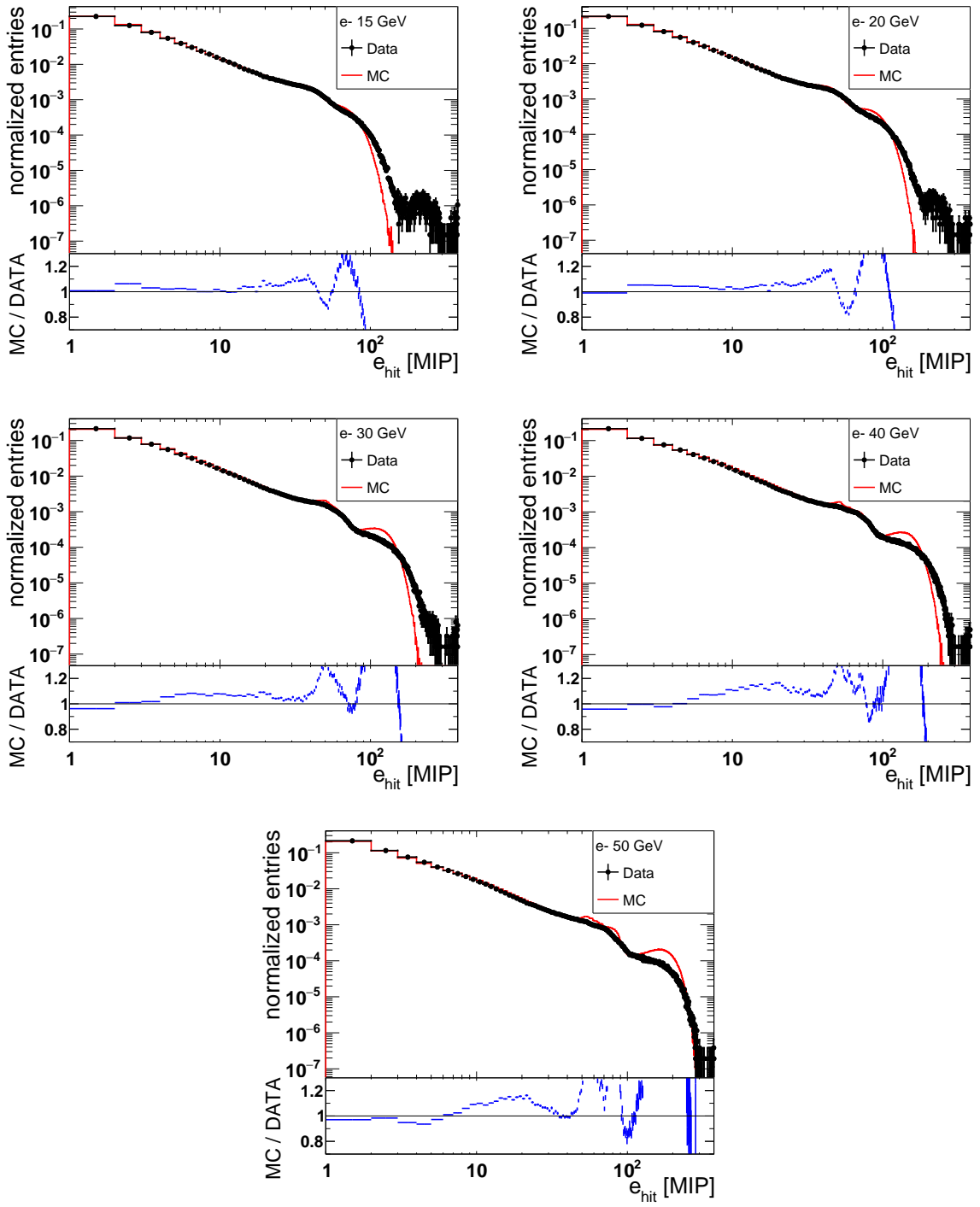
Figure B.3.: Hit energy e_{hit} distributions of the complete detector for 15, 20, 30, 40 and 50 GeV electrons in data and simulation. On the bottom of each plot, the ratio between simulation and data is shown.
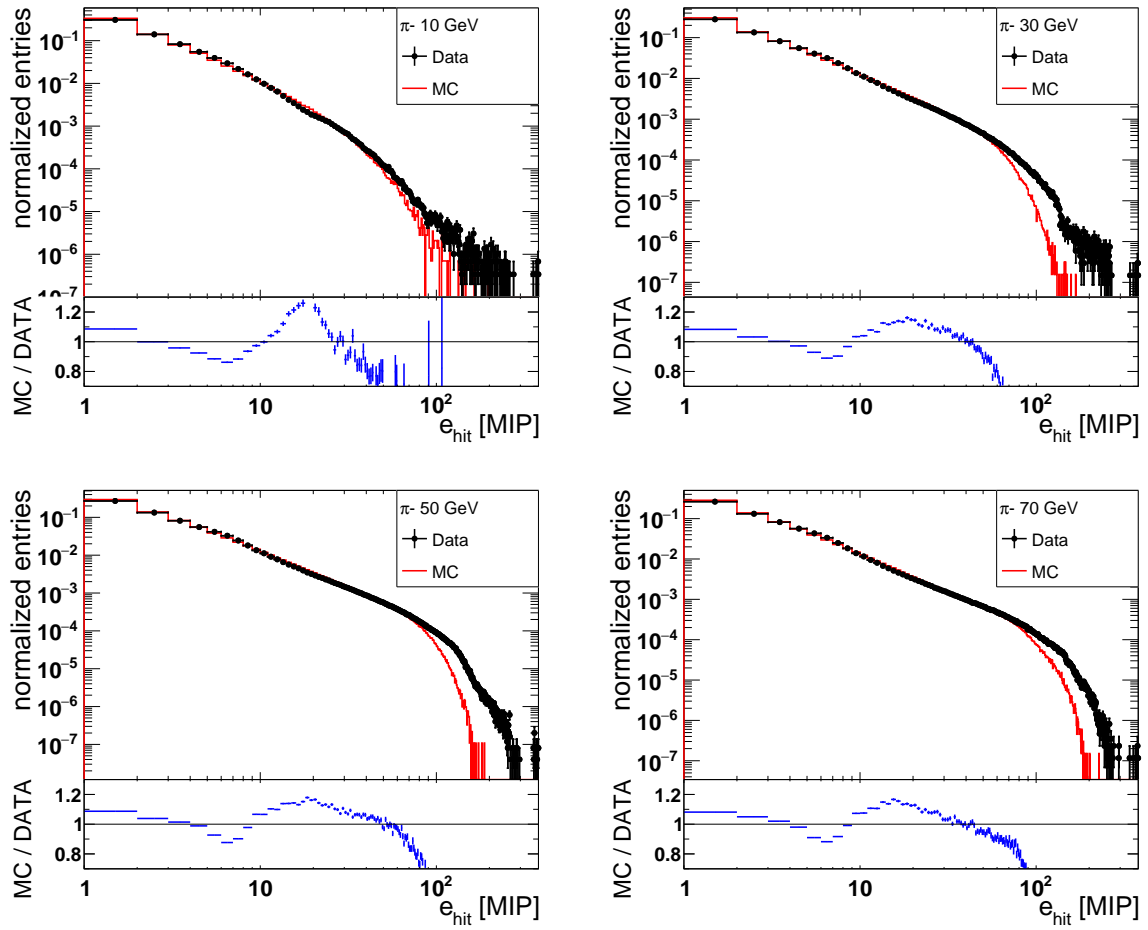
Figure B.4.: Hit energy e_{hit} distributions of the complete detector for 10, 30, 50 and 70 GeV pions in data and simulation. On the bottom of each plot, the ratio between simulation and data is shown.

Appendix: Data Based Electron Event Selection due to Low-energy Background in Data - Additional Plots

This appendix shows additional plots used for the estimation of data based electron event selections, which are required to reject low-energy background in electron data. For detailed information and discussion, please refer to Section 8.5.1.

Therefore, the observable of the ratio between the energy of layer 3 and the total energy, E_3/E_{total}, is utilized and shown in Figure C.1 for electron data and simulation at various beam
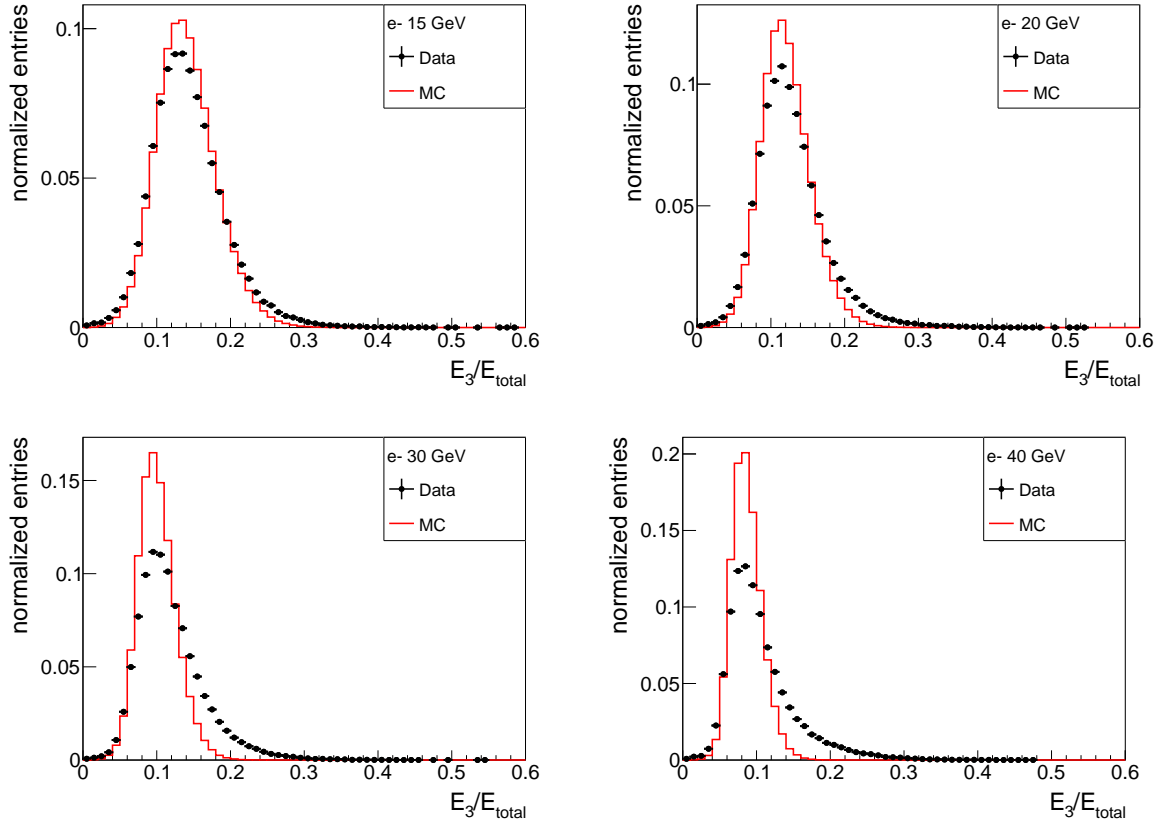
Figure C.1.: Ratio E_3/E_{total} for event-selected electrons of 15, 20, 30 and 40 GeV for data and simulation.

energies.

After applying additional selections on the ratio E_3/E_{total}, the low-energy background in data can to some extend be reduced. This is shown in Figure C.2 which shows the total energy E_{total} distribution for data and simulation of various beam energies with and without the E_3/E_{total} selection.
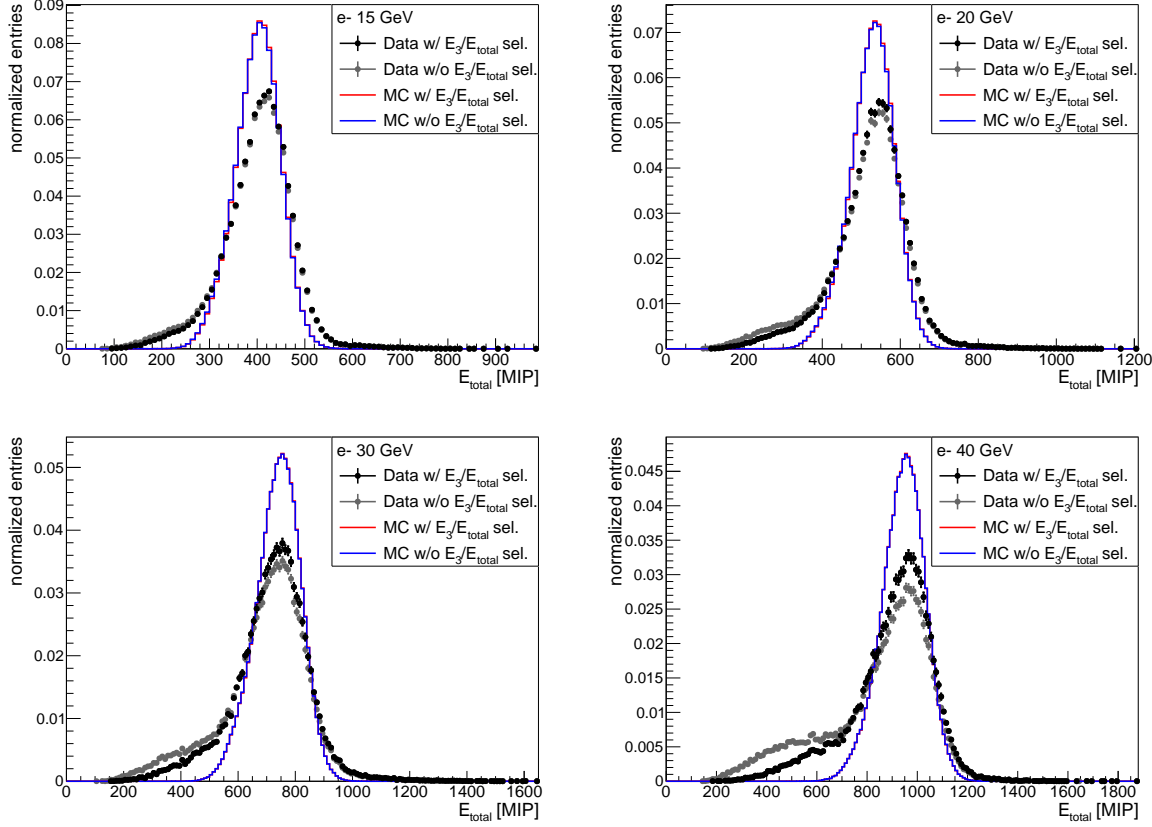
Figure C.2.: Additional plots showing the impact of E_3/E_{total} selection on the total energy, E_{total}, for 15, 20, 30 and 40 GeV electrons for data and simulation.

D

Appendix: Electron Data and Simulation after Simulation Tuning - Additional Plots

The additional upstream absorber thickness in the simulation and the tile-to-tile crosstalk factor in the digitization have been optimized as discussed in Section 8.6. In this appendix, additional plots concerning the comparison between data and simulation after the tuning of the simulation are shown for various beam energies. For detailed information and discussion, please refer to Section 8.6.3.

Additional shower profiles of the mean number of hits per layer, $\langle N_l \rangle$ and of the mean energy in layers, $\langle E_l \rangle$, are shown for electrons in Figure D.1 and for pions in Figure D.2. No de-saturation by an inverted response model is applied so far. On the bottom of each plot, the ratio between simulation and data is shown.
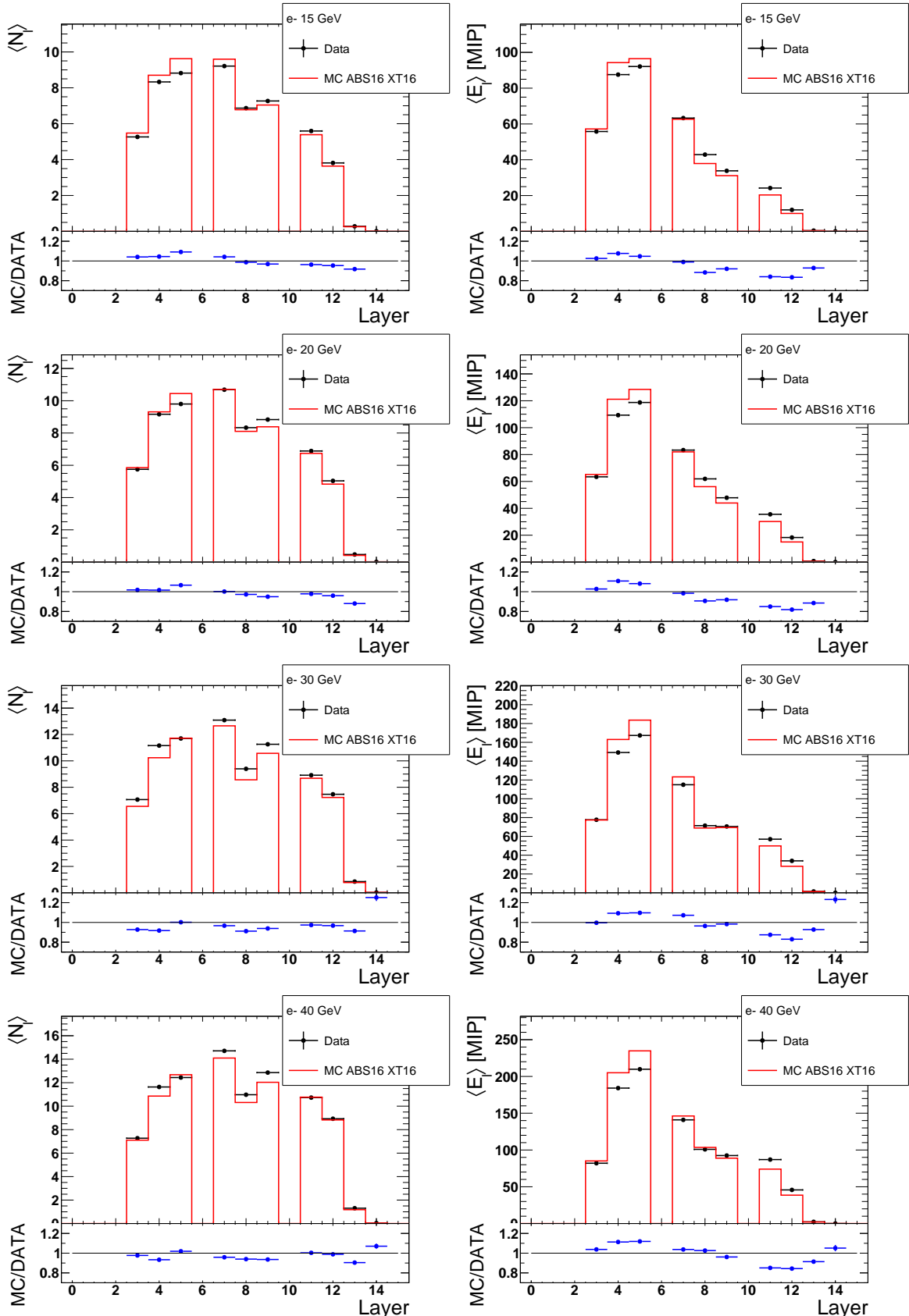
Figure D.1.: Additional shower profiles of the mean number of hits per layer, $\langle N_l \rangle$ (left) and of the mean energy in layers, $\langle E_l \rangle$ (right), for data and simulation of 15, 20, 30 and 40 GeV electrons. No de-saturation is applied. On the bottom of each plot, the ratio between simulation and data is shown.
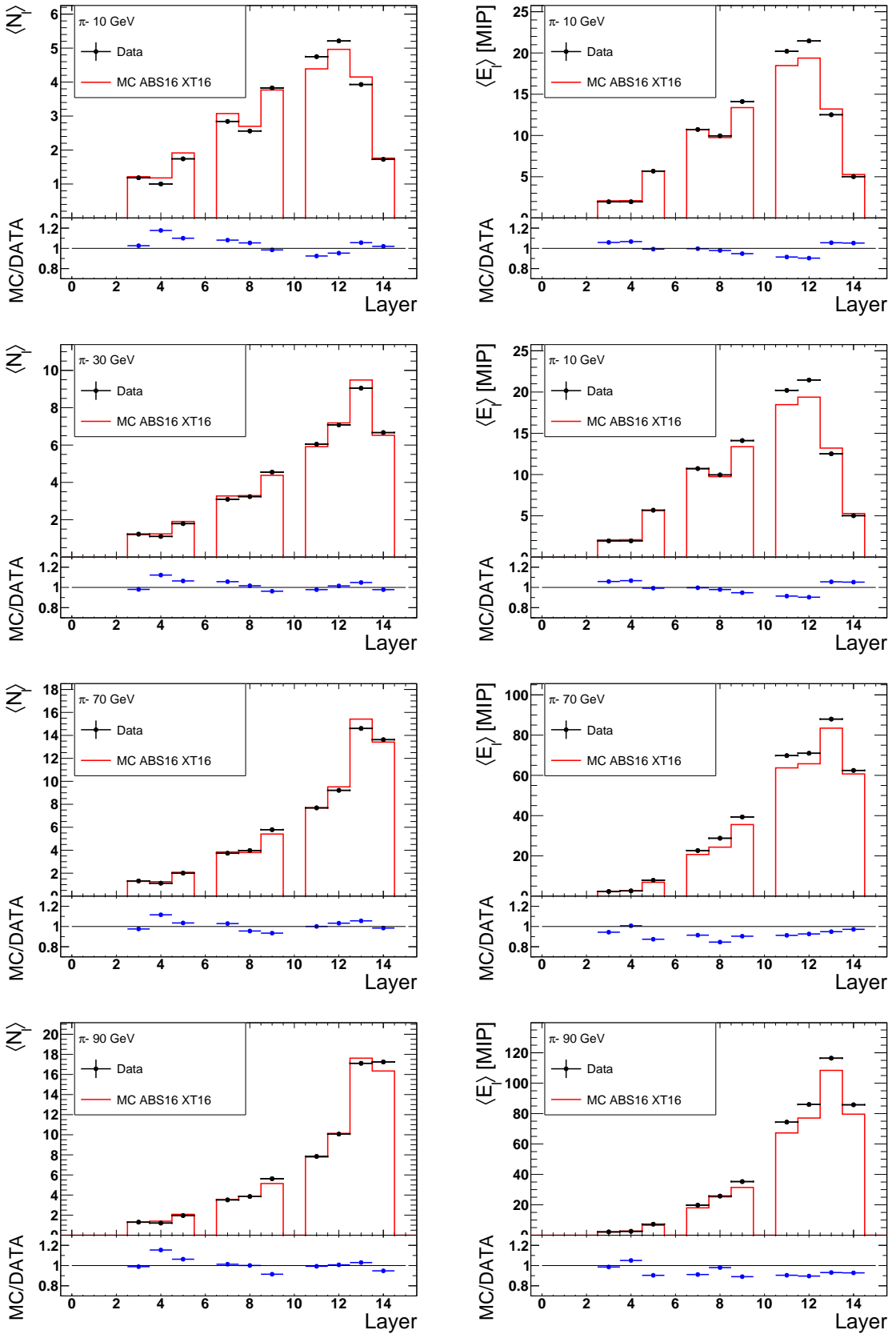
Figure D.2.: Additional shower profiles of the mean number of hits per layer, $\langle N_l \rangle$ (left) and of the mean energy in layers, $\langle E_l \rangle$ (right), for data and simulation of 10, 23, 70 and 90 GeV pions. No de-saturation is applied. On the bottom of each plot, the ratio between simulation and data is shown.

E

Appendix: Crosstalk-Extended Response Model Studies - Additional Plots

This appendix includes additional plots used for the crosstalk-extended (XT-ext) response model studies. As a reminder, different response model parameters are applied to the simulation in order to saturate the simulation. For the XT-ext model, these parameters are the (effective) total number of pixels N_{total}, the crosstalk factor ϵ_C and the ratio $R = N_{fired}/N_{total}$, which defines a threshold from which on a linear behavior of the response is assumed. After applying the response model to the simulation, the result is compared to data. As a variety of different SiPM and tile combinations are utilized in different layers of the AHCAL prototype, different layers have to be analyzed separately. The main observables for the response model study are the combined observables M_{E_l}, X_{E_l} and X_{e_l} of layer l, as defined in Section 9.3. In short, M_{E_l} takes into account the deviation from 1 of the ratio between the mean energy of each considered layer between data and simulation, for all beam energies. On the other hand, X_{E_l} and X_{e_l} take into account the χ^2 calculated with Pearson's chi-squared test between the distributions of the layer-wise energy E_l, or the layer-wise hit energy e_l, respectively, between data and simulation. The additional plots of the combined observables are shown in Figure E.1 for layer 5, in Figure E.2 for layer 8 and 9 and in Figure E.3 for layer 12 and 14. For detailed information and discussion, please refer to Section 9.5.
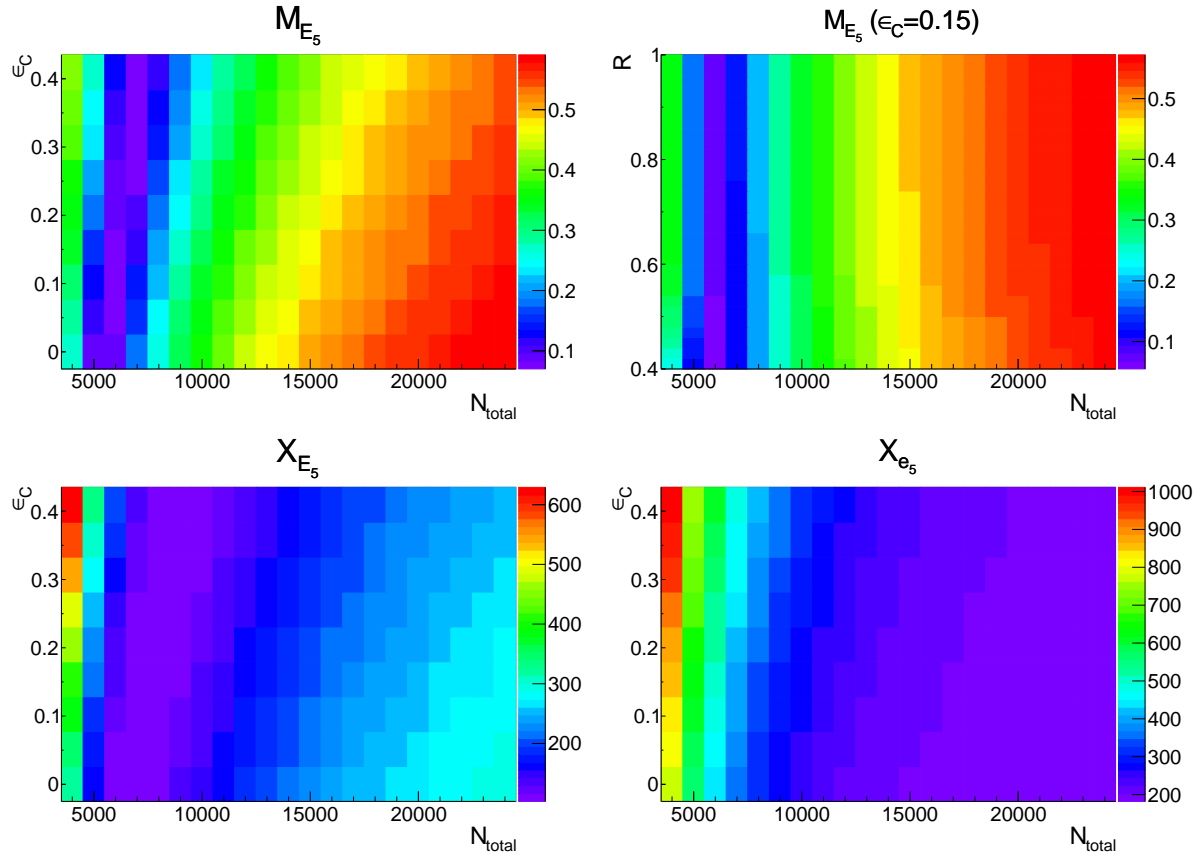
Figure E.1.: The combined observables M_{E_5} (top left and right), X_{E_5} (bottom left) and X_{e_5} (bottom right) for the XT-ext response model as two-dimensional histograms as a function of N_{total} and ϵ_C or R for layer 5. Except for the top right plot, the parameter R is fixed to 1. Estimated with electron data and simulation.
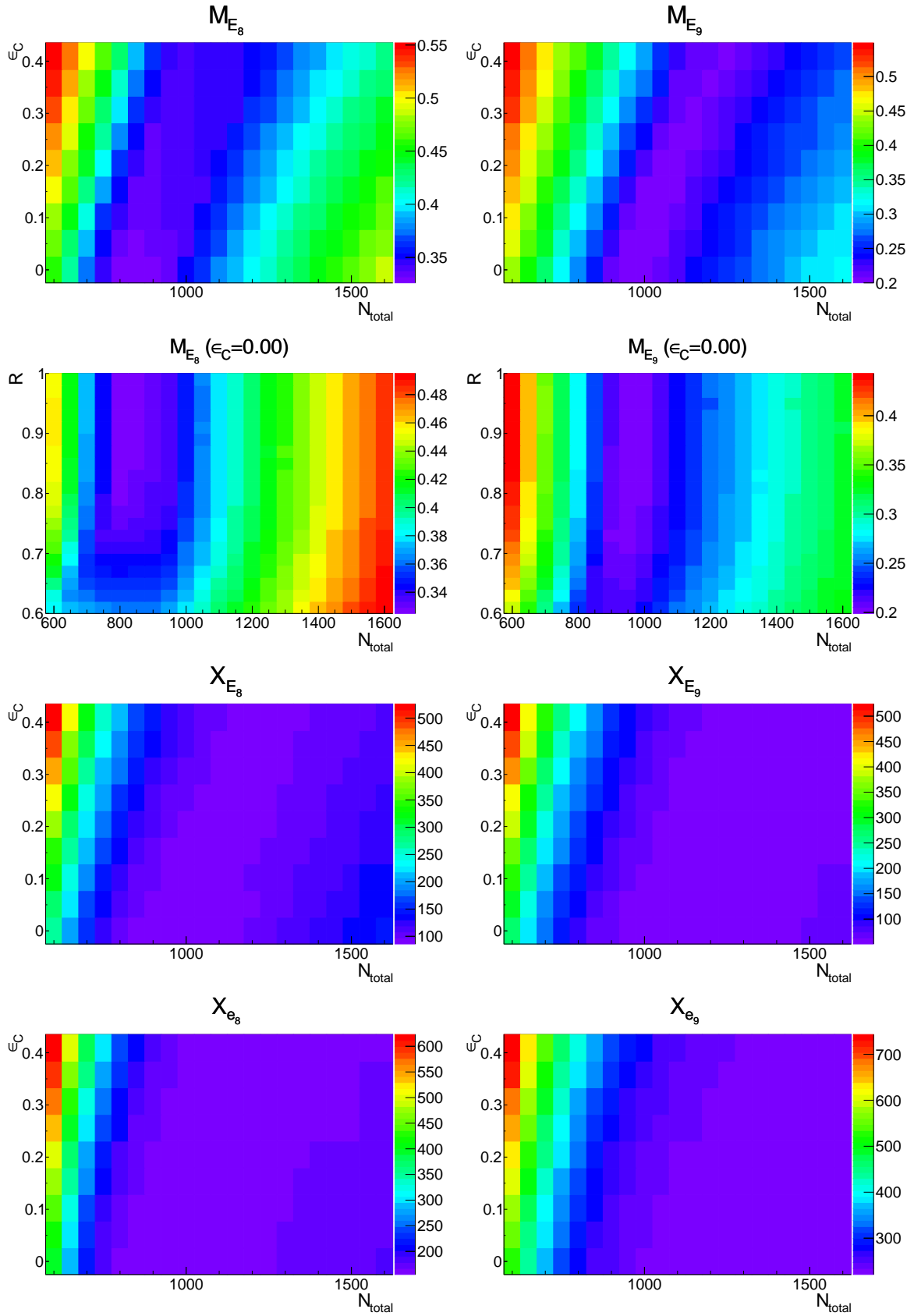
Figure E.2.: The combined observables M_{E_l}, X_{E_l} and X_{e_l} for the XT-ext response model as two-dimensional histograms as a function of N_{total} and ϵ_C or R for layer $l = 8$ (left) and layer 9 (right). Except for the second plots from the top, the parameter R is fixed to 1. Estimated with electron data and simulation.
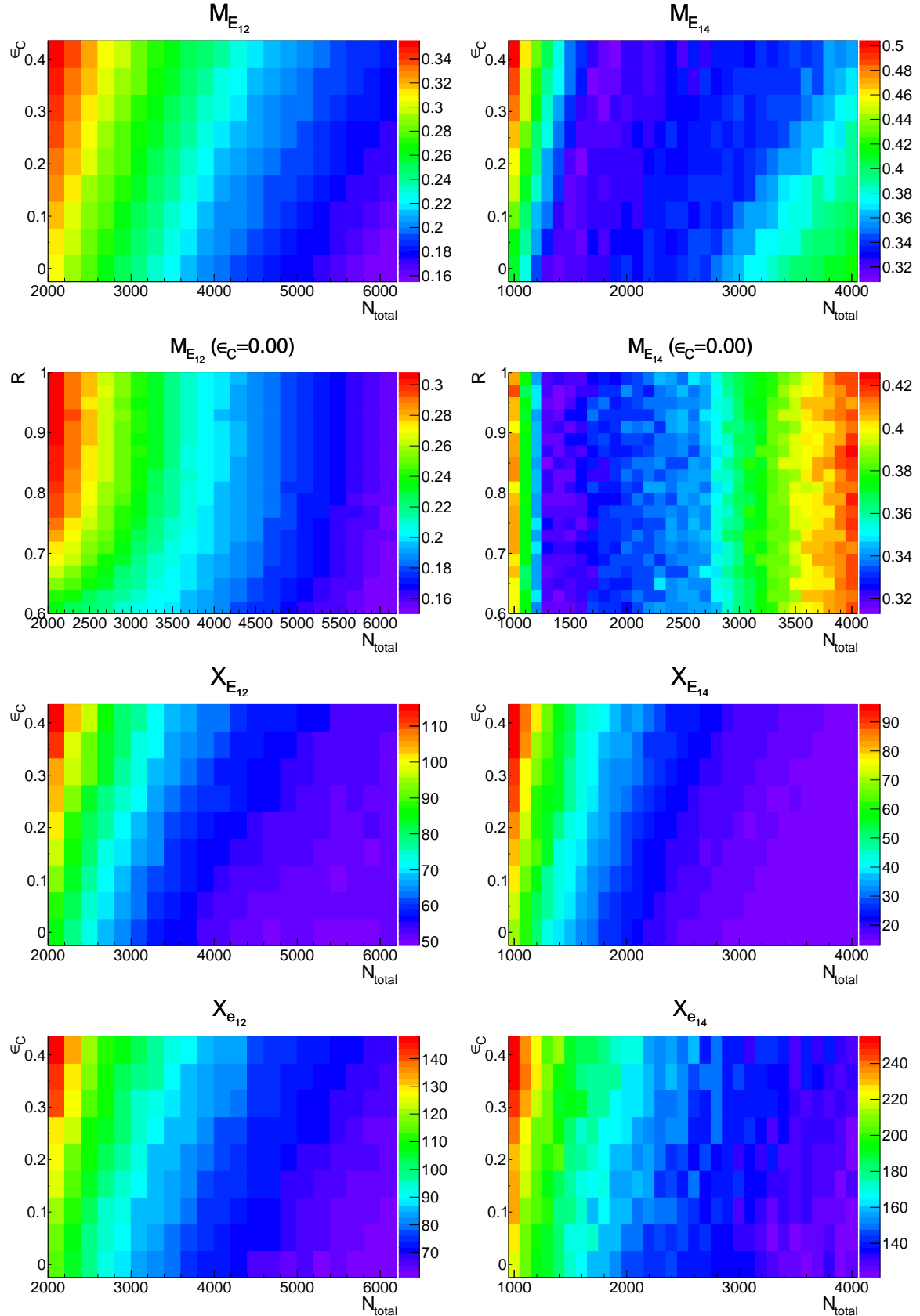
Figure E.3.: The combined observables M_{E_l}, X_{E_l} and X_{e_l} for the XT-ext response model as two-dimensional histograms as a function of N_{total} and ϵ_C or R for layer $l = 12$ (left) and layer 14 (right). Except for the second plots from the top, the parameter R is fixed to 1. Estimated with electron (layer 12, left) and pion (layer 14, right) data and simulation.

F

Appendix: Final Comparison between De-saturated Data and Simulation - Additional Plots

This appendix shows additional plots with data and simulation after de-saturation by the inverted response model for various beam energies including estimated systematic uncertainties. Additional total energy distributions are shown in Figure F.1 for electrons and pions. Also, additional shower profiles of the mean number of hits per layer, $\langle N_l \rangle$, and of the mean energy in layers, $\langle E_l \rangle$, are shown in Figure F.2 for electrons and in Figure F.3 for pions. For detailed information and discussion please refer to Section 9.8.2.
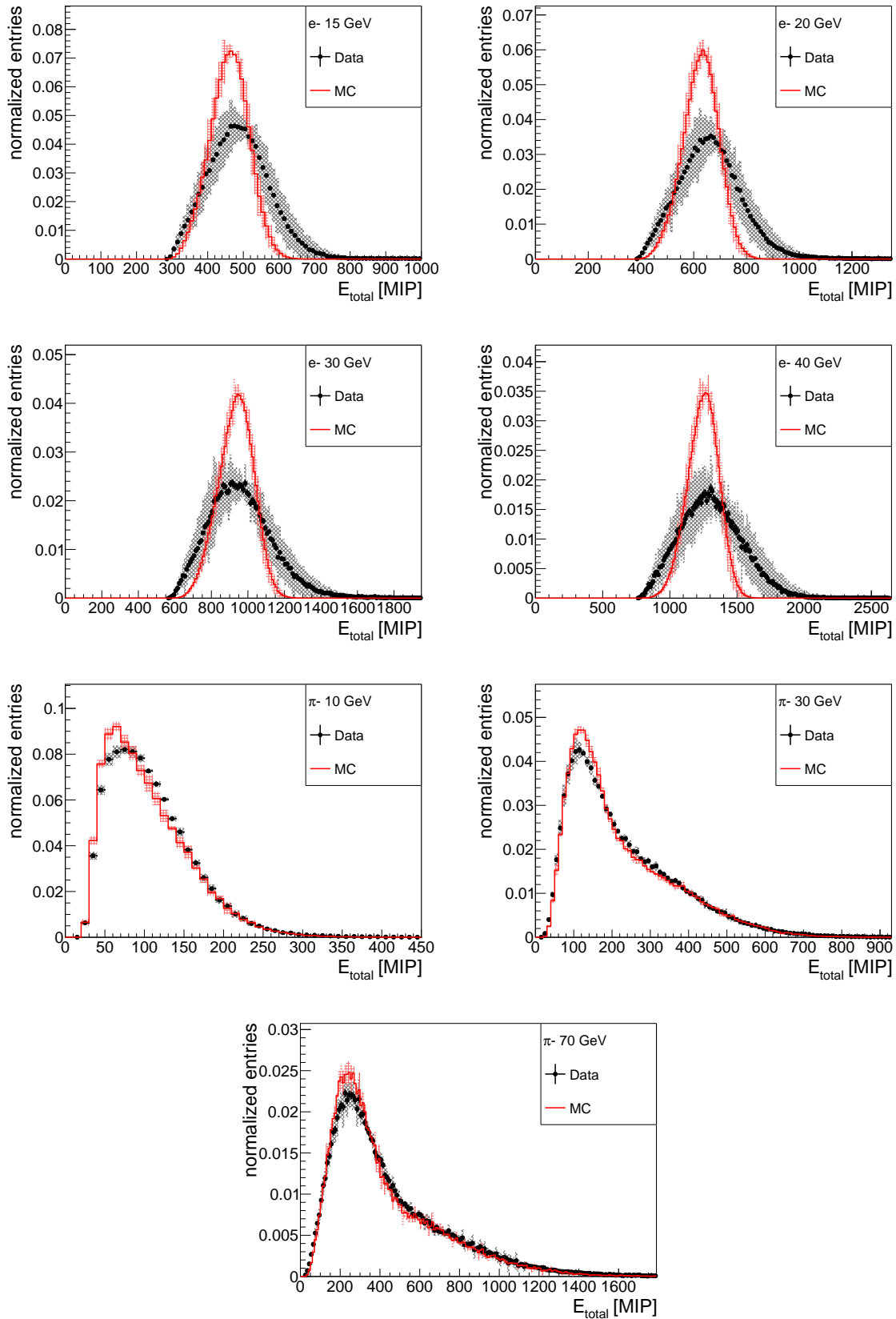
Figure F.1.: Additional total energy distributions, E_{total}, for data and simulation of 15, 20, 30 and 40 GeV electrons and of 10, 30 and 70 GeV pions. The inverse response model is applied and systematic uncertainties are estimated. A minor fraction of entries of less than 1 % exceeds the shown energy range.
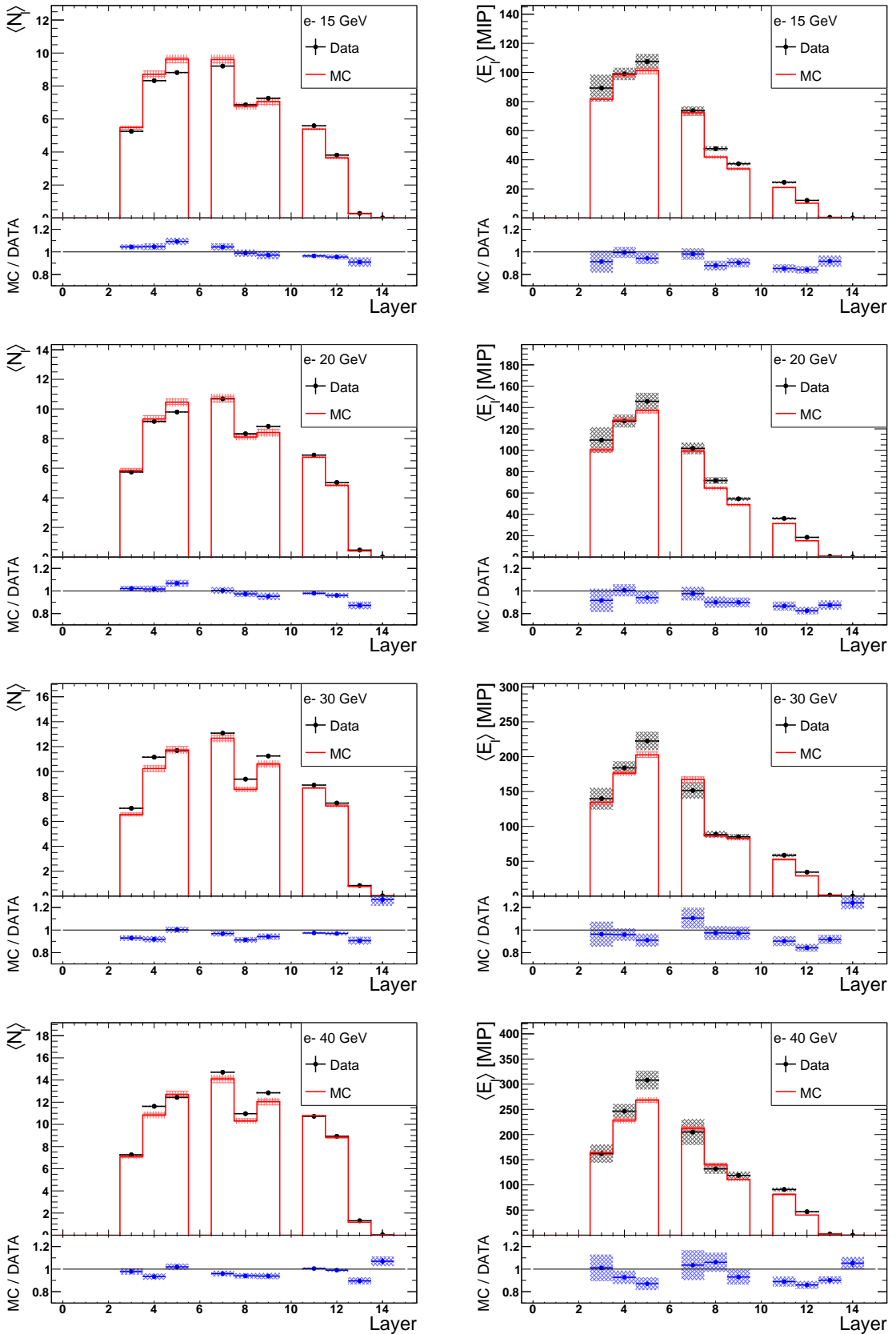
Figure F.2.: Additional shower profiles of the mean number of hits per layer, $\langle N_l \rangle$, (left) and of the mean energy in layers, $\langle E_l \rangle$, (right), for data and simulation of 15, 20, 30 and 40 GeV electrons. The inverse response model is applied and systematic uncertainties are estimated. On the bottom of each plot, the ratio between simulation and data is shown.
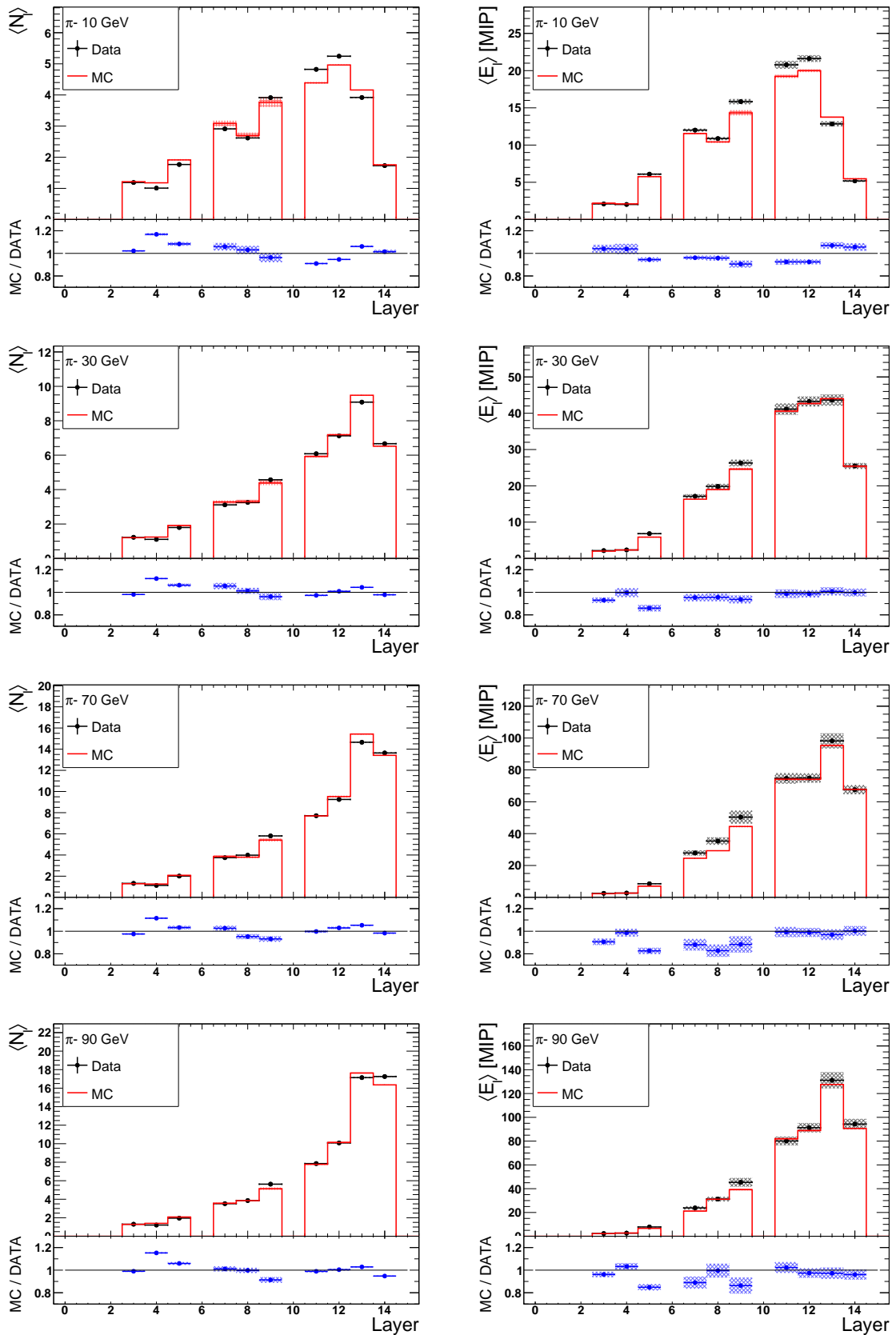
Figure F.3.: Additional shower profiles of the mean number of hits per layer, $\langle N_l \rangle$, (left) and of the mean energy in layers, $\langle E_l \rangle$, (right), for data and simulation of 10, 30, 70 and 90 GeV pions. The inverse response model is applied and systematic uncertainties are estimated. On the bottom of each plot, the ratio between simulation and data is shown.

G
Appendix: SiPM After Pulses

Figure G.1 shows the after pulse-pulse probability of the S1336x series of HAMAMATSU SiPMs. For a wide range of over-voltages, the probability is below 1 % and increases with rising over-voltage. According to the manufacturer, the after-pulse probability of the S1257x series is comparable. [134]
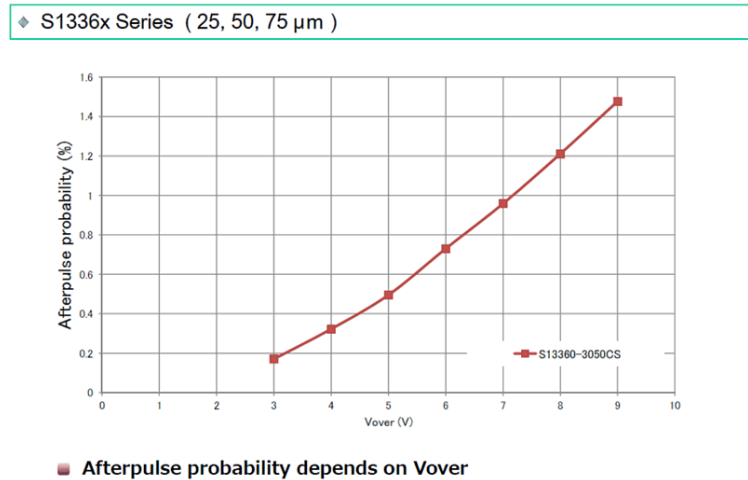

Figure G.1.: After-pulse probability of HAMAMATSU MPPC S1336x series, kindly provided by HAMAMATSU [134].

H

Appendix: Inactive Channels

Figure H.1 includes 2-D maps of layers 3 to 14, showing all active and inactive channels. Channels are marked as inactive, if they do not respond, are too noisy or can in any way not be calibrated. In this context, channels connected the external validation like T_0- and Cherenkov-signals also count as inactive.
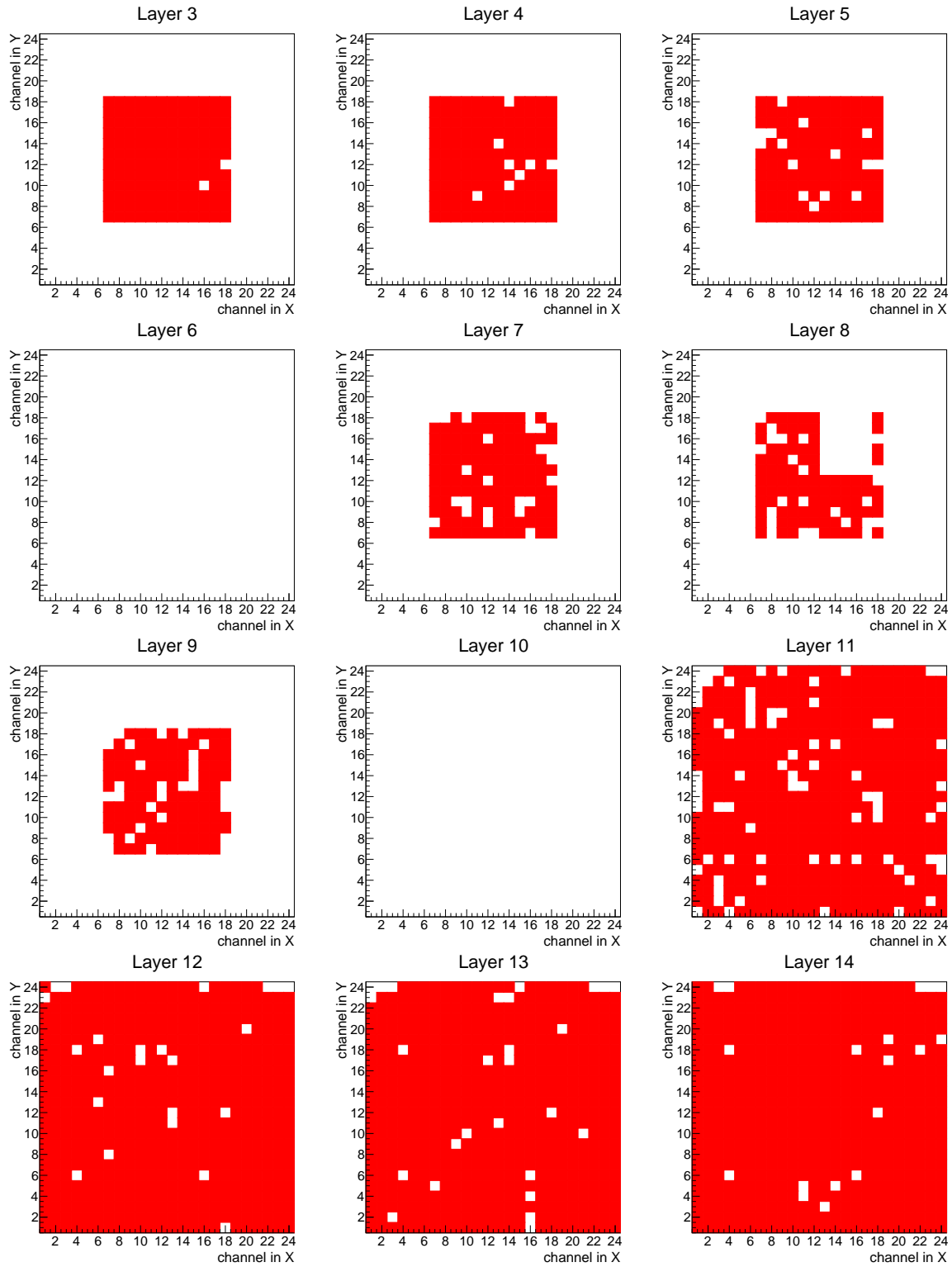
Figure H.1.: Maps of active and inactive channels for all AHCAL layers. Layers 3 to 10 consist of centered single HBUs and layers 11 to 14 consist of four HBUs. Red areas correspond to active channels, while white spots belong to inactive or unequipped channels. Layers 6 and 10 are completely rejected in this analysis.

Bibliography

[1] ATLAS Collaboration. Observation of a new particle in the search for the Standard Model Higgs boson with the ATLAS detector at the LHC. *Physics Letters B*, 716:1–29, 2012.

[2] CMS Collaboration. Observation of a new boson at a mass of 125 GeV with the CMS experiment at the LHC. *Physics Letters B*, 716:30–61, 2012.

[3] Ties Behnke et al. The International Linear Collider Technical Design Report - Volume 1: Executive Summary. 2013. URL `http://bib-pubdb1.desy.de/record/166034`.

[4] Ties Behnke et al. The International Linear Collider Technical Design Report - Volume 4: Detectors. 2013. URL `http://bib-pubdb1.desy.de/record/166033`.

[5] PRISMA Detector Lab. Webpage of PRISMA Detector Lab. URL `https://www.prisma.uni-mainz.de/facilities/prisma-detector-lab/`. Accessed: 2019-06-10.

[6] C. N. Yang and R. L. Mills. Conservation of Isotopic Spin and Isotopic Gauge Invariance. *Phys. Rev.*, 96:191–195, Oct 1954. doi: 10.1103/PhysRev.96.191. URL `https://link.aps.org/doi/10.1103/PhysRev.96.191`.

[7] Sheldon L. Glashow. Partial-symmetries of weak interactions. *Nuclear Physics*, 22(4):579 – 588, 1961. ISSN 0029-5582. URL `http://www.sciencedirect.com/science/article/pii/0029558261904692`.

[8] Steven Weinberg. A Model of Leptons. *Phys. Rev. Lett.*, 19:1264–1266, Nov 1967. doi: 10.1103/PhysRevLett.19.1264. URL `https://link.aps.org/doi/10.1103/PhysRevLett.19.1264`.

[9] A. Salam and J.C. Ward. Electromagnetic and weak interactions. *Physics Letters*, 13(2): 168 – 171, 1964. ISSN 0031-9163. doi: https://doi.org/10.1016/0031-9163(64)90711-5. URL `http://www.sciencedirect.com/science/article/pii/0031916364907115`.

[10] Peter W. Higgs. Broken Symmetries and the Masses of Gauge Bosons. *Phys. Rev. Lett.*, 13:508–509, Oct 1964. doi: 10.1103/PhysRevLett.13.508. URL `https://link.aps.org/doi/10.1103/PhysRevLett.13.508`.

[11] F. Englert and R. Brout. Broken Symmetry and the Mass of Gauge Vector Mesons. *Phys. Rev. Lett.*, 13:321–323, Aug 1964. doi: 10.1103/PhysRevLett.13.321. URL `https://link.aps.org/doi/10.1103/PhysRevLett.13.321`.

[12] Bogdan Povh, Klaus Rith, Christoph Scholz, and Frank Zetsche. *Teilchen und Kerne*. Springer-Lehrbuch. Springer, 2014. ISBN 978-3-642-37821-8.

[13] David Griffiths. *Introduction to elementary particles*. 2008. ISBN 9783527406012.

[14] F. Halzen and Alan D. Martin. *QUARKS AND LEPTONS: An Introductory Course In Modern Particle Physics*. 1984. ISBN 0471887412, 9780471887416.

[15] Lars Finke. Das Standardmodell der Teilchenphsik (Eine Einführung), 2001. URL `https://web.physik.rwth-aachen.de/~hebbeker/lectures/sem0102/finke2.pdf`.

[16] Alberto Zannoni. On the Quantization of the Monoatomic Ideal Gas, 1999.

[17] Bose. Plancks Gesetz und Lichtquantenhypothese. *Zeitschrift für Physik*, 26(1):178–181, Dec 1924. ISSN 0044-3328. doi: 10.1007/BF01327326. URL `https://doi.org/10.1007/BF01327326`.

[18] Francesco Capozzi, Eleonora Di Valentino, Eligio Lisi, Antonio Marrone, Alessandro Melchiorri, and Antonio Palazzo. Global constraints on absolute neutrino masses and their ordering. *Phys. Rev. D*, 95:096014, May 2017. doi: 10.1103/PhysRevD.95.096014. URL `https://link.aps.org/doi/10.1103/PhysRevD.95.096014`.

[19] M. Tanabashi et al. Review of Particle Physics. *Phys. Rev.*, D98(3):030001, 2018. doi: 10.1103/PhysRevD.98.030001.

[20] Hideki Yukawa. On the Interaction of Elementary Particles. I. *Progress of Theoretical Physics Supplement*, 1:1–10, 01 1955. ISSN 0375-9687. doi: 10.1143/PTPS.1.1. URL `https://doi.org/10.1143/PTPS.1.1`.

[21] MissMJ. Standard Model of Elementary Particles. URL `https://en.wikipedia.org/wiki/Standard_Model#/media/File:Standard_Model_of_Elementary_Particles.svg`. Accessed: 2019-06-29.

[22] Michael E. Peskin and Daniel V. Schroeder. *An Introduction to quantum field theory.* Addison-Wesley, Reading, USA, 1995. ISBN 9780201503975, 0201503972. URL `http://www.slac.stanford.edu/~mpeskin/QFT.html`.

[23] Emmy Noether. Invariant Variation Problems. *Gott. Nachr.*, 1918:235–257, 1918. doi: 10.1080/00411457108231446. [Transp. Theory Statist. Phys.1,186(1971)].

[24] Tadao Nakano and Kazuhiko Nishijima. Charge Independence for V-particles. *Progress of Theoretical Physics*, 10(5):581–582, 11 1953. ISSN 0033-068X. doi: 10.1143/PTP.10.581. URL `https://doi.org/10.1143/PTP.10.581`.

[25] G. Arnison et al. Experimental observation of isolated large transverse energy electrons with associated missing energy at s=540 GeV. *Physics Letters B*, 122(1):103 – 116, 1983. ISSN 0370-2693. doi: https://doi.org/10.1016/0370-2693(83)91177-2. URL `http://www.sciencedirect.com/science/article/pii/0370269383911772`.

[26] P. Bagnaia et al. Evidence for $Z^0 \to e^+e^-$ at the CERN pp collider. *Physics Letters B*, 129 (1):130 – 140, 1983. ISSN 0370-2693. doi: https://doi.org/10.1016/0370-2693(83)90744-X. URL `http://www.sciencedirect.com/science/article/pii/037026938390744X`.

[27] Howard Baer et al. The International Linear Collider Technical Design Report - Volume 2: Physics. 2013. URL `http://bib-pubdb1.desy.de/record/165642`.

[28] Owe Philipsen. *Quantenfeldtheorie und das Standardmodell der Teilchenphysik: Eine Einführung.* 01 2018. ISBN 978-3-662-57819-3. doi: 10.1007/978-3-662-57820-9.

[29] Andrei D Sakharov. Violation of CP invariance, C asymmetry, and baryon asymmetry of the universe. *Soviet Physics Uspekhi*, 34(5):392–393, may 1991. doi: 10.1070/pu1991v034n05abeh002497. URL https://iopscience.iop.org/article/10.1070/PU1991v034n05ABEH002497.

[30] Eiichiro Komatsu et al. Results from the Wilkinson Microwave Anisotropy Probe. *Progress of Theoretical and Experimental Physics*, 2014(6), 06 2014. ISSN 2050-3911. doi: 10.1093/ptep/ptu083. URL https://doi.org/10.1093/ptep/ptu083.

[31] Gaëlle Giesen, Julien Lesgourgues, Benjamin Audren, and Yacine Ali-Haïmoud. CMB photons shedding light on dark matter. *Journal of Cosmology and Astroparticle Physics*, 2012(12):008–008, dec 2012. doi: 10.1088/1475-7516/2012/12/008. URL https://doi.org/10.1088%2F1475-7516%2F2012%2F12%2F008.

[32] Elia S. Battistelli et al. *Galaxy clusters as probes for cosmology and dark matter*, pages 576–601. doi: 10.1142/9789813226609_0032. URL https://www.worldscientific.com/doi/abs/10.1142/9789813226609_0032.

[33] Timothy J. Sumner. Experimental Searches for Dark Matter. *Living Reviews in Relativity*, 5(1):4, Jul 2002. ISSN 1433-8351. doi: 10.12942/lrr-2002-4. URL https://doi.org/10.12942/lrr-2002-4.

[34] A. R. Vieira, Brigitte Hiller, M. C. Nemes, and Marcos Sampaio. Naturalness and theoretical constraints on the Higgs boson mass. 2012. doi: 10.1007/s10773-013-1652-x.

[35] Hermann Kolanoski and Norbert Wermes. *Teilchendetektoren.* Springer, 2016. ISBN 9783662453490, 9783662453506. doi: 10.1007/978-3-662-45350-6.

[36] Bruno Benedetto Rossi. *High-energy particles.* New York : Prentice-Hall, 1952. Bibliography: p. 547-561.

[37] Egidio Longo and Ignazio Sestili. Monte carlo calculation of photon-initiated electromagnetic showers in lead glass. *Nuclear Instruments and Methods*, 128(2):283 – 307, 1975. ISSN 0029-554X. doi: https://doi.org/10.1016/0029-554X(75)90679-5. URL http://www.sciencedirect.com/science/article/pii/0029554X75906795.

[38] O. Hartbrich. Scintillator Calorimeters for a Future Linear Collider Experiment, Dissertation. 2016.

[39] K. A. Olive et al. Review of Particle Physics. *Chin. Phys.*, C38:090001, 2014. doi: 10.1088/1674-1137/38/9/090001.

[40] Nils Feege. Low-energetic hadron interactions in a highly granular calorimeter. DESY-THESIS-2011-048.

[41] R. Wigmans. *Calorimetry: Energy Measurement in Particle Physics*. International series of monographs on physics. Oxford University Press, 2017. ISBN 9780198786351. URL `https://www.oxfordscholarship.com/view/10.1093/oso/9780198786351.001.0001/oso-9780198786351`.

[42] T.A. Gabriel, D.E. Groom, P.K. Job, N.V. Mokhov, and G.R. Stevenson. Energy dependence of hadronic activity. *Nuclear Instruments and Methods in Physics Research Section A: Accelerators, Spectrometers, Detectors and Associated Equipment*, 338(2):336 – 347, 1994. ISSN 0168-9002. doi: https://doi.org/10.1016/0168-9002(94)91317-X. URL `http://www.sciencedirect.com/science/article/pii/016890029491317X`.

[43] P. Lecoq, I. Dafinei, E. Auffray, M. Schneegans, M.V. Korzhik, O.V. Missevitch, V.B. Pavlenko, A.A. Fedorov, A.N. Annenkov, V.L. Kostylev, and V.D. Ligun. Lead tungstate (PbWO4) scintillators for LHC EM calorimetry. *Nuclear Instruments and Methods in Physics Research Section A: Accelerators, Spectrometers, Detectors and Associated Equipment*, 365(2):291 – 298, 1995. ISSN 0168-9002. doi: https://doi.org/10.1016/0168-9002(95)00589-7. URL `http://www.sciencedirect.com/science/article/pii/0168900295005897`.

[44] Cristina Biino. The CMS electromagnetic calorimeter: overview, lessons learned during run 1 and future projections. *Journal of Physics: Conference Series*, 587:012001, feb 2015. doi: 10.1088/1742-6596/587/1/012001. URL `https://doi.org/10.1088%2F1742-6596%2F587%2F1%2F012001`.

[45] Ana Maria Henriques Correia. The ATLAS Tile Calorimeter. Technical Report ATL-TILECAL-PROC-2015-002, CERN, Geneva, Mar 2015. URL `https://cds.cern.ch/record/2004868`.

[46] The ATLAS Collaboration. The ATLAS Experiment at the CERN Large Hadron Collider. *Journal of Instrumentation*, 3(08):S08003–S08003, aug 2008. doi: 10.1088/1748-0221/3/08/s08003. URL `https://doi.org/10.1088%2F1748-0221%2F3%2F08%2Fs08003`.

[47] A. Bernstein et al. Beam tests of the ZEUS barrel calorimeter. *Nuclear Instruments and Methods in Physics Research Section A: Accelerators, Spectrometers, Detectors and Associated Equipment*, 336(1):23 – 52, 1993. ISSN 0168-9002. doi: https://doi.org/10.1016/0168-9002(93)91078-2. URL `http://www.sciencedirect.com/science/article/pii/0168900293910782`.

[48] M.A. Thomson. Particle flow calorimetry and the PandoraPFA algorithm. *Nuclear Instruments and Methods in Physics Research Section A: Accelerators, Spectrometers, Detectors and Associated Equipment*, 611(1):25 – 40, 2009. ISSN 0168-9002. doi: https://doi.org/10.1016/j.nima.2009.09.009. URL `http://www.sciencedirect.com/science/article/pii/S0168900209017264`.

[49] M. A. Thomson. Particle Flow Calorimetry and the PandoraPFA Algorithm. 2009. doi: 10.1016/j.nima.2009.09.009. URL `https://arxiv.org/pdf/0907.3577.pdf`.

[50] The CALICE collaboration and C Adloff et al. Tests of a Particle Flow Algorithm with CALICE test beam data. *Journal of Instrumentation*, 6(07):P07005–P07005, jul 2011. doi: 10.1088/1748-0221/6/07/p07005. URL `https://doi.org/10.1088%2F1748-0221%2F6%2F07%2Fp07005`.

[51] Chris Adolphsen et al. The International Linear Collider Technical Design Report - Volume 3.I: R&D in the Technical Design Phase. 2013.

[52] Nicholas Walker. The International Linear Collider Technical Design Report - Volume 3.II: Accelerator Baseline Design. 2013. doi: 10.3204/PUBDB-2017-10108. URL `http://bib-pubdb1.desy.de/record/391165`.

[53] A. Arbey et al. Physics at the e$^+$ e$^-$ Linear Collider. *Eur. Phys. J.*, C75(8):371, 2015. doi: 10.1140/epjc/s10052-015-3511-9.

[54] Keisuke Fujii et al. Physics Case for the International Linear Collider. 2015.

[55] Marco Farina, Maxim Perelstein, and Nicolas Rey-Le Lorier. Higgs Couplings and Naturalness. 2013. doi: 10.1103/PhysRevD.90.015014.

[56] Mark Thomson. Model-independent measurement of the e$^+$ e$^-$ $\to$ HZ cross section at a future e$^+$ e$^-$ linear collider using hadronic Z decays. *Eur. Phys. J.*, C76(2):72, 2016. doi: 10.1140/epjc/s10052-016-3911-5.

[57] Claude Fabienne Duerig. *Measuring the Higgs Self-coupling at the International Linear Collider*. Dr., Universität Hamburg, Hamburg, 2016. URL `http://bib-pubdb1.desy.de/record/310520`. Universität Hamburg, Diss., 2016.

[58] Junping Tian. Study of Higgs self-coupling at the ILC based on the full detector simulation at $\sqrt{s} = 500$ GeV and $\sqrt{s} = 1$ TeV. 04 2013. URL `http://inspirehep.net/record/1475534/files/1238328_224-247.pdf`.

[59] Katja Seidel, Frank Simon, Michal Tesar, and Stephane Poss. Top quark mass measurements at and above threshold at CLIC. 2013. doi: 10.1140/epjc/s10052-013-2530-7.

[60] Lyn Evans and Shinichiro Michizono. The International Linear Collider Machine Staging Report 2017, 2017.

[61] Massimo Altarelli et al., editor. *XFEL: The European X-Ray Free-Electron Laser. Technical design report*. 2006. ISBN 9783935702171. doi: 10.3204/DESY_06-097. URL `http://inspirehep.net/record/740352/files/european-xfel-tdr.pdf`.

[62] G. Brown, K. Halbach, J. Harris, and H. Winick. Wiggler and undulator magnets — a review. *Nuclear Instruments and Methods in Physics Research*, 208(1):65 – 77, 1983. ISSN 0167-5087. doi: https://doi.org/10.1016/0167-5087(83)91105-5. URL `http://www.sciencedirect.com/science/article/pii/0167508783911055`.

[63] Anna Rosmanitz. Study of Electron Showers in a Prototype Hadron Calorimeter for a Future Linear Collider, Masterarbeit, 2017. URL `https://flc.desy.de/sites/sites_custom/site_flc/content/e21140/e26716/e26721/e77211/Masterarbeit_AnnaRosmanitz_eng.pdf`.

[64] Marc Winter et al. Development of CMOS Pixel Sensors fully adapted to the ILD Vertex Detector Requirements. In *International Workshop on Future Linear Colliders (LCWS12) Arlington, Texas, USA, October 22-26, 2012*, 2012.

[65] I Valin et al. A reticle size CMOS pixel sensor dedicated to the STAR HFT. *Journal of Instrumentation*, 7(01):C01102–C01102, jan 2012. doi: 10.1088/1748-0221/7/01/c01102. URL `https://doi.org/10.1088%2F1748-0221%2F7%2F01%2Fc01102`.

[66] M. Boronat. DEPFET pixel detector for future e^- e^+ experiments. *Nuclear and Particle Physics Proceedings*, 273-275:982 – 987, 2016. ISSN 2405-6014. doi: https://doi.org/10.1016/j.nuclphysbps.2015.09.154. URL `http://www.sciencedirect.com/science/article/pii/S2405601415006434`. 37th International Conference on High Energy Physics (ICHEP).

[67] J.J. Velthuis et al. DEPFET, a monolithic active pixel sensor for the ILC. *Nuclear Instruments and Methods in Physics Research Section A: Accelerators, Spectrometers, Detectors and Associated Equipment*, 579(2):685 – 689, 2007. ISSN 0168-9002. doi: https://doi.org/10.1016/j.nima.2007.05.278. URL `http://www.sciencedirect.com/science/article/pii/S016890020701162X`.

[68] Yasuhiro Sugimoto et al. R&D Status of FPCCD Vertex Detector for ILD, 2012.

[69] Y. Giomataris, Ph. Rebourgeard, J.P. Robert, and G. Charpak. MICROMEGAS: a high-granularity position-sensitive gaseous detector for high particle-flux environments. *Nuclear Instruments and Methods in Physics Research Section A: Accelerators, Spectrometers, Detectors and Associated Equipment*, 376(1):29 – 35, 1996. ISSN 0168-9002. URL `http://www.sciencedirect.com/science/article/pii/0168900296001751`.

[70] F. Sauli. GEM: A new concept for electron amplification in gas detectors. *Nuclear Instruments and Methods in Physics Research Section A: Accelerators, Spectrometers, Detectors and Associated Equipment*, 386(2):531 – 534, 1997. ISSN 0168-9002. doi: https://doi.org/10.1016/S0168-9002(96)01172-2. URL `http://www.sciencedirect.com/science/article/pii/S0168900296011722`.

[71] Particle Data Group. Atomic and nuclear properties of materials: Tungsten (W), 2012. URL `http://pdg.lbl.gov/2012/AtomicNuclearProperties/HTML_PAGES/074.html`. Accessed: 2019-07-04.

[72] Particle Data Group. Atomic and nuclear properties of iron (Fe), 2019. URL `http://pdg.lbl.gov/2019/AtomicNuclearProperties/HTML/iron_Fe.html`. Accessed: 2019-07-04.

[73] The CALICE collaboration. AHCAL Testbeam Campaign at CERN 2015 (July/August), 2015. URL `https://flcwiki.desy.de/AHCALTestBeamCERN2015`. Accessed: 2019-06-29.

[74] The CALICE collaboration and C Adloff et al. Construction and commissioning of the CALICE analog hadron calorimeter prototype. *Journal of Instrumentation*, 5(05):P05004–P05004, may 2010. doi: 10.1088/1748-0221/5/05/p05004. URL `https://doi.org/10.1088%2F1748-0221%2F5%2F05%2Fp05004`.

[75] Felix Sefkow and Frank Simon. A highly granular SiPM-on-tile calorimeter prototype, 2019. URL `https://arxiv.org/pdf/1808.09281.pdf`.

[76] E. Brianne. Time development of hadronic showers in a Highly Granular Analog Hadron Calorimeter, Dissertation. 2018.

[77] Sascha Krause. Experimentelle Charakterisierung von Silizium-Photomultipliern, Diplomarbeit, 2014.

[78] S. Krause, B. Bauß, A.S. Brogna, V. Büscher, P. Chau, R. Degele, K.H. Geib, Y. Liu, U. Schäfer, R. Spreckels, S. Tapprogge, R. Wanke, and Q. Weitzel. Comparison of Silicon Photomultiplier Characteristics using Automated Test Setups. *Journal of Instrumentation*, 11(02):C02067, 2016. URL `http://stacks.iop.org/1748-0221/11/i=02/a=C02067`.

[79] DESY. FEB - Projects - CALICE AHCAL: Electronics for a high granular hadronic calorimeter. URL `http://wof-cluster.desy.de/sites/site_fe/content/feb/projects/`. Accessed: 2019-07-05.

[80] D. Lomidze et al. Design and Calibration of Scintillator Tiles and SiPMs for the AHCAL. URL `https://twiki.cern.ch/twiki/bin/view/CALICE/LCWS2016`. Accessed: 2019-07-05.

[81] Yong Liu, Volker Büscher, Julien Caudron, Phi Chau, Sascha Krause, Lucia Masetti, Ulrich Schäfer, Rouven Spreckels, Stefan Tapprogge, and Rainer Wanke. A Design of Scintillator Tiles Read Out by Surface-Mounted SiPMs for a Future Hadron Calorimeter, 2015.

[82] OMEGA. OMEGA - SPIROC Website. URL `https://portail.polytechnique.edu/omega/en/products/products-presentation/spiroc`. Accessed: 2019-07-05.

[83] M Bouchel et al. SPIROC (SiPM integrated read-out chip): dedicated very front-end electronics for an ILC prototype hadronic calorimeter with SiPM read-out. *Journal of Instrumentation*, 6(01):C01098–C01098, 2011. doi: 10.1088/1748-0221/6/01/c01098. URL `https://doi.org/10.1088%2F1748-0221%2F6%2F01%2Fc01098`.

[84] S Conforti Di Lorenzo et al. SPIROC: design and performances of a dedicated very front-end electronics for an ILC analog hadronic CALorimeter (AHCAL) prototype with SiPM read-out. *Journal of Instrumentation*, 8(01):C01027–C01027, jan 2013. doi: 10.1088/1748-0221/8/01/c01027. URL `https://doi.org/10.1088%2F1748-0221%2F8%2F01%2Fc01027`.

[85] Oskar Hartbrich. Commissioning and LED system tests of the engineering prototype of the analog hadronic calorimeter of the CALICE collaboration. Master's thesis, Wuppertal U., Dept. Math., 2012. URL `http://www-library.desy.de/cgi-bin/showprep.pl?thesis12-040`.

[86] Omega. Performance of 2nd generation ASICs for CALICE/EUDET. URL `https://indico.ihep.ac.cn/event/910/session/5/contribution/206/material/slides/`. Accessed: 2019-06-28.

[87] N. Charitonidis and B. Rae. The H2 Secondary Beam Line of EHN1/SPS, 2017. URL `http://sba.web.cern.ch/sba/BeamsAndAreas/h2/H2manual.html`.

[88] Yong Liu. AHCAL Latest Results & Future Plans, 9th Annual Helmholtz Alliance Workshop on Physics at the Terascale, 2015. URL `https://indico.desy.de/indico/event/12812/session/4/contribution/74`. Accessed: 2019-07-05.

[89] Linear Collider Collaboration. AHCAL Testbeam Campaign at CERN 2015 (July/August). URL `http://flcwiki.desy.de/AHCALTestBeamCERN2015`.

[90] Phi Chau on behalf of the CALICE AHCAL groups. Construction, Commissioning and First Results of a Highly Granular Hadron Calorimeter with SiPM-on-Tile Read-out. URL `https://twiki.cern.ch/twiki/pub/CALICE/IEEE2018/PID5743349_%282%29.pdf`.

[91] Katja Krüger. AHCAL Testbeams in 2018 - Combination of HCAL and AHCAL data, 2018. URL `https://agenda.linearcollider.org/event/8082/`. Accessed: 2019-07-05.

[92] Stephan Martens. Tile reflector wrapping, 2017. URL `https://agenda.linearcollider.org/event/7807/`. Accessed: 2019-07-05.

[93] Arabella Martelli. The CMS HGCAL detector for HL-LHC upgrade, 2017.

[94] Yong Liu. Megatile studies, 2017. URL `https://agenda.linearcollider.org/event/7454/contributions/38717/`. Accessed: 2019-07-06.

[95] HAMAMATSU PHOTONICS K.K. MPPC (Multi-Pixel Photon Counter), S13360 series. 2016. URL `http://www.hamamatsu.com/resources/pdf/ssd/s13360_series_kapd1052e.pdf`.

[96] Claudio Piemonte. A new silicon photomultiplier structure for blue light detection. *Nuclear Instruments and Methods in Physics Research A*, 568:224–232, 2006.

[97] D Renker and E Lorenz. Advances in solid state photon detectors. *Journal of Instrumentation*, 4(04):P04004, 2009. URL `http://stacks.iop.org/1748-0221/4/i=04/a=P04004`.

[98] P. Buzhan, B. Dolgoshein, A. Ilyin, V. Kantserov, V. Kaplin, A. Karakash, A. Pleshko, E. Popova, S. Smirnov, Yu. Volkov, L. Filatov, S. Klemin, and F. Kayumov. An advanced study of silicon photomultiplier. 2007.

[99] Hamamatsu Corporation & New Jersey Institute of Technology Slawomir S. Piatek. A technical guide to silicon photomultipliers (SiPM). URL `https://www.hamamatsu.com/us/en/community/optical_sensors/articles/technical_guide_to_silicon_photomultipliers_sipm/index.html`. Accessed: 2018-02-19, the website is not online anymore.

[100] Hamamatsu Corporation & New Jersey Institute of Technology Slawomir Piatek. Physics and operation of the MPPC silicon photomultiplier. URL `https://www.hamamatsu.com/us/en/community/optical_sensors/articles/physics_and_operation_of_mppc/index.html`. Accessed: 2018-04-11, the website is not online anymore.

[101] HAMAMATSU PHOTONICS K.K. MPPC (Multi-Pixel Photon Counter), S12571-025, -050, -100C/P. 2013. URL `http://pdf1.alldatasheet.com/datasheet-pdf/view/575350/HAMAMATSU/S12571-050.html`.

[102] S. Hidalgo J. Rosado. Characterization and modeling of crosstalk and afterpulsing in Hamamatsu silicon photomultipliers, arXiv:1509.02286v2. 2012.

[103] A. Ghassemi et al. MPPC Technical note. 2017. URL `https://www.hamamatsu.com/resources/pdf/ssd/mppc_kapd9005e.pdf`.

[104] Gerhard Lutz. *Semiconductor Radiation Detectors*. Springer Berlin Heidelberg New York. Springer, 1999. ISBN 978-3-540-71678-5.

[105] Enrico Junior Schioppa. Exact solutions for silicon photomultipliers models and application to measurements, 2017. URL `https://arxiv.org/pdf/1710.11410.pdf`.

[106] P Eckert, R Stamen, and H C Schultz-Coulon. Study of the response and photon-counting resolution of silicon photomultipliers using a generic simulation framework. *Journal of Instrumentation*, 7(08):P08011–P08011, aug 2012. doi: 10.1088/1748-0221/7/08/p08011. URL `https://doi.org/10.1088%2F1748-0221%2F7%2F08%2Fp08011`.

[107] Katsushige Kotera, Weonseok Choi, and Tohru Takeshita. Describing the response of saturated SiPMs, arXiv:1510.01102v4. 2016. URL `https://arxiv.org/abs/1510.01102v4`.

[108] L. Gruber, S.E. Brunner, J. Marton, and K. Suzuki. Over saturation behavior of SiPMs at high photon exposure. *Nuclear Instruments and Methods in Physics Research Section A: Accelerators, Spectrometers, Detectors and Associated Equipment*, 737(Supplement C): 11 – 18, 2014. ISSN 0168-9002. doi: https://doi.org/10.1016/j.nima.2013.11.013. URL `http://www.sciencedirect.com/science/article/pii/S0168900213015520`.

[109] K. Kotera. Applying a SiPM response function to 7608 SiPMs of AHCAL physics prototype, 2016. URL `https://agenda.linearcollider.org/event/7304/contributions/37323/attachments/30512/45645/0g915SiPMfuncApplyingAHCAL2.pdf`.

[110] B.W. Kernighan and D.M. Ritchie. *The C Programming Language*. Prentice-Hall software series. Prentice Hall, 1988. ISBN 9780131103627. URL `https://books.google.de/books?id=161QAAAAMAAJ`.

[111] cplusplus.com. Cplusplus Information Homepage. URL `http://www.cplusplus.com/info/`. Accessed: 2019-06-28.

[112] Q. Weitzel, P. Bernhard, A.S. Brogna, R. Degele, S. Krause, U. Schäfer, and S. Tapprogge. Measurement of the response of Silicon Photomultipliers from single photon detection to saturation. *Nuclear Instruments and Methods in Physics Research Section A: Accelerators, Spectrometers, Detectors and Associated Equipment*, 2018. ISSN 0168-9002. doi: https://doi.org/10.1016/j.nima.2018.10.074. URL `http://www.sciencedirect.com/science/article/pii/S0168900218313883`.

[113] Diego Ramirez Garcia. Steering software in C for the movable stage, 2017.

[114] Advanced Laser Diode Systems. Nano second / picosecond laser datasheet. URL `http://alsgmbh.de/img/products/pilas_datasheet.pdf`. Accessed: 2018-03-27, the website is not online anymore.

[115] Thorlabs. FC488-99B-FC - 2x2 Fiber Optic Coupler, 488 nm, 99:1 Split, FC/PC, 2011. URL `https://www.thorlabs.com/thorproduct.cfm?partnumber=FC488-99B-FC`.

[116] Thorlabs. ED1-S20-MD - SM1-Threaded Mount, Ø1" 20° Square Engineered Diffuser, 2009. URL `https://www.thorlabs.com/thorproduct.cfm?partnumber=ED1-S20-MD`.

[117] Thorlabs. DG10-220 - Ø1" Unmounted N-BK7 Ground Glass Diffuser, 220 Grit, 2004. URL `https://www.thorlabs.com/thorproduct.cfm?partnumber=DG10-220`.

[118] PI. Datasheet M-403: Precision Translation Stage. URL `https://static.physikinstrumente.com/fileadmin/user_upload/physik_instrumente/files/datasheets/M-403-Datasheet.pdf?_ga=2.249325447.1624360909.1522159314-1001670847.1522159314`. Accessed: 2018-03-27.

[119] PI. Four Axis Motion Controller C-884, 2013. URL `http://www.pi-usa.us/products/PDF_Data/C884_Motion_Controller.pdf`.

[120] CAEN SpA. DS3769 A1423B Wideband Amplifier Data Sheet. URL `http://www.caen.it/jsp/Template2/CaenProd.jsp?showLicence=false&parent=13&idmod=942`.

[121] Mathias Reinecke. Diagram of the direct circuit box, 2017.

[122] Struck. SIS1100/3100 Standard design Firmware Version 5/6 User Manual, 2008. URL `http://www.struck.de/sis3100-M-1-1-v135-hardware.pdf`.

[123] CAEN. MOD. V965/V965A Technical Information Manual, 2008. URL `https://www.caen.it/products/v965a/`.

[124] CAEN. MOD. V895 series Technical Information Manual, 2009. URL `https://www.caen.it/products/v895/`.

[125] Struck. SIS3808 32 Channel 20-bit deadtimed multi channel scaler. URL `http://www.struck.de/sis3808.htm`.

[126] Thorlabs. FDS1010, Calibrated Si Photodiode, 350 - 1100 nm, 10 x 10 mm Active Area. URL `https://www.thorlabs.com/thorproduct.cfm?partnumber=FDS1010-CAL`.

[127] Thorlabs. Maximum deviation from linearity for FDS1010-CAL smaller 1% for photo currents smaller 3 mA, 2017. private discussion.

[128] Keithley. Model 6485/E 5-1/2 digit Picoammeter. URL `http://www.keithley.de/products/dcac/sensitive/lowcurrent/?mn=6485E`.

[129] Elektro Automatik. EA PSI 6150-01 Datasheet. URL `http://www.farnell.com/datasheets/43587.pdf`.

[130] Keysight Technologies. 33500B and 33600A Series Trueform Waveform Generators. URL `https://literature.cdn.keysight.com/litweb/pdf/5992-2572EN.pdf?id=2937598`. Accessed: 2018-03-28.

[131] CERN. ROOT Data Analysis Framework, Webpage. URL `http://root.cern.ch/`.

[132] H. Orth. Webpage of ICASiPM - International Conference on the Advancement of Silicon Photomultipliers, 2018. URL `https://indico.gsi.de/event/6990/`. Accessed: 2019-07-28.

[133] Q. Weitzel, P. Bernhard, A.S. Brogna, R. Degele, S. Krause, U. Schäfer, and S. Tapprogge. Poster - Measurement of the Response of Silicon Photomultipliers from Single Photon Detection to Saturation, 2018. URL `https://agenda.infn.it/event/17834/timetable/?view=standard`.

[134] HAMAMATSU. Afterpulse probability of MPPC S1336x series, private communication. 07.03.2018.

[135] DESY. ILC Soft Portal. URL `https://ilcsoft.desy.de/portal`. Accessed: 2019-06-28.

[136] Frank Gaede, Ties Behnke, Norman Graf, and Tony Johnson. LCIO: A Persistency framework for linear collider simulation studies. *eConf*, C0303241:TUKT001, 2003.

[137] F. Gaede. Marlin and LCCD—Software tools for the ILC. *Nuclear Instruments and Methods in Physics Research Section A: Accelerators, Spectrometers, Detectors and Associated Equipment*, 559(1):177 – 180, 2006. ISSN 0168-9002. doi: https://doi.org/10.1016/j.nima.2005.11.138. URL `http://www.sciencedirect.com/science/article/pii/S0168900205022643`. Proceedings of the X International Workshop on Advanced Computing and Analysis Techniques in Physics Research.

[138] A. Provenza and E. Brianne. Internal technical discussion about the AHCAL calibration, 2016.

[139] Ambra Provenza. Calibration and Analysis of Data taken with the Technological Prototype of the Analog Hadron Calorimeter (AHCAL) for a Detector at the International Linear Collider, Dissertation. 2018.

[140] Y. Sudo. Internal technical discussion about HG/LG calibration, 2016.

[141] C Adloff et al. Track segments in hadronic showers in a highly granular scintillator-steel hadron calorimeter. *Journal of Instrumentation*, 8(09):P09001–P09001, sep 2013. doi: 10.1088/1748-0221/8/09/p09001. URL `https://doi.org/10.1088%2F1748-0221%2F8%2F09%2Fp09001`.

[142] J. Allison et al. Recent developments in Geant4. *Nuclear Instruments and Methods in Physics Research Section A: Accelerators, Spectrometers, Detectors and Associated Equipment*, 835:186 – 225, 2016. ISSN 0168-9002. doi: https://doi.org/10.1016/j.nima.2016.06.125. URL `http://www.sciencedirect.com/science/article/pii/S0168900216306957`.

[143] Agostinelli, S. et al. GEANT4: A Simulation toolkit. *Nucl. Instrum. Meth.*, A506:250–303, 2003. doi: 10.1016/S0168-9002(03)01368-8.

[144] P. Mora de Freitas and H. Videau. Detector simulation with MOKKA / GEANT4: Present and future. In *Linear colliders. Proceedings, International Workshop on physics and experiments with future electron-positron linear colliders, LCWS 2002, Seogwipo, Jeju Island, Korea, August 26-30, 2002*, pages 623–627, 2002.

[145] B. Bilki et al. Pion and proton showers in the CALICE scintillator-steel analogue hadron calorimeter. *Journal of Instrumentation*, 10(04):P04014–P04014, apr 2015. doi: 10.1088/1748-0221/10/04/p04014. URL `https://doi.org/10.1088%2F1748-0221%2F10%2F04%2Fp04014`.

[146] C Adloff et al. Validation of GEANT4 Monte Carlo models with a highly granular scintillator-steel hadron calorimeter. *Journal of Instrumentation*, 8(07):P07005–P07005, jul 2013. doi: 10.1088/1748-0221/8/07/p07005. URL `https://doi.org/10.1088%2F1748-0221%2F8%2F07%2Fp07005`.

[147] V N Ivanchenko, O Kadri, M Maire, and L Urban. Geant4 models for simulation of multiple scattering. *Journal of Physics: Conference Series*, 219(3):032045, apr 2010. doi: 10.1088/1742-6596/219/3/032045. URL `https://doi.org/10.1088%2F1742-6596%2F219%2F3%2F032045`.

[148] Vladimir Ivanchenko et al. Recent Improvements in Geant4 Electromagnetic Physics Models and Interfaces. *Progress in NUCLEAR SCIENCE and TECHNOLOGY*, 2:898–903, 10 2011. doi: 10.15669/pnst.2.898.

[149] Geant4 Collaboration. Physics Reference Manual. URL `http://geant4-userdoc.web.cern.ch/geant4-userdoc/UsersGuides/PhysicsReferenceManual/fo/PhysicsReferenceManual.pdf`. Accessed: 2019-06-26.

[150] D.H. Wright and M.H. Kelsey. The Geant4 Bertini Cascade. *Nuclear Instruments and Methods in Physics Research Section A: Accelerators, Spectrometers, Detectors and Associated Equipment*, 804:175 – 188, 2015. ISSN 0168-9002. doi: https://doi.org/

10.1016/j.nima.2015.09.058. URL `http://www.sciencedirect.com/science/article/pii/S0168900215011134`.

[151] Aatos Heikkinen, Nikita Stepanov, and Johannes Peter Wellisch. Bertini intranuclear cascade implementation in GEANT4. *eConf*, C0303241:MOMT008, 2003.

[152] G. Folger and J. P. Wellisch. String parton models in GEANT4. *eConf*, C0303241: MOMT007, 2003.

[153] Geant4 Homepage. Physics Lists, 2017. URL `https://geant4.web.cern.ch/support/physics_lists`. Accessed: 2019-06-22.

[154] A. Galán Ribón et al. Status of Geant4 hadronic physics for the simulation of LHC experiments at the start of LHC physics program, 2010.

[155] Geant4 Homepage. Reference physics lists. URL `https://geant4.web.cern.ch/node/155`. Accessed: 2019-06-22.

[156] Nanda Wattimena. Calorimetry at the International Linear Collider: From Simulation to Reality. 2009.

[157] C. Adloff et al. Construction and performance of a silicon photomultiplier/extruded scintillator tail-catcher and muon-tracker. *Journal of Instrumentation*, 7(04):P04015, 2012. URL `http://stacks.iop.org/1748-0221/7/i=04/a=P04015`.

[158] O. Hartbrich. AHCAL Digitisation - AHCAL ILD vs. Testbeam Simulation Models & Data. URL `http://desy.de/~ohartbri/2015_04_20_CALICE_AHCAL.pdf`. Accessed: 2019-06-22.

[159] E. Brianne. Noise file for the digitization of the simulation, 2016.

[160] K. Gadow et al. Concept, Realization and Results of the Mechanical and Electronics Integration Efforts for an Analog Hadronic Calorimeter. 2010.

[161] HAMAMATSU PHOTONICS K.K. MPPC (Multi-Pixel Photon Counter), S12571-010, -015C/P. 2018. URL `https://www.hamamatsu.com/resources/pdf/ssd/s12571-010_etc_kapd1044e.pdf`.

[162] CERN. How to control the north area beam lines, 2017. URL `http://sba.web.cern.ch/sba/documentations/how2controlnabeams.htm`. Accessed: 2019-01-30.

[163] A Gerbershagen. Overview over CERN SPS test beams. URL `https://indico.desy.de/indico/event/18050/session/7/contribution/7/material/slides/0.pdf`. Accessed: 2019-07-17.

[164] N. Charitonidis and L. Gatignon. E-Mail communication about H2 beamline configuration in 2015, 2019.

[165] K. Krüger et al. Internal communication about electron contamination in H2 beamline, during weekly EPT-meeting, 2016.

[166] D. Dannheim et al. Particle Identification with Cherenkov detectors in the 2011 CALICE Tungsten Analog Hadronic Calorimeter Test Beam at the CERN SPS. 2013. URL `http://inspirehep.net/record/1692694/files/LCD-Note-2013-006.pdf`.

[167] A. Provenza. Internal communication during meeting, 2016.

[168] E. Brianne. Internal communication during meeting, 2015.

[169] A. Provenza. Analysis of July 2015 CERN test beam electron data, Update on the center of gravity in Z, AHCAL Weekly Meeting, 2017. URL `https://indico.desy.de/indico/event/16790/session/2/contribution/2/material/slides/0.pdf`.

[170] Peter Scott. CHI-SQUARE: TESTING FOR GOODNESS OF FIT. URL `http://maxwell.ucsc.edu/~drip/133/ch4.pdf`. Accessed: 2019-04-10.

[171] Hamamatsu Corporation Slawomir Piatek and New Jersey Institute of Technology. How does temperature affect the performance of an SiPM?, 2017. URL `https://hub.hamamatsu.com/us/en/technical-note/sipm-temperature-performance/index.html`. Accessed: 2019-04-11.

[172] The CALICE collaboration. Offline Data Analysis, 2015. URL `https://flcwiki.desy.de/AHCALTestBeamCERN2015/OfflineDataAnalysis`. Accessed: 2019-05-17.

[173] KETEK. Device parameters. URL `https://www.ketek.net/sipm/technology/device-parameters/`. Accessed: 2019-04-24.

[174] The CALICE collaboration. Electron data with the CALICE tile AHCAL prototype at the CERN test-beam — Update, 2008. URL `https://twiki.cern.ch/twiki/pub/CALICE/CaliceAnalysisNotes/CAN-010.pdf`. CALICE Analysis Note 010.

[175] B. Bobchenko et al. Optimization of the light yield properties from scintillator tiles read out directly by silicon photomultipliers, 2016. URL `https://iopscience.iop.org/article/10.1088/1742-6596/675/4/042044/pdf`. Journal of Physics: Conference Series 675 (2016) 042044.

[176] M. Ramilli et al. Silicon Photomultiplier characterization and radiation damage investigation for high energy particle physics applications, 2013. URL `http://www.bo.infn.it/sm/sm13/abstract/S13/m-ramilli.pdf`. Accessed: 2019-04-25.

[177] Ambra Provenza. CALICE Collaboration Meeting 2017: Analysis of July 2015 CERN test beam electron data. URL `https://agenda.linearcollider.org/event/7630/contributions/39791/attachments/32078/48543/CaliceMeeting_27092017_lastVersion.pdf`.

[178] The CALICE collaboration. Database tags for analysis of 2015 data. URL `http://flcwiki.desy.de/DBtagsCERN2015#Database_Tags_for_Analysis_of_2015_data`. Accessed: 2019-03-15.

[179] Olaf Behnke, Kevin Kroeninger, Gregory Schott, and Thomas Schoerner-Sadenius. *Data Analysis in High Energy Physics: A Practical Guide to Statistical Methods*. Wiley-VCH, 2013. ISBN 978-3-527-41058-3.

[180] The CALICE collaboration. Electromagnetic response of a highly granular hadronic calorimeter. *Journal of Instrumentation*, 6(04):P04003–P04003, apr 2011. doi: 10.1088/1748-0221/6/04/p04003. URL https://doi.org/10.1088%2F1748-0221%2F6% 2F04%2Fp04003.

[181] C. Adloff et al. Hadronic energy resolution of a highly granular scintillator-steel hadron calorimeter using software compensation techniques. *Journal of Instrumentation*, 7(09), sep 2012. doi: 10.1088/1748-0221/7/09/p09017. URL https://doi.org/10.1088% 2F1748-0221%2F7%2F09%2Fp09017.

Danksagung

Entfernt aus datenschutzrechtlichen Gründen.

Entfernt aus datenschutzrechtlichen Gründen.

Lebenslauf

Entfernt aus datenschutzrechtlichen Gründen.